# Novel insights and approaches for the analytical characterization of tangible cultural heritage objects

Proefschrift voorgelegd tot het behalen van de graad van doctor in de wetenschappen: chemie aan de Universiteit Antwerpen te verdedigen door

## Andrea Marchetti



Promotor
Prof. dr. Karolien De Wael

Universiteit
Antwerpen

University of Antwerp

Faculty of Science – AXES research group

# Novel insights and approaches for the analytical characterization of tangible cultural heritage objects

## Nieuwe inzichten en benaderingen voor de analytische karakterisering van tastbaar cultureel erfgoed

Thesis submitted in fulfillment of the requirements for the degree of
**Doctor in Science – Chemistry**
at the University of Antwerp, defended by
**Andrea Marchetti**

Promotor:
Prof. Dr. Karolien De Wael (University of Antwerp)

Antwerp, 2021

# Acknowledgements

This PhD thesis is the final result of a challenging but wonderful journey started almost exactly four years ago to the day. Looking back now, it feels unbelievable that so much time has gone by. Yet, thinking of all the wonderful people I had the chance to cross lives with and all the things I had the opportunity to learn, it also feels like it could have easily been eight full years. I wish there was enough time to thank every single person that guided me throughout this journey and helped me reaching this goal, but the acknowledgments would easily end up being longer than the thesis itself. I will do my best to fight my long-winded nature and acknowledge you all nonetheless.

First of all, none of this would have been possible without the trust, guidance and support of my supervisor, Prof. Dr. Karolien De Wael. I cannot thank her enough for giving me this extraordinary opportunity and for believing in me since the beginning of this PhD. Thank you for giving me the freedom to follow my ideas and for teaching me where to stop before getting too lost on wild goose chases. Beside my advisor, I would also like to sincerely thank Prof. Dr. Koen Janssens. Your precious suggestions and collaboration had a great influence on the content and quality of this PhD work. Thank you for sharing your great expertise and experience in the field of conservation science.

I am extremely grateful to Prof. Dr. Ligia Maria Moretto (Ca' Foscari University of Venice, IT), who initiated me to the field of analytical methods almost ten years ago and who was the first person to suggest me to consider Antwerp for my PhD studies. Without your help we would probably not be here today, thank you.

Special thanks go to all my friends and colleagues who have been always there with me throughout this journey, I would have never made it without your moral and professional support. I will be forever grateful to Victoria for her invaluable help and guidance during these years. This research, this thesis and this whole experience would certainly not have been the same without your expertise, your friendship, and your undying optimism even in the most tragicomic situations (fingers always crossed). My sincere gratitude goes to Oli, for his great support and help since the beginning of this PhD both in and outside the lab and for currently detaining the record for the person who managed to convince me to go to the gym for the longest (beating the previous record of a whole month). A huge thank you also to Gert, for being always extremely helpful, patient and available (even when asked to translate the abstract to this thesis in Dutch). It is always a pleasure

monitoring. I would also like to thank Elke Otten, Marjolijn Depulpaep, Dr. Marina Van Bos (KIK-IRPA, Brussels), Prof. Dr. Lieve Watteeuw (KU Leuven) and all the ARTGARDEN members, for showing me the capital importance of a multidisciplinary team to achieve great results in the field of conservation. Thank you also for granting me access to the samples and laboratories of KIK-IRPA. I truly hope we will have the opportunity to collaborate further in the future.

I am very grateful also to Prof. Dr. Claudia Pelosi (University of Tuscia, Viterbo, IT), for kindly providing us with in-house synthesized lead pyroantimonate pigments and historical paint samples; Margje Leeuwstein (Kröller-Müller Museum, Otterlo, NL) for the fruitful discussions and precious inputs in the study of the painting *L'Arlésienne (Portrait of Madame Ginoux)* by Van Gogh included in this PhD work; Dr. Ferenc Borondics and Dr. Christophe Sandts (Synchrotron Soleil, Saint-Aubin, FR) for their fundamental help and assistance during the SR-μ-FTIR and especially O-PTIR analyses described in this thesis; Dr. Jakub Jaroszewicz (Warsaw University of Technology, PL) for welcoming me in his laboratory and for patiently introducing me to the fascinating field of computed tomography.

My special gratitude goes to Clementina, for always being a good friend and for her huge help in the very last steps of this PhD. I would also like to thank all my friends from Vittorio Veneto e dintorni, for always being there during all these years, throughout the distance, pandemic and all. I would have probably never found the strength to move abroad and start (and complete) a PhD were it not for you all always setting the best possible example. Seeing you constantly striving to do better and be better while bravely following your dreams has been a huge inspiration. Grazie fioi.

Most of all I thank my family, and above all my brother Enrico and my parents Ezio and Elisabetta. There is truly no words to fully express my gratitude. You always supported me in every possible way along every single step of this journey (and beyond). I hope you can feel this achievement is as yours as it is mine, because I would certainly not be here if it weren't for you. Truly, I could not have asked for a better family. Grazie.

Finally, I would like to thank Iwona. For staying at my side even when it looked like my choices made no sense. For being incredibly brave and strong (much more than you think) and for truly being my center of gravity throughout these years. Without your love and support nothing would have been the same. Dziękuje Ci z całego serca.

# Abstract

Cultural heritage represents the vehicle of our cultural identity, handed over from past to future generations throughout human history. As a repository of fundamental cultural and social values, the preservation of all forms of cultural heritage is a responsibility of every society and of humankind as a whole. When it comes to tangible cultural heritage, preservation of heritage translates into preservation of objects and, therefore, of the materials they are constituted of. This crucial task relies heavily on the application of scientific analytical methods to answer material and conservation-related questions.

The fundamental contribution of this analytical approach led, in the past decades, to an ever-deepening understanding of the factors governing the degradation of cultural heritage. However, the extreme complexity of the heritage object-environment system results in a massive research field, which inevitably presents relevant open questions. This is where the present PhD work comes into play, attempting to fill knowledge gaps in literature by starting from specific case studies and un-answered research questions. A wide range of unexplained material-environment interactions is considered, from cases in which well-studied materials do not behave as expected, to specific materials whose properties are still not resolved. In addition, shifting the focus from the material-environment interaction to the analytical characterization of specific materials or to the monitoring of the environment, innovative analytical strategies or methodological approaches are introduced in order to overcome current limitations.

The multianalytical research conducted during this PhD unraveled fundamental information on the properties governing the reactivity and long-term behavior of different classes of materials, from $\alpha$-brass in an indoor environment to artists' pigments in the presence of light, moisture and soluble particulate matter (PM). The paramount importance of the synthesis conditions on the composition, physical properties and reactivity of heritage materials was also demonstrated, in particular for stable lead pyroantimonate and unstable Geranium lake artists' pigments. Moreover, the study and characterization of specific heritage objects, namely a series of 16th century reliquary altarpieces and the painting *L'Arlésienne (portrait of Madame Ginoux)*, by Vincent Van Gogh, allowed to obtain relevant insights into their composition and on potential risks for their conservation. The challenging nature of the samples considered, created the perfect opportunity to test an innovative spectroscopic technique, optical photo-thermal IR (O-PTIR), for the characterization of heritage materials. Striking results were

obtained, highlighting a great potential for the application of this non-destructive sub-micron molecular spectroscopy to the analysis of cultural heritage. Finally, in the last section of this work, strategies to implement the continuous monitoring of PM levels in indoor environmental quality studies were also considered, with a particular focus on the identification of environmental hazards for the collections housed in specific conservation environments (War Heritage Institute in Brussels and St. Martin's church in Aalst, BE).

The fundamental knowledge obtained in this doctoral study will ultimately contribute to deepen the understanding of the heritage object-environment system, helping to better characterize, study, interpret and, in the last instance, preserve our cultural heritage for the generations to come.

# Samenvatting

Cultureel erfgoed vertegenwoordigt het vehikel van onze culturele identiteit, overgedragen van vroegere aan toekomstige generaties doorheen de menselijke geschiedenis. Als bewaarplaats van fundamentele culturele en sociale waarden is het behoud van alle vormen van cultureel erfgoed een verantwoordelijkheid van iedere samenleving op zich en van de mensheid in zijn geheel. Als het gaat om tastbaar cultureel erfgoed, vertaalt dit zich in het behoud van objecten en dus van de materialen waaruit ze zijn samengesteld. Het correct uitvoeren van deze cruciale taak hangt af van de mogelijkheid van wetenschappelijke analytische methoden om een antwoord te bieden op materiële en conservatie gerelateerde vraagstukken.

De fundamentele bijdrage van deze analytische benadering heeft in de afgelopen decennia geleid tot een steeds verbeterd inzicht in de factoren die de degradatie van cultureel erfgoed bepalen. De extreme complexiteit van het object-omgeving systeem resulteert echter in een enorm onderzoeksveld, dat uiteraard relevante open vragen opwerpt. Het gepresenteerde doctoraatswerk bevindt zich net in dit onderzoeksveld, waarbij wordt getracht hiaten in de literatuur op te vullen door te vertrekken van specifieke casestudy's en onbeantwoorde onderzoeksvragen. Er wordt gekeken naar een breed gamma aan onverklaarde materiaal-omgevingsinteracties, gaande van gevallen waarin goed bestudeerde materialen zich niet gedragen zoals verwacht tot specifieke materialen waarvan de eigenschappen nog steeds niet zijn ontrafeld. Bovendien, door de focus te verleggen van de materiaal-omgevingsinteractie naar de analytische karakterisering van specifieke materialen of naar het monitoren van de omgeving, worden innovatieve analytische strategieën of methodologische benaderingen geïntroduceerd om de huidige beperkingen te overwinnen.

Het multi-analytisch onderzoek dat tijdens dit doctoraat werd uitgevoerd liet ons toe fundamentele informatie te bekomen omtrent de eigenschappen die de reactiviteit en het lange termijn gedrag van verschillende materialen beheersen, van α-messing in een binnenomgeving tot kunstenaarspigmenten in aanwezigheid van licht, vocht en oplosbaar fijnstof (PM). Het doorslaggevende belang van de synthese omstandigheden voor de samenstelling, fysische eigenschappen en reactiviteit van erfgoedmaterialen werd eveneens aangetoond, in het bijzonder voor stabiel lood pyroantimonaat en onstabiele pigmenten van Geraniumlakken. Bovendien hebben de studie en karakterisering van specifieke erfgoedobjecten, namelijk een reeks 16e-eeuwse

reliekschrijnaltaarstukken en het schilderij *L'Arlésienne (portret van Madame Ginoux)* van Vincent van Gogh, het mogelijk gemaakt om relevante inzichten te bekomen over hun samenstelling en over mogelijke risico's bij de conservatie ervan. De aard van de onderzochte monsters bood de perfecte gelegenheid om een innovatieve spectroscopische techniek, meer bepaald optische fotothermische IR (O-PTIR), te testen voor de karakterisering van erfgoedmaterialen. Er werden opvallende resultaten behaald die het groot potentieel aantonen voor de toepassing van deze niet-destructieve submicron moleculaire spectroscopische techniek voor de analyse van cultureel erfgoed. Ten slotte werden in het laatste deel van dit werk ook strategieën overwogen om de continue monitoring van PM-niveaus in onderzoeken naar de binnenmilieukwaliteit te implementeren, met een bijzondere focus op de identificatie van milieurisico's voor de collecties die zijn ondergebracht in specifieke conservatie omgevingen (Koninklijk Museum van het Leger en de Krijgsgeschiedenis in Brussel en de Sint-Maartenskerk in Aalst, BE).

De fundamentele kennis verkregen in deze doctoraatsstudie zal uiteindelijk bijdragen tot het verdiepen van het inzicht in het erfgoedobject-omgeving systeem, waardoor we ons cultureel erfgoed beter kunnen karakteriseren, bestuderen, interpreteren en, in laatste instantie, bewaren voor de komende generaties.

# Table of contents

# List of abbreviations

**A**

AFM           Atomic force microscopy

ATR           Attenuated total reflectance

**B**

[BMIM][BF4]    1-butyl-3-methylimidazolium tetrafluoroborate

BSE           Back-scattered electrons

**C**

C              Canvas

CA            Chrono-amperometry

CB            Conduction band

CBM           Conduction band minimum

**D**

DO            Drying oil

DR-UV-Vis    Diffuse reflectance UV-Vis spectroscopy

**E**

EDX           Energy-dispersive X-ray

$E_F$            Fermi level

$E_g$            Band gap size

**F**

FTIR          Fourier-transform infrared spectroscopy

**G**

GL            Ground layer

**H**

HVAC         Heating, ventilation and air-conditioning

**I**

IC             Ion chromatography

| ICA | Independent component analysis |
| IEQ | Indoor environmental quality |
| I/O | Indoor to outdoor ratio of pollutants |
| $I_{ph}$ | Photocurrent |
| IR | Infrared |
| IRCELINE | Belgian Interregional Environment Agency |

**L**

| LAY | Lead antimonate yellow |
| LTAY | Lead tin antimonate yellow ($Pb_2SnSbO_{6.5}$) |
| LAY1 | $Na_{0.5}Pb_{1.5}Sb_2O_{6.75}$ in a pyrochlore structure |
| LAY2 | $NaPbSb_2O_{6.5}$ in a pyrochlore structure |
| LOD | Limit of detection |
| LSV | Linear sweep voltammetry |
| LW | Lead white |

**M**

| μ-CT | Micro-computed tomography |
| μ-Raman | Micro Raman spectroscopy |
| MA-XRF | Macro- X-Ray Fluorescence spectroscopy |
| μ-XRF | Micro- X-Ray Fluorescence spectroscopy |

**O**

| OCP | Open circuit potential |
| OM | Optical microscopy |
| OPC | Optical particle counter |
| O-PTIR | Optical photothermal infrared spectroscopy |

**P**

| PTIR | Photothermal infrared spectroscopy |
| PL | Paint layer |
| PM | Particulate matter |
| p-XRF | Portable X-Ray Fluorescence spectroscopy |

**Q**

| QC | Quantum cascade |

**R**

R               Embedding resin

RH            Relative humidity

**S**

SE            Secondary electrons

STEM-EDS   Scanning transmission electron microscopy with energy dispersive X-ray detector

SEM-EDX    Scanning electron microscope with energy dispersive X-Ray detector

SR            Synchrotron radiation

STEM-HAADF  Scanning transmission electron microscopy with high angle annular dark field detector

**U**

UV            Ultraviolet

**V**

VB            Valence band

VBM         Valence band maximum

Vis           Visible

**W**

WE            Working electrode

WHI         War Heritage Institute

**X**

XRPD        X-Ray powder diffraction

# |1

Tangible cultural heritage: objects in their environment

# Abstract

In this first chapter, the reader is introduced to the complexity of the issue of the conservation of cultural heritage and to the multiple facets of the interaction between objects and their environment. An overview of the main factors affecting the stability and degradation of cultural heritage objects, both intrinsic to the object and extrinsic (i.e. environmental), is presented. The role of analytical methods in answering fundamental conservation-related questions is then briefly reviewed, with a particular focus on the specific research questions tackled in this PhD work. At the end of the chapter, the outline and content of this doctoral thesis are presented.

## 1.1 Conservation of tangible cultural heritage

Tangible cultural heritage is a product of human creativity invested with a unique cultural significance and value. However, strictly from a material point of view, it can always be seen as a combination of materials shaped into the form of objects. This is a central concept to this thesis and needs to be the starting point for any consideration on the degradation and preservation of cultural heritage.

This **materiality**, indispensable to express and give shape to what would otherwise remain merely an abstract concept, is in fact also intrinsically linked to an inevitable tendency to degrade. A damage or loss to these materials has an impact that goes well beyond the mere material damage, since they are the medium through which the values are expressed that justify the election of the object to a higher state of cultural significance and to the very status of heritage. Thus, preserving this material component is a task of capital importance in order to preserve our cultural identity for present and future generations.

Conservation and degradation of cultural heritage are two faces of the same coin. Understanding how materials degrade is the first fundamental step to prevent this from happening. The often complex and multifaceted problem of the degradation of tangible cultural heritage can, however, always be traced back to the interaction of two main actors: the **object** and its **environment.** The central role played by the environment in the behavior of heritage objects is at the core of the modern discipline of preventive conservation.

**Preventive conservation** developed from the pioneering work of Garry Thompson, culminated in 1978 in the publication of The Museum Environment.[1] This tome, in which a series of environmental guidelines is introduced for the most optimal conditions in which heritage objects have to be stored and displayed, represents to this day a major inspiration and reference in the field of conservation.

Today, preventive conservation is defined, by the Conservation Committee of the International Council of Museums (ICOM-CC) as "all measures and actions aimed at avoiding and minimizing future deterioration or loss. They are carried out within the context or on the surroundings of an item, but more often a group of items, whatever

their age and condition. These measures and actions are indirect – they do not interfere with the materials and structures of the items. They do not modify their appearance."[2]

In layman's terms, preventive conservation therefore aims at identifying potential risks for the object to be preserved and at preventing them by optimizing the conservation conditions. It is self-evident that, in order to achieve such an ambitious goal, a **detailed knowledge** of the system in exam is necessary. In practical terms, this translates into a need to thoroughly know:

1) the **object**, i.e. to study and characterize its composition and conservation state;
2) the **expected reactivity** for the materials in the object, i.e. to research and investigate the response of single materials and material combinations to specific environmental conditions;
3) the **conservation environment**, i.e. to understand and monitor the environmental conditions and the potential risk factors for the object, better if with high time resolution to immediately identify possible hazards.

This chapter introduces the reader to the main factors, both intrinsic and extrinsic to the object, governing the interaction of tangible cultural heritage with the environment. Given the plethora of possible materials, intrinsic and environmental properties and forms of damage, the focus is kept on parameters relevant in the context of the present PhD work, including examples and references dealing with materials closely related to the ones in exam.

## 1.2 The object

The **reactivity** of any object towards the environment is intuitively a direct result of the properties of the single materials and/or combination of materials constituting it. Every material is characterized by a series of **chemical** and **physical properties** which determine its overall stability in relation to specific environmental stimuli, as well as to different materials.[3] These properties strongly depend on the nature of the material and on its chemical composition.

From a thermodynamic point of view, materials are rarely in a condition of equilibrium in relation to the atmospheric environment.[4] For this reason, when exposed to

meteorological and/or chemical environmental agents, they undergo **physicochemical transformations** in order to reach an energetically more favorable state. Such transformations, normally involving significant changes in the structure and chemical composition of the materials, can result in altered physical or mechanical properties and are, therefore, at the core of the degradation problem for heritage objects.[5] Changes in the bulk or surface properties of cultural heritage materials can, in fact, have dramatic consequences for the conservation of tangible cultural heritage.



*Figure 1.1_Examples of the severe effect of material degradation on the structural and aesthetical properties of different types of heritage objects: a) well-preserved (left) and heavily corroded (right) 16th-century brass sequins; b) Roman round-bottomed glass vase, the heavy rainbow luster is a product of weathering;[6] c) "The Bedroom" by Vincent Van Gogh before (left) and after (right) digital reconstruction of the original colors, the color change from purple to blue is attributed to the fading of red lake pigments (credits to the Van Gogh Museum).*

A clear example is represented by the loss of structural properties associated with the corrosion of historical metals taking place, for example, in archaeological contexts.[7,8] The

oxidation of metals and alloys, in particular in contact with moisture and soluble salts but also with weathering glass,[9–11] can in fact lead to extreme levels of corrosion, to the point that the very **structure of the object is lost** (Figure 1.1a).

The chemical alteration of heritage materials can also show a less extreme nature while remaining, nonetheless, damaging for the object as cultural heritage. This is the case, for example, for glass weathering and color change in paintings. For the glass, the interaction with moisture and gaseous pollutants can give rise to hydration and cation leaching processes on the surface of the glass, which can result in the formation of superficial silica-rich gel layers.[12] These iridescent and opaque layers can ultimately translate into a complete transformation in the appearance of the once transparent glass object (Figure 1.1b).[13–15] In a similar fashion, the chemical alteration of pigments in paintings can lead to significant changes in their properties and, among others, of their color and appearance (Figure 1.1c).[16–21] In a form of art so intimately interconnected with color, such a transformation can significantly disrupt the perception and message of the artistic representation, potentially leading to a **loss of value** that goes well beyond the mere economical meaning of the word.[22–24]

## 1.2.1   Intrinsic properties of materials

The nature of every material is characterized by a great number of intrinsic properties, ultimately traceable to either the chemical or physical domain.[25] These properties are strongly linked to the type of material in analysis and to its synthesis and manufacturing conditions. Changes (even minor) in these conditions can therefore significantly affect the properties of the material and consequently alter its reactivity. This needs to be a central concept when aiming at accurately reproducing the reactivity of heritage objects. **Synthetizing historically accurate materials**, by studying historical sources and optimizing the synthesis conditions in the laboratory to match the material features observed in the objects, is in fact of capital importance in order to draw relevant conclusions.

The **chemical composition** is a first fundamental parameter determining the overall reactivity of a material. This is true for major chemical components, as clearly exemplified by the completely different reactivities of different metals and alloys (e.g. gold, silver, iron and copper alloys)[5,26] or of glasses with higher or lower silica content,[5,12,27] but it is also true for minor and even trace components. A clear example

30

of the fundamental effect of minor components on the reactivity of materials is the case of brass. Brass is an alloy of copper and zinc characterized by a good resistance to corrosion, but also by a certain predisposition to tarnishing (i.e. surface oxidation causing mostly aesthetical but not structural damage) and dealloying.[28–30] The presence of minor components in the alloy, among others Ni, Sn, As and Al in concentrations below 0.2-0.3%, can increase the stability of the material, while small amounts of Fe and Pb might favor its degradation.[31]

Different **physical properties** can, depending on the nature of the material, play a key role in the reactivity. For instance, properties such as **metallographic structure** and **surface morphology** can positively or negatively influence the long-term stability of metals. Smaller metallographic grains and higher strain, for example, can lead to an increased reactivity in Cu-alloys.[31,32] In a similar fashion, a higher surface roughness is normally associated with a higher tendency to corrode.[33–35] For different materials, however, the physical properties affecting the tendency to degrade can be completely different. For light-sensitive artists' pigments and dyes, for example, the **properties regulating the interaction with light**, e.g. energy of fundamental and excited electronic states and absorbance of UV and visible light,[36–40] together with strictly related factors such as **particle size** and **crystalline structure**,[41–44] normally play a more central role. The strong link between these properties and the chemical composition of the material is evident. An artists' pigment clearly summarizing the intercorrelation between all these parameters is Chrome Yellow. The name Chrome Yellow refers to a family of synthetic lead chromate pigments which can, depending on the synthesis protocol and conditions, contain different amounts of sulfur in their structure. The reactivity of these pigments, often showing a tendency to darken when exposed to visible light, moisture and soluble salts, can be traced back to their semiconducting nature and optoelectronic properties.[20,36,45] In this case, the presence of increasing amounts of S in the crystalline lattice causes 1) a change in the crystalline structure (shift from a monoclinic to an orthorhombic geometry), 2) a change in the optoelectronic structure and absorbance properties (increase in band gap size and in the position of valence and conduction bands) which result in 3) a higher tendency for $Cr^{6+}$ to be reduced to $Cr^{3+}$, translating into higher darkening and therefore a more severe degradation.

It is important to mention that changes in reactivity induced by structural changes, but not linked to a different chemical composition, are also possible. This is the case, among others, for different forms of titanium dioxide ($TiO_2$) and for some chalcogenide semiconducting pigments, such as CdS and HgS. In the first case, rutile and anatase, the

two most common forms of $TiO_2$, show different optoelectronic properties and photocatalytic reactivity due to changes in the type of crystalline lattice.[46,47] In the second case, both CdS and HgS can show an increased tendency to oxidize and degrade if characterized by a lower degree of crystallinity (depending on the synthesis conditions).[41,43]

All these examples clearly demonstrate why the thorough **characterization** of chemical composition, but also of material-specific physical properties, is of capital importance in order to **understand and predict** the reactivity and long-term behavior of tangible cultural heritage.

## 1.2.2   Material-material interactions

Since objects are often composed of more than one material, specific material-material interactions can also significantly affect the stability of cultural heritage. This form of degradation can be caused by a direct **chemical** reaction between the materials, or by a **physical** (e.g. mechanical) or **indirect** (e.g. due to the off-gassing of pollutants) form of interaction.

<u>Examples of chemical interactions between materials</u>

One of the most common and understood forms of degradation, mediated by a chemical interaction between heritage materials, is the **galvanic corrosion** of different metals in electronic and electrolytic contact. Two different metals put in contact in the presence of an electrolyte (e.g. moisture and soluble particulate matter), in fact, creates the equivalent of a galvanic cell.[10,26] The metal characterized by the lowest electrochemical potential then behaves as an anode in the cell, being oxidized and solubilized in the electrolytic solution. The cathode, on the other hand, receives electrons from the anode and transfers them to electron acceptors in solution (e.g. $O_2$). The final result is normally the formation and precipitation of corrosion products of the anodic metal.[5] Often, however, the chemical interaction between heritage materials is also initiated by the degradation of at least one of the components. A relatively straightforward example is the **glass-induced corrosion of metals** (Figure 1.2a). In this case, the degradation is initiated by the hydration and cation exchange processes involved in the weathering of glass.[9,12] One of the results of this deterioration process is the formation of a thin liquid
32

film characterized by high pH and alkali content on the surface of the glass. $CO_2$ and other acidic gaseous species in the conservation environment can also be solubilized in this film.[48] If this concentrated alkaline solution comes in contact with the metal, as it can happen in joint metal-glass objects, this can promote the oxidation and solubilization of the metal component, ultimately reprecipitated in the form of mixed metal corrosion products.[9,48–50] No interaction is observed, however, if the glass is not deteriorated in the first place. A similar phenomenon is observed in the **iron gall ink-mediated oxidative degradation of historical paper** (Figure 1.2b), where the initial hydrolysis of the ink triggers degradation processes ultimately leading to the depolymerization of the cellulosic component of the paper.[51]
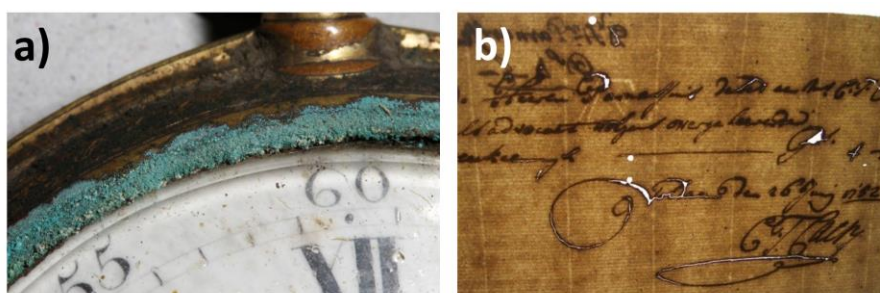


*Figure 1.2_Examples of chemical interactions between heritage materials: a) glass-induced metal corrosion;[48] b) iron gall ink-mediated corrosion of paper.[52]*

A more complex case of chemical interaction between materials is the formation of **metal carboxylates** in paintings, often forming surface efflorescence resulting in specific conservative issues.[53] These species, in fact, might form during the ageing of the paint film due to a chemical interaction between metallic salts (mostly Pb or Zn) and a siccative oil, but they might also be voluntarily included as additives to modify the mechanical properties of the paint. Despite extensive research in the past decade, a full understanding of this issue has not been achieved yet.[53,54]

A catalytic degradation of paintings associated to a **chemical interaction between pigments and oil binder** can occur also in the case of semiconducting pigments.[39,46,55] Whether intrinsically stable, such as $TiO_2$,[46,55] or unstable, such as CdS,[39,56] the absorption of UV or visible light by the pigment particles can, in fact, trigger an oxidative degradation of the binding medium.

Examples of physical/mechanical interactions between materials

The degradation of heritage objects due to material-material interactions can take place also when no direct chemical interaction is observed. The close contact between materials with **different physical and mechanical properties**, for example, can also result in **mechanical and structural damage**. An object where two (or more) materials are present that show a different volumetric response to changes in the thermo-hygrometric conditions, in fact, can develop severe mechanical stress at the interface. This is the case, among others, for easel paintings.[57] These are complex multilayered objects, with significant differences in chemical composition and hygroscopicity between different layers.[58] Such an intrinsic heterogeneity, can result in severe deformation and mechanical damage upon changes in the relative humidity (RH) of the conservation environment[57] (Figure 1.3a).

Structural damage due to mechanical stress between two materials in contact, can also result from the formation of **corrosion products at the interface**. For example, if corrosion products of metals are formed at the interface with a different rigid material, the increase in volume can cause some severe mechanical damage. This is clearly the case for oil paints on metal supports, where the corrosion of the metallic substrate can cause the detachment of large parts of the polymerized, and therefore relatively rigid, paint layer[59,60] (Figure 1.3b).
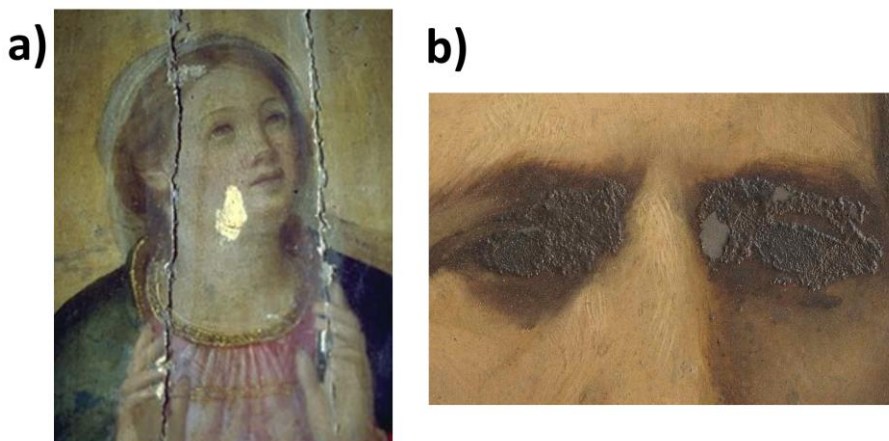


*Figure 1.3_Examples of structural damage induced by physical interactions between heritage materials: a) damaged paint layers in a panel painting due to the RH induced deformation of the wooden substrate;[61] b) blistering and loss of material from an oil paint layer due to the corrosion of an underlying metal substrate.[60]*

<u>Indirect interactions between materials</u>

An additional possible scenario is the degradation of heritage objects due to material-material interactions in which, not only the materials do not show a direct chemical interaction, but they are not in physical contact either. Such an interaction can take place when the ageing of one of the materials results in the **off-gassing of pollutants** causing the degradation of the second material.[62,63] Such an interaction straddles the border between material-material interactions in the objects and object-environment interactions. Even though these gaseous pollutants are a product of a material in the object, in fact, once they enter the conservation environment, they rather become an extrinsic (i.e. environmental) factor of degradation.

### 1.2.3   Other object-specific properties

Another property which cannot be referred to a specific material nor a combination of materials, but rather only to a fully formed object, is the overall **shape**. Such a factor might play a relevant role especially in objects characterized by a complex three-dimensional geometry, such as sculptures and historical buildings. In this case, in fact, different areas of the object will be differently exposed to weathering and other environmental agents even in indoor conditions, potentially also favoring phenomena of condensation or accumulation of degradation products.[3]

## 1.3  The conservation environment

It was believed, in the past, that an object was safe as long as it was housed in a museum or similar institution. Today, thanks to the extensive scientific research conducted in the last decades, one is conscious that the environmental quality, even in indoor environments (i.e. the **indoor environmental quality - IEQ**), plays a central role in the degradation of cultural heritage.

The building undoubtedly offers a substantial protection to the object compared to the outdoor conditions. However, depending also on the type of building and on its functionality/use (e.g. art museums, historical churches, archives, libraries, other

institutions housing a heritage collection, …), specific hazards can arise for the objects. In Figure 1.4, a schematic representation of a generic indoor conservation environment housing heritage objects is presented (based on Anaf[64]). The surroundings of the object can be interpreted as concentric shells, where every shell offers a certain degree of protection against the influence of the **outdoor environment**. The first level of protection is offered by the building, or the specific room, in which the object is kept, insulating to a certain extent the indoor environment from the outdoor. For further protection, the objects in the room can also be housed in smaller "boxes", such as showcases or cabinets. The higher the number of concentric boxes enclosing the object, and the higher their efficiency, the more the object will be protected from the influence of outdoor environmental hazards. However, **indoor sources of pollution** also exist and, depending on their source (e.g. the object itself or the building materials of showcases and cabinets), their concentration might increase significantly inside smaller "shells".[65]
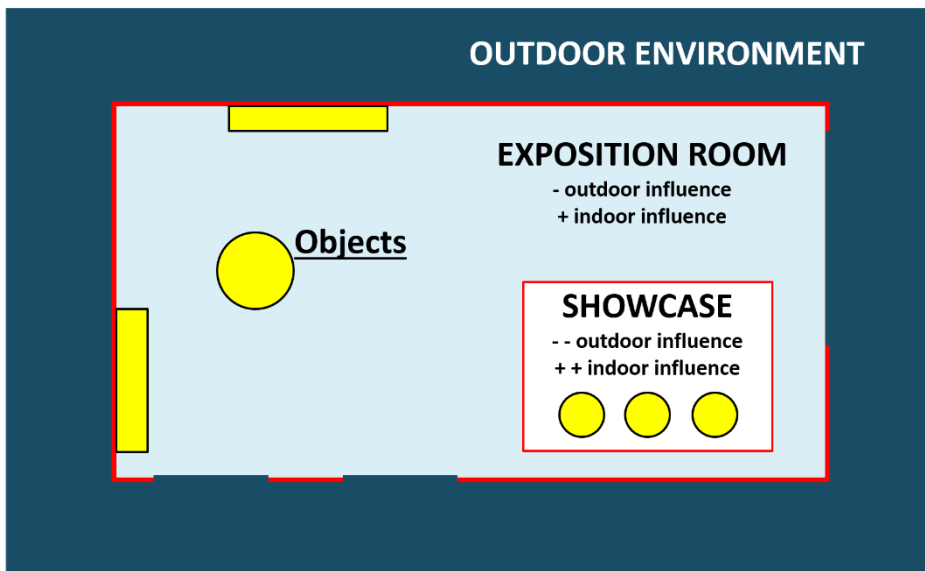


*Figure 1.4_Schematic representation of a generic indoor conservation environment as a series of concentric shells offering increasing insulation from the outdoor environment (based on Anaf[64]).*

Such a general sketch can help to visualize the different "levels" of the conservation environment, but the indoor environmental quality (IEQ) itself is a much more complex matter. Several **meteorological** and **chemical factors** can in fact interact and influence the object, often synergistically. In the following sections the main factors at play are schematically introduced. Since, in the words of an expert of environmental quality and

cultural heritage such as Prof. Dario Camuffo, "It *is absolutely restrictive to consider the individual parameters separately [...] omitting interactions and feedbacks between them and the surfaces."*,[66] the focus is kept on the potential risks for the objects associated with groups of environmental factors ascribable to "outdoor" or "indoor" influences. A more detailed overview of the complexity of the conservation environment and of the parameters, extrinsic to the object, affecting the stability of tangible cultural heritage is given in Figure 1.5.
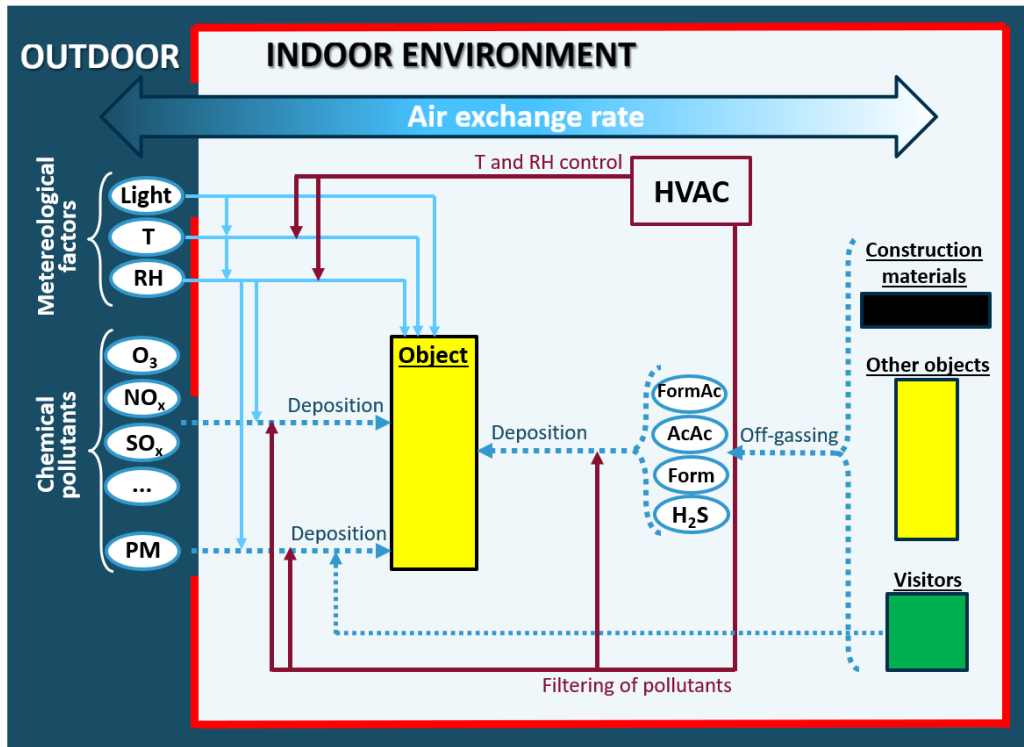


*Figure 1.5_Schematic representation of (some of) the factors potentially affecting the IEQ and their complex interactions in an indoor environment (based on Anaf[64]). AcAc = acetic acid, FormAc = formic acid, Form = formaldehyde.*

## 1.3.1    Outdoor influences

The outdoor environment always exerts a certain influence on the indoor conservation conditions. Meteorological factors such as **temperature (T)**, **relative humidity (RH)** and **light**, intimately interconnected and strongly related to the solar cycle,[66] often play a key role in degradation.[1] Higher temperatures are generally associated to higher reactivity

and faster degradation.[64] The outdoor temperature can cause the cooling or heating of the outer building walls, resulting in an increase or decrease of the indoor temperature (if not accurately controlled) and in a thermal gradient between wall and indoor air.[67] An increase in thickness or in the insulating efficiency of the walls, however, can increase their buffering capacity and help controlling the indoor temperature.[68] RH is negatively correlated with T and, like indoor T, is strongly influenced by the outdoor conditions (e.g. absolute humidity).[66] Local T gradients thus result in local changes in RH, potentially favouring the condensation of moisture on heritage surfaces (if colder than the surrounding air).[66] Since liquid water plays central roles in most forms of degradation, e.g. by solubilizing gaseous species and particulate pollutants and favouring their reaction with sensitive materials, or by acting as a medium for biological degradation processes, this represents a great risk for the object.[9,12,39,45,56,69–72] Even in conditions of RH in which condensation does not directly take place, hygroscopic objects will absorb and desorb water vapour until reaching an equilibrium with the environment.[69] Given the volumetric changes often associated to hydration or dehydration of materials, fluctuations of the environmental RH value can lead to severe mechanical stress, deformation and damage, especially in fragile, degraded and/or composite materials.[57,69,73,74]

An additional meteorological factor that influences the indoor environmental quality and is potentially linked to the outdoor environment is light illumination. The exposure to sunlight, and in particular to visible and UV light, can trigger photochemical processes of degradation in several organic (e.g. varnish and binding media in paintings, dyes, textiles, paper[1,75]) but also in some inorganic materials (e.g. semiconducting pigments in paintings[36,39,55,76]). Moreover, light is also intuitively connected to T. The exposure to light can cause local increases of temperature on the surface of the objects, which can result in dehydration, dimensional changes and damage.[75] Furthermore, the heat-component of sunlight can also give rise to a greenhouse effect in (semi-)enclosed translucent environments (e.g. showcases and cabinets), resulting in extreme temperature variations.[64] Nowadays, sunlight is normally substituted by artificial light in the vast majority of museums and conservation institutions. Although easier to control in order to limit the exposure of the objects and slow down the degradation, however, artificial light will still trigger photochemical degradation in sensitive materials.[1,75]

In addition to meteorological factors, the indoor environmental quality can be also affected by the infiltration of **outdoor pollutants** through the building shell.[63] Gaseous and particulate pollutants can, in fact, reach levels nearly equal to the outdoor

38

environment in naturally ventilated buildings (e.g. through open windows and doors).[63] Even in better insulated buildings, however, gases and fine particles (size fraction of 0.1 to 1 µm) can anyway penetrate in the indoor conservation environment.[77,78] The major **gaseous** outdoor pollutants that can be found indoor and that represent a risk to cultural heritage are sulfur dioxide, nitrogen oxides, carbon dioxide and ozone.[63,79] These gases, in combination with atmospheric moisture, are in fact well known to promote the oxidation and acidic degradation of several types of heritage materials, from stone and metals to dyes and textiles.[63,79–82]

In addition to gaseous pollutants, also **airborne particulate matter (PM)** can have a significant impact on the conservation of heritage objects. In general, the deposition of PM in combination with other environmental factors can result into visual, mechanical, biological, and chemical damage. Visual damage, due to the accumulation of particles on the surface of the object (i.e. soiling) which can ultimately alter its aesthetic appearance and overall message, is one of the most obvious and known effects of PM.[79,83] Furthermore, mechanical damage can be directly caused by particles with high hardness (e.g. silicates) scratching the surface of the object,[84] or indirectly caused by aggressive treatments used to clean soiled surfaces.[85] Biological forms of degradation can be associated either with the direct deposition of biological particles which can cause biodeterioration of sensitive materials in favourable microclimatic conditions,[86] or can be indirectly favoured by the deposition of hygroscopic PM facilitating the condensation of moisture.[87] In a similar fashion, the chemical damage induced by PM is often also closely related to their capacity to absorb water from the atmosphere. The combination of soluble salts and moisture can, in fact, form electrolytic solutions with a fundamental role in the corrosion of metals[11,88] and in the photochemical degradation of semiconducting pigments.[36,39,55,76]

The amount in which these outdoor pollutants enter the conservation environment is ultimately determined by the **air exchange rate** between indoor and outdoor.[89] This air exchange can occur in a natural and non-controlled manner through windows, doors and small gaps in the construction materials, or mechanically, through **heating, ventilation and air-conditioning (HVAC)** systems.[64] When high levels of pollutants are present in the outdoor environment, lowering the air exchange rate (e.g. by closing windows and doors) can help to prevent the contamination of the indoor environment and an increased risk for the objects.[77] Low concentration of pollutants in the outdoor environments are, anyway, always an advantage for conservation purposes.[77,78] Nowadays, the outdoor influence on the indoor environment is normally further limited

by means of HVAC and filtering systems. HVAC can help controlling T and RH values and prevent extreme fluctuations,[90] while filtering systems can reduce the indoor levels of outdoor chemical pollutants to values as low as five percent of the outdoor concentrations.[91] Although appearing, at first sight, like an ideal solution to control the indoor environmental quality, vigilance is advised when employing HVAC-systems.[77,92–94] A breakdown of the system, for example, could strongly impact the indoor environmental quality, potentially inducing drastic changes in T and RH. Moreover, the malfunctioning of the filtering system, could potentially spread outdoor pollutants at a high rate in the conservation environment.

## 1.3.2   Indoor influences

Even in the hypothetical case in which the conservation environment could be perfectly controlled and shielded against outdoor influences, the IEQ could still be significantly affected by indoor sources of pollution. The most common **indoor-generated gases** posing a threat to heritage objects are acetic acid, formic acid, acetaldehyde, formaldehyde, hydrogen sulfide and carbonyl sulfide.[63] In indoor conservation environments, these pollutants are normally produced due to off-gassing reactions taking place during the ageing of either building materials (e.g. acetic acid and formaldehyde from wood and glues in showcases and cabinets) or materials in the objects to be preserved (e.g. S-containing gases from degrading silk or wool).[63] In partially **enclosed environments** such as showcases and cabinets, especially if characterized by low air exchange rates, these indoor-generated gases can easily **build-up** and represent a severe threat for heritage objects.[65] In particular, reduced sulfur gases can be particularly dangerous for metals, and especially for silver,[1,63] and for specific artistic pigments, especially if Cu- or Pb- based,[95] due to the formation of dark metal-sulfides. Formaldehyde and acetaldehyde, on the other hand, are normally converted into their corresponding acid forms due to the interaction with moisture and $O_2$ or other oxidizing species. Formic acid and acetic acid (which can also be directly off-gassed by indoor sources) are then deposited onto heritage materials, promoting their corrosion and the formation of acetates and formates as final degradation products.[63] Materials such as glass and metal, particularly sensitive to acidic environmental conditions, can be severely damaged by this type of degradation processes.[9,49,62,63] In addition, several other volatile organic compounds (VOCs) (e.g. acetone, α-pinene, limonene, hexane) can be generated due to off-gassing from indoor sources however, fortunately, most of these gases do not pose a threat to collections.[63]

40

An additional source of pollutants in the indoor environment can be represented by the **human presence** (e.g. visitors). Although playing an indispensable part in the valorisation of the heritage objects, visitors can in fact negatively affect the overall environmental quality by inducing a local increase in T and RH, by emitting a wide range of organic and inorganic gaseous pollutants (e.g. aldehydes, $CO_2$, CO, $NH_3$, $H_2S$),[64,96] and by either introducing new PM in the environment (e.g. soil dust sticking to the shoes, clothing fibers, skin flakes) or resuspending previously settled particles with their passage.[79,97,98] In addition, indoor sources causing the increase in PM levels can be **construction or restoration works**,[99] due to either newly generated particles or to the resuspension of deposited PM.

In conclusion, in addition to the intrinsic factors described in the previous sections, a great number of environmental factors extrinsic to the heritage object and often intercorrelated in a complex manner can play a fundamental role on its degradation. This makes the **simultaneous monitoring** of all these parameters a cardinal point in the preventive conservation of the object.

## 1.4  The role of analytical methods to answer fundamental conservation questions

The capital need for an in-depth knowledge of the heritage object-environment system led, over the years, to an increasing contribution of analytical chemistry in the field of conservation.[100] Nowadays, a plethora of material characterization techniques are employed on a daily basis to **identify original materials and degradation products** in heritage objects. In addition to non-invasive methods of analysis (i.e. the object can be analyzed as it is, no sampling is necessary and no damage is induced), the invasive collection of microscopic samples is often necessary to further the understanding. Samples are also frequently embedded in optically transparent resins and cross- or thin-section are prepared, in order to highlight specific stratigraphic, structural or compositional features. Moreover, the **reactivity of heritage materials** in response to specific environmental conditions is **modelled in the laboratory** by 1) synthesizing historically accurate materials (the accuracy is normally confirmed by an in-depth characterization), 2) naturally or artificially ageing them (e.g. by exposing the material to high T and RH, intense UV-Vis light, high concentrations of specific pollutants) and 3)

verifying eventual changes in composition or in the physical properties of the material and comparing them with the findings in real historical objects.

To give a comprehensive overview of all the analytical techniques applied to the study of cultural heritage would be extremely complex and, certainly, beyond the scope of the present work. In the following sections, some of the family of techniques most commonly employed to study cultural heritage materials or environments and most relevant for the present work are briefly introduced. More detail is reserved, on the other hand, to the description of novel techniques employed in this PhD work.

## 1.4.1   Atomic spectroscopies

**Spectroscopy** is a general term referring to a broad family of analytical methods studying the interactions of different types of **radiation** with **matter**. Traditionally, interactions between electromagnetic radiation and matter are considered (although interactions between matter and other forms of energy, such as acoustic waves and beams of particles such as ions and electrons are also studied).[101]

Atomic spectroscopic methods, in particular, exploit these quantized material/energy interactions in order to obtain qualitative and/or quantitative information on the **elements** present in a given sample. The most common families of atomic spectroscopic methods are optical spectrometry, mass spectrometry and X-ray spectrometry. In the first two cases, the samples need to be converted to gaseous atoms or elementary ions, and therefore destroyed, in order to obtain elemental information. This is often a drawback in the field of Conservation Science given the value of the objects in exam (although the need for high sensitivity can justify the use of such methods in specific cases).[100] For this reason, X-ray-based methods are much more commonly employed for the elemental (but not only) characterization of heritage materials.

X-ray-based methods

X-ray spectroscopy can be based on the measurement of emission, absorption, scattering, fluorescence and diffraction of X-rays by a specific material.[100,101] These interactions can unravel fundamental material information not only in a **non-destructive** (i.e. a sample needs to be taken but is not destroyed during the analysis), but potentially also in a **non-invasive** manner. Furthermore, the use of micro and nano-sized X-ray

beams, such as the ones produced in **synchrotron** facilities, can allow to unravel material information down to a sub-micrometric scale.[102]

**X-ray fluorescence (XRF)** based laboratory techniques, in particular, are some of the most commonly employed methods for the **elemental analysis** of heritage objects.[103] By exploiting the element-specific nature of X-ray-induced fluorescence, in fact, these methods allow a non-invasive material characterization in qualitative and, if appropriately calibrated, quantitative terms. One of the main limitations of non-invasive XRF analysis is the low sensitivity towards light elements (such as Mg, Na or lower) due to the low energy of their fluorescent X-Rays which are then easily re-absorbed by the sample or by air.

In this PhD work, different types of non-invasive instrumental solutions based on the XRF principle were employed to study historical objects: handheld portable-XRF (p-XRF) and laboratory micro-XRF (μ-XRF), in particular, were used for point analysis at different spatial resolutions (around 9 mm and 70 μm in diameter respectively) (Chapter 2 and Chapter 3), macro-XRF (MA-XRF), on the other hand, was used for the high-resolution elemental imaging of relatively flat and large samples (Chapter 3). A benchtop energy dispersive XRF (EDXRF) instrument was also used to characterize the elemental composition of PM sampled in a museum environment (Chapter 7).

A strongly related analytical method, also based on the emission and detection of element-specific fluorescent X-rays but induced by an incident electron beam, and not by incident X-rays, is **energy-dispersive X-ray (EDX) spectroscopy**.[101] EDX probes are normally implemented in electron microscopy in order to complement the morphological information normally obtained with microscopy with **elemental analysis** and imaging at micrometric resolution. The fact that the analysis are normally performed in high-vacuum, allows to detect lighter elements than in conventional XRF. The small dimensions of the sample chamber, however, makes the sampling of large objects necessary in order to be analyzed with this technique.

In this PhD, EDX analysis were often employed both in association with scanning electron microscopy (SEM) and scanning transmission electron microscopy (STEM), in order to obtain semi-quantitative information on the composition and elemental distribution of different types of original (Chapter 2, Chapter 3, Chapter 6) and in-house synthesized materials (Chapter 4, Chapter 5).

In addition to elemental information, the study of the interaction between X-rays and matter can unravel fundamental information also on the structural properties of materials and objects. Due to the short wavelength of the X-region of the electromagnetic spectrum, in fact, the diffraction patterns of X-rays due to the interaction with matter can unravel fundamental information on the arrangement and spacing of atoms in crystalline materials. **X-ray powder diffraction (XRPD)** methods, therefore, can help to qualitatively **characterize crystalline materials** in heritage objects (e.g. original or degradation products). Furthermore, given the influence of crystalline structure on the reactivity of materials, XRPD is a fundamental technique to preliminarily verify the historical accuracy of in-house synthesized materials for degradation studies. Some of the limits in the application of XRPD on real samples are the relatively low sensitivity, especially in complex mixed samples, and the constraints associated with the instrumental geometry (especially for non-invasive analysis in reflection mode), which make the study of highly irregular three-dimensional surfaces extremely complex if not impossible.

In this PhD work, XRPD was specifically employed to characterize degradation products on heritage objects (non-invasively in a reflection geometry, Chapter 3) and in-house synthesized artists' pigments (non-destructively in a transmission geometry, Chapter 4 and Chapter 5).

An additional family of X-ray-based techniques, which allows to obtain micro-spatial and micro-structural information on heritage objects, is the group of radiographic and tomographic techniques.[103] In general, **X-ray radiographic and tomographic techniques** are both imaging techniques which rely on the differential attenuation of X-Rays passing through an object, due to local differences in density and structural composition, to non-invasively **visualize the morphology and structure of objects**.

In this thesis, laboratory micro computed tomography (μ-CT) was used in order to non-invasively investigate the conservation state of historical glass beads, mapping in particular the distribution of degradation products of the interaction between glass and metal (Chapter 3).

### 1.4.2   Molecular spectroscopies

Molecular spectroscopic methods, unlike atomic spectroscopies, generally exploit the interaction between matter and electromagnetic radiation at energies lower than the X-region. These radiations at lower energy can induce **electronic** (UV and Visible light), **vibrational** (IR region of the spectrum) and **nuclear spin** (Radio frequencies) **transitions**.[101] Techniques based on these principles allow, therefore, to obtain information on the fundamental and excited state of organic and inorganic materials (UV-Vis based spectroscopic methods), as well as on their molecular composition and structural properties (IR, Raman and NMR spectroscopies). In addition, molecular mass spectrometric methods also exist, based on the ionization of the sample and separation of molecular ions based on their mass/charge ratio, which allow to identify molecules with extremely high sensitivity.[101]

In this PhD work, techniques based on the **UV-Vis** range of the electromagnetic spectrum (and in particular on the absorption/reflection of this radiation by the sample) were employed to obtain information on the **electronic structure and optical properties** of pigments in the solid state and to characterize soluble species in solution. In particular, diffuse reflectance UV-Vis (DR-UV-Vis) spectroscopy was used to probe the opto-electronic structure of semiconducting pigments and to calculate the size of their optical band gap (Chapter 4). UV-Vis absorption spectroscopy in solution, on the other hand, was employed to characterize the nature of colored species in solution (Chapter 5).

Vibrational spectroscopies based on the **IR** region of the spectrum were also extensively used in this PhD work. In the first place, **Fourier-transform infrared spectroscopy (FTIR)** both in transmission and in attenuated total reflectance (ATR-FTIR) mode were employed. FTIR (in particular in the mid-IR region) is an extremely widely employed technique in the field of Conservation science. This is mainly thanks to its highly specific instrumental response, directly dependent on the vibrational properties of the functional groups in the sample and therefore uniquely linked to its **molecular composition**. Despite its great advantages, some common drawbacks of the technique are: 1) the need for sampling and the normally complex sample preparation, usually involving the need for preparing pellets with IR-transparent materials and/or thin sections (e.g. for the analysis with Synchrotron sources in transmission, SR-μ-FTIR); 2) a **low spatial resolution** (5-10 $\mu m^2$) due to the diffraction limit of the IR radiation, which strongly hinders the imaging potential for small samples (often the case for heritage materials).

In this thesis, ATR-FTIR was applied to the study of the surface of historical metal elements (Chapter 2) and soluble dyes in solution (Chapter 5), while transmission FTIR was employed to characterize in-house synthesized lake pigments and monitor their natural degradation (Chapter 5). In addition, SR-μ-FTIR (analysis performed at synchrotron SOLEIL) was employed to study degradation products of the interaction between metal and glass (Chapter 3) and paint samples in cross section (Chapter 6).

A type of vibrational spectroscopy often employed as a complementary method to FTIR is **Raman spectroscopy**. This technique is based on the analysis of the inelastic scattering of visible or near-IR light from a laser source by the sample. Changes in the energy of the scattered light are, in fact, normally related to changes in the vibrational state of the molecules in the sample and, therefore, to its overall molecular composition. The complementarity with FTIR arises from the fact that Raman-active and IR-active functional groups are often different, with Raman generally offering information also about the crystalline structure of the sample. Moreover, Raman is often combined with an optical microscope (μ-Raman) in order to obtain spatially resolved molecular information ($\geq 2$ $\mu m^2$). Given the use of focused laser radiation, one of the main risks associated with Raman is to "burn" or in general alter the composition of the materials in analysis.

In this PhD, μ-Raman was often employed for the analysis of historical samples (Chapter 2, Chapter 3 and Chapter 6) and for the characterization of in-house synthesized artists' pigments (Chapter 4 and Chapter 5).

In addition, in Chapter 3 and more in detail in Chapter 6, a recently developed IR-based spectroscopic method, **optical photothermal IR (O-PTIR) spectroscopy**, is applied for the first time to the analysis of heritage materials.

O-PTIR: beyond the limits of FTIR

**O-PTIR** presents strong similarities but also some fundamental differences with another type of sub-micron IR spectroscopy: photothermal IR (PTIR).[104] Like for photothermal IR, in fact, the fundamental effect exploited by O-PTIR is the **photo-induced thermal expansion** of the sample. In both cases, a highly tunable quantum cascade (QC) laser is focused onto a small area of the sample. The energy of the laser is then tuned over a wide range of wavelengths in the mid-IR spectrum. When the sample absorbs radiation

46

of a certain wavelength, due to the specific vibrational properties of its molecular components, the absorbed energy is converted into heat, which causes a thermal expansion of the sample.

The difference between photothermal IR and O-PTIR lies in the strategy employed to monitor this photothermal event. In photothermal IR, commonly also known as AFM-IR, the photothermal expansion is detected by means of a scanning probe microscope. The probe of the microscope is represented by the tip of a cantilever in contact with the sample. By operating the QC IR laser in a pulsed mode, a periodic motion of the cantilever is produced which contains information on the magnitude of the photothermal event. Hence, by plotting the magnitude of this oscillation against the wavelength of the incident IR radiation, a photothermal IR (PTIR) spectrum is obtained that is comparable to the spectra obtained with traditional absorption FTIR. However, the spatial resolution of the analysis, ultimately determined by the size of the probe, can be as high as 20 nm. PTIR has been recently employed in conservation science to successfully characterize organic materials in painting samples.[105,106] However, the need for a continuous contact between microprobe and sample can create problems when analyzing fragile or irregular materials (e.g. damage to the sample or interferences in the data).

In the case of O-PTIR, instead of a mechanical probe, the photothermal event is monitored by means of a **focused monochromatic visible light probe**. The green (532 nm) laser used as a probe is focused on the surface of the sample and is coaxial and confocal with the QC IR laser pump (Figure 1.6). The absorption of IR radiation by the sample and the consequent photothermal event, in this case, results into a measurable change in the intensity of the reflected or scattered visible light. This change is proportional to the absorption of infrared radiation, hence, if plotted as a function of the wavelength of the incident IR pump radiation, a photothermal infrared (O-PTIR) spectrum can be obtained that is comparable to traditional FTIR spectra. The spatial resolution, in this case, is determined by the diffraction limit of the visible light probe and, therefore, it can reach ~450-500 nm. Moreover, this value remains constant across the IR spectral range, unlike traditional FTIR methods where the resolution depends on the wavelength of the incident IR radiation.
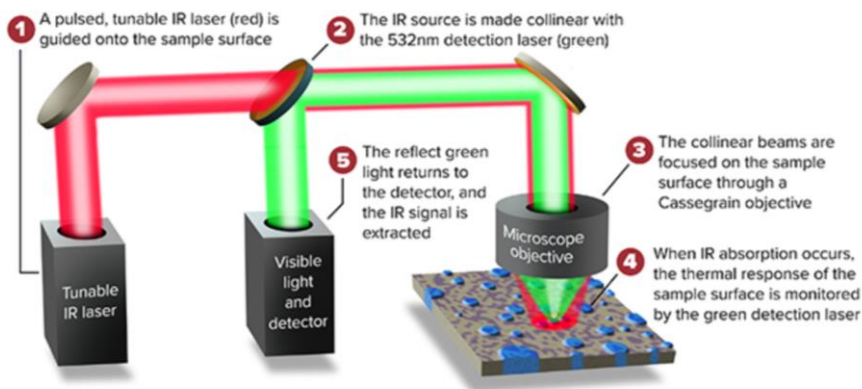
*Figure 1.6_Schematic representation of the working principle and optical components of an O-PTIR instrument (From Photothermal Spectroscopy Corp website[107]).*

In conclusion, O-PTIR represents a great innovation in the field of micro-spectroscopy since it allows to simultaneously overcome the traditional diffraction limit to the spatial resolution of FTIR, **increasing the spatial resolution by ten times**, while also **avoiding a direct contact with the sample** (unlike photothermal IR). This allows also to by-pass the need for a complex sample preparation, often a problem when it comes to the IR analysis of historical samples.

In this PhD work, I had the opportunity to employ this technique, in collaboration with synchrotron SOLEIL, for the characterization of metal-glass corrosion products on challenging samples (Chapter 3) and for the molecular imaging in cross-section of an extremely small paint sample from the painting *L'Arlésienne (portrait of Madame Ginoux)* by Vincent Van Gogh (Chapter 6).

### 1.4.3   Microscopy

The use of microscopes in order to visualize objects and features invisible to the naked eye is one of the oldest forms of material analysis.[101] Traditionally, three main branches of microscopy are routinely applied to the analysis of heritage materials: **optical microscopy (OM)**, using a series of lenses to obtain a magnified image of the sample based on reflected (or transmitted) visible light; **electron microscopy**, increasing the level of magnification by substituting visible light with an electron beam with far smaller

wavelength (i.e. lower diffraction limit); and **scanning probe microscopy**, using the physical contact of a solid probe tip to scan the surface of an object.

In this thesis, OM and scanning electron microscopy (SEM) were extensively employed for the morphological characterization and microscopic imaging (also in cross-section) of historical samples (Chapter 2, Chapter 3, Chapter 6). In Chapter 2, the application of OM and SEM in combination with chemical etching of cross sections of the metal samples was particularly relevant to investigate their metallographic structure. In addition, SEM and scanning transmission electron microscopy (STEM) where used to study and characterize at high spatial resolution in-house synthesized artists' pigments (Chapter 4). As previously mentioned, the electron microscopy techniques were normally coupled with an EDX probe in order to obtain complementary elemental information. Furthermore, Atomic Force Microscopy (AFM), one of the most common types of scanning probe microscopy, was also employed to obtain morphological information and average roughness values for a series of metallic samples (Chapter 2).

### 1.4.4 Electroanalytical methods

Electrochemistry is situated in between the field of electricity and chemistry, investigating the reactions occurring at the interface between a working electrode (with or without adsorbed particles) and a solution.[108] **Redox reactions**, induced by environmental, chemical or physical phenomena, can be easily monitored by means of electroanalytical methods. Furthermore, qualitative and quantitative information on redox active species in solution or deposited on the surface of the electrode can also be obtained.[101]

My research group started applying electrochemical techniques as a fast method to monitor the (in)stability of inorganic pigments.[44,55,76,109] In this thesis, linear sweep voltammetry (LSV) and chrono-amperometry (CA) were employed to study the **photo-reactivity** of in-house synthesized artists' pigments. By monitoring changes in the current flowing in the system upon illumination of a pigment-modified working electrode in contact with an electrolytic solution, in fact, fundamental information was obtained on the response of the pigment to specific environmental stimuli (Chapter 4).

### 1.4.5 Chromatographic techniques

Chromatography is a general term referring to a diverse group of methods allowing the separation, identification and quantification of closely related components in complex mixtures.[101] In chromatography, the sample is always dissolved in a **mobile phase**, mostly a gas or a liquid, which is the forced through an immiscible **stationary phase** most of the time fixed in a column. The different components in the sample distribute themselves between the mobile and stationary phases while they move along the column. The analytes more strongly held by the stationary phase move only slowly, while the ones that are weakly retained travel rapidly through the column. The **separation** is therefore achieved based on differences in the relative affinity of the components with the two phases. Although destructive in nature, chromatographic techniques are widely applied for the characterization of organic species in the field of cultural heritage, in particular when hyphenated with mass spectrometry.[110,111]

In this work, only one type of chromatographic technique, namely ion chromatography (IC), was employed. This technique allows the detection and quantification of inorganic (and some small organic) anions and cations in aqueous solution.[101] In this specific case, IC was employed for the characterization of the soluble fraction of PM sampled in a museum environment (Chapter 7).

### 1.4.6 Sensors for the monitoring of environmental parameters

For the purpose of preventive conservation, having a deep knowledge of the object and of the environment-specific reactivity of the single materials composing it is not sufficient. Identifying potential threats in the conservation environment by **continuously monitoring** its quality is also of capital importance. Although not strictly belonging to the field of traditional analytical methods, environmental sensors rely on different analytical principles in order to obtain quantitative information on specific environmental parameters. Several well-calibrated, commercial off-the-shelf sensors exist for the monitoring of **RH** and **T** levels[112] and **light illuminance** (UV and Vis).[113] In addition, a large number of sensors for the continuous monitoring of **PM** and **gaseous pollutants** was developed in the last years.[114,115] Even though these solutions are usually not appositely designed for the application in museums and conservation environments, the small size and low cost make them extremely promising solutions for heritage applications.

In this work (Chapter 7), several commercial sensors are employed for the analysis of T and RH levels, Vis and UV illuminance, $CO_2$, $NO_2$, $O_3$ and total VOCs levels and airborne PM concentrations in different conservation environments. In addition, traditional discrete sampling methods for the analysis of PM (Harvard impactors[116]) and gaseous pollutants (Radiello passive samplers[117]) were also used.

In Chapter 7, particular attention is dedicated to the testing of low-cost commercial PM sensors against a well-calibrated and more expensive monitor. All the PM sensors considered are **optical particle counters (OPC).** This means that the detection of airborne PM is based on the principle of light scattering: a light beam enters a partially enclosed chamber, a continuous stream of air draws the airborne particles from the environment into the chamber and across the light path, the particles crossing the light beam causes scattering and the intensity of the scattered light over time is measured.[118] Most OPC also perform a **size discrimination** of the airborne particles based on their scattering properties. Being directly estimated from the optical properties of PM rather than on its aerodynamic behavior, the particle diameter measured by such counters might differ from the one traditionally used to define PM fractions (e.g. $PM_{2.5}$, $PM_{10}$).[64] In addition, some commercial particle counters allow to obtain information on **PM mass concentrations ($\mu g/m^3$).** However, although number of particles (calculated from light scattering) and PM mass are intuitively related, the nature of this relationship is strongly affected by properties that can vary over time, such as the chemical composition, the density, the shape and the optical properties of the aerosol.[118–121]

## 1.5  Overview of the present PhD work

This PhD research aims at filling knowledge gaps in the massive research field of conservation science, by starting from specific **case studies** and **un-answered research questions**. A wide range of unexplained material-environment interactions is considered and innovative analytical strategies are introduced in order to overcome current limitations in the characterization of heritage objects and conservation environments.

A schematic overview of the content of this doctoral thesis is shown in Figure 1.7 and a diagram of the analytical techniques employed is given in Figure 1.8.

**Chapter 1**

Tangible cultural heritage: objects in their environment

*Filling knowledge gaps by focusing on specific case studies and materials*

**Environment**    **Material 1**    **+ Material 2**

**Chapter 2**

All that glitters is not gold: unraveling the material secrets behind the pristine appearance of 16th-century brass sequins

**Chapter 3**

Glass-induced metal corrosion of otherwise extraordinarily stable brass decorative elements

**Chapter 4**

Unraveling the role of lattice substitutions on the stabilization of the intrinsically unstable $Pb_2Sb_2O_7$ pyrochlore: explaining the lightfastness of lead pyroantimonate artists' pigments

**Chapter 5**

Geranium lake pigments: the role of the synthesis on structure, composition and reactivity

**Chapter 6**

High resolution analysis of historical paintings by means of O-PTIR spectroscopy

**Chapter 7**

Implementation of real-time PM analysis in IEQ monitoring

— Unexplained stability
— Unexplained instability
— Novel analytical/ methodological approach

**Chapter 8**

Conclusions and outlook

*Figure 1.7_Schematic overview of the conducted PhD research.*
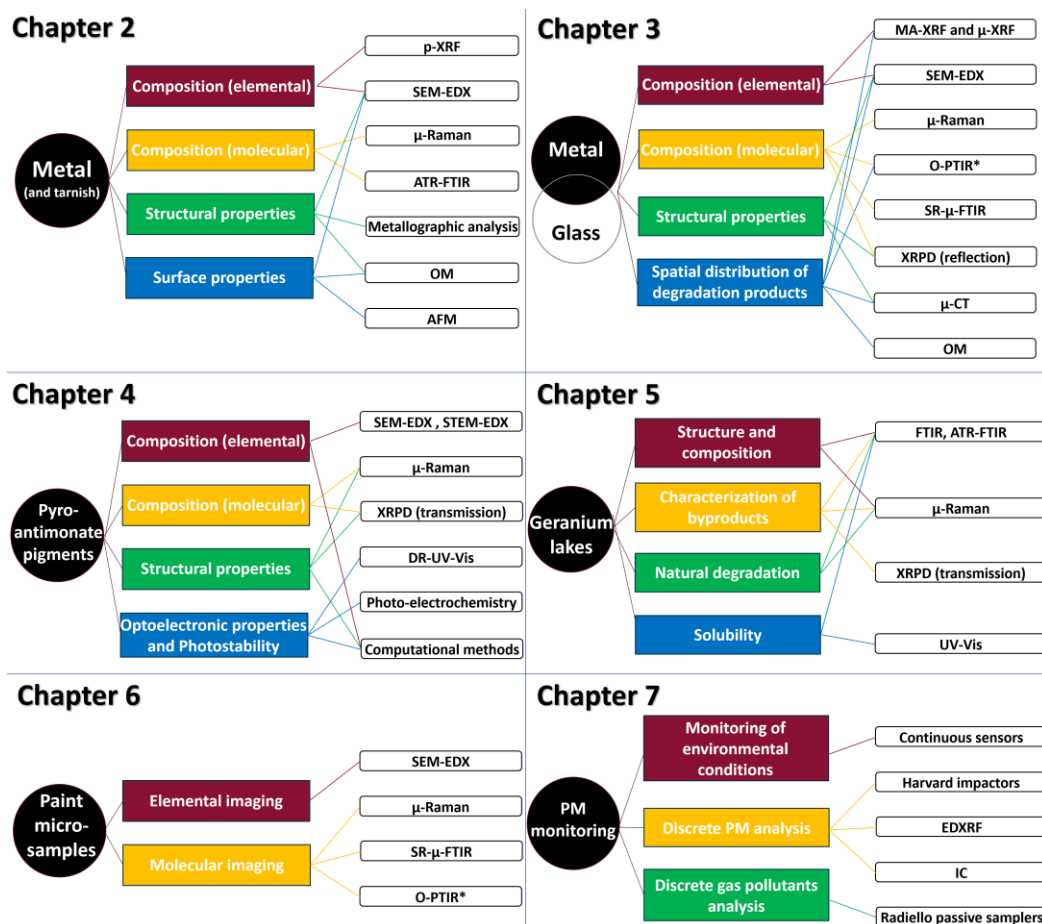
*Figure 1.8_Schematic overview of the analytical techniques employed in this PhD research.*

By starting from a specific case study, the analysis and conservation of the enclosed gardens (a series of unique 16th century reliquary altarpieces) in the collection of the Museum Hof Van Busleyden (Mechelen) (Figure 1.9a), in Chapter 2 and 3 fundamental questions about the reactivity of historical brass in indoor conditions are answered.

In particular, **Chapter 2** focuses on unraveling the material properties behind the extraordinarily pristine conservation state of a series of brass sequins (Figure 1.9b-e). The central role played by surface roughness and micromorphology on the reactivity of the objects is highlighted through comparison with different brass decorative elements, similar in composition but heavily tarnished. Ultimately, the capital importance of the manufacturing process on the long-term stability of historical brass is revealed.
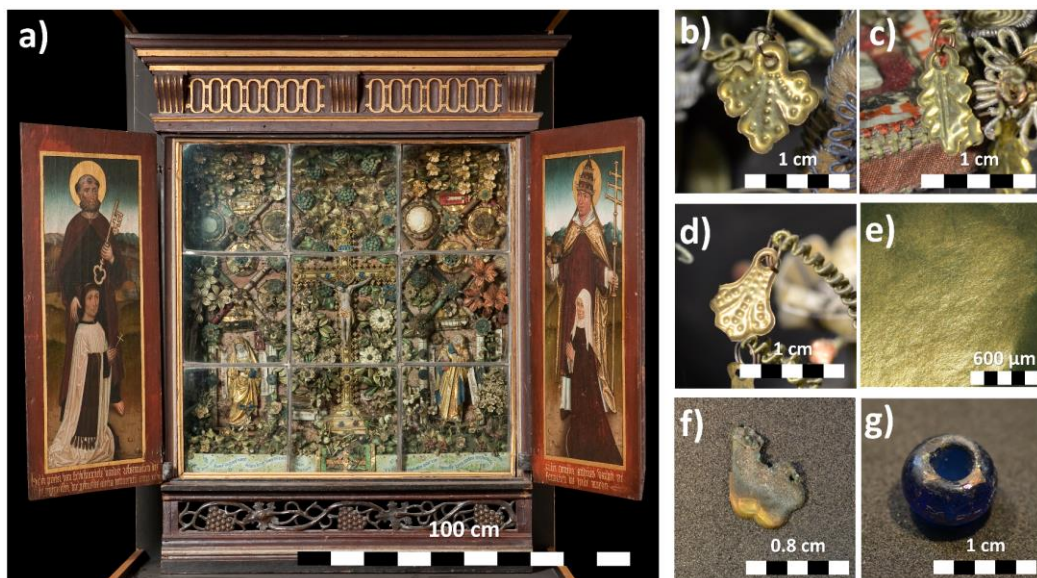
*Figure 1.9_Enclosed gardens of the Museum Hof Van Busleyden (Mechelen, BE): a) garden with Calvary, the Virgin Mary and St John the Evangelist; b), c), d) pictures of pristinely preserved brass sequins and e) OM photomicrograph of their non-degraded surface (Chapter 2); f) example of heavily corroded sequin (Chapter 3); g) weathered glass bead (Chapter 3).*

**Chapter 3** furthers the understanding of the reactivity of the brass decorative elements studied in Chapter 2 by zooming in on a small subset of objects which appear, in an opposite fashion, severely corroded (Figure 1.9f). The challenging nature of the samples in analysis forced the authors to test innovative analytical strategies to finally understand the reasons behind their extreme corrosion. In conclusion, the deleterious effect of the contact with weathered glass (Figure 1.9g) on the otherwise extraordinarily stable metal objects is demonstrated.

The two subsequent chapters are dedicated to the study of a different aspect of the interaction between heritage materials and environment: the photo-reactivity of specific artists' pigments.

**Chapter 4** discusses the interesting case of the semiconducting pyroantimonate pigments Naples Yellow and lead tin antimonate yellow. By means of a combined multi-faceted analytical and computational approach, the electronic structure and light-induced behavior of these compounds is probed, with the final aim of explaining their exceptional stability in paintings. Novel insights on the factors determining the reactivity

of semiconducting artists' pigments in the presence of light, moisture and soluble PM are presented.

**Chapter 5** is dedicated to the study of the enigmatic reactivity of Geranium lakes, a family of highly unstable lake pigments based on metal complexes of the synthetic dye eosin Y. The effect of the synthesis conditions on the overall composition of the pigments is first thoroughly investigated. A detailed spectroscopic characterization of the pigments is presented in this section, which is then used as a reference to monitor the molecular changes occurring during their natural ageing. The role played by differences in composition introduced by changes in the synthesis protocols on the natural ageing of the pigments is demonstrated.

**Chapter 6** continues in part along the lines of Chapter 5, while also shifting the focus from the material-environment interaction more towards the characterization of materials. This chapter deals, in fact, with another challenging aspect of the study of Geranium lake pigments: their identification in real paint samples. The analysis of a microscopic sample from Van Gogh's painting *L'Arlésienne (portrait of Madame Ginoux)* (Figure 1.10) presents the perfect opportunity to test the potential and limits of optical photo-thermal IR (O-PTIR) spectroscopy for the sub-micron molecular characterization of paint cross sections. The striking results, including the identification of Geranium lake particles in the paint layers of the sample, clearly highlight the great potential of this technique for the study of micrometric particles in paint samples.

**Chapter 7**, while also introducing methodological novelties, focuses on the environmental side of the material-environment equation, in an opposite fashion as Chapter 6. In this chapter, in fact, a straightforward methodology to evaluate and visualize in a continuous manner the indoor environmental quality (IEQ) of a conservation environment is introduced. The innovative aspect is represented by the inclusion of continuous PM monitoring, a factor normally overlooked in previous studies, in the calculation of an IEQ-index. The results of this first part of the study clearly show how, including PM in the IEQ calculation, allows to identify potential risks for museum collections that remain invisible when only traditional parameters are considered. In a second part of this chapter, the performances of a selection of low-costs sensors for PM and gaseous pollutants monitoring are tested on the field (monitoring campaign in the St. Martin's church in Aalst, Belgium). Advantages and drawbacks are highlighted with the final aim of verifying their applicability in conservation environments, which would

make the implementation of continuous PM monitoring in the practice of museums and heritage institutions affordable and realistic.

**Chapter 8** concludes this doctoral thesis by summarizing the findings of this PhD work and highlighting the main outcomes and implications of the conducted research.



*Figure 1.10_Vincent Van Gogh, L'Arlésienne (portrait of Madame Ginoux). 1890.*
*Kröller-Müller Museum, Otterlo.*

# |2

All that glitters is not gold: unraveling the material secrets behind the pristine appearance of 16th-century brass sequins

**A. Marchetti\*, V. Beltran\*, P. Storme, G. Nuyts, L. Van Der Meeren, A. Skirtach, E. Otten, M. Debulpaep, L. Watteeuw, K. De Wael**

**\* Contributed equally**

# Abstract

Brass is a relatively stable alloy but it tends to tarnish over time due to the interaction with the atmosphere. Therefore, it is rare to observe centuries-old brass objects untouched by the passing of time. For this reason, the pristine appearance of hundreds of brass sequins in the enclosed gardens of Mechelen (reliquary altarpieces produced between 1530 and 1550) is remarkable. In this chapter, the in-depth chemical and metallographic characterization of such unexpectedly well-preserved objects is presented. The results revealed the reason for their stability to be a combination of high-quality materials (i.e. medium Zn content, low impurities) and optimal surface properties (i.e. high homogeneity, low roughness), indicating the high level of expertise of the craftsmen who produced them. Novel fundamental insights on the manufacturing method of metallic sequins, previously overlooked despite their great popularity throughout history, were also obtained.

## 2.1 Introduction

The enclosed gardens[122] are a unique form of mixed-media devotional art produced between 1530 and 1550.[123,124] First appeared in the late medieval Low Countries, an enclosed garden is a retable offering complex representations of an ideal, paradisiacal garden, often enclosed by painted side panels. The central section is an impressive combination of narrative sculptures, relics, hand-worked textiles, metallic elements and all kind of adornments. Although common in the past, only few of these stunning multi-material artefacts survived the test of time. The enclosed gardens in the collection of the Museum Hof Van Busleyden (Mechelen, BE), are one of the few exceptions.[123,124]

Within the ArtGarden project (KIK-IRPA, University of Antwerp, KU Leuven) five of these masterpieces, kept by the sisters of the Onze-Lieve-Vrouwegasthuis of Mechelen for over 500 years, were the subject of a detailed analytical investigation in the occasion of their restoration. Upon visual observation, one of the predominant features in these artworks is the presence of hundreds of round and leaf-shaped sequins with an extremely shiny appearance. Such a pristine state is in striking contrast with the high degree of degradation observed for the other materials constituting the artworks (e.g. faded and embrittled textiles, corroded glass beads and tarnished metals).

Metallic sequins consistently appear as clothes, ornaments and symbol of wealth throughout ancient history,[125–128] transcending both geographical and temporal distances from as far back as the third millennium BC.[129] In the middle ages, they were extremely popular as fashion accessory among nobility as well as decoration in religious art and liturgical fabrics.[130–137] Both in ancient and early medieval times, the sequins were usually made of gold or of gilded metal.[125,127,129,138,139] The use of gold granted both the characteristic shiny appearance and a certain exclusivity to the sequins. Between the 14th and the 15th century, cheaper metals, such as copper or brass, started being used for the production of sequins as well.[137,140,141] Initially linked to counterfeit, the mass production of cheaper shiny sequins likely turned into a parallel industry of its own.[137] Probably due to the low prestige of these objects compared to their gold counterparts, only few clear mentions exist in the literature.[140–142]

Apart from the sequins, the most common type of metallic objects found in the enclosed gardens are wires. These are used, alone or in combination with silk, to structure decorative elements and hang sequins and other adornments. If the sequins are in a

pristine conservation state, the wires show an opposite situation, with heavy tarnishing and a complete loss of their metallic appearance. Despite the extreme differences in appearance, preliminary in-situ p-XRF analyses (discussed later in the chapter) showed that both sequins and wires are made of a brass alloy similar in composition.

Brass is a relatively stable alloy of copper and zinc but it is sensitive to oxidation, tarnishing over time due to the interaction with the atmosphere.[10,29,143–146] It is therefore extremely unusual to observe centuries-old brass objects which appear almost completely untouched by the passing of time.

Several factors, including changes in the composition and in the metallographic structure of the alloy, can have a significant positive or negative influence on the stability of brass.[28,31,147] In particular, the alloying with Zn increases the corrosion resistance compared to pure copper, but Zn percentages higher than ~15% can cause an increased risk of dealloying, leading to a loss of mechanical and aesthetical properties.[28–30] The minor components of brass can also significantly affect the resistance to degradation. Among others, Ni, Sn, As and Al, in concentrations below 0.2-0.3%, can increase the stability of the alloy, while Fe and Pb might favor its degradation.[31] The metallographic features of the alloy, such as average grain size and residual strain, are also known to affect the stability of brass. Smaller grains and higher strain, in particular, can lead to an increased reactivity.[31,32] In a similar fashion, the surface morphology also plays a role in the corrosion of metal alloys, with an increase in roughness being linked to a higher tendency to corrode.[33–35] This is particularly evident in metals prone to passivation (like Cu alloys), especially when unidirectional roughness[34] or deep scratches[35] are present. Furthermore, different types of surface coatings (e.g. tinning, gilding, silvering)[146,148–150] were also used since antiquity to improve and preserve the aesthetic properties of Cu-alloy surfaces.

When it comes to metal sequins in particular, the information in the literature is sparse, and mostly limited to historical sources and archaeological findings.[140–142] Despite their popularity throughout human history, little is known about composition, metallography and stability of these objects. This study, therefore, represents a unique occasion to investigate and shed light on the material properties of this previously overlooked type of metallic ornament and, in general, on the stability of stamped brass elements.

Based on these premises, several fundamental research questions arise: why is the conservation state of wires and sequins so different even though they are made of a

62

similar alloy and they were preserved in exactly the same environment? What is the secret behind the pristine appearance of the brass sequins even after five centuries of exposure to the environment? Three possible reasons for the different conservation state were investigated in particular:

- differences in the chemical composition of the alloy (Zn concentration and minor elements);
- presence of a surface coating on the sequins (metallic or organic);
- differences in the metallographic structure and surface morphology of the objects (role of the manufacturing process).

In order to give an answer to these questions, an in-depth historical research was performed in combination with a multifaceted analytical approach to investigate the chemical composition (SEM-EDX, p-XRF, FTIR and μ-Raman spectroscopy), metallographic structure (alcoholic ferric chloride etching followed by OM and SEM observation) and surface morphology (OM, SEM and AFM) of 65 sequins and 19 wires from five different enclosed gardens. Our results demonstrated how the manufacturing process, strongly affecting metallographic structure and surface morphology of the objects, ultimately determined the different conservation state of brass sequins and wires. In addition, the material information obtained allowed to reconstruct in detail, for the first time, the historical manufacturing process of metallic sequins.

## 2.2  Materials and methods

Non-invasive p-XRF analysis were first performed in-situ on a total of 84 metallic objects (65 sequins and 19 wires) from five different enclosed gardens (enclosed gardens of Mechelen Hospital sisters, Museum Hof Van Busleyden, Mechelen, BE). A selected number of objects (21 sequins and 19 wires), representative of the different stylistic groups and chosen because easily removable from loose decorative elements, was then further studied in the laboratory by means of FTIR and μ-Raman spectroscopy, AFM, OM and SEM-EDX both on a surface level and in cross section. Metallographic analyses were also performed on these samples.

### 2.2.1    Portable XRF (p-XRF)

The portable X-Ray Fluorescence instrument Olympus-InnovX Delta Professional was used to perform in-situ measurements. This device generates primary X rays by means of a Rh-tube with a maximum acceleration voltage of 40 kV and a maximum beam current of 200 µA. All the analyses were performed at 40 kV with a 90 s Live Time. The software used for the qualitative and quantitative analysis was Innov-X Delta Advanced PC Software. The accuracy of the software for quantitative analysis was verified by analyzing the CHARM set of certified reference copper alloys.[151] The level of accuracy observed allows a meaningful comparison between the two groups of brass objects in exam.

### 2.2.2    ATR-FTIR

The FTIR spectra were collected with a spectrometer Bruker Alpha II equipped with a DTGS detector and a diamond ATR accessory. A total of 128 scans have been accumulated in each sample, using a resolution of 4 $cm^{-1}$ and a wavenumber range between 4000 to 400 $cm^{-1}$. The spectra showed have not been corrected in order to avoid any kind of distortion.

### 2.2.3    µ-Raman

Raman spectroscopy measurements were performed by means of a Xplora Plus Microscope (Horiba) under a 785 nm laser, considering the effective range of 150-1000 $cm^{-1}$. At each point, 5 accumulations were collected during 10 seconds each one. The spectra showed have not been corrected in order to avoid any kind of distortion.

### 2.2.4    OM

The OM images were collected with an Olympus DSX510 digital microscope. Both bright field and polarized light modes at different magnifications were employed. The specific conditions for the single images are specified throughout the text.

## 2.2.5   SEM-EDX

The samples were examined with a Field Emission Gun – Environmental Scanning Electron Microscope (FEG-ESEM) equipped with an Energy Dispersive X-Ray (EDX) detector (FEI Quanta 250, USA; at AXES and EMAT research groups, University of Antwerp), using an accelerating voltage of 20kV, a take-off angle of 30°, a working distance of 10 mm and a sample chamber pressure of $10^{-4}$ Pa. Imaging was performed based upon secondary electrons (SE), back-scattered electrons (BSE). EDX point spectra were acquired, using a beam current of ~0.5 nA and a dwell time of 60 s per spectrum. The same beam current was used for EDX mapping. Different maps were collected at different resolution, with pixel size values from 18 to 420 nm and dwell time from 1 to 4 ms/pixel. The line scans analyses were performed with a spatial resolution of 500 nm.

## 2.2.6   AFM

The AFM instrument used during all experiments is the nanowizard 4™ with a manual stage (JPK BioAFM, Bruker). All imaging experiment were performed using a beam shaped cantilever on the AIO chip (cantilever D) which has a nominal spring constant of 40 N/m and a nominal tip radius of <10 nm (Budget sensors, Bulgaria) All images were acquired in the Quantitative Imaging® mode using a setpoint of 200 nN. Calculation of RMS roughness and processing of the images were performed in the JPK SPM DP software (v 6.1.163).

## 2.2.7   Cross section preparation and chemical etching

Selected fragments of the metallic objects in analysis were prepared by first embedding them in acrylic resin (ClaroCit). The surface was then polished with silicon carbide discs, followed by diamond and alumina pastes. The samples were then cleaned and chemically etched with an alcoholic ferric chloride solution (240ml of ethanol - Supelco, ref. 8.18760 -, 60 ml of HCl - Sigma Aldrich, ref. 320331 - and 20 g of $FeCl_3 \cdot 6H_2O$. The cross sections were immersed during 2 seconds in the etching solution and afterwards rinsed gently with water. They were then inspected with OM (Bright Field and Polarized light) and SEM.

## 2.3 Results and discussion

In order to facilitate the design of the experiments and the discussion of the results, the 65 sequins were divided in eight groups based on their macroscopic appearance and stylistic features (Figure 2.1a-h). Some examples of metallic wires encountered in the enclosed gardens are also presented in Figure 2.1i-k. All 19 wires and a selection of 21 sequins (taken from each group) were investigated both in- and ex-situ (Figure 2.1l).
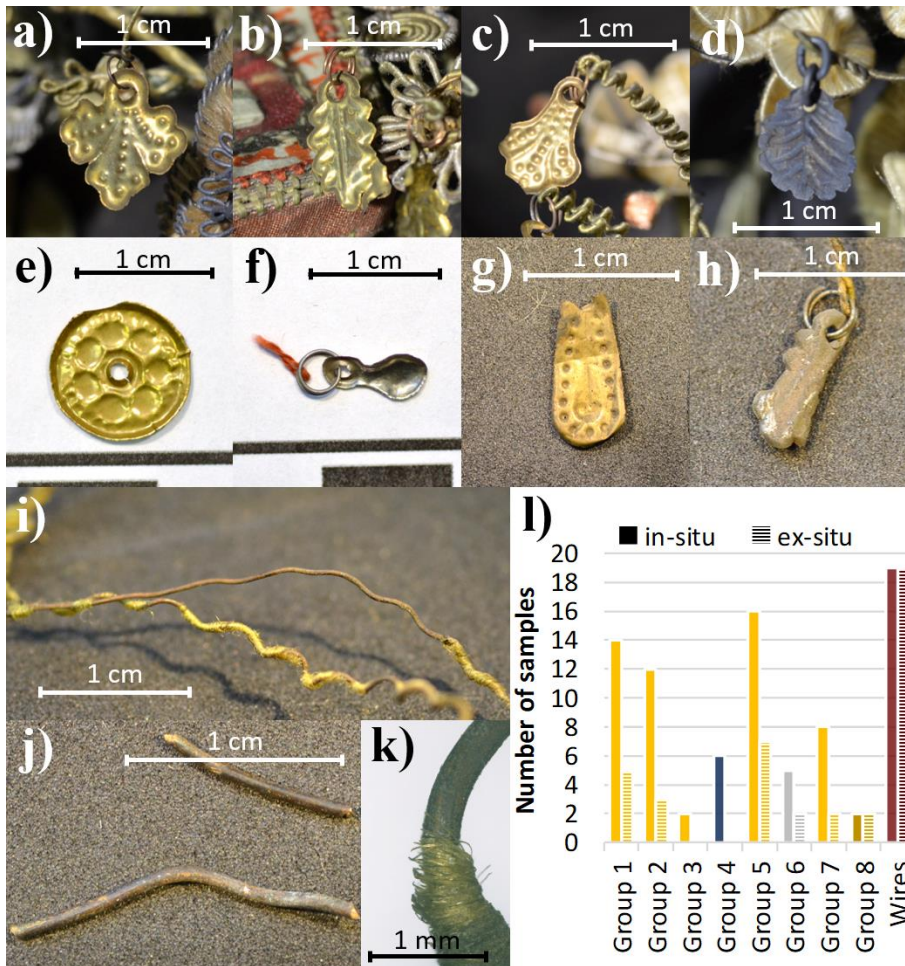


*Figure 2.1_Overview of the type of metallic objects in exam. Categories of sequins: a) Group 1, b) Group 2, c) Group 3, d) Group 4, e) Group 5, f) Group 6, g) Group 7 and h) Group 8. i), j) and k) examples of brass wires. l) number of samples selected per category for in-situ and ex-situ analyses.*

## 2.3.1   Chemical composition of the alloy

The thorough elemental characterization performed in this study demonstrated that, despite the clearly different conservation state, no substantial systematic difference exists in the composition of brass sequins and wires. The different conservation state of the two types of objects cannot therefore be explained by a difference in the chemical composition of the alloy.

In detail, the in-situ p-XRF analysis confirmed that the large majority of sequins and wires is made of brass (78 out of 84 objects). The only exception are six silver sequins, all belonging to the stylistic Group 4 (Figure 2.1d), which also appear completely tarnished in contrast with the other sequins. Since the main aim of the study is to explain the conservation state of the well-preserved brass sequins, these few degraded silver objects have been excluded from further analysis.

The remaining brass sequins show a pristine conservation state and a glossy appearance, with only seven presenting localized signs of degradation. These tarnished sequins do not belong to one specific stylistic group, but they rather represent isolated exceptions belonging to different groups (one in Group 1, one in Group 2, two in Group 5, two in Group 7, one in Group 8). The wires, albeit appearing systematically and significantly tarnished, show a similar bulk composition to the sequins (Figure 2.2).

Both types of objects are made of an α-brass alloy with a medium-high Zn content (∼20%), but always lower than 30%. This is in agreement with the composition normally encountered in historical brass (pre-19th century) produced with the cementation process.[152] The Zn content and the low impurity levels indicate a high-quality metal alloy, most likely produced by directly smelting copper and zinc ores, and not by recycling existing brass objects.[141] Such an alloy, due to the complex and very technical nature of its production technique, would have been relatively expensive compared to other copper alloys or more impure brasses.[141] For this reason, as seen in other late-medieval European findings, it was used mostly to produce liturgical and more luxurious objects.[141,143,153] However, when compared to gold, whose appearance was likely supposed to imitate, this would have been a much cheaper option.

The content of Zn (Figure 2.2b) appears lower in the bulk of the wires (∼15%) than in the sequins (∼20%). Such a difference is not clearly visible in the p-XRF results likely due to the contribution of the tarnished layer on the surface of the wires. A higher Zn content

is normally associated to a higher tendency to degrade, with the conventional safety "threshold" set at 15%.[28] Since the sequins show a higher Zn concentration, but also a much better conservation state, the Zn content does not seem to play a preeminent role in the long-term stability of these objects.
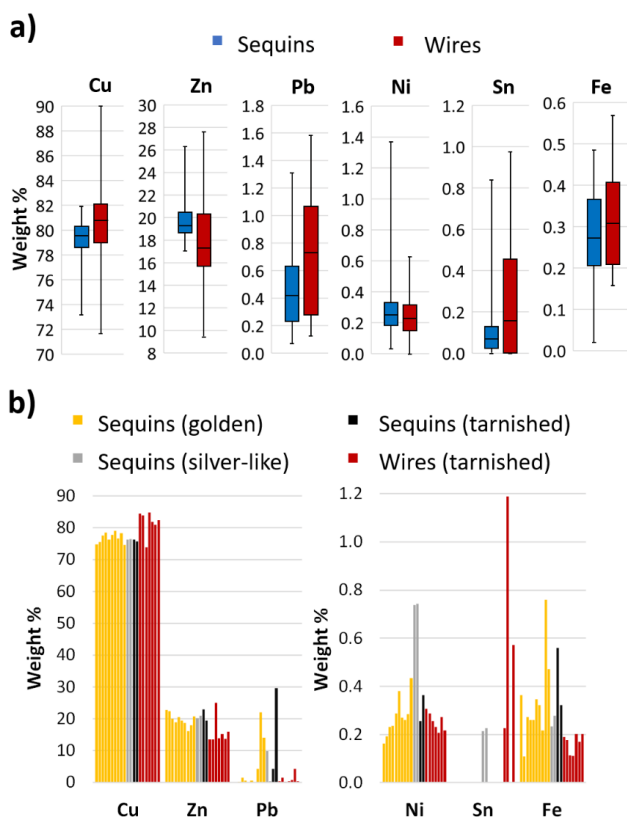


*Figure 2.2_Elemental composition of the brass samples. a) p-XRF results (78 objects), box-plots; b) SEM-EDX results in cross section, average of 20 points (10 µm long line) in the bulk of the object.*

On the other hand, the concentration of minor elements in all the samples is so low (Figure 2.2) that they most likely represent impurities in the starting ores rather than voluntary additions.[143,152,154] Pb is the impurity in the highest proportion. This metal was often added to improve the castability and reduce the price of Cu alloys.[143] In small amounts it can improve the machinability of brass but in larger than few percentage points it negatively affects the aesthetical and mechanical properties.[152] Since Pb is not soluble in the brass alloy and therefore is sparsely distributed in the volume,[155] only the p-XRF bulk results are considered representative of the real average concentration

(Figure 2.2a). The large majority of samples contains less than 1% Pb, low enough to be certainly not voluntarily added[143] and to not affect negatively the properties of the alloy. Such a low-Pb alpha brass alloy, in fact, would have had a golden color and ideal mechanical properties for the drawing of wires as well as for the battering of thin sheets.[152,156] The other minor components observed in the samples are Fe, Sn and Ni. Fe is often present as an impurity in historical brasses[141,143] and it can lead to a decrease in the resistance to corrosion of both alpha and beta phases.[31] In an opposite fashion, Ni and Sn concentrations might increase the resistance to corrosion of brass alloys.[31] Similar amounts of Fe and Ni are observed in the two different groups of objects. Sn is certainly present only in few tarnished wires and non-tarnished silver-colored sequins (Group 6, Figure 2.1f). Few wires show Sn concentrations high enough to potentially have a positive effect on the long-term stability of the alloy. Since these wires appear as heavily tarnished as all the others, Sn does not play an active role on the long-term stability of these objects.

## 2.3.2   Presence of surface coatings on the sequins

The elemental and molecular analyses also demonstrated that neither gilding nor any other organic or inorganic surface finishing is present on the sequins. The only exception is a small group of sequins with a silver-like appearance, which showed residues of a tinning treatment. The pristine conservation and gold-like appearance of the sequins in the enclosed gardens cannot therefore be explained by the presence of a protective coating.

In detail, the results of the ATR-FTIR analysis allow to discard the presence of a varnish or any other organic protective layer on the outer surface of the sequins (Figure 2.3). The spectra show mainly the presence of silicates, resulting from dust, and carboxylates, resulting from the reaction between the dust and the fatty acids deposited on the surface when the pieces where touched with naked hands.[157] The presence of carboxylates can be seen at 2919 and 2850 cm$^{-1}$ (C-H stretching from CH$_2$ groups) and 1590 and 1418 cm$^{-1}$ (asymmetric and symmetric stretching of COO$^-$ groups). The bands related to silicates are found at ≈3300 (O-H stretching) and ≈1100 cm$^{-1}$ (Si-O stretching).[158,159] Additionally, there are smaller amounts of free fatty acids (band at 1739 cm$^{-1}$, C=O stretching) and oxalates (1321 cm$^{-1}$, C-O stretching) related to the degradation of organic compounds.[160–162]

In any case, the FTIR signal has very low intensity, indicating that these compounds are found in a very low amount.
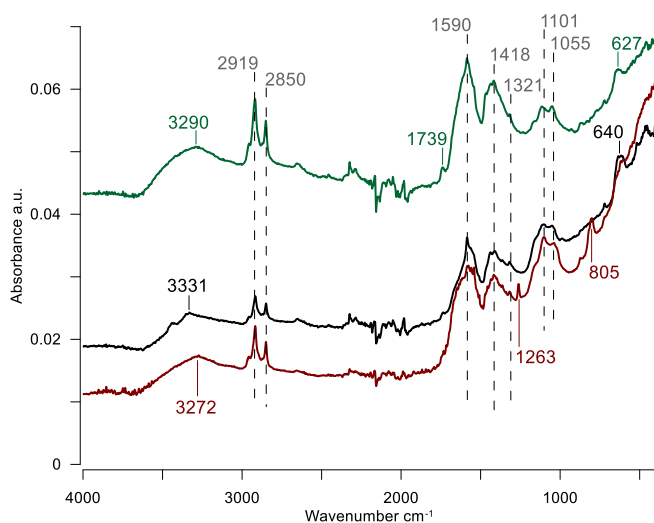


*Figure 2.3_ATR-FTIR analysis: typical spectrum for the pristinely preserved sequins. The spectra of three sequins are displayed, the dashed lines indicate the bands present in all spectra.*

The possible presence of a metallic coating was investigated by means of p-XRF and SEM-EDX analysis. In the first place, it is particularly relevant to notice that no gold was detected in any of the sequins (Figure S2.1). This excludes the possibility of a gilding treatment being responsible for the gold-like appearance and confirms the existence of a brass-sequins production in Belgium, previously only mentioned by historical sources.[136] The use of brass represents a clear distinction with early medieval and ancient sequins, most of the time made of gold or gilded metals,[138,163] but it is in agreement with the choice of non-luxurious materials usually encountered in these shrines.[123,124]

A protective surface coating, and in particular a tinning treatment, was observed only on three sequins. These are samples that also show a different macroscopic appearance compared to the gold-like majority of the sequins: two silver-looking sequins belonging to the stylistic Group 6 (Figure 2.1f), which were already found to have small amounts of Sn also in the bulk of the alloy (Figure 2.2b), and one tarnished sequin belonging to the stylistic Group 8 (Figure 2.1h). A thin discontinuous Sn layer was observed on the surface of these samples (Figure S2.2). The limited thickness of the Sn layer suggests that the finished objects might have been tinned through a galvanic process, such as contact
70

tinning, rather than through hot tinning with molten Sn.[148] Such a process, already well-known in late-medieval Europe,[148] produces extremely shiny but also very thin finishing layers completely covering the surface of the object. Due to the very thin nature of the coating, the Sn layer appears discontinuous and completely abraded in the areas where slight friction took place (Figure S2.2d,e).

### 2.3.3   Surface-confined dezincification

Even though no voluntary coating was observed on the surface of the sequins, the SEM-EDX analyses highlighted a systematic decrease of the Zn concentration on the surface of both sequins and wires (Figure 2.4).
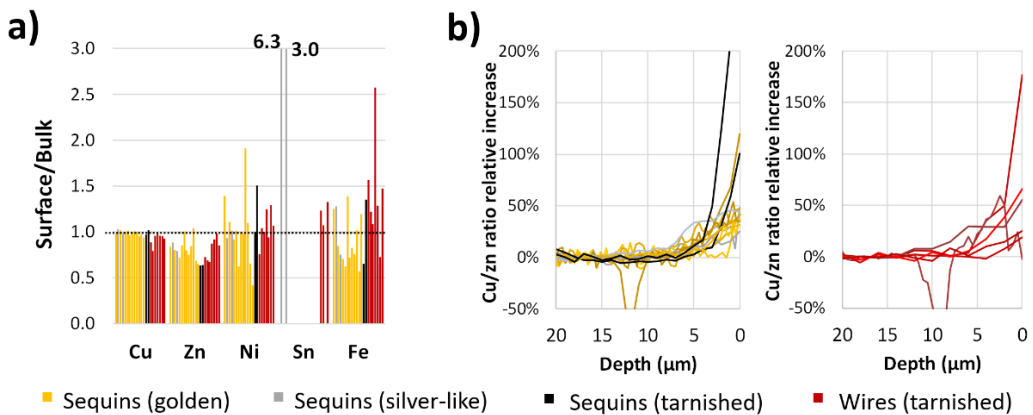


*Figure 2.4_SEM-EDX elemental analysis in cross section. a) ratio between surface and bulk concentration (average of 20 points, 10 µm long line across the outer surface of the object and in the bulk); b) Relative increase in the Cu/Zn ratio from the bulk to the surface of the samples.*

The leaching of a portion of Zn from the surface of Cu/Zn alloys due to the interaction with the environment is a widely documented phenomenon.[29,30,143,164–166] Zn, in fact, is more readily oxidized than Cu, can form soluble degradation products when interacting with the environment (e.g. Zn chlorides and hydroxides[28]) and can migrate, to a certain extent, through the metallic lattice of the alloy.[29,30,165] The level of dezincification in the samples in analysis, however, is much less pronounced than the one normally described in the literature on both modern and archaeological brasses.[164,166,167] In both sequins and wires, in fact, the average Zn concentration is only 15% lower on the surface than in the bulk, and the dezincification only affects the outermost 5-10 µm (Figure 2.4b). This is an

extremely important detail when it comes to the macroscopic appearance and aesthetical qualities of the sequins. Even when degradation products are not present on the surface of the samples, in fact, the dezincification of brass alone might negatively affect the aesthetical properties of the alloy. In particular, the leaching out of part of the Zn might shift the color of the alloy from a yellow/gold-like color towards a more reddish/copper-like hue.[28] In this specific case, however, the Zn fraction on the surface remains high enough (16.2 wt% on average) for the alloy to still preserve its gold-like appearance.

The lower level of dezincification observed in the samples might be due to the fact that the enclosed gardens' environment (indoor and partially enclosed) is not as aggressive towards the metal as the ones usually considered in the literature (e.g. seawater, soil, acidic solutions).[164,166,167] The selective solubilization of Zn from the most superficial layers of the alloy is in fact the first phase of brass dealloying, followed only in a later stage by the formation of Cu-rich deposits.[29,165] On one hand, a non-corrosive atmosphere could therefore explain the small scale of the dezincification observed. On the other hand, however, a chemical interaction in a relatively dry environment should have left nonetheless some Zn degradation products and a clearer degradation layer on the surface.[29,30,145] This is the case for the wires, where a thick crust with a layered structure is visible (Figure S2.3b and Figure S2.4d,e), but not for the sequins, where only small amounts of extremely thin and localized degradation products are visible (Figure S2.3a and Figure S2.4a,b,c). The dezincification not associated to a clear degradation layer in the sequins might also be a result of their production process. Procedures such as intensive hammering and annealing, necessary to produce thin sheets of metal, can in fact also lead to a loss of Zn from the alloy.[28,168]

### 2.3.4   Metallographic structure and surface morphology

Metallographic features, such as grain size, homogeneity and orientation,[147] and surface properties, such as average roughness and the presence of deep scratches,[33–35] can significantly affect the resistance to corrosion of metallic objects. Both properties are ultimately determined by the production process of the artefacts.

The metallographic analysis and microscopy investigations performed in this study highlighted striking differences in grain size, surface roughness and morphology for sequins and wires. The surface properties in particular, direct consequence of the

72

distinct production processes for the two types of objects, are the ultimate reason for the differences observed in their conservation state. In detail, the metallographic analysis of the wires (Figure 2.5a and Figure S2.5) showed recrystallized and twinned grains (average size from 9.3 µm to a maximum of 43.8 µm), with no clear elongation in the direction of drawing and no residual strain (see supplementary information section 2.5.2).
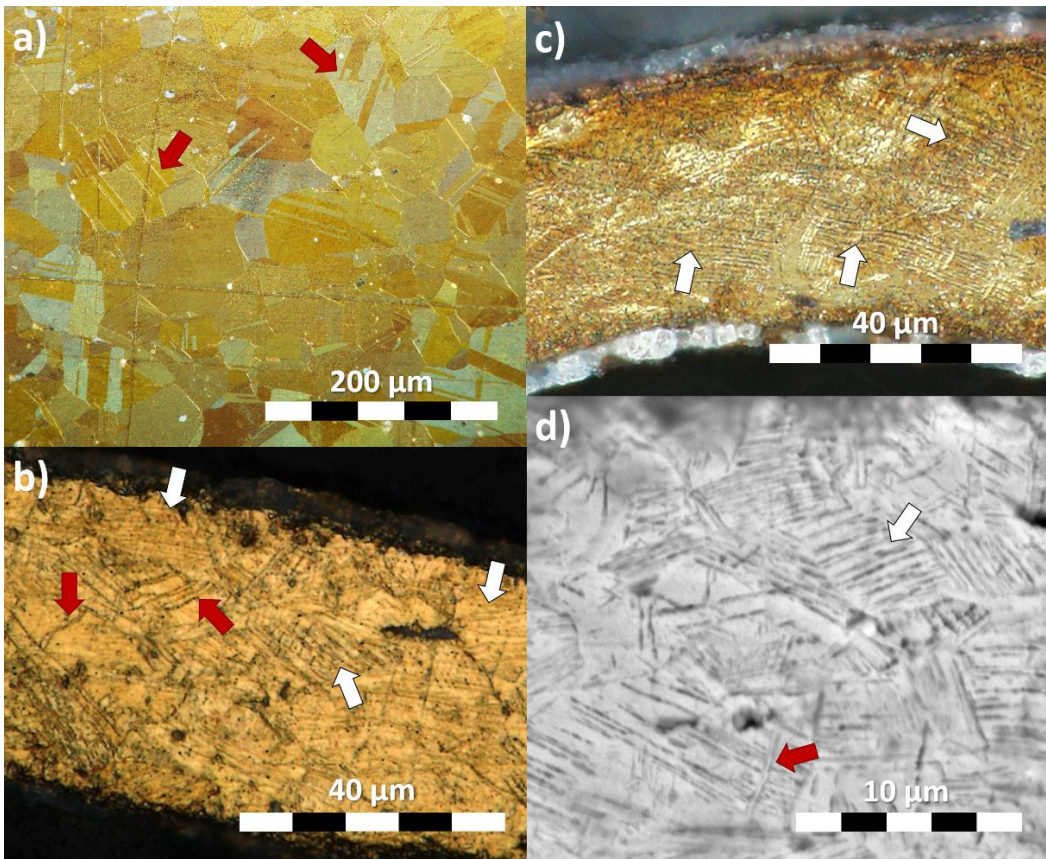


*Figure 2.5_Photomicrographs of the transversal cross-section of the samples after metallographic etching. a) wire, polarized light; b) Sequin (Group 5), bright field; c) Sequin (Group 1), polarized light; d) Sequin (Group 2), SEM secondary electron imaging. The main metallographic features are highlighted (red=twin lines; white=strain lines).*

In the sequins, on the contrary, the α-brass alloy is finely divided in micro-sized grains which are always smaller than in the wires (average size=5.4 µm). An extremely high amount of strain lines is also observed throughout the whole volume. Smaller grains and higher strain are often linked to an increased reactivity for the alloy.[31,32] In this case,

however, the smallest grains and the highest strain are encountered in the pristinely preserved sequins and not in the tarnished wires. It is true that, in an alloy prone to passivation, an enhanced reactivity would translate into a faster and more efficient passivation.[32] Nevertheless, no clear passivating layer is observed in the sequins. Therefore, the metallographic structure of the alloy does not seem to play a preeminent role in the conservation state of the objects. If this was the case, in fact, a higher level of tarnishing would be expected for the sequins rather than for the wires.

The microscopy analysis of the sequins showed that, on a microscopic level, the surface is not always as pristine as it appears macroscopically (Figure 2.6a-c), although a clear difference remains when compared with the heavily tarnished surface of the brass wires (Figure 2.6d-f).
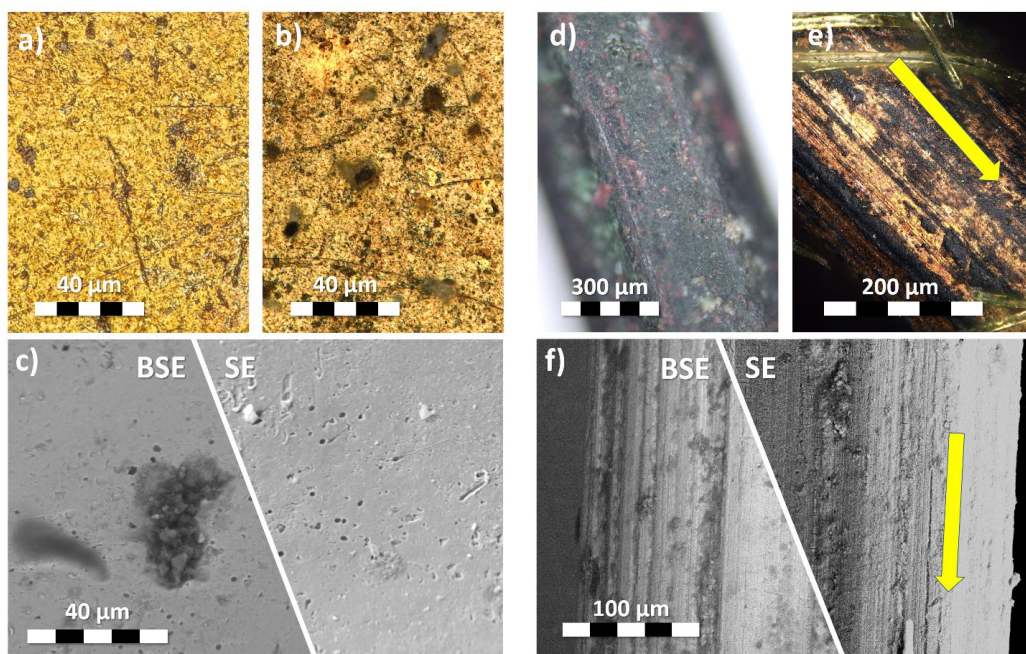


*Figure 2.6_Photomicrographs of the surface of some of the metallic samples in analysis. OM (a, b) and SEM (c) of macroscopically non-degraded sequins; OM (d, e) and SEM (f) of heavily tarnished wires. The direction of drawing of the wires is highlighted in yellow. BSE=back-scattered electrons, SE=secondary electrons.*

Furthermore, a connection between surface morphology and degradation can be noted in both cases. On the surface of the sequins, in fact, the distribution of the few corrosion products appeared linked to the few microscopic imperfections. In a similar fashion, on

the wires the tarnishing clearly follows the direction of drawing (yellow arrows), which is also the direction along which most imperfections and irregularities are distributed.[169] In addition to the similarities in the spatial distribution, the degradation products on sequins and wires show also a similar composition (see Supplementary information section 2.5.3). In both cases, in fact, Cu, C, S, O and/or Cl, are mainly observed in the degraded areas (Figure S2.3 and Figure S2.4). These are elements normally encountered in the degradation products on the surface of historical copper alloys due to the interaction with environmental agents.[1,10,144,170,171] The presence of mostly oxides, chlorides and hydroxy-chlorides of copper on both sequins and wires is confirmed by Raman spectroscopy (Figure S2.7). Al and Si containing dust is also observed (Figure S2.3 and S2.6). These similarities suggest that the mechanisms responsible for the degradation of sequins and wires are likely the same, but on a significantly different scale.

The link between surface defects and tarnishing should be considered in conjunction with the different roughness and homogeneity of the surfaces of wires and sequins, highlighted by the AFM analysis (Figure 2.7). These two factors together, in fact, substantiate a clear connection between the different surface morphology (Figure 2.7a,b,c) and roughness (Figure 2.7d) and the differences observed in the conservation state of the objects. The surface of the non-degraded sequins is extremely smooth, non-porous and shows only few tiny imperfections (as seen in Figure 2.6a,b,c, Figure 2.7a and Figure S2.4a). Such a smooth surface is different from the one the wires would have shown after being drawn, even before any oxidation process took place. The very act of drawing, in fact, often produces defects and imperfections developed in the direction of drawing.[169] The edge of the drawplates used to shape the wire tends to develop microscopic defects and imperfections as a consequence of usage.[169] These imperfections are transferred onto the wires while they are drawn, thus affecting the regularity of the circumference and the homogeneity of the surface. Such deep unidirectional scratches are clearly visible in the 3D imaged surface of the samples in analysis (Figure 2.6e,f and Figure 2.7b,c). Their presence creates preferential spots for the degradation process to start,[34,35] negatively affecting the overall stability of the wires. This clearly confirms the link between these imperfections and the longitudinal distribution of the corrosion products (Figure 2.6e,f). It is important to notice that scratches with nanometric thickness were observed also on the surface of the sequins (Figure 2.7a). However, these are much more superficial than in the wires and show no preferential orientation, which suggests that they are probably linked to the handling and usage of the objects rather than to their production.
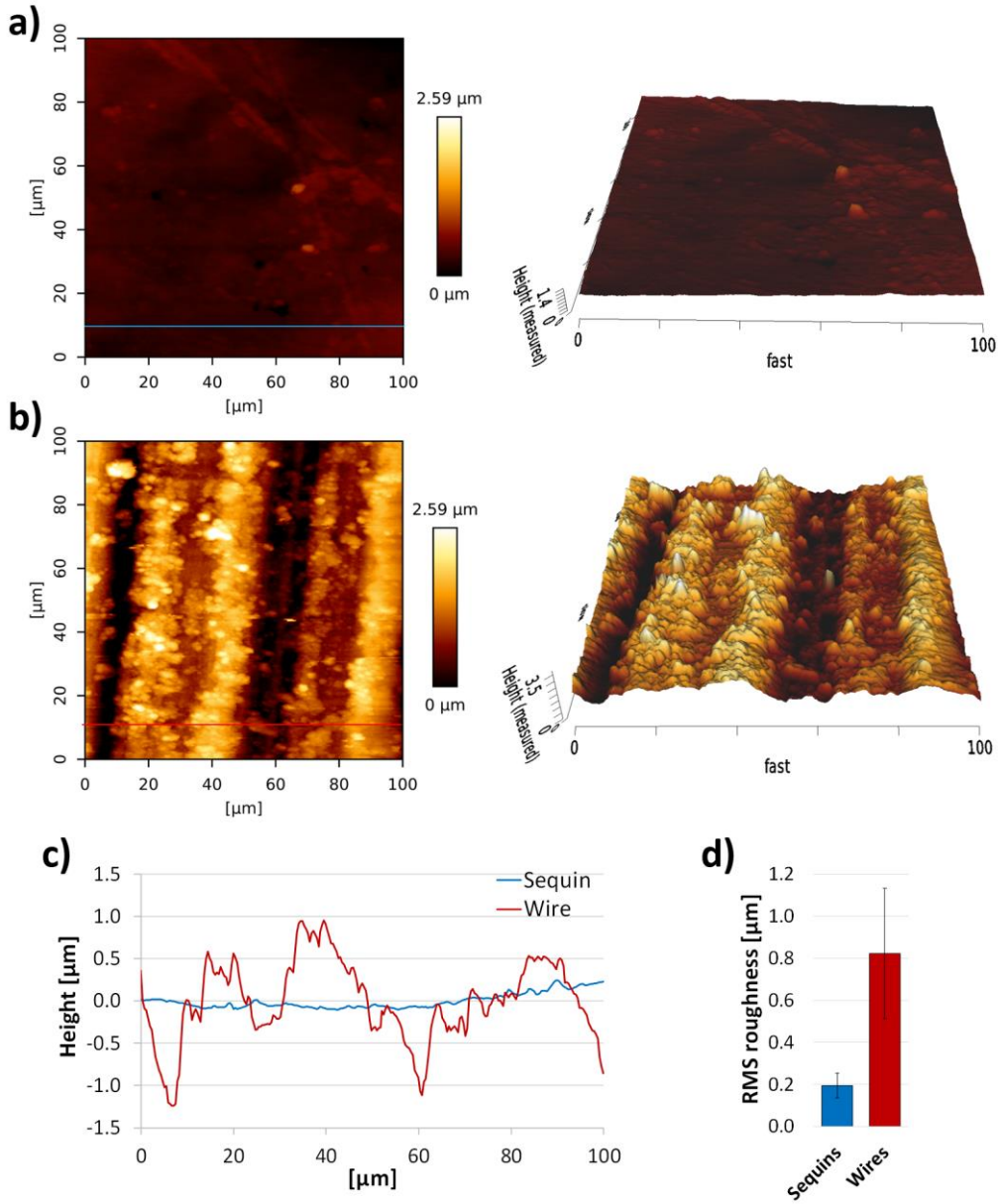
*Figure 2.7_AFM analysis. Representative height and 3D images for a) sequins and b) wires (the drawing direction is vertical); c) height profile along two lines (highlighted in a and b); d) average surface roughness (RMS) for all the areas considered (six for sequins and three for wires).*

All things considered, the striking differences observed in the surface morphology of sequins and wires, which translate into a higher roughness and therefore a higher

reactivity for the latter, justify the completely different appearance of the two types of objects despite their similar composition. The good surface properties alone, however, are not enough to explain the pristine appearance of the brass sequins. This is clear when we consider the conservation state of the small group of sequins made of silver (Figure 2.1d). Despite being likely produced in a similar way as their brass counterparts, in fact, these appear completely tarnished. This is a result of the higher reactivity of silver in the conservation environment: large amounts of silk and other sulfur-containing proteinaceous textiles in a partially enclosed environment likely lead to a build-up of $H_2S$[63] and to the consequent formation of dark $Ag_2S$.[1,63] Therefore, rather than by the mere surface morphology, the pristine conservation state of the sequins in the enclosed gardens of Mechelen is better described by a combination of relatively stable materials (brass with low Pb and impurities) and optimal surface properties. Both factors are needed to ensure such outstanding results.

It is important to mention, that the difference in conservation state of sequins and wires might have also been extremized by the presence of textiles (mostly silk[123]) wrapped around the latter. The fibers in contact with the metal, in fact, could have negatively affected its stability due to the off-gassing of aggressive pollutants[63] or by increasing the retention of humidity.[172] However, since some of the heavily tarnished wires considered in this study were not wrapped in textile, this mechanism might have had a negligible effect on the degradation. The similar composition of the degradation products found on sequins and wires, both in contact and not in contact with silk (Figure S2.3, S2.4, S2.6 and S2.7), confirms this hypothesis.

### 2.3.5    Historical manufacturing process of metallic sequins: uncovering the past.

Ultimately, the optimal surface properties of the metallic sequins were undoubtedly a result of the way they were produced. On the basis of the experimental evidences just discussed, novel fundamental insights on the historical production method of these objects were obtained. To the authors' best knowledge, no previous material evidence exists in the literature on these regards.

Based on historical sources, it is today ascertained that sequins were in high demand in Europe in the 15th-century.[137,139,140] Given their high popularity and low price, compared to the metals used to produce them,[173] the manufacturing process of these decorative

items must have been fast and simple enough to allow a large scale production. However, the only detailed information on the process available in the literature, based on the interpretation of 15th century Italian notary deeds, describe a complex procedure involving several steps, including casting in specific molds, piercing and finishing through the use of hammers and plies.[142] In the rest of the literature, on the contrary, only sporadic mentions exist of a generic stamping process based on the use of punches on sheet metal[174] and performed by specialized metalworkers.[140] This second process, even though never described in detail, presents interesting resemblances with a similar and better studied type of object: the thin, uni-faced medieval silver coins called bracteates.[175] Extremely diffuse in central and northern Europe, these coins were hammer-struck using only one coin die and pre-cutting a round flan from a thin metal sheet. A piece of soft material, such as leather or lead, placed on top or below the flan allowed to impress the design without using a two-part die. The data collected in this study highlighted important similarities and differences with bracteates, ultimately shedding light on the historical manufacturing process of sequins.

In the first place, the micro size of the α-brass grains observed in the sequins (Figure 2.5b,c,d) suggests that several cold working/annealing steps were alternated in the process.[176] This indicates that the first manufacturing step was the battering of the metal to form thin sheets, as opposed to the casting mentioned in the Italian sources.[142] To obtain such a thin foil, in fact, an excessive hardening of the alloy should be prevented by annealing it.[169] This hammering/annealing step might have also caused a loss of Zn from the metal,[28] justifying the slight dezincification observed on the surface of the otherwise pristinely preserved sequins. The use of a thermal treatment is confirmed also by the twin lines observed in several grains (Figure 2.5b,d). The fact that these twin lines are frequently bent and that a high amount of strain lines is present in the grains through the whole volume, however, suggests that the last step in the production of the sequins was some heavy cold-working.[146,176] This likely means that the single sequins were produced by embossing the three-dimensional decors applying a strong pressure to the metal sheet, in a similar fashion to what observed for the bracteates. The much higher precision in the centering of the design observed for the sequins (Figure 2.1) than for bracteates,[177] however, suggests that in this case the embossing and cutting were realized in one single step. Such a procedure is normally referred to as blanking, and the sharp-edged punches needed to stamp out these three-dimensional forms are called blanking punches.[169] Given the slight curvature observed at the edges of the sequins, it is likely that a more complicated procedure using a two-part die was employed. In this case, a matrix would have been used in addition to the (blanking/shearing) punch to

78

shear away a three-dimensional shape from the sheet metal. To facilitate the action of shearing, the edge of the matrix could be angled. This would explain the curved edges of the sequins (Figure 2.1 and Figure 2.8a,b,c), since the brass would have flown into the die just prior to fracture[169] (Figure 2.8d). Such a stamping process would cause a decrease in the thickness of the metal sheet, explaining the high residual strain observed and the very thin nature of the sequins (on average between 25 and 50 μm). This represents another difference with the bracteates, since the thickness of the flan would not decrease during their striking, leaving a thicker final product.[175]
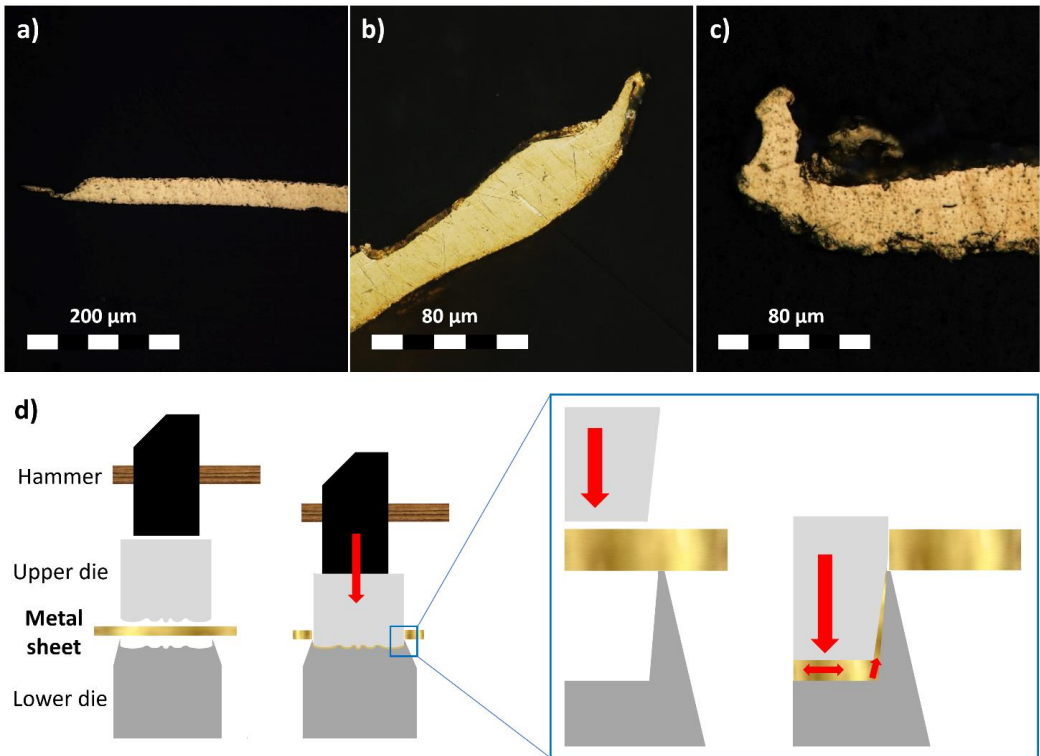


*Figure 2.8_Evidence of the stamping of metallic sequins. a), b), c) Photomicrographs of the curved outer border of three different sequins (in cross section); d) schematic representation of the stamping process likely used for the manufacture of the sequins in analysis. In evidence the link between the use of a two-part blanking die and the curved shape of the sequins' borders.*

In order to obtain a pristine strike with a single die, it would have been necessary to change spot on the slab of soft material after every single sequin. This would have clearly slowed down and complicated the production. The use of a two-part die, on the contrary, increased the productivity and the quality of the final product, a benefit for the

craftsmen. The use of punches and dies to impress three-dimensional designs onto metal plates was a technique certainly diffused in Belgium already in the early middle ages. In particular, the use of dies to "beat and stamp" Dinanderies, embossed brass objects mainly produced in Dinant and in the Meuse valley, is mentioned by Theophilus in the 12th century in its *De diversis artibus*.[178] Dinant was the biggest brass production center in Europe until the second half of the 15th century, thanks to its rich Zn ore deposits and its strategic position on the river Meuse.[152,179] Once the city was sacked and destroyed in 1466 by the Burgundian forces of Charles the Bold, most of the expert metalworkers (Dinandiers) fled the city and moved their activities to other large centers in the region, including Mechelen.[180–182] On top of this historical connection and transfer of knowledge between the two cities, a similarity in bulk composition also exists between pre-16th century Dinanderies from the Meuse valley[152] and the early-16th century objects analyzed in this study (Figure 2.2). A resemblance in the type of impurities present in the alloys suggests that not only the craftsmen wanted to achieve similar aesthetical and mechanical properties, but also that similar starting materials were likely used. Fe, Pb and Ni, in particular, are reported as possible impurities in Swedish and German Cu ores,[154] most likely used in the production of brass objects in Dinant in the 14th and 15th century[152,154] and, possibly, also of the sequins in analysis. The existence of sequins production centers in the southern Low Countries at the time of the creation of the enclosed gardens is also confirmed by the historical sources. A clear reference to the purchase of sequins of "Flemish making", made of brass rather than of gold, is in fact found in the description of a traditional English folk dance from 1515.[136]

Historically, a close link also exists between metal stamping processes and the development of techniques for mass production. Leonardo Da Vinci, in his codex Atlanticus (1480-1482), included a series of sketches for a "puncher device for the production of sequins".[183] In a similar fashion, some types of presses, adapted from the printing trade (e.g. screw press), were already used in the stamping of coins, medals and tokens at the beginning of the sixteenth century.[184] In the same century, presses using a two-part die could be found in Germany and France, with guides to ensure the correct alignment of punch and matrix.[185] The introduction of machines in late medieval times to impress three-dimensional designs "on small pieces of thin metal" is also mentioned by Tavenor-Perry in his monographic work on Dinanderie.[186] This author, while discussing the techniques employed in the production of metal reliefs, criticizes the introduction in the manufacture of "machinery" and "dies of hard wood or steel, such as those used by bookbinders for stamping leather" to produce little ornaments which were then "soldered on to the face of other work in so exact a manner as to make the

80

whole appear as if cast in one piece". It is therefore not impossible that the production of hundreds of identical small decorative items was relying on similar presses and not completely done by hand in 16th century Flanders. A large-scale production process would have likely increased the productivity and decreased the cost of production. This would have ultimately transformed the manufacturing of brass sequins into a more profitable profession than in 15th-century Italy, where the manufacturers strove to make ends meet probably due to the more complex and less efficient production process.[142]

Whether fully performed by hand or partially mechanized, this last stamping step has a fundamental role in determining the mechanical and surface properties of the objects. On one hand, in fact, it grants a certain residual strain and rigidity to the sequins, necessary to allow them to be hung and maintain their shape. On the other hand, the pressure needed to impress the three-dimensional design and shear the sequin out of sheet metal produces the smooth homogenous surface behind their pristine appearance.

## 2.4  Conclusions

The multifaceted analytical approach discussed in this chapter allowed to expose the material properties behind the extraordinarily pristine conservation state of the brass sequins in the 16th century enclosed gardens of Mechelen. The main reason why these objects survived so surprisingly well the test of time is a combination of good quality materials (low Pb and impurities) and optimal surface properties (low roughness and no scratches or imperfections). These qualities are a direct consequence of their manufacturing process and a clear manifestation of the high level of expertise of the craftsmen who produced them.

It is a widely accepted concept that late- and post-medieval craftsmen were well-aware of the effect the composition of the brass alloy would have on its mechanical and aesthetical properties.[141] This clearly emerges also from the results of the present study. The composition of the brass alloy, in fact, is ideal when it comes to the plastic properties needed for the stamping of sequins and the drawing of wires, as well as to obtain a material resembling gold. Evidently, the artisans who produced the objects in analysis

were skilled and had a great knowledge of the properties of brass, likely inherited from the centuries-long experience of the metalworkers of Dinant and the Meuse valley. Such mastering of brass technology played a key role in the history of sequins. The great expertise of the Flemish metalworkers, in fact, allowed to improve their manufacturing process, making the use of brass more profitable and thus offering a concrete, cheaper but high-quality alternative to gold. This transition from more expensive towards cheaper materials is historically extremely relevant, since it represents a first fundamental step towards sequins becoming the universal fashion accessory they are nowadays.

The key role played by the final steps of the manufacturing process on the long-term stability of the brass alloy is revealed. It cannot be inferred, however, whether or not the craftsmen were fully aware and concerned with the effect of the production process on the stability of the objects. The sequins were stamped out of sheet metal likely using a two-parts blanking die. The pressure involved in the process produces a highly strained structure, but also an extremely smooth and homogenous surface with few to no imperfections. The compositionally similar brass wires, on the other hand, shaped through several drawing/annealing cycles, show defects and deep scratches developed in the direction of drawing that created preferential points for the degradation to start, negatively affecting the overall stability of the objects. In this context, the choice of manufacturing process was most likely subordinated to the achievement of specific mechanical and aesthetical properties. Therefore, the effect these methods had on the surface properties and long-term stability of the alloy, positive in the first case and negative in the second, were probably not the main concern of the artisans that produced them. This means that, although the composition of the alloy and the expertise of the craftsmen undoubtedly played a fundamental role, the exceptional long-term stability of the sequins might not have been fully foreseeable at the time of their production.

Additionally, this work represents a significant step towards a deeper understanding of the long-term behavior of α-brass, in particular in an indoor environment. The results show how historical brass can still present unaltered aesthetical properties after a five-century long exposure to the environment, even when the Zinc content is above the arbitrary 15% limit that conventionally defines alloys at high risk of dezincification. Such information has a clear relevance well beyond the field of conservation science and cultural heritage. Furthermore, the novel insights obtained on the historical

manufacturing process of metallic sequins, shed light on a key-moment in the evolution of this preeminent fashion accessory recurring throughout human history.

## 2.5  Supplementary information

### 2.5.1    Figures
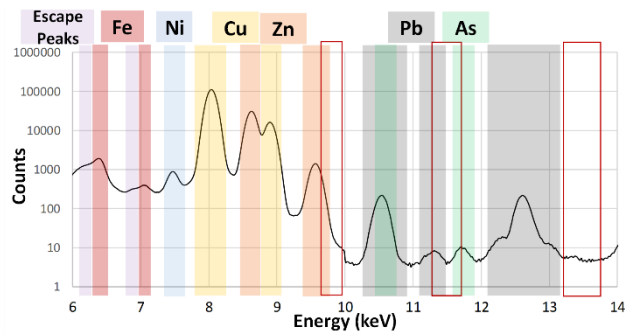


*Figure S2.1_Average XRF spectrum of the brass sequins analyzed and interpretation of the main features. In evidence the areas in which fluorescence peaks would have been observed if gold was present in the samples (empty red rectangles). As is present in too low concentrations to be accurately quantified.*
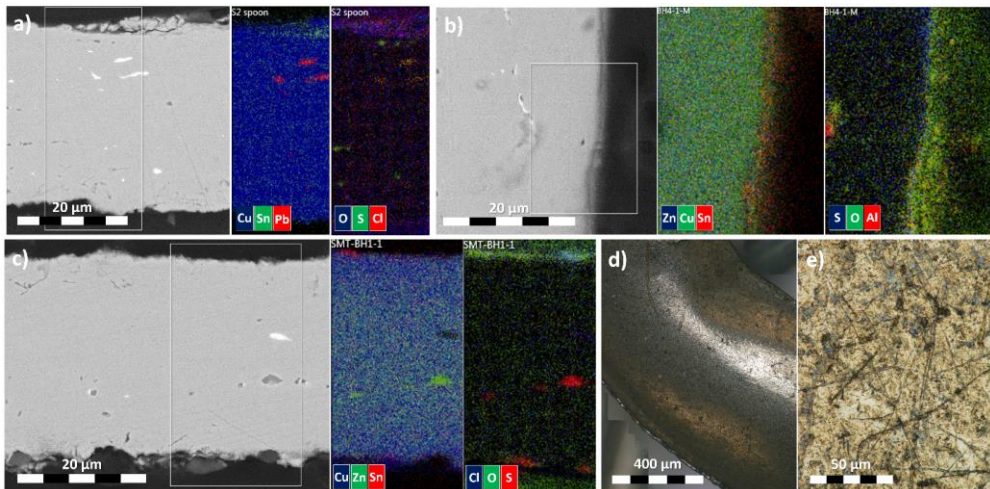


*S2.2_Partially abraded and oxidized remnants of a tinning treatment on the surface of three sequins. a, b, c) SEM-EDX in cross-section of two non-degraded, silver-like sequins (stylistic group 6) and one tarnished sequin (stylistic group 8); d, e) microphotographs of a macroscopically non-degraded sequin (Stylistic group 6).*
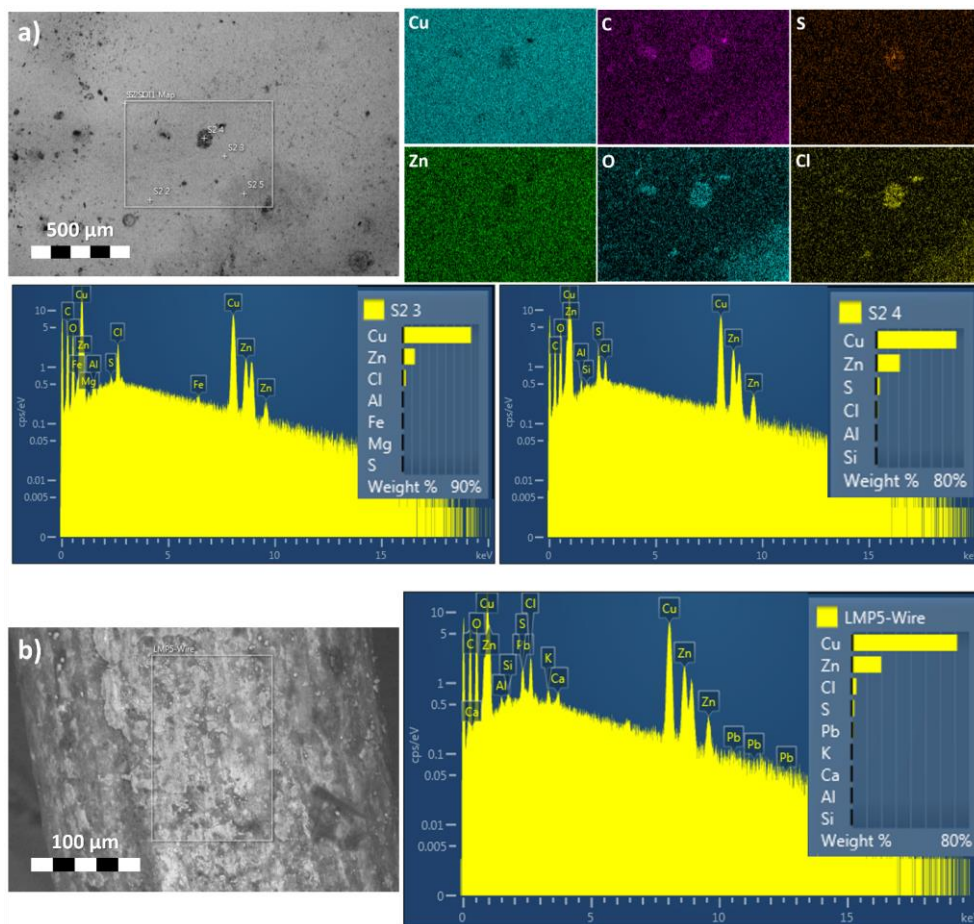
*Figure S2.3_SEM-EDX elemental surface analysis. a) Macroscopically non-degraded sequin (Group 5) and b) heavily tarnished wire.*
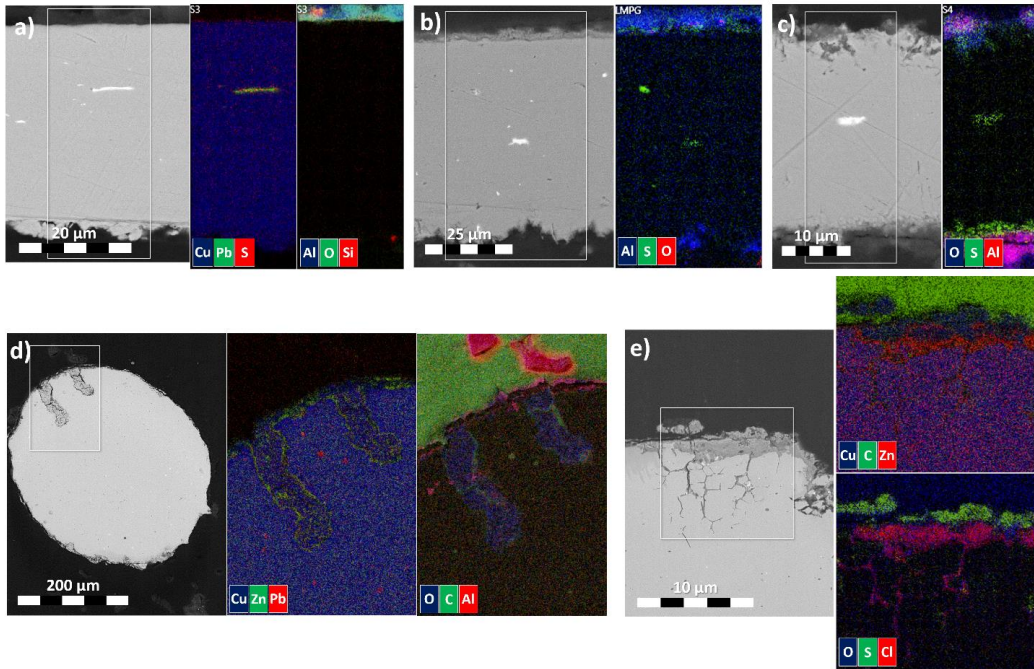
*Figure S2.4_SEM imaging (back-scattered electrons) and EDX elemental mapping of a selection of samples in cross section. a) non-degraded sequin (stylistic group 5); b) slightly tarnished sequin (stylistic group 2); c) tarnished sequin (stylistic group 8); d) and e) heavily tarnished wires.*



*Figure S2.5_Photomicrographs in polarized light of the transversal cross-section of one wire after metallographic etching. The main metallographic features are highlighted (red=twin lines; white=strain lines).*
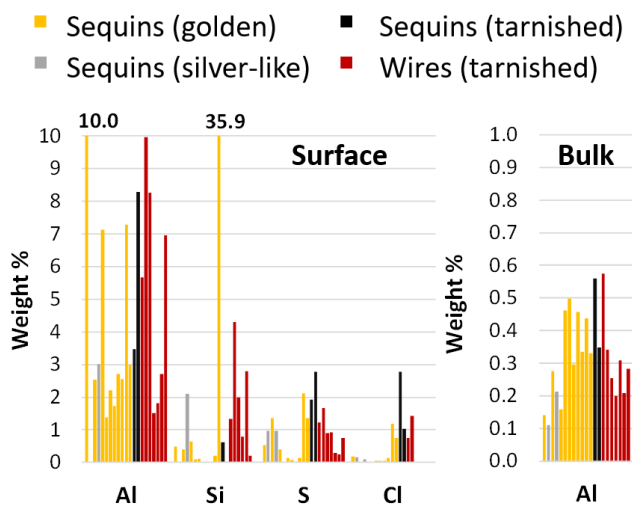
*Figure S2.6_SEM-EDX results in cross section. Average surface and bulk concentration of elements linked to degradation or surface deposition.*
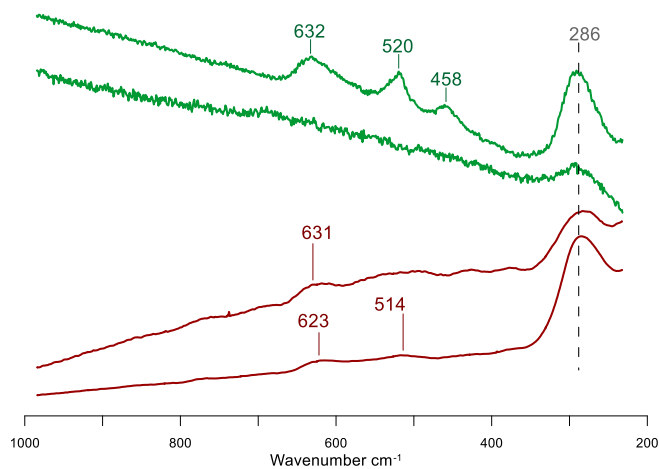


*Figure S2.7_µ-Raman spectra of the degradation products on the sequins (green) and the wires (red).*

### 2.5.2 Metallographic analysis of the wires

The metallographic analysis of the wires showed some differences in grain size but overall similar features in all the samples (Figure 2.5a and Figure S2.5). All the wires show recrystallized and twinned grains, with no clear elongation in the direction of drawing. The presence of annealing twins is not surprising, since the wires are normally annealed in between the different drawing stages in order to maintain a certain plasticity.[169] Such a cyclic alternation of thermal treatment and cold working reduced the size of the grains to few tenths of microns on average (from a minimum average diameter of 9.3 μm to a maximum of 43.8 μm). As expected, the thinnest wires present also the smallest grain sizes (Figure S2.5), due to the higher number of cycles they were subjected to. The lack of elongation and the absence of visible residual strain suggests that the last step of the production was either the annealing of the wire or a very light cold work. This would have produced extremely ductile wires, with the necessary plasticity to build the complex structure of the fine floral decorative elements in the enclosed gardens. Some of the smallest wires show a certain amount of strain lines in the most superficial grains (Figure S2.5). This might be the result of a final drawing step but might also be due to the folding of the wire while assembling the decorative elements. Either way, this limited amount of strain would not significantly affect the overall mechanical properties of the wire.

### 2.5.3 Degradation products on the surface of sequins and wires

Only small amounts of extremely localized corrosion products (Figure S2.3a and Figure S2.4a) or, in the few macroscopically degraded samples, thin degradation layers (Figure S2.4b and c) are observed on the surface of the sequins. These contain mostly Cu, C, S, O and/or Cl. In the wires, on the contrary, a thick crust with a layered structure is visible (Figure S2.3b and Figure S2.4d,e). In detail, an inner Zn- and Cl-rich layer is present, which is covered by a series of overlapping layers containing mostly Cu and Cl, O and S respectively. In general, S is more systematically present than Cl in both types of objects (Figure S2.6). This is possibly a result of the large presence of silk and other proteinaceous textiles (felt, wool) containing sulfur in the enclosed gardens.

μ-Raman analyses on the degraded areas of sequins and wires (Figure S2.7) confirmed the hypothesis that similar degradation mechanisms take place on the two different

types of objects. Since all the samples showed an intense fluorescence band above 1000 cm$^{-1}$, only lower frequencies are shown. In this region some characteristic bands can be observed, which highlight striking similarities on a molecular level between the degraded areas of sequins and wires. These results complement the elemental similarities previously described. In detail, the main band appears at 286 cm$^{-1}$ and has been assigned to CuCl.[187] Other minor signals can also be noticed, around 515 cm$^{-1}$ (probably related to Cu$_3$Zn(OH)$_6$Cl$_2$),[187] at 458 cm$^{-1}$ (probably related to Cu$_2$Cl(OH)$_3$, mainly found on the sequins)[188] and around 630 cm$^{-1}$ which, together with the shoulder at 220 cm$^{-1}$ is probably linked to the presence of Cu$_2$O.[188] Following the SEM-EDX analysis, additional compounds containing S would be expected. The lack of Raman signals related to these compounds is likely due to the fact that these tend to fall at higher wavenumber and thus, in this case, they are likely hidden by the fluorescence band.[189] The analyses show also the presence of Al and Si on the outer surface of most sequins and wires (Figure S2.6), mostly in combination with O in what appears as a surface deposit (Figure S2.4), in agreement with the FTIR data (Figure 2.3). Al, unlike Si, appears to be present not only on the surface, but also in the bulk of both sequins (tarnished and non-degraded) and wires (Figure S2.6). Al is an element often added to brass in order to improve its resistance to degradation, due to its tendency to form a passivating Al$_2$O$_3$ layer on the surface of the metal.[190] The addition of Al to brass, however, is a modern practice and the amount of Al added in order to obtain a protective effect is much larger (~2 wt%) than the one encountered in all the samples.[191]

Based on this evidence there are three possible reasons for the presence of an Al- and O-rich layer on the surface of sequins and wires. The first hypothesis is that the Al observed in cross-section is the result of a contamination during the preparation of the samples. An alumina sub-micron sized powder was in fact used during the mechanical polishing and it might have been partially embedded in the soft metal. This contamination might also account, at least in part, for the higher Al concentration observed on the surface of the objects in cross section. The Al$_2$O$_3$ polishing paste might in fact accumulate at the interface between the metal and the resin due to the presence of discontinuities and cracks. However, since Al was observed on the surface of most samples even before embedding them, a certain amount of Al is undoubtedly present on the surface of the objects and is not a product of contamination. A second possibility is that the Al rich layer observed on the surface is the result of the deposition of Al-containing dust. The presence of high amounts of Al in the dust of the enclosed gardens would not be surprising. The very large amount of textiles in the gardens, in fact, were most likely dyed using alum as a mordant (the most commonly used mordant in

antiquity) and are now heavily oxidized, embrittled and pulverized. A third hypothesis is that Al is actually present in the bulk of the metal as yet another minor impurity rather than as a voluntary addition, and that small amounts of $Al_2O_3$ are formed on the surface during the oxidation of the alloy. Since similar amounts of surface and bulk Al are present both on non-degraded and heavily tarnished objects (Figure S2.4 and Figure S2.6), however, this process clearly does not play a significant role in the different conservation state of sequins and wires. All things considered, it is not unlikely for the real situation to be a combination of these three possible scenarios. What is certain, however, is that the Al distribution cannot account for the different appearance of sequins and wires.

# |3

# Glass-induced metal corrosion of otherwise extraordinarily stable brass decorative elements

**A. Marchetti\*, V. Beltran\*, G. Nuyts, J. Jaroszewicz, F. Borondics, C. Sandt, M. Van Bos, S. De Meyer, E. Otten, M. Debulpaep, K. De Wael**

**\* Contributed equally**

# Abstract

In the previous chapter, it was demonstrated how the stamped metal sequins of the enclosed gardens of Mechelen present an extraordinary stability, mainly thanks to their optimal surface properties (low roughness and limited imperfections). It was also shown how the brass wires in the same enclosed gardens, with a similar composition but worse surface properties, appear heavily tarnished and strongly degraded from an aesthetical point of view. Nonetheless, even in this case, the corrosion did not generally spread deeply in the alloy and did not cause a loss of structural properties. This is probably a result of the good chemical composition (medium Zn content and low impurities) and of the "mild" conservation environment represented by the enclosed gardens (indoor and partially enclosed).

This chapter shifts the focus on a very small selection of sequins and wires from the enclosed gardens that, in striking contrast with the exceptional stability previously described, appear severely corroded. This behavior was observed, in particular, when the metal was found in proximity of glass beads. The two materials were probably in close contact but, given the extreme corrosion and loss of structural properties of the metallic elements, the original position was not always certain. Interestingly, not only the supposed contact with glass negatively affected the stability of the brass alloy, but a more pronounced degradation with green-blue corrosion products was observed also on the glass surface. This section of this doctoral thesis, focuses on the application of innovative analytical strategies to investigate the reason for the severe corrosion of this limited amount of brass objects. In particular, the presence of markers of a glass-induced corrosion of the metal alloy is thoroughly verified.

# 3.1  Introduction

The glass-induced corrosion of metals has been the object of an in-depth research over the past decade.[9,48–50,192–200] This has led to the identification of some of the most common degradation products on the surface of different types of metals found in contact with glass, as well as to the deciphering of the main mechanism behind this chemical interaction.[9]

The starting point for the glass-induced degradation of metals is the hydration and corrosion of glass. The exposure of historical glass to atmospheric moisture, in fact, can trigger a series of chemical reactions which can ultimately produce highly reactive alkaline solutions,[27] extremely dangerous for the conservation of metals. In detail, the weathering of historical glass starts with the condensation of moisture and the penetration of molecular water into the glass surface.[12,201] This produces structural changes in the silica network by breaking siloxane bonds (Si-O) and forming silanols (Si-OH).[202] This first step is followed by the selective leaching of the metallic ions acting as network modifiers in the glass. The most mobile cations, such as the monovalent alkali $Na^+$ and $K^+$, are substituted by protons through an ion exchange reaction favored at lower pH values (e.g. due to the solubilization of acidic gaseous pollutants in the deposited moisture).[13,203,204] This process creates a leached surface layer with a lower density than the bulk glass and causes a local increase of the pH in the solution deposited on the glass surface.[205]

Such an increase, particularly relevant in alternate wet/dry conditions in which the solution is not regularly replenished, represents a high risk for further degradation of glass but also for the corrosion of metals.[9,49,205] In the case of glass, the $OH^-$-rich solution can attack the silicate network, structurally weakening it by breaking Si-O bonds.[205] This ultimately leads to the formation of a low-density cation-depleted "gel" layer increasing in thickness until it eventually cracks off, thus exposing a new surface of healthy glass to moisture and degradation.[205] In the case of metal, the contact with the alkaline liquid film formed during glass degradation can promote corrosion and the formation of degradation products.[9] Such products are often mixed metal salts containing both alkali cations from the glass and additional species from the corroding metal.[9,48,49,192,197] The counter anions are not only the $OH^-$ produced during the ion exchange process, but also $CO_3^{2-}$, $CH_3COO^-$ and, more often, $HCOO^-$, all formed due to the solubilization of gaseous species in the alkaline liquid film[48,206] (namely atmospheric $CO_2$ and acetic acid, formic

acid and formaldehyde off-gassed during the ageing of wood and other organic materials[62]).

When it comes to Cu alloys, a wide range of glass-induced green to blue $Cu^{2+}$ corrosion products has been observed and identified.[9,48,50,192,195] The most common are the basic sodium copper formate with formula $Cu_4Na_4O(HCOO)_8(OH)_2 \cdot 4H_2O$ [192] and the basic copper formate $Cu_2(OH)_3HCOO$ [195], however carbonates and acetates are also observed (e.g. chalconatronite, $Na_2[Cu(CO_3)_2] \cdot 3H_2O$ [50]; basic sodium copper carbonate, $Na_3[Cu_2(CO_3)_3(OH)] \cdot 4H_2O$ [9]; sodium copper formate acetate, $NaCu(HCOO)_{1+x}(CH_3COO)_{2-x}$ [9]; sodium copper acetate carbonate, $NaCu(CO_3)(CH_3COO)_{2-x}$ [48]). In the specific case of brass, the Zn component of the alloy is also attacked by the alkaline liquid film, with the formation of white zinc formate dihydrate ($Zn(HCOO)_2 \cdot 2H_2O$) [48] and of a more complex basic zinc copper formate[193] with varying stoichiometry (general formula $Zn_{(10-6x)}Cu_{(3+6x)}(HCOO)_8(OH)_{18} \cdot 6H_2O$) and color (from whiteish to greenish and bluish).

Most of the glass-induced brass corrosion products identified until now therefore contain $Na^+$, $Cu^{2+}$ and/or $Zn^{2+}$. However, even though not yet identified, $K^+$ and $Ca^{2+}$ degradation products are also expected to be formed, in particular in the case of potash-lime-silica glass.[9] This type of glass, diffused in Northern and Central Europe from the 11th century onwards, is in fact richer in K and Ca and has lower Na and Si content than soda-lime-silica glasses.[207] Moreover, the low Si/high K levels should also result in a higher tendency to undergo cation leaching processes[203,204] and, therefore, in a higher risk for metals in contact with this specific type of glass. In addition, also nitrates, sulphates and additional metal carboxylates were not previously identified but are expected to be present on the surface of brass corroded due to glass (due to the deposition of atmospheric gas pollutants),[9] especially in indoor environments where soluble degradation products cannot be easily washed away (such as the one of the enclosed gardens[123]).

In this study, a thorough characterization of the degradation products present on the surface of the corroded brass elements as well as on a series of glass beads were performed, with the final aim of identifying the degradation processes responsible for the poor conservation state of the different samples. In particular, similarities in composition between metal and glass degradation were investigated, aiming at identifying a material proof of the possible role played by weathered glass in the corrosion of the otherwise stable metal.

In detail, a multi-faceted analytical approach was employed to verify the presence of three possible markers of a glass-metal interaction:

- Presence of elemental markers of the reciprocal interaction between the materials, e.g. leached-out glass alkaline cations such as $Na^+$ and/or $K^+$ on the surface of the metal and metallic ions such as $Cu^{2+}$ or $Zn^{2+}$ in the degraded areas of the glass);
- Mapping of the distribution of the corrosion products on the surface of the glass beads, e.g. discrete distribution in the central shaft or in other areas of possible contact with a brass wire;
- Presence of molecular markers of the glass-induced metal corrosion in the degraded areas of the samples, e.g. formate, acetate and/or carbonate basic salts.

Given the small amounts of degradation products available for analysis, in particular on the surface of the glass beads, and due to the complex geometry of most samples, this study presented significant analytical challenges especially in the second and third steps. Therefore, in order to map the distribution of the corrosion products on the surface of the glass beads in a non-destructive (and non-invasive) manner, in particular in non-easily accessible areas such as the central shaft, micro-computed tomography (μ-CT) analysis were performed. By relying on differences in chemical composition and attenuating power between the corrosion products and the bulk glass, and in particular exploiting the presence of heavier and more attenuating elements in the corrosion products, it was possible to easily visualize their distribution in the final reconstructed volume.

When it comes to the molecular characterization of glass-induced metal corrosion products, the two techniques more commonly employed are XRPD and μ-Raman.[9,48,50,192,195] The application of these techniques in this specific case, however, was extremely challenging and led to no resolutive and clear identification, mainly due to the limited amount of corrosion products available, to the complex geometry of the samples and to an extreme sensitivity of the degradation products to the Raman laser. Thus, in order to overcome the limits encountered with the traditional spectroscopic and crystallographic approaches, a novel molecular spectroscopy technique, optical photothermal IR (O-PTIR), was employed. This non-destructive and contactless analytical method allows to obtain vibrational information on the materials analyzed with a sub-micron resolution and without the need for samples preparation. A detailed description and evaluation of the advantages and drawbacks of this technique are presented in the introduction (Section 1.4.2) and in a dedicated chapter of this thesis (Chapter 6).

## 3.2 Materials and methods

### 3.2.1 OM

The optical microscopy (OM) observation of the samples in analysis was performed with a Nikon Eclipse LV100 microscope in dark field mode.

### 3.2.2 µ-XRF and MA-XRF

The µ-XRF point analysis were performed with an Artax portable micro-XRF spectrometer (Bruker GmbH, Germany) equipped with a Rh-probe. The X-ray generator was operated at 50 kV and 600 µA, while the acquisition time was 300 s. The beam was focused on the analysis spot with the help of a laser and a camera, point analysis with a spotsize of approximately 70 µm were performed. The analysis of the XRF spectra, including the integration of the characteristic fluorescence signals, was carried out using PyMCA.[208] Further multivariate analysis were performed with the open-source Quasar 1.0.0 software.[209,210]

The MA-XRF elemental imaging of the sequin in analysis was performed with an M6 Jetstream macro-XRF scanning spectrometer (Bruker GmbH, Germany) equipped with a Rh-probe. The X-ray generator was operated at 50 kV and 600 µA. The elemental imaging data were obtained with a 50 µm spotsize, a distance between measuring points of 40 µm and a dwell time of 40 ms. The data analysis, including the calculation of the elemental distribution maps, was performed with the software of the instrument.

### 3.2.3 SEM-EDX

The samples were examined with a Field Emission Gun – Environmental Scanning Electron Microscope (FEG-ESEM) equipped with an Energy Dispersive X-Ray (EDX) detector (FEI Quanta 250, USA; at AXES and EMAT research groups, University of Antwerp), using an accelerating voltage of 20kV, a take-off angle of 30°, a working distance of 10 mm and a sample chamber pressure of $10^{-4}$ Pa. Imaging was performed based upon secondary electrons (SE), back-scattered electrons (BSE). Different EDX maps were collected, using a beam current of ~0.5 nA, at different resolution, with pixel

size values from 0.5 to 2.7 µm and dwell time from 0.1 to 10 ms/pixel. From these EDX maps several EDX spectra were extracted for quantification. The dwell time of these spectra lie in the range of 1-7 s per spectrum.

### 3.2.4   µ-CT

The glass samples were initially scanned by means of a benchtop tomographic scanner SkyScan 1172 (Bruker, Belgium). Different X-ray tube voltage (40 kV or 100 kV) and current (250 µA and 100 µA) were applied depending on the attenuation properties of the single samples.  500 projection images were collected with a step size of 0.4 degrees and a final resolution between 4 and 8 µm, depending on the size of the sample. The latest SkyScan (Bruker, Belgium) softwares (NRecon, DataViewer, CTAn, and CTVox) were used to reconstruct and process images and to obtain virtual slices and volume rendering reconstructions. Higher resolution scans were obtained with a different X-ray tomographic system (MICRO XCT-400, Xradia - Zeiss), at 40 kV and 200 µA. 800 projection images were collected with a step size of 0.25 degrees and a final resolution between 2 and 4 µm, depending on the size of the sample. The volume was reconstructed with the instrument software and was then exported to Avizo Fire (FEI Visualization Sciences Group) for further 3D image analysis.

### 3.2.5   O-PTIR

O-PTIR measurements (spectra and images) were collected on the mIRage Infrared Microscope (Photothermal Spectroscopy Corp.). Spectra were collected in reflection mode, 2 cm$^{-1}$ spectral data point spacing, through a 40x, 0.78 NA, 8 mm working distance Schwarzschild objective. The pump IR source was a pulsed, tunable four-stage QCL device, scanning from 800 to 1900 cm$^{-1}$. The probe was a CW 532 nm visible variable power laser. To obtain a good signal-to-noise ratio to interpret the spectral difference, 20 scans spectra were averaged at each point. The data treatment was performed using the Quasar 1.0.0 software.[209,210] Spectral maps were generated by normalizing the spectra by the min-max method (using the most intense band) and plotting the integrated area of selected peaks (with a linear baseline computed using two wavenumbers at the feet of the peak). To ensure a fair comparison, no smoothing, baseline correction or any other adjustment were applied to the spectra.

### 3.2.6   SR-μ-FTIR

SR-μ-FTIR measurements have been performed in SMIS beamline at Synchrotron Soleil (France) using a Thermo Fischer NEXUS FTIR spectrometer Nicolet 5700 attached to a microscope Continuum XL. Samples were analysed in transmission mode accumulating 256 scans at 4 cm$^{-1}$ spectral resolution, the wavenumber range is between 4000 to 800 cm$^{-1}$. The wire corrosion products considered were analyzed in a diamond compression cell.

### 3.2.7   μ-Raman

Raman spectroscopy measurements were performed by means of a Xplora Plus Microscope (Horiba) with a 100 mW 785 nm laser (the effective power used was always ≤1%), considering the effective range of 50-2000 cm$^{-1}$. At each point, five accumulations were collected during 10 seconds each one. The spectra presented have not been corrected in order to avoid any kind of distortion

### 3.2.8   XRPD

The analysis was carried out with a custom-built diffraction setup in reflection geometry at a fixed incident angle of 10 degrees between the X-ray source and sample. The X-ray source generates a beam of monochromatic Cu-Ka radiation (8.04 keV) with a photon flux of 2.9 x 10^8 and a focal diameter of 0.15 mm. A 2D single photon counting PILATUS 200K detector was used to register the emerging diffraction signals. Analysis of the data was performed with the in-house developed software package XRDUA[211] while the structural information was obtained from the American Mineralogist Crystal Structure Database and additional references mentioned in the text.

## 3.3 Results and discussion

In contrast to the exceptionally stable brass sequins, a limited number of highly degraded objects attracted our attention. In order to shed light on the severe degradation affecting these brass elements, one heavily corroded sequin and ten fragments of corroded wires were considered (Figure 3.1a,b). In addition, to verify the hypothesis of a contact interaction between glass and metal, four glass beads belonging to two different stylistic groups (i.e. different shape and macroscopic appearance) were also analyzed (Figure 3.1c,d). The two glass beads Type 1 (Figure 3.1c) are dark blue and glossy in appearance, with clearly degraded areas showing a partially detached brown-iridescent layer. The glass beads Type 2 (Figure 3.1d), on the other hand, are slightly smaller than the Type 1 beads, brown to greenish in color and opaque. All the samples in analysis, both glass and metal, showed different amounts of white and green-blue degradation products on their surface (Figure 3.1).
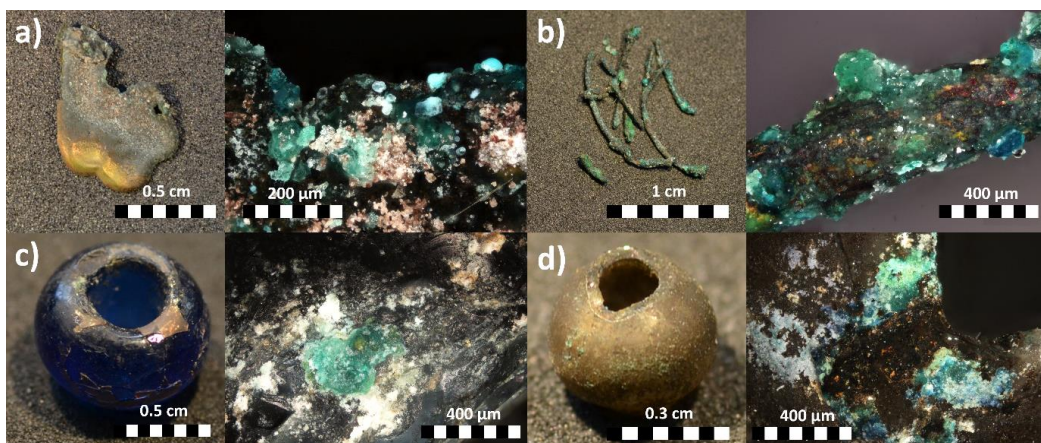


*Figure 3.1_Samples overview: pictures and photomicrographs of corrosion products (OM in polarized light). Examples of a) corroded brass sequin, b) fragments of corroded brass wires, c) glass bead Type 1, d) glass bead Type 2.*

### 3.3.1 Elemental markers of glass-metal interaction

To identify possible markers of a glass-metal interaction, the elemental composition of the corroded areas of the metal objects was first determined. The results of MA-XRF analysis, performed only on the sequin (Figure 3.1a) being it the only relatively flat and large sample, confirmed the presence of Cu and Zn in the bulk of the material, as seen

for all the other sequins previously analyzed (Chapter 2). The analysis also clearly highlighted a close link between the distribution of elements such as K, Zn and to a minor extent Ca, and the severe corrosion observed (Figure 3.2a). The abundant presence of K only in the corroded areas of the sequin was confirmed also by the SEM-EDX analysis, which also excluded the presence of significant amounts of other light elements (too light to be detected by XRF), such as Na (Figure 3.2c and Figure S3.2). In a similar fashion, K was also systematically found in the corroded areas of the brass wires in analysis (Figure 3.2b), often in association with higher Zn concentrations (Figure S3.1 and Figure S3.2).
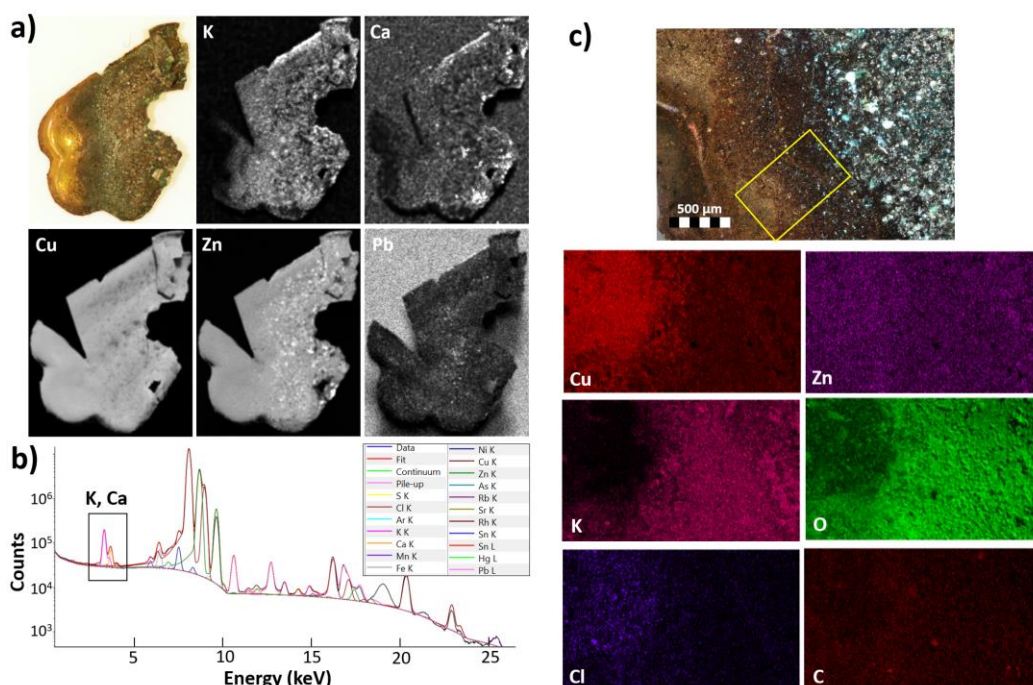


*Figure 3.2_Elemental analysis of the corroded sequin and wires: a) MA-XRF elemental maps for the sequin; b) SUM μ-XRF spectrum of the degraded areas of the wire fragments, in evidence the presence of K and Ca; c) SEM-EDX elemental maps for a selected area on the surface of the sequin (yellow rectangle).*

The presence of Zn in the degraded areas is expected for brass, since this component of the alloy is more readily oxidized than Cu and, therefore, it is often selectively leached out from the bulk metal and, if not washed away, reprecipitated in oxidation products on the surface.[145,212] The systematic presence of K, on the other hand, is likely a result of the interaction with weathered historical glass. Like Na$^+$, more often encountered in the products of glass-induced metal corrosion identified,[9,50,192,195] K$^+$ can in fact leach out

100

from the silica network during the hydration and degradation of glass and then reprecipitate, possibly in the form of mixed salts.[9,48,213] Zn and K mixed salts (possibly carboxylates), have in fact been recently described by Fischer et al.[48] as products of a glass-induced metal corrosion on the surface of historical brass objects.

The hypothesis of K originating from the glass beads is clearly supported by the chemical composition of the glass, since both Type 1 and Type 2 beads contain significant amounts of K (Figure 3.3, more details in Supplementary information section 3.5.2), and by the poor conservation state of the beads. A partially detached iridescent gel layer is in fact visible on the surface, in particular on the blue Type 1 beads (Figure 3.1a and Figure S3.3). This indicates that severe hydration and cation exchange processes took place on the surface of the glass. Such degradation processes would have produced an alkaline K-rich aqueous layer on the surface,[213] which could have ultimately interacted with the brass and caused the observed K-enrichment of the metal samples.[196]

In order to confirm the hypothesis of an interaction between glass and metal, the elemental composition of the colored corrosion products on the surface of the glass beads were also studied. Interestingly, a systematic difference between the areas containing corrosion products and the remaining part of the glass objects was observed (Figure 3.3). In the first place, an exploratory PCA analysis on the μ-XRF data for the glass beads (Figure 3.3a,b) clearly showed a relative increase of Cu, Zn and Pb in the visibly corroded areas (red cluster), in addition to differences in composition between Type 1 (blue cluster) and Type 2 beads (green cluster) (more details in Supplementary information section 3.5.2 and Figure S3.4).

A more detailed analysis of the composition of these Cu- and Zn-rich areas allowed to clearly identify the copresence of alkaline metals, Cu and Zn in green-blue but also in white corrosion products on the glass surface. Significant differences in the composition of the degraded areas were observed between the two types of beads, probably as a reflection of the different bulk composition of the glass (See supplementary information section S3.4.2). In particular, in addition to K, Cu and Zn, the Type 1 beads showed also significant amounts of Ca both in the glass and in the degraded areas (Figure 3.3b). The Type 2 beads (Figure 3.3a), on the other hand, did not contain Ca but Na both in the glass and in the corrosion products. Such a copresence in the corrosion products of Cu and Zn, main components of all the metallic sequins and wires in the enclosed gardens (in this thesis, Chapter 2), with the specific alkaline cations present in the two different types of glass in analysis, strongly supports the hypothesis of an interaction with metal.
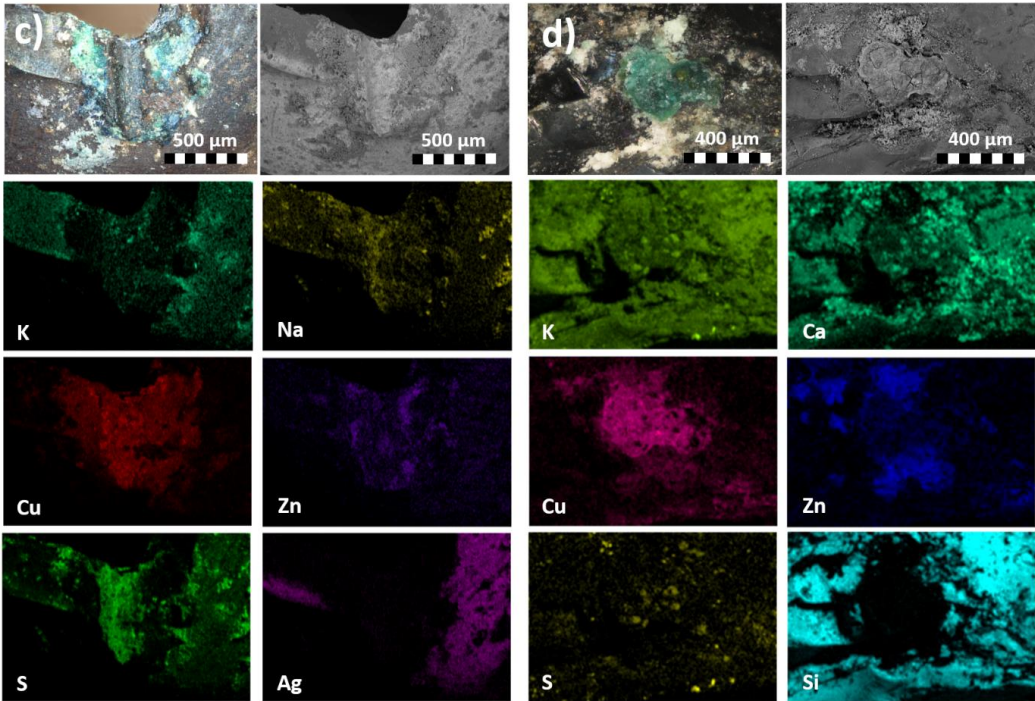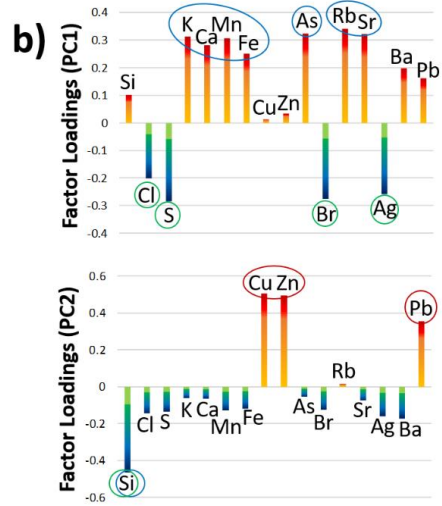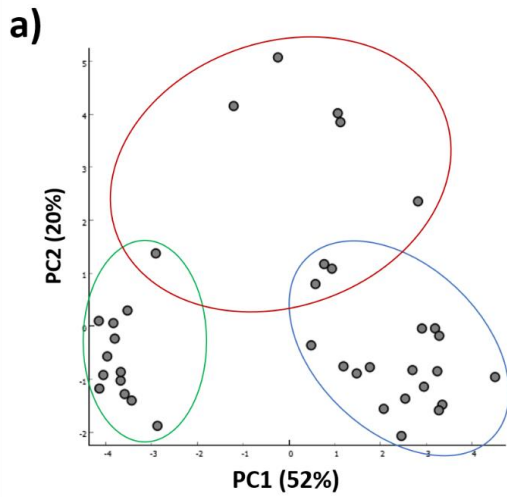
*Figure 3.3_Elemental analysis of corrosion products on glass: PCA of μ-XRF data (a,b) and SEM-EDX elemental maps (c,d). a) scatter plot of the first two components, in evidence three clusters corresponding to potash glass (Blue), silvered potash glass (Green), areas enriched in Cu, Zn and Pb (Red); b) Factor loadings for the first two principal components; c) EDX maps of green-blue corrosion on a Type 2 bead; d) EDX maps of green-blue corrosion on a Type 1 bead.*

Both types of beads also showed some S on the surface, which is likely linked to the large presence of silk and wool in the enclosed gardens. The partially enclosed environment and the off-gassing from the degrading textiles, in fact, likely led to a build-up of $H_2S$ and other S containing gases,[63] which could have then reacted either directly with the cationic species leached from the bulk of the glass[15,213] or indirectly, forming secondary products through the interaction with existing carbonate or formate salts.[214] This is clearly seen on the surface of both glass beads, with S often localized in small spots and often in co-presence with K and/or Ca, for Type 1 glass, and K or Na, for Type 2 glass. In this second case, however, significant amounts of S are also found in combination with Cu and Ag. The presence of S in some of the Cu-containing corrosion products, together also with Na, possibly indicates a three sided interaction between glass (leached $Na^+$ in alkaline solution), brass (solubilized $Cu^{2+}$) and atmospheric S-containing gases, in a similar fashion as described by Eggert et al..[9] On the contrary, the co-presence of Ag and S, as observed also in the μ-XRF analysis (Figure 3.3a,b and Figure S3.4), indicates the presence of a thin opaque layer of $Ag_2S$ on the beads, likely formed due to the interaction of a silver surface layer with the off-gassed $H_2S$.[1,63] This suggests that the now dull and dark-colored Type 2 beads were originally silvered and therefore highly reflective.

In conclusion, the simultaneous presence of Cu, Zn and K in the corrosion products encountered on the surface of both metal and glass samples, strongly supports the hypothesis of an interaction between glass and metal. In this case, the absence of significant amounts of Na and the presence of K and Ca on the surface of the corroded metal objects, possibly indicates that all the wires and the sequins in analysis were in contact with glass with a similar composition to the Type 1 beads, rather than to the Type 2 (richer in Na). However, it needs to be mentioned that the presence of Ca and K in the corrosion products of a copper alloy is not sufficient, on its own, to confirm a chemical interaction with glass. These cations, in fact, often occur in airborne particulate matter (PM)[91,215] and might simply be present on the metal due to deposition and soiling. In order to confirm the hypothesis of a glass-induced metal corrosion, therefore, further proves were non-invasively collected by means of μ-CT and O-PTIR spectroscopy.

### 3.3.2 Distribution of metal corrosion products on the surface of glass

Additional evidence of the interaction between metal and glass in the samples in analysis was obtained by studying the distribution of the Cu- and Zn-containing products on the surface of the glass beads. Since Cu and Zn are significantly heavier atoms than the Si, O

and the alkaline metals mostly present in the glass, this distribution can be studied non-invasively by means of μ-CT analysis. These corrosion products containing higher concentrations of (relatively) heavy atoms are in fact characterized by higher attenuating properties compared to the lighter atoms in the silica network, and are therefore well-distinguishable in the final reconstructed volume.

In Figure 3.4, the μ-CT analysis of three different beads clearly showed that highly attenuating (i.e. heavier) species are distributed mainly on the surface of the central shaft and on the inner rim. These are areas where the glass certainly came in contact with a metallic wire (ubiquitously employed to assemble the decorative elements in the enclosed gardens[123]) and, therefore, the areas where an interaction between metal and glass would have been more likely to take place. The hypothesis of a glass-metal interaction is therefore further strongly supported by the experimental findings.
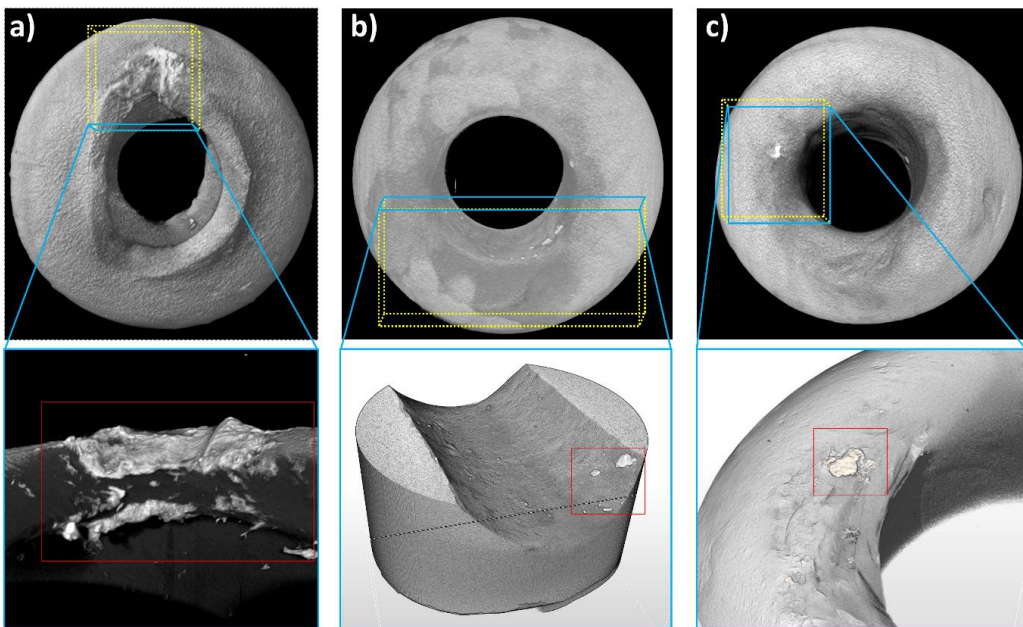


*Figure 3.4_μ-CT scan results: reconstructed volume and localization of highly attenuating corrosion products (red rectangles) on the inner rim and central shaft of one Type 2 glass bead (a) and two Type 1 beads (b, c).*

### 3.3.3    Molecular characterization of the corrosion products

The final confirmation of the hypothesis of a chemical interaction between weathered glass and brass in the samples in analysis, was obtained by means of the molecular characterization of the corrosion products. XRPD and µ-Raman are the two techniques most commonly employed in the study of the products of metal-glass interaction.[9,48,50,192,195] Unfortunately, in our case, the limited amount of corrosion products available and the complex geometry of the samples in analyses, in particular when it comes to the glass beads and brass wires, made the application of XRPD extremely challenging. Moreover, the analysis by means of µ-Raman spectroscopy were also complex for the samples under investigation, due to the extreme sensitivity of the corrosion products to the laser source. For this reason, only a very low laser power (≤1%) could be used with long accumulation times and, even then, a very low signal was obtained. Additionally, lower wavelength lasers, 540 nm, showed intense fluorescence bands. More in depth analysis are, however, planned in the near future thanks to the purchase of a new state-of-the-art Raman spectrometer in my group that will include additional lasers at 633 and 1064, providing new possible configurations.

In order to overcome the limits encountered with the traditional spectroscopic and crystallographic approaches, a novel molecular spectroscopy technique, optical photothermal IR (O-PTIR), was employed.

The first fundamental information obtained with OPTIR regards the extreme complexity and heterogeneity of the surface of the samples. Several different peaks are always found completely overlapped in the region between 1700 and 1300 cm$^{-1}$, complicating and in some cases hindering the exact identification of the species present. Nonetheless, relevant information on the composition of the glass and metal samples could be obtained, also by supporting the OPTIR interpretation with complementary SR-FTIR analysis of small amounts of degradation products scratched from the surface of one brass wire (Figure S3.5). In Figure 3.5, the results of the O-PTIR analysis of a small area (28x60 µm) on the surface of the corroded sequin are presented.

These results are particularly interesting for several reasons. First of all, a glass particle is clearly identified on the surface of the metal object (Figure 3.5b spectrum 1 and Figure 3.5c) due to the very broad and intense band between 1250 and 950 cm$^{-1}$ (Si-O-Si and Si-O region[14]). The fact that a very similar glass spectrum is observed on the surface of a

Type 2 potash glass bead (Figure 3.6a), strongly supports the hypothesis of a direct contact between this type of glass and the brass objects.
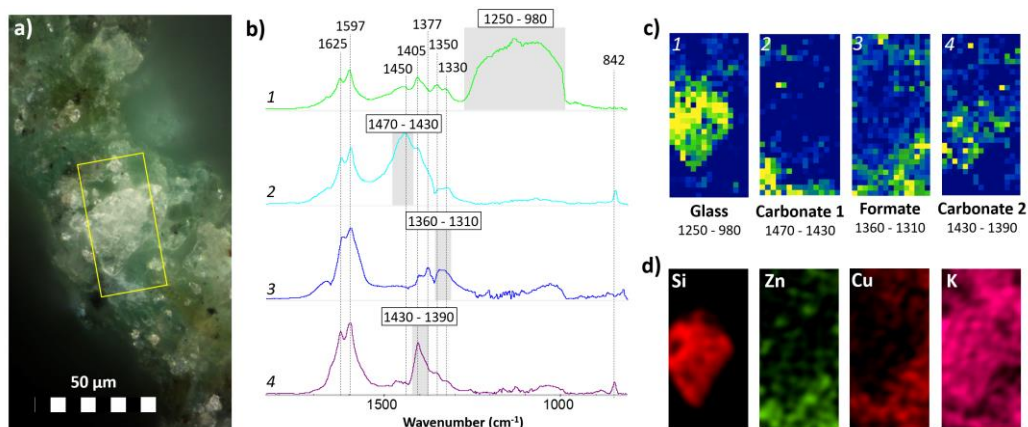


*Figure 3.5_High-resolution O-PTIR molecular imaging of degradation products on the surface of the degraded brass sequin: a) OM photomicrograph of the area in analysis (yellow rectangle=imaged area); b) representative spectra of the imaged species and c) corresponding integration maps with tentative interpretation (integration range in cm$^{-1}$); d) complementary SEM-EDX elemental imaging of the scanned area.*

The presence of additional bands in the 1650-1300 cm$^{-1}$ region is likely the results of the co-presence of other species (spectra 2, 3 and 4 in Figure 3.5b) overlapping and in close contact with the glass particle. In particular, the presence of bands in the regions between 1600-1500 and 1500-1400 cm$^{-1}$ is likely a result of the presence of carboxylate (formate and/or acetate) species (C-O asymmetric and symmetric respectively), while the region between 1450-1350 cm$^{-1}$ may also contain the bands related to carbonate (C-O stretching).[216–219] The fact that similar features are observed also on the surface of the glass beads (Figure 3.6a and Figure S3.5) indicates that these species might result from the weathering of glass.[9,214,220] The interpretation of the O-PTIR spectrum is confirmed by the SEM-EDX elemental analysis (Figure 3.5d), showing the presence of Si and K in the area identified as glass.
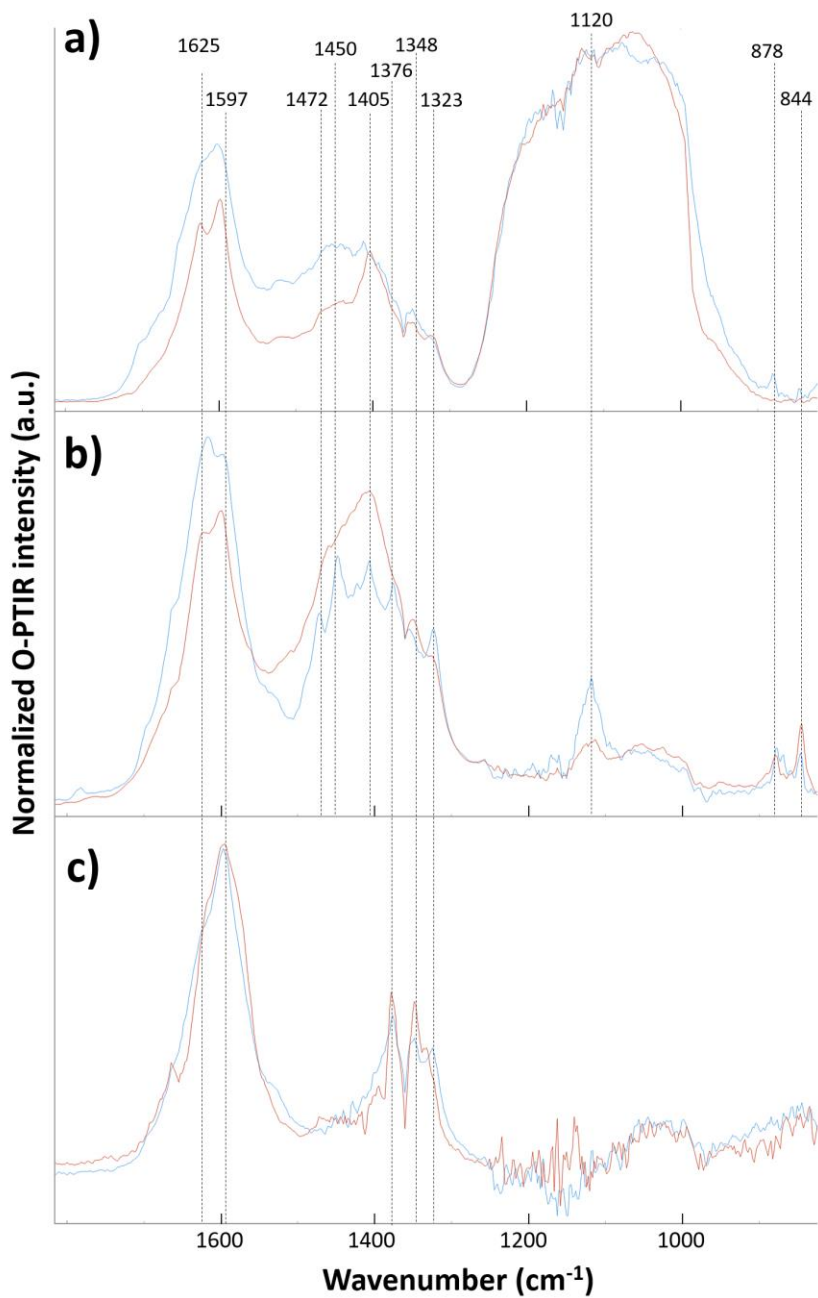
*Figure 3.6_O-PTIR spectra highlighting the similarities between the degradation products on metal (sequin, red) and glass (bead Type 1, blue): a) visually non degraded glass and glass particle on metal surface; b) complex mixture of overlapping carbonate and/or carboxylate corrosion products; c) basic copper formate.*

Spectrum 2 in Figure 3.5b is characterized by an intense and broad absorption at around 1440 $cm^{-1}$. One explanation for the broad nature of the band can be the overlapping of the signals from several species, such as the ones in spectrum 3 and spectrum 4 (Figure 3.5b), with a metal carbonate (e.g. Zn carbonate, asymmetric C-O stretching at 1440 $cm^{-1}$ and sharp $CO_3^{2-}$ bending at ≈842 $cm^{-1}$ [218]). This co-presence of different species could also explain the overlapping of Zn, Cu and K signals in these areas (Figure 3.5d).

In principle, the complex nature of the band at 1440 $cm^{-1}$ and the co-presence of several elements could also suggest the presence of mixed carbonate species in these areas. A mixed K and Zn carbonate, for example, was likely identified in the corrosion products of the wire analyzed by SR-FTIR (Figure S3.5 spectra 3 and 4). In this case, in fact, a $CO_3^{2-}$ asymmetric stretching vibration shifted to higher wavenumbers (1480 $cm^{-1}$) and two bending vibrations at 880 $cm^{-1}$ and 842 $cm^{-1}$ were observed in areas containing mostly Zn (~30%wt), K (~16%wt), and O (~35%wt) (and Cu, ~19%wt, due to the overlapping with a Cu-containing specie, Figure S3.5 spectrum 1). Such a mixed K, Zn salt is certainly observed in the corrosion products of this metal wire, but its presence, in principle, cannot be excluded also in the other samples. The interpretation of the O-PTIR data for the glass and sequin samples, in fact, could be potentially hindered by the large number of overlapping bands observed in the 1400-1500 $cm^{-1}$ region (Figure 3.6b). Nonetheless, the identification of this product even only on the corroded wire is remarkable. In order for a mixed K, Zn carbonate to be formed, in fact, $Zn^{2+}$, $K^+$ and solubilized atmospheric $CO_2$ would have to be simultaneously present in an alkaline solution[9]. Such a condition would have been likely met, in the enclosed gardens, only in the case of a direct contact and interaction between weathered potash glass (such as the one of the glass-beads in analysis) and the brass alloy.

Spectrum 3 of Figure 3.5b is one of the spectra most commonly encountered in the green-bluish areas of glass beads, sequin and wires alike (Figure 3.6c). Complementary data for this compound were also obtained from the SR-FTIR analysis of the corrosion products of one wire and from the μ-Raman analysis (Figure 3.7). This compound is mostly observed in areas containing Cu and O and close to no Zn and K (Figure 3.5c,d and Figure S3.5 spectrum 1). The presence of intense peaks in the 1650-1580 $cm^{-1}$ and 1400-1320 $cm^{-1}$ regions indicates the presence of a carboxylate and, in particular, of a Cu formate.[70] The intense peak at ~ 1600 $cm^{-1}$ is assigned to the asymmetric stretching vibration of the carboxylate group, while the peak at 1350 $cm^{-1}$ is assigned to the symmetric stretching vibration.[217] The bands at 2800 and 1377 $cm^{-1}$ respectively represent the stretching and in-plane bending of the CH group in the formate moiety.[221]

The good match of the Raman peaks at 213, 170 and 59 cm⁻¹ with the in plane lattice vibrations of copper formate tetrahydrate,[222] confirms the band assignment proposed.
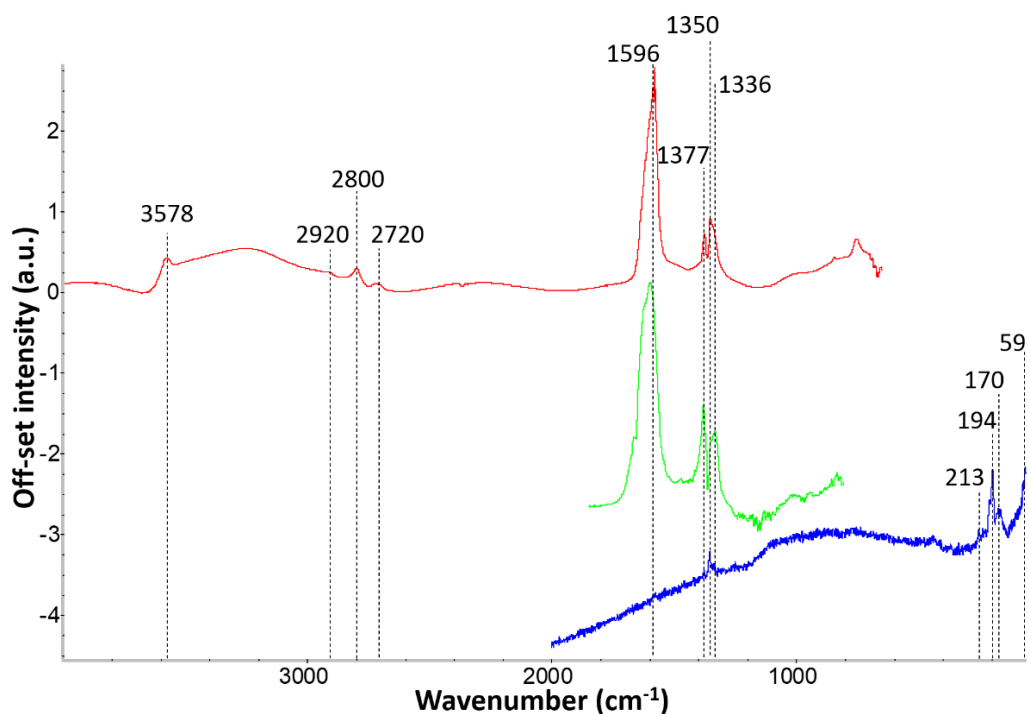


*Figure 3.7_Analysis of a green-blue corrosion product repeatedly encountered in all the samples in analysis: SR-FTIR of a wire sample (Red); O-PTIR (green) and μ-Raman (Blue) of a glass bead Type 1 sample.*

In addition, a sharp peak at 3578 cm⁻¹ indicates that free (non-hydrogen bonded) OH groups are also present in the corrosion product in analysis,[70] suggesting the presence of Cu-OH moieties in the lattice. The 194 cm⁻¹ vibration in the Raman spectrum can therefore be assigned to the O-Cu-OH out of plane bending (together with an overlapped band at 170 cm⁻¹).[223] The presence of a basic copper formate, and in particular of $Cu_2(OH)_3(HCOO)$ [9], was confirmed also by the XRPD analysis of the sequin, the only sample flat and large enough to be successfully analyzed with this technique (Figure S3.7).

In conclusion, the greenish-blue corrosion product observed on both the glass and metal samples in analysis is identified as a form of basic copper formate. The occurrence of copper formates as degradation products on the surface of historical metal objects is generally extremely rare.[9] However, when Cu alloys are found in contact with weathered

glass, basic copper formates become some of the most common corrosion products.[9,48] The alkaline liquid film formed during the degradation of glass, in fact, favors both the solubilization of the metal alloy and the conversion of formaldehyde to formic acid through the Cannizzaro reaction,[48] ultimately leading to the precipitation of the metal formate. A high pH is therefore a fundamental requisite for the formation of such corrosion product on the surface of brass. In the context of this study, this means that the diffuse presence of basic copper formate on the samples in analysis decisively confirms the existence of an interaction between glass and brass. In addition, the strong connection between this formate corrosion product and glass is further supported by the evidence that, in Figure 3.5, this is distributed in close contact with the glass particle previously observed (Figure 3.5c,d).

The remaining spectrum in Figure 3.5b (spectrum 4) is tentatively assigned to an additional carbonate specie ($CO_3^{2-}$ stretching at ~1400 cm$^{-1}$ and bending at 875 cm$^{-1}$ [224]). Based on the SEM-EDX results (Figure 3.5d), this could be potassium carbonate resulting from the degradation of the potash glass.[225]

In conclusion, even though traditional characterization techniques such as XRPD and μ-Raman proved mostly unsuccessful for the study of the samples in analysis, the application of the novel O-PTIR spectroscopy (in combination with complementary techniques) allowed us to: 1) demonstrate the presence of small glass particles on the surface of the corroded metal, suggesting a close contact between metal and glass objects; 2) verify the presence of similar corrosion products on the surface of glass and metal samples; 3) identify clear products of the glass-induced metal corrosion, such as basic copper formate ($Cu_2(OH)_3(HCOO)$) and, possibly, a mixed Zn, K carbonate-containing salt.

## 3.4 Conclusions

In conclusion, the proposed multi-analytical approach allowed to unequivocally identify processes of glass-induced metal corrosion as the main cause for the severe corrosion of few selected brass objects in the enclosed gardens. The presence of basic Cu formate and of mixed K and Zn salts distributed mainly in the areas of potential contact between glass and metal (e.g. in the inner shaft of the glass beads), in fact, clearly confirms the initial hypothesis of a material-material interaction. A chemical interaction therefore

took place at the glass-metal interface, driven by the formation of K-rich alkaline liquid films on the surface of the weathered potash glass in analysis. This clearly indicates how, even objects extraordinarily stable in indoor environmental conditions, such as the brass sequins in the enclosed gardens of Mechelen (Chapter 2), can completely corrode when their (micro-)environment is modified (e.g. by the contact with alkaline liquid films formed from the weathering of historical glass). This information is extremely relevant for the purpose of conservation. In the future, in fact, conditions of T and RH potentially resulting in moisture condensation on the surface of glass should be avoided. A particular focus should be also kept on the evolution of the conservation state of brass objects in the proximity of potash glass decorative elements.

Moreover, the results of this study also clearly highlight the huge potential for the application of novel analytical techniques, such as O-PTIR spectroscopy, for the non-invasive analysis of cultural heritage objects. In addition, the possibility to employ laboratory μ-CT to non-invasively image the conservation state of small glass objects is also confirmed.

Further analyses are planned in order to better understand the nature of the mixed K, Zn products, likely carbonates, observed on the surface of the corroded objects. In a similar fashion, also the Cu-, Na-, S-containing degradation products observed on the surface of one of the Type 2 glass beads will be further investigated. The elemental and molecular microanalysis of the objects in cross section, in particular, will likely help to unequivocally characterize these new products of the glass-induced corrosion of brass.

# 3.5 Supplementary information

## 3.5.1 Figures
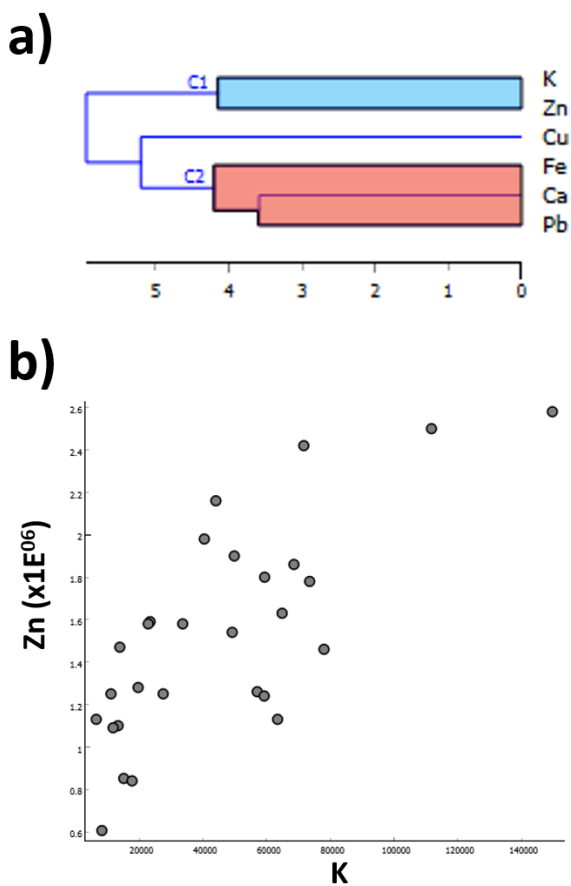


*Figure S3.1_Correlation observed between the µ-XRF responses of K and Zn (integrated K Lines) in the degraded areas of the corroded brass wires: a) hierarchical clustering analysis of the most relevant variables (Euclidean distance, Ward's method); b) elemental scatter plot for Zn and K.*
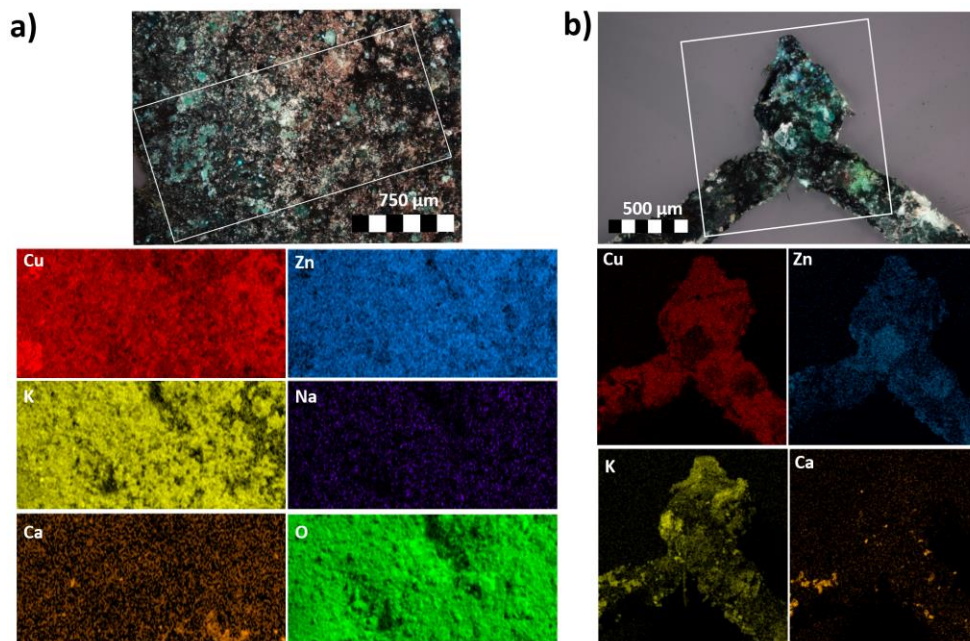
*Figure S3.2_OM photomicrographs and SEM-EDX elemental maps of the corrosion products on the surface of a) the metallic sequin and b) a corroded wire fragment.*
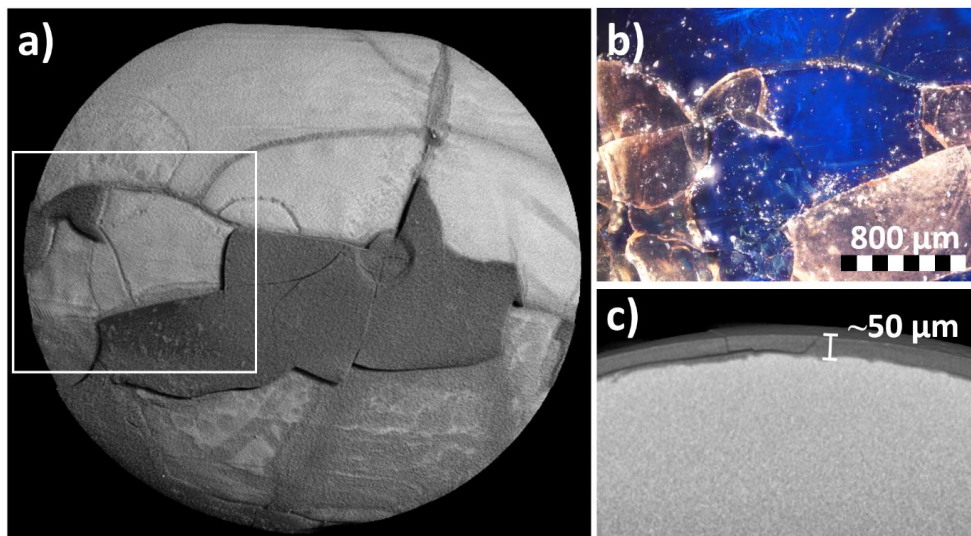


*Figure S3.3_Partially detached iridescent gel layer on the surface of a Type 1 glass bead: a) μ-CT reconstructed volume, the less electronically dense gel layer appears darker than the healthy glass; b) photomicrograph (OM, polarized light); c) virtual cross-section of the gel layer clearly showing the partial detachment and the thickness of the layer.*
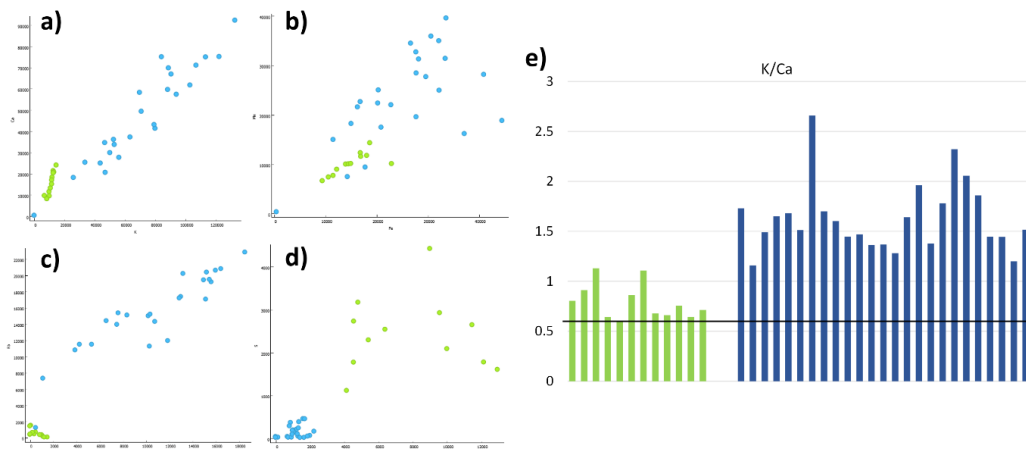
*Figure S3.4_Results of the μ-XRF elemental analysis for the glass beads (Blue = Type 1; Green = Type 2): scatter plots of a) Ca/K; b) Mn/Fe; c) Rb/As; d) S/Ag and e) K/Ca ratio.*
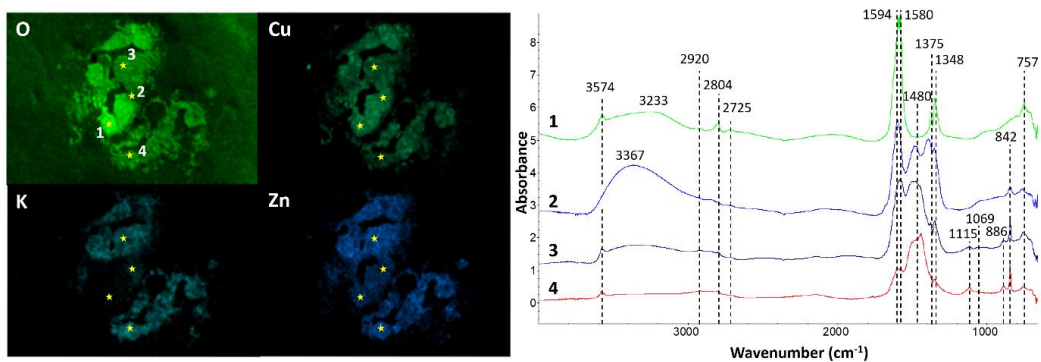


*Figure S3.5_SEM-EDX elemental maps and SR-μ-FTIR spectra of the degradation products scratched from the surface of one corroded wire. The material was pressed in a diamond compression cell prior to the analysis. In evidence the spots analyzed with SR-μ-FTIR and the most intense absorption peaks in the spectra.*
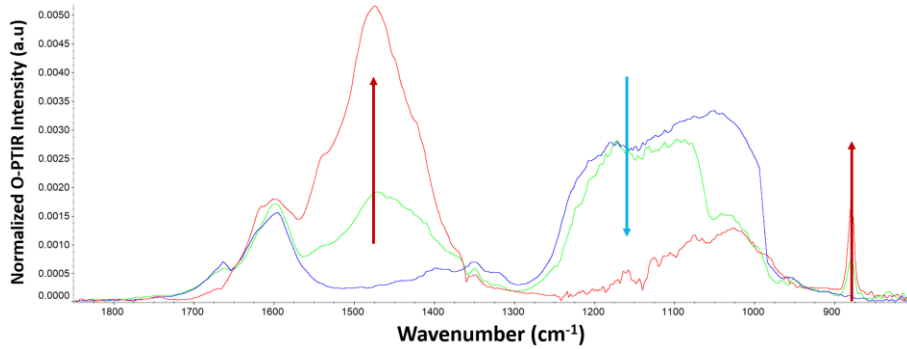
*Figure S3.6_O-PTIR spectra of the surface of a Type 1 glass bead clearly showing a progressive increase in degradation associated with a decrease of the Si-O-Si component between 1250 and 1050 cm$^{-1}$ and an increase of the carbonate-related bands at ∼1480 cm$^{-1}$ and ∼878 cm$^{-1}$. Blue = non degraded,  Green = partially degraded and red = heavily degraded.*
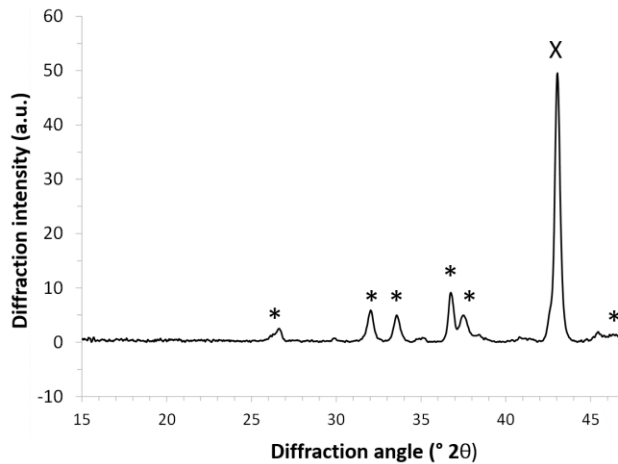


*Figure S3.7_XRPD results for the corroded sequin in analysis. Average diffractogram for a 5mm long line in the degraded area of the sample. In evidence the diffraction peaks associated to Cu$_2$(OH)$_3$(HCOO) [9] (*) and high-Cu brass [226] (X).*

## 3.5.2   Elemental analysis of the glass beads

The non-invasive μ-XRF analysis of the glass samples in analysis highlighted similarities but also clear differences in composition between the two types of glass beads. Both are most likely examples of potash glass with a limited lime content, as indicated by the K/Ca ratio always higher than 0.6 (Figure S3.4) and by the low contribution of Pb in the average XRF spectrum.[207,227] It is important to mention that the experimental K/Ca ratio

is likely affected by the poor conservation state of the glass, since the degradation is normally associated with the leaching of alkali ions from the surface. However, this process would cause a decrease of the ratio due to the leaching of K rather than an increase, hence not changing the attribution of the samples is analysis to the potash glass category.

Despite the overall similarity in composition, some clear differences were observed between the two types of beads (Figure S3.4). In the first place, a different linear relationship between K and Ca is observed for the two types of glass (Figure S3.4a), with higher concentrations and higher K/Ca ratios for the Type 1 beads. Other diagnostic elements such as Fe and Mn,[227] on the other hand, did not allow a clear distinction between the two groups (Figure 3.3b). Particularly interesting is the correlation between As and Rb, as well as their presence only in the Type 1 beads. As might in fact be an impurity of a Co-based colorant in the glass,[228] which could explain the deep-blue color observed only in this type of beads`. The absence of a clear Co signature in the XRF spectrum, in this case, could be due to the low concentration of the chromophore (Co concentrations as low as 0.02%, below the detection limit of the technique, can already produce an intense color). A characteristic feature of the Type 2 glass beads is the presence of Ag and S (Figure 3.3a,b,c and Figure S3.4d), which can be traced back to the thin degraded silvering finish observed on the surface of these beads. Higher amounts of Cl and Br are also observed in the silvered sequins (Figure 3.3a,b), suggesting the possible presence of Ag chlorides in addition to $Ag_2S$ on the degraded surface (Br is often found in traces in chloride salts). The presence of a degraded Ag film on the surface might also cause an attenuation of the X-ray fluorescence signal from the bulk of the glass, which might be the reason for the lower intensities observed for the glass-related elements (Figure S3.4a,b,c and Figure 3.3a,b).

The differences in composition between Type 1 and Type 2 glass beads are confirmed also by the SEM-EDX analysis of their surface (Figure 3.3c,d). The presence of Na on the surface of the glass beads Type 2 and its absence on the glass beads Type 1, in fact, suggests that a certain amount of Na (too light to be detected with XRF methods) might be present in the bulk of the Type 2 glass. Since a through quantification of Na would require the destructive sampling of the bead (e.g. to prepare a cross section), however, no further analyses were performed at this stage.

# |4

# Unraveling the role of lattice substitutions on the stabilization of the intrinsically unstable $Pb_2Sb_2O_7$ pyrochlore: explaining the lightfastness of lead pyroantimonate artists' pigments

**A. Marchetti, R. Saniz, D. Krishnan, L. Rabbachin, G. Nuyts, S. De Meyer, J. Verbeeck, K. Janssens, C. Pelosi, D. Lamoen, B. Partoens, K. De Wael**

# Abstract

The pyroantimonate pigments Naples Yellow and lead tin antimonate yellow are recognized as some of the most stable synthetic yellow pigments in the history of art. However, this exceptional light-fastness is in contrast with experimental evidence suggesting that this class of mixed oxides is of semiconducting nature. In this chapter, the electronic structure and light-induced behavior of the lead pyroantimonate pigments are investigated by means of a combined multi-faceted analytical and computational approach (photo-electrochemical measurements, UV-Vis diffuse reflectance spectroscopy, STEM-EDS, STEM-HAADF and density functional theory calculations). The results demonstrate both the semiconducting nature and the lightfastness of these pigments. Poor optical absorption and minority carrier mobility are the main properties responsible for the observed stability. In addition, novel fundamental insights into the role played by Na atoms in the stabilization of the otherwise intrinsically unstable $Pb_2Sb_2O_7$ pyrochlore are obtained.

# 4.1 Introduction

Lead antimonate yellow ($Pb_2Sb_2O_7$), commonly referred to as Naples Yellow, is one of the synthetic yellow pigments most frequently encountered in pre-20th century Western European art.[229–232] The reason behind the appreciation of artists for this pigment lies not only in its intense bright hue and high opacity, but also in its reported lightfastness and overall stability.[230]

Lead antimonate yellow has been lost and rediscovered several times throughout history. After enjoying a great popularity in ancient Egyptian, Mesopotamian and Roman cultures,[230,233,234] where it was the main yellow colorant and opacifier used in glass and glazes, by the end of the 4th century A.D. the pigment fell into disuse throughout Europe. From that moment on, during the Middle Ages, the utilization of lead antimonate yellow was limited to the Slavonian, Islamic and Byzantine world.[231,235] Only in the 16th century the pigment returned to Western Europe, reappearing in the Italian art of the beginning of the century. The reasons for the resurgence of interest for this pigment is still not clear. The most likely hypothesis is that the know-how on the production of lead antimonate was introduced to the Venetian glass workshops by foreign glassworkers, mostly Arab, during large waves of immigration from the Eastern Mediterranean.[229,231] Throughout the 16th century, the production of Naples yellow remained intimately related to the glass and ceramic industries.[236] Several recipes from this period of time describe the synthesis of yellow pigments to be used as colorants and opacifiers in glass. However, the complex terminology used in the sources and the tendency to refer to different pigments with the same name of Giallolino created a certain confusion on the topic in the past.[236–238] In 1540, Biringuccio, in his treatise *Pirotechnia* wrote about the use of antimony in making yellow glass enamels. Few years later, in the late 1550s, Piccolpasso published a treatise on the potter's craft (*Li tre libri dell'arte del vasaio*), where he reported a series of central Italian recipes for the synthesis of lead antimonate pigments, used to obtain yellow glazes on majolica. The largest concentration of manuscripts containing recipes for the production of this yellow pigment for the glass industry, however, may be found in Venice and Murano,[229,239–244] where the glass manufacture was concentrated. A great amount of examples of the use of Naples Yellow in colored glass and pottery glazes exist in literature.[234,245–251]

The first reference to Naples yellow as a painting pigment dates back to the early 17th century, when Valerio Mariani da Pesaro (1568–1625?) in his treatise about miniature

painting, gives a detailed description of the production of so-called giallo de' vasari (potter's yellow), corresponding to lead antimonate yellow.[252] Before this time Naples yellow was already but sporadically used by some Italian artists like Giovanni Bellini (1430-1516), Lorenzo Lotto (1480-1556/7), Raphael (1483-1520), and Titian (1490-1576),[236,253] that however still preferred the use of other yellow pigments in most of their paintings. In some of these cases of early use of Naples yellow in easel paintings, namely *Feast of the Gods* by Bellini (1514) and *The nativity* by Lotto (1523), Berrie[253] observed how the lead-antimony mixed oxide is found in the form of crystallites suspended in a siliceous glass matrix. It is not clear if in this case the pigment was produced by grinding of a yellow lead-antimony glass (in a similar fashion as with blue smalt) or if a glassy frit was rather used, but the presence of silicon confirms the close relationship of this pigment with the glass and ceramic industries. The Naples Yellow commonly found in later paintings, however, does not contain silicon, indicating a complete transition from the glass to the easel painting world. Whether embedded in a glass matrix or directly mixed with siccative oil, lead antimonate yellow is always regarded as extremely stable and lightfast.[230]

In the last decade of the 20$^{th}$ century, a variant of Naples Yellow was rediscovered and identified in a series of 17$^{th}$ century Italian paintings[254] and 18$^{th}$-19$^{th}$ century Mid-European paintings.[255] The new form, called lead tin antimonate yellow, contains tin as an additional cation ($Pb_2SnSbO_{6.5}$). The effect of the Sn substitution on the overall properties of the material is still unclear, mostly due to the recent rediscovery of this pigment.[230]

From a structural point of view, lead (tin) antimonate yellows belong to the pyrochlore class, a group of cubic compounds described by the general formula $A_2B_2X_6Y$ (where A and B are metals and X and Y are most of the time oxygen atoms, X=O and Y=O').[256,257] The "backbone" of this structure is constituted by a network of corner shared octahedra formed by $B_2X_6$ units. This interpenetrates a second network of $A_2Y$ units, where every oxygen atom is surrounded by four A atoms in a tetrahedral coordination. In the case of lead antimonate A=$Pb^{2+}$ and B=$Sb^{5+}$, while in the case of lead tin antimonate half of the B sites are occupied by $Sb^{5+}$ and half by $Sn^{4+}$.

The pyrochlore structure tolerates a wide range of substitutions at the A, B and Y sites, as well as vacancies at the A and Y sites, which leads to a large diversity of electrical properties for the compounds belonging to this class.[256] When it comes to the stability and light-fastness of artistic pigments, these electric properties play a major role. A

semiconducting behavior, in particular, is generally associated with a poor stability of the paint film.[19,39,76,109,258,259] In the specific case of pyroantimonates with A=$Pb^{2+}$, the information in literature is still very limited. Past authors have even questioned the very existence of a $Pb_2Sb_2O_7$ mixed oxide in the pyrochlore structure,[256,260,261] suggesting that the lattice would either present a rhombohedral distortion (if the composition is exactly $Pb_2Sb_2O_7$) or a partial substitution of $Sb^{5+}$ in the octahedral sites (stabilizing the cubic structure). The UV-Vis reflectance spectra of Naples Yellow reported in literature[230,262] seem to suggest a semiconducting behavior for this pigment. A steep absorption edge between 400 and 500 nm is in fact observed, in a similar fashion to other light-sensitive semiconducting pigments such as cadmium yellow (CdS) and chrome yellow ($PbCrO_4$).[109,230,259] This hypothesis is supported by the evidence that other pyroantimonates (e.g. $Sn_2Sb_2O_7$, $Cd_2Sb_2O_7$, $Ag_2Sb_2O_6$) show a semiconducting behavior.[263–266] With the replacement of $Sb^{5+}$ by $Sn^{4+}$ (in the B sites) causing an additional shrinking of the conduction band and an increase in the band gap.[265] However, the extraordinary lightfastness of lead (tin) antimonate seems incompatible with the hypothesis of a semiconducting nature for this pigment.

Several research questions remain therefore still open when it comes to the stability of this family of pigments. Is pure $Pb_2Sb_2O_7$ actually stable in a pyrochlore structure? What is the explanation for the extraordinary stability of Naples Yellow, given the probable semiconducting nature of the pigment? What is the effect of the $Sn^{4+}$ substitution on the optoelectronic properties and on the stability of the material? With these fundamental questions in mind, in-house synthesized lead antimonate yellow and lead tin antimonate yellow powder samples (further referred to as LAY and LTAY, respectively) were studied by means of a combined multi-faceted analytical and computational approach. The synergic experimental and theoretical strategy allowed to probe the chemical composition, crystalline structure, optoelectronic properties and photochemical behavior of the pigments, leading to fundamental insights on the intimate relationship between their composition and stability.

## 4.2 Materials and methods

### 4.2.1 Synthesis

The LAY and LTAY powders considered in this study were synthesized in-house in the laboratories of the Department of Economics, Engineering, Society and Business Organization of Tuscia University (Viterbo, Italy). The choice of the recipes for the two compounds was the result of an in-depth historical research and laboratory testing described in detail in the work of Agresti.[232,237,267,268] Agresti et al. considered a wide selection of recipes for the production of Naples yellow, with a particular focus on those by Cipriano Piccolpasso,[269] by Giambattista Passeri (*Istoria delle Pitture in Majolica fatte in Pesaro*, 1758[270]) and by Valerio Mariani da Pesaro.[229,252] For lead tin antimonate yellow the recipes contained in the Danzica Manuscript[244] as well as the modern recipes described by Cascales et al.[271] were tested.

The LAY sample selected for this study (sample PSAPZ1 in the PhD thesis of Agresti[267] and sample 21 in Agresti et al.[232]) was prepared according to the recipes by Piccolpasso *Zalulino A* and *Castelli A*: Sb 1 lb; Pb 1.5 lb; feccia 1 on; salt 1 on. Where 1 lb (Roman libra) = 327.168 g , 1 on (Roman oncia) = 27.267 g and feccia corresponds to lees. The LTAY sample considered in this study (sample APSA1 in the PhD thesis of Agresti[267] and APSA in Capobianco et al.[268]) was synthesized following the optimized recipe and the recommendations in the work by Cascales et al.[271]: molar proportion Pb:Sn:Sb=2:1:1 in the starting oxides. The list of ingredients and the experimental conditions for both the pigments are summarized in Table 4.1. The pure grade chemicals employed in the synthesis were supplied by Sigma-Aldrich (St. Luis, Missouri), Acros Organics (New York City, New York) and MP Biomedicals (Santa Ana, California). The reagents were mixed in agate mortars and the obtained powders were put in a kiln on a terracotta tile for 5 hours at different temperatures (Table 4.1).

*Table 4.1_Reagents and conditions employed in the synthesis of the LAY and LTAY samples.*

|  | Source | Pb | Sb | Sn | Flux 1 | Flux 2 | Conditions |
|---|---|---|---|---|---|---|---|
| LAY | Piccolpasso[269] | $Pb_3O_4$ 4.91 g | $Sb_2O_3$ 3.27 g | - | $C_4H_4K_2O_6$ 2.76 g | NaCl 2.76 g | 800 ℃ x 5 h |
| LTAY | Cascales et al.[271] | PbO 8.90 g | $Sb_2O_3$ 2.90 g | $SnO_2$ 3.00 g | - | - | 925 ℃ x 5 h |

## 4.2.2   SEM-EDX

The samples were examined with a Field Emission Gun-Environmental Scanning Electron Microscope (FEG-ESEM) equipped with an Energy Dispersive X-Ray (EDX) detector (FEI Quanta 250, USA), using an accelerating voltage of 20kV, a take-off angle of 30°, a working distance of 10 mm and a sample chamber pressure of $10^{-4}$ Pa. Imaging was performed based upon secondary electrons (SE) and back-scattered electrons (BSE). EDX point spectra were acquired using a beam current of ~0.3 nA and a dwell time of 30 s per spectrum. The samples were previously coated with a thin carbon layer in order to obtain a conductive surface.

## 4.2.3   STEM-HAADF and STEM-EDX

STEM-HAADF (Scanning Transmission Electron Microscopy with High Angle Annular Dark Field detector) imaging and STEM-EDX (STEM with Energy Dispersive X-ray spectroscopy) spectrum imaging were performed using an aberration corrected FEI Titan 60-300 kV transmission electron microscope operating at an acceleration voltage of 300 kV. An aberration-corrected angstrom-sized probe with an electron probe current of 50 pA was used for atomic resolution imaging and 200 pA was used for EDS maps. For EDS mapping 512 × 512 maps were acquired with a dwell time of 10 μs. Such spectra were acquired cumulatively for 12 minutes. The quantification of the EDS spectra was performed using Cliff-Lorimer method. Independent component analysis (ICA)[272] of the spectrum images was performed using Hyperspy software.

## 4.2.4   XRPD

XRPD (X-Ray powder diffraction) measurements were performed using a Cu anode tube as X-ray source, operated at 40 kV and with 30 mA. The diffracted X-rays were detected by a Huber G670 Guinier camera. Of each sample four repetitions were recorded with a 15 min measuring time each. The obtained diffractograms were summed per sample and further analysed using XRDUA, an in-house software package.[211]

### 4.2.5   µ-Raman

µ-Raman (micro Raman spectroscopy) spectra were acquired with a Renishaw inVia multiple laser Raman spectrometer with a Peltier-cooled (203K), near-infrared enhanced, deep-depletion CCD detector (576x384 pixels) and coupled to a Leica optical microscope. Raman spectra were collected using an air-cooled argon laser (Stellar-Pro 514/50) operating at 514.5 nm wavelength (green) in combination with a 1800 l/mm grating with a maximum laser output power of 50mW. The laser was focused onto the samples through a 50x objective achieving a spatial resolution of a few micrometers. A power density of 1.6 kW/cm$^2$ and exposure times of 60 seconds were used. Measurements were repeated on different sample grains. Data acquisition was carried out with Renishaw WiRE 2.0 software.

### 4.2.6   DR-UV-Vis

Diffuse reflectance UV-Vis spectroscopy (DR-UV-Vis) measurements were carried out with an Evolution 500 UV-Vis double-beam spectrophotometer with RSA-UC-40 DR-UV integrated sphere (Thermo Electron Corporation, USA). The pigment powders were mixed with KBr dried at 200°C (0.02 g of pigment powders in 0.98 g KBr) and homogenized in a mortar. The mixtures were then positioned in the DR-UV-Vis cell and measured in the 300 to 800 nm range. The Kubelka-Munk function F(R) was then calculated from the diffuse reflectance results[273] and used as an approximation of the absorption coefficient α for the pigments considered. An estimation of the band gap energy from the experimental data was performed based on the Tauc relation[274]:

$$(\alpha h v)^{\frac{1}{n}} = A(h v - E_g)$$

where α is the absorption coefficient of the material in m$^{-1}$, which for small homogenous particles is assumed proportional to F(R) and independent on incident wavelength λ, hv is the energy of the incident photon in eV, n is a constant dependent on the nature of the band gap (n=1/2 for direct allowed transitions, n=3/2 for direct forbidden transitions, n=2 for indirect allowed transitions, n=3 for indirect forbidden transitions), A is a constant and $E_g$ is the size of the optical band gap in eV. On the basis of the computational results, the optical band gap for LAY and LTAY was treated as indirect (i.e. n=2 in the Tauc relation used to calculate the experimental band gap).

126

### 4.2.7    Photo-electrochemical methods

The electrochemical experiments were performed with an Autolab PGSTAT101 potentiostat (Metrohm, Switzerland) and the software NOVA 2.1. Graphite working electrodes (Ø = 3 mm) were pretreated by mechanical polishing with a P600 SiC-paper to obtain a rough surface. To remove any adherent SiC-particles, the electrodes were rinsed with deionized water in an ultrasonic bath for 20 s. The working electrode (WE) was modified by drop-casting a 1.50 μL droplet of ethanol-pigment suspension (50 mg/mL). After the evaporation of the solvent, a thin layer of the chosen pigment was left at the electrode surface. A saturated calomel electrode (SCE) and a glassy carbon electrode were used as the reference (RE) and counter electrode (CE), respectively. WE, with the pigment side oriented upward, CE and RE were positioned in an open container. The latter was filled with a 4 mL solution of electrolyte (1 mM NaCl solution or the nonaqueous ionic liquid 1-butyl-3-methylimidazolium tetrafluoroborate ([BMIM][BF4]). The effect of light on the electrochemical response of the different pigments was tested by exposing the WE to alternating cycles of darkness (∼20 s) and illumination (∼20 s) using different 30 mW laser sources (blue, 405 nm; green, 532 nm; red, 655 nm). Both chronoamperometric measurements (CA, changes of current VS time upon illumination at a constant potential) and linear sweep voltammetry (LSV, current VS potential when the latter is slowly but constantly increased over time) were performed. The light-chopped illumination conditions allowed for a fast and simple correction of the signal for background currents. The recorded photocurrent is a direct indicator of the photoactivity of the pigment considered, allowing for a relative comparison between different species.

### 4.2.8    Computational section

The density functional theory (DFT) calculations in this work were performed with the VASP code,[275] using the projector augmented wave (PAW) method to describe electron-ion interactions.[276] The Cd 4d5s, Na 3s, O 2s2p, Pb 5d6s6p, S 3s3p, and Sb 4d5s5p electrons were treated as valence. The compounds studied using DFT methods are introduced as needed in the Results section. The total energy calculations and geometry optimizations were done using the Perdew-Burke-Ernzerhof (PBE)[277] exchange-correlation functional in the case of metals, and the Heyd-Scuseria-Ernzerhof (HSE06)[278] hybrid-functional in the case of semiconductors. The plane wave basis set energy cutoff

(optimized) was set to 450 eV, and total energies were converged to within $10^{-4}$ eV. Geometry optimizations were done using the conjugate gradient algorithm implemented in the VASP code, and forces were converged to within 0.05 eV $\text{Å}^{-1}$.

The formation energies of the compounds with Pb partially substituted with Na and/or with O vacancies (in neutral charge state) were calculated via[279]:

$$E_f[D] = E_T[D] - E_T[P] + \sum_i n_i \mu_i$$

where $E_T[D]$ ($E_T[P]$) is the total energy of the defect (pristine) cell, and $n_i$ is the number of atoms of type $i$ introduced ($n_i < 0$) or removed ($n_i > 0$) from the cell, with $\mu_i$ the corresponding chemical potential.

# 4.3 Results and discussion

## 4.3.1 Chemical and structural characterization

The SEM/EDX analysis showed that the LTAY sample consists of a finely distributed powder (Figure S4.1 a), relatively homogenous in terms of both particle size (Φ≈0.1-2.0 µm) and chemical composition (Table S4.1). Furthermore, XRPD spectroscopy confirmed the presence of one single cubic pyrochlore phase with a lattice parameter a=10.56 Å (Figure 4.1a). This crystalline structure, together with the average chemical composition corresponding to the formula $Pb_2SnSbO_{6.5}$ (Table S4.1), matches the information available in literature on this pigment.[255,280]

LAY, on the contrary, showed a more irregular size distribution (Φ≈0.1-20.0 µm, Figure S4.1 b) and a deviation from the ideal composition (Table S4.1). Two different pyrochlore phases with slightly different lattice parameters were in fact observed via X-Ray powder diffraction (Figure 4.1b). A similar behavior is observed by Dik et al.[229] in in-house synthesized Naples Yellow samples calcinated at low temperatures (650˚C), and it is linked to changes in the Pb/Sb molar ratio. In the study by Dik, no metallic element other than Pb and Sb is present in the sample. In a different fashion, the change in the Pb/Sb ratio observed in the LAY pigment considered in this study is related to the substitution of $Pb^{2+}$ by $Na^+$ (originated from the NaCl used as a flux agent in the historical recipe followed for the synthesis). A significant and variable amount of Na is in fact observed in

128

all the pigment grains analyzed with SEM-EDX (Table S4.1) and while the molar ratio Pb/Sb is systematically lower than 1 (0.69±0.08), the ratio (Na+Pb)/Sb is much closer to 1 (1.06±0.15). The high tolerance to substitution in the pyrochlore structure and the similarity in the ionic radii of $Na^+$ and $Pb^{2+}$,[281] support the conclusion that the widespread presence of Na in the sample is caused by a partial substitution of Pb in the A sites of the lattice. The tendency of $Na^+$ to substitute $Pb^{2+}$ in the A sites is observed also in the naturally occurring mineral oxyplumboroméite (also known as bindheimite[282]), often referred to as the isostructural hydrated analogue of $Pb_2Sb_2O_7$.[257,270,280,283] On the basis of these results, the average stoichiometry of the LAY powder was calculated following the general recommendations by Atencio et al..[257] The resulting average formula is $Na_{0.74}Pb_{1.38}Sb_2O_{6.75}$.

Of the two phases experimentally observed in the LAY sample, the most abundant phase (≈55±10%) showed a good match with the diffraction pattern of bindheimite (PDF 42-1355, a=10.40 Å), normally used as an XRD reference for Naples Yellow. The second phase (≈45±10%, cubic pyrochlore with lattice parameter a=10.505 Å), on the contrary, showed no perfect match with any reference compound. The presence of dishomogeneities in the composition of LAY was confirmed also by μ-Raman spectroscopy. The presence of two pyrochlore phases intimately mixed in the sample, in fact, leads to variations in the Raman spectra recorded on different LAY grains (Figure 4.2). In particular, the ratio between the intensities of the peak at 198 $cm^{-1}$ and the one at 228 $cm^{-1}$ changes. These two bands have not been univocally identified but, as reported by Rosi et al.,[280] additional bands in the Raman spectrum of lead pyroantimonates can be linked to the distortion of the $SbO_6$ octahedra (very sensitive due to the rigidity of the Sb-O bond). In addition, different spectra show a shift of the most intense scattering peak at about 510 $cm^{-1}$ towards lower values (≈500 $cm^{-1}$), accompanied by a decrease in intensity and a broadening, with a shoulder appearing at around 455 $cm^{-1}$. This peak can be ascribed to the totally symmetric elongation of the $SbO_6$ octahedra ($A_{1g}$ mode). This confirms the relationship between the changes in the Raman spectra and the symmetry of the octahedral sites, suggesting a different degree of distortion of the crystalline lattice for the two phases. An increase in the lattice dimension and distortion of the octahedral sites in Pb pyroantimonates was observed in two cases before: when a different cation such as $Sn^{4+}$, $Zn^{2+}$, $Fe^{3+}$ or $Pb^{4+}$ partially substitutes $Sb^{5+}$ in the B sites,[280,283] or when high amounts of $K_2CO_3$ are used in the synthesis, causing $K^+$ to enter the lattice.[270] In our study, however, $Na^+$ is the only additional cation present in detectable amounts. The effect of the $Na^+/Pb^{2+}$ substitution on the lattice structure has not been described in literature before, but it is likely to be

responsible for the structural changes observed. Given the strong relationship observed between the symmetry of the octahedral sites in Sb pyrochlores and their electronic structure,[264,265] these changes will affect the overall properties of the pigment.
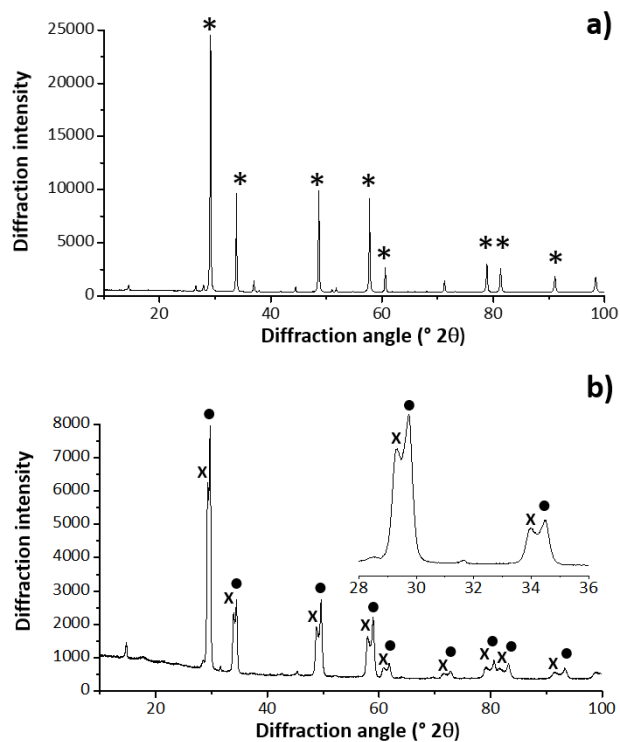


*Figure 4.1_X-Ray diffractograms for the a) LTAY and b) LAY samples. (\*) Pb$_2$SnSbO$_{6.5}$ (PDF 39-928, a=10.56 Å). (•) Bindheimite (PDF 42-1355, a=10.40 Å), (x) unidentified pyrochlore phase (a=10.505 Å).*
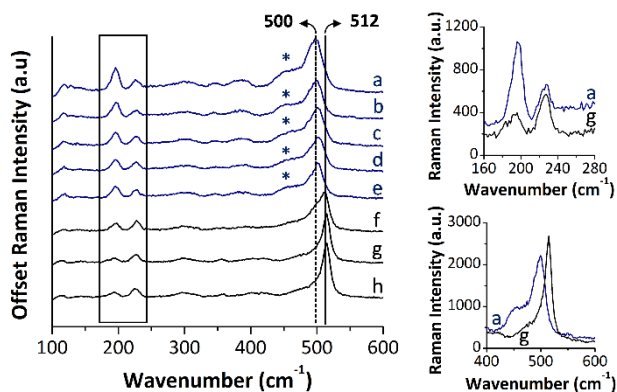


*Figure 4.2_μ-Raman spectra of different grains of LAY. Insets: enlarged view of the two peaks at 198 and 228 cm$^{-1}$ (upper panel) and of the main band at around 510 cm$^{-1}$ (lower panel) of spectra (a) and (g).*

Different binary combinations of compounds with a general formula $Na_xPb_{2-x}Sb_2O_{7-x/2}$ could translate into the experimental results obtained for LAY. According to the results of the DFT calculations (Figure S4.2), $Na_{0.5}Pb_{1.5}Sb_2O_{6.75}$ (LAY1) and $NaPbSb_2O_{6.5}$ (LAY2) are the two compounds that show the best combination between low formation energies and good correspondence with the experimental lattice parameters. The coexistence of these two Na-substituted lead pyroantimonate phases in the LAY sample was experimentally confirmed by means of high-resolution STEM-HAADF imaging and STEM-EDX analysis (Figure 4.3 and Figure S4.3). The experimental EDS results show a good agreement with the stoichiometry of the two computed phases. Furthermore, the distribution of Na-rich and Pb-rich areas in the STEM-HAADF images, identified by means of independent component analysis (ICA), confirms how intimately mixed the two phases are in the pigment powder.



| Area | Na (%) | Pb (%) | Sb (%) | O (%) | Formula |
|---|---|---|---|---|---|
| Pb rich (Green) | 4.35 | 14.01 | 18.14 | 63.50 | $Na_{0.5}Pb_{1.5}Sb_2O_{6.75}$ |
| Pb poor (red) | 8.67 | 6.70 | 20.31 | 64.32 | $NaPbSb_2O_{6.5}$ |
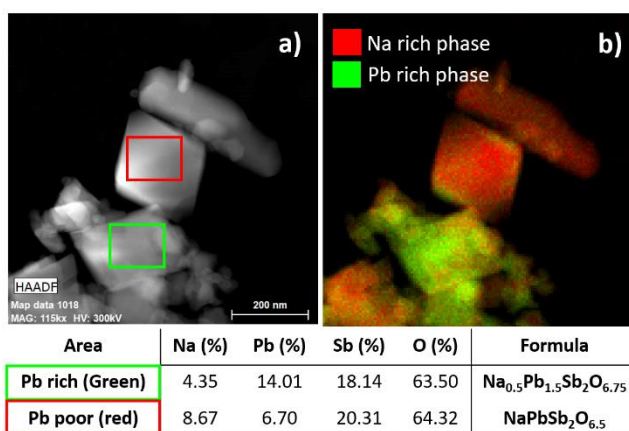
*Figure 4.3_a) STEM-HAADF image (at a magnification of 115 kX). The quantification of EDS spectra from the area within the green and red rectangles are respectively given in the table. b) EDX map from the same region in (a) showing a Pb-rich and a Na-rich phase identified by independent component analysis (ICA).*

It is extremely interesting to notice how the theoretical $Pb_2Sb_2O_7$ pyrochlore phase is not present in the sample. This information is in contradiction with the literature about Naples yellow as an artists' pigment ($Pb_2Sb_2O_7$ with a≈10.4 Å), but is in agreement with the computed information on this compound. The pure lead antimony mixed oxide, in fact, appears to be intrinsically unstable in the cubic pyrochlore structure (instability arising from a sharply peaked density of states at the Fermi level, Figure 4.4 and Figure S4.4), as previously suggested by other authors outside the field of conservation science.[256,260,261]

a)



b)
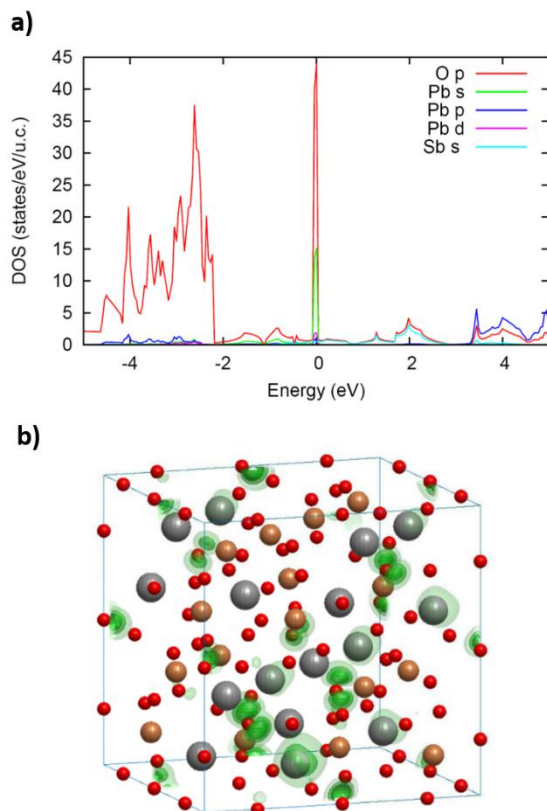


*Figure 4.4_Computed density of states (a) and crystalline structure (b) for the Pb$_2$Sb$_2$O$_7$ pyrochlore. The spheres represent single atoms in the structure: grey = Pb, brown = Sb and red = O. In evidence in green the charge density isosurfaces of the highly localized states at the Fermi level arising from the O' atom at the center of the Pb4O' tetrahedra.*

In addition, this phase shows a computed lattice parameter much larger than the literature value for this pigment (a=10.87 Å). These results therefore suggest that Pb$_2$Sb$_2$O$_7$ is not the correct formula to describe the pyrochlore pigment commonly referred to as Naples yellow. Our computational and experimental approach demonstrates for the first time an alternative pathway for the stabilization of lead antimonate in a pyrochlore structure, with Na$^+$ partially substituting Pb$^{2+}$ in the A sites.

## 4.3.2    Optoelectronic properties and photostability

Once completed the chemical and structural characterization of the pigment powders, the study of their optoelectronic properties was performed. As a starting point, it is particularly interesting to notice how the partial substitution of both $Pb^{2+}$ with $Na^+$ in LAY1 and LAY2 and $Sb^{5+}$ with $Sn^{4+}$ in LTAY have a similar effect on the overall stoichiometry and band structure for the pigments. First of all, we found that the sharp peak in the density of states at the Fermi energy in LAY (in the pyrochlore structure this compound would be metallic) arises essentially from highly localized O' p-states (O' is the O atom at the center of Pb tetrahedra) (Figure 4.4). Thus, compositional changes that allow to eliminate these states can lower the energy of the system and result in a stable compound. Because of their lower valency, the partial substitution of $Sb^{5+}$ with $Sn^{4+}$ in LTAY and of $Pb^{2+}$ with $Na^+$ in both LAY phases allows for the formation of O vacancies and, as expected, these occur preferentially at the O' sites for all the structures (Figure S4.5). As the states at the Fermi level are eliminated, these substitutions cause the resulting compounds to be semiconductors.

In order to better understand the photostability of these semiconductors, their optical properties were studied both experimentally (DR-UV-Vis spectroscopy) and computationally using CdS as a reference yellow semiconducting compound. Both approaches showed a significantly lower absorption coefficient for the pyroantimonate pigments in analysis than for the reference semiconductor, with a less steep absorption edge in the visible region of the spectrum (Figure 4.5). This behavior is explained by the indirect nature of the computed band gap for all the pyrochlore phases (lower probability for the optical transition). Note that phonon-assisted transitions are typically not included in first-principles computational codes. Even though this type of optical transitions in indirect gap semiconductors are of second order, their effect is not negligible and contributes to the difference between the experimental and theoretical spectra. Further differences may arise from the non-perfectly homogenous and relatively large size of the particles ($\Phi_{particle} > \lambda$ on average), which could increase the unwanted specular reflection contribution in the spectrum.
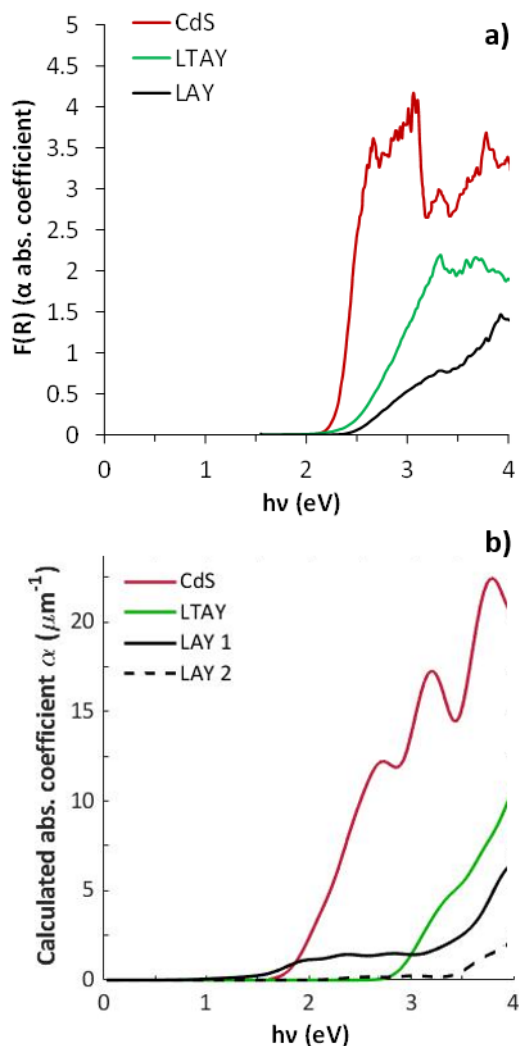
*Figure 4.5_a) Experimental Kubelka-Munk function (proportional to the absorption coefficient) for LAY, LTAY and CdS and b) computed absorption coefficient for LAY 1 (= $Na_{0.5}Pb_{1.5}Sb_2O_{6.75}$), LAY 2 (= $NaPbSb_2O_{6.5}$), LTAY and CdS as a function of the energy of the incident light.*

In general, the size of the computed band gaps is consistent with the results of the optical measurements (Table 4.2 and Figure S4.6). Only in the specific case of $Na_{0.5}Pb_{1.5}Sb_2O_{6.75}$, a significant difference in size between the computed and experimental band gaps is observed. However, as shown in Figure 4.5b, the computed absorption at the threshold is extremely weak, and only becomes significant above ~2eV. This behavior is justified by the character of the bands in the vicinity of the valence band maximum and conduction band minimum for this phase (Figure S4.7). The upper lying valence bands are of p character, while the lower lying conduction bands are of dominant s character.

Thus, in principle optical transitions can take place. However, the former arise mainly from the 2p states of the O' atoms at the center of the Pb-Na tetrahedra, while the latter arise mainly from Sb 5s states. These atoms are only third neighbors in the $Na_{0.5}Pb_{1.5}Sb_2O_{6.75}$ structure (Figure S4.5c). Thus, the corresponding optical transition matrix elements are small, and the absorption is weak. Most likely too weak to be macroscopically observed and experimentally detected.

*Table 4.2_Nature and size of the experimental ($E_g$ exp) and computed ($E_g$ comp) band gaps for the pigments considered.*

|      | Composition | Band Gap | $E_g$ exp (eV) | $E_g$ comp (eV) |
|------|-------------|----------|----------------|-----------------|
| LTAY | $Pb_2SnSbO_{6.5}$ | indirect | 2.22 [indirect] | 2.36 [indirect] 2.91 [direct] |
| LAY | $Na_{0.5}Pb_{1.5}Sb_2O_{6.75}$ | indirect | 2.31[a] [indirect] | 0.42 [indirect] 0.56 [direct] |
|     | $NaPbSb_2O_{6.5}$ | indirect | 2.31[a] [indirect] | 1.96 [indirect] 2.28 [direct] |
| CdS | CdS | direct | 2.40 [direct] | 2.10 [direct] |

[a] *Experimental value for the mixture of two phases.*

The chrono-amperometric measurements under chopped illumination conditions (at the open circuit potential, OCP) showed a positive photocurrent ($I_{ph}$) when the pigment-modified working electrodes (WE) are exposed to light with $hv > E_g$ (Table 4.3). This is a typical behavior for n-type semiconductors, due to minority carrier ($h^+$) mediated oxidation processes taking place at the pigment surface (Figure 4.6).[259,284,285] The absorption of a supra-bandgap photon causes in fact the excitation of one electron ($e^-$) from the valence band (VB) to the conduction band (CB) of the semiconductor. This process leaves behind a positively charged hole ($h^+$) in the VB, resulting in a displacement from equilibrium of the concentration of each charge carrier ($e^-$ and $h^+$). In an n-type semiconductor, the amount of photo-generated $e^-$ does not alter significantly the total

concentration of majority carriers in the CB, while the amount of photo-generated $h^+$ strongly increases the total concentration of minority carriers in the VB. For this reason, the quasi-fermi level defined for $e^-$ in this non-equilibrium condition ($_nE_F^*$) remains approximately the same as the general $E_F$ observed for the semiconductor in the dark. On the contrary, $_pE_F^*$ (quasi-fermi level for $h^+$ upon light exposure) drastically increases in energy compared to pre-illumination $E_F$. This translates into a higher minority carrier-related reactivity of the pigments upon light exposure. The presence of band bending at the pigment/electrolyte interface promotes the charge separation upon illumination, preventing the recombination of electron-hole pairs due to the existing electric field at the surface. N-type semiconductors most of the time present an upward band bending due to the accumulation of positive charges at the interface (mostly due to the transfer of $e^-$ to the solution during the equilibration of the respective Fermi levels in the dark).[259] In this case, the electric field at the surface forces the free holes formed upon illumination towards the external solution, while the photo-generated electrons are pushed away from the surface. This leads to minority carrier ($h^+$) mediated oxidation processes taking place at the pigment surface upon illumination (Figure 4.6),[259,284,285] translating into an overall positive current in the cell.

*Table 4.3_$I_{ph}$ values measured for LAY, LTAY and CdS-modified electrodes in different light conditions and electrolytes at the OCP.*

|  | NaCl 1 mM | | | | Ionic Liquid | | | |
|---|---|---|---|---|---|---|---|---|
|  | LOD[a] | LAY | LTAY | CdS | LOD[a] | LAY | LTAY | CdS |
| $I_{ph}$ (nA) RED | 0.2 | <LOD | <LOD | 4±3 | 3.8 | <LOD | <LOD | <LOD |
| $I_{ph}$ (nA) GREEN | 0.2 | 1.6±0.3 | 3.6±0.5 | 34±8 | 5.1 | <LOD | <LOD | 28±9 |
| $I_{ph}$ (nA) BLUE | 0.8 | 6.6±0.8 | 19±5 | 233±41 | 3.0 | 5.5±1.4 | 18±3 | 203±68 |

[a] LOD=3*σblank, where LOD=limit of detection and σblank=standard deviation of the blank.

CB = conduction band;
VB = valence band;
$E_F$ = Fermi level of semiconductor;
$E_{F\,sol}$ = Fermi level of electrolyte (in aqueous environment = reduction potential of water, $H_2O$ red);
$_nE_F^*$ = Quasi Fermi level for $e^-$ upon illumination;
$_pE_F^*$ = Quasi Fermi level for $h^+$ upon illumination;
$H_2O$ Ox = oxidation potential of water;
$\Phi$ Ox = surface self-oxidation potential of the semiconductor;
$E_g$ = band gap size;
$X_0$ = thickness of the surface space-charge layer.

*Figure 4.6_Mechanism responsible for the anodic photocurrent observed on LAY, LTAY and CdS-modified WE upon illumination with Vis light. a) Energy levels alignment before illumination in an aqueous solution; b) effect of the absorption of light with different wavelengths.*

Comparable results are obtained in an aqueous electrolyte (1mM NaCl) and in an ionic liquid with a large potential stability window ([BMIM][BF$_4$]). This confirms that the anodic photocurrent observed is the result of the $h^+$-mediated self-oxidation of the pigment grains, and not of water oxidation. The significantly lower $I_{ph}$ observed for LAY ad LTAY in both media, however, confirms the extreme stability of these pigments compared to CdS. A small photocurrent, in fact, is the direct result of a much lower tendency of the pigments to be oxidized when exposed to light with hv ≥ $E_g$.[259] The dependency of the $I_{ph}$ magnitude on the energy of the incident light is in agreement with the experimental size of the band gap and the absorption properties for all the pigments (Figure 4.5 and Table 4.2). In fact, the anodic $I_{ph}$ was higher in all samples when illuminated with a blue laser (3.06 eV), and progressively lower with a green (2.33 eV) and a red (1.89 eV) laser (Table 4.3). When an increasing positive over-potential (compared to the OCP) is applied to the WE, a clear increase in the relative anodic $I_{ph}$ is observed for both pyroantimonate pigments (Figure 4.7, Figure S4.8).

137
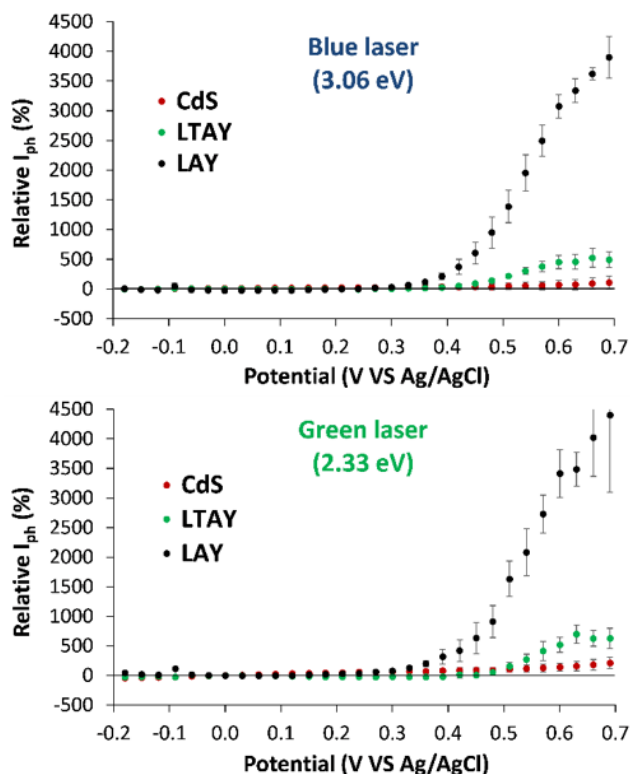
*Figure 4.7_I_{ph} (Blue and Green laser) dependency on the potential applied at the WE. Scan rate = 0.5 mV/s in 1 mM NaCl.*

A poor p-type conductivity in the pyrochlore phases is most likely responsible for the experimental results obtained. As observed in the computed band structures (Figure 4.8), in fact, a clear difference in the degree of dispersion of the upper lying valence bands exists between these phases and CdS. In the pyrochlore pigments, these energy levels originate essentially from the same states, i.e. the p-states from the octahedral O atoms surrounding the Sb atoms. The very flat nature of these bands, as often observed for metal oxides presenting corner-sharing octahedral structures,[286] translates into high $h^+$ effective masses. An accurate calculation of these effective masses requires taking into account various factors, such as the multiplicity of concerned extrema in the Brillouin zone and possible temperature effects.[287] In the present case, however, the band structures are relatively simple, with a single band at the valence band maximum (VBM) for all the phases except CdS, where degenerate bands are present. It is thus possible to have a good idea of the differences in effective mass among the compounds we study by considering the effective mass corresponding to the VBM along a high

138

symmetry line. In the case of CdS, there are two effective masses because of the degeneracy at the CBM, resulting in what are dubbed as light and heavy holes. Mobility in that case will obey to the average of these effective masses. The results are presented in Table 4.4. Since the carrier mobility depends directly on the inverse of the carrier effective mass, this material property results into a low minority carrier mobility for all the pyrochlore phases. Mobility which is likely to be further hindered by the presence of grain boundaries in the pigment powders.[288,289]
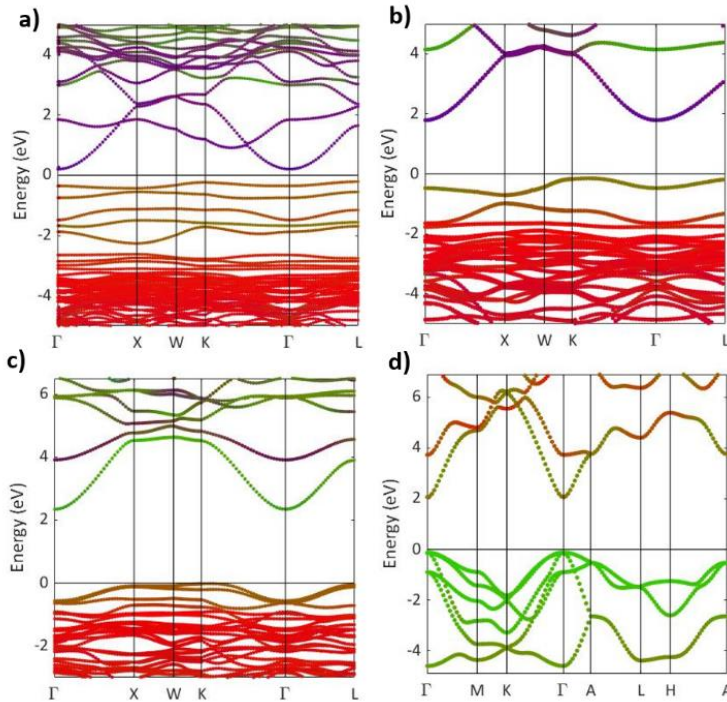


*Figure 4.8_Band character with respect to the atomic species present in the compounds considered. a) $Na_{0.5}Pb_{1.5}Sb_2O_{6.75}$ and b) $NaPbSb_2O_{6.5}$ (Blue=Sb, Green=Pb, Red=O; Na relative contribution is negligible). c) $Pb_2SnSbO_{6.5}$ (Blue=Sb, Green=Pb, Red=O; Sn contribution does not differ significantly from Sb). d) CdS (Green=S, Red=Cd).*

*Table 4.4_Hole effective masses (in units of $m_e$) for all the phases considered.*

| Phase | VBM | Effective $m_h$ |
|---|---|---|
| $Pb_2SnSbO_{6.5}$ | along the K-$\Gamma$ line | 1.89 |
| $Na_{0.5}Pb_{1.5}Sb_2O_{6.75}$ | at L | 2.68 |
| $NaPbSb_2O_{6.5}$ | at L | 1.32 |
| CdS | at $\Gamma$ | 0.64[a] |

[a]*harmonic average of 0.40 (light hole) and 1.63 (heavy hole)*

Since conductivity depends both on mobility and charge carrier concentration, the combination between low $h^+$ mobility and low optical absorption coefficients explains the extreme stability of LAY and LTAY pigments. In fact, this means not only that less $e^-$/$h^+$ pairs are formed upon light exposure in LAY and LTAY compared to CdS, but also that the photo-generated holes struggle to reach the surface and react before a recombination takes place. For this reason, when an external potential is applied driving the positive charges towards the surface of the pigment grains,[259] a significant increase in $I_{ph}$ is observed. The similar lightfastness observed for LAY and LTAY can therefore be ascribed to the analogous effect of Sn and Na substitutions on the band structure of the pigments. These substitutions, in fact, affect mainly the position of the upper valence band energy levels, but only weakly their nature and dispersion. This translates into $h^+$ mobilities which remain low and are not significantly affected by the nature of the substituent cation. The only difference observed in the valence band structures of Na- and Sn-substituted phases is the larger density of states near the valence band maximum for the latter (Figure 4.8 and Figure S4.9). This means that more electrons are potentially available for excitation near the band maximum, which explains the small experimental differences previously encountered: namely the slightly higher near-edge optical absorption (Figure 4.5), the slightly larger photocurrent at the OCP (Table 4.3) and the consequently smaller relative $I_{ph}$ increase with the applied potential for LTAY (Figure 4.7). Nonetheless, it is important to mention that also the different particle size observed for these pigments (Figure S4.1), slightly lower for LTAY, might account for their partially different photoelectrochemical behavior. A smaller diameter, in fact, might increase the chances of the photogenerated charges reaching the surface of the particles before a recombination takes place,[290] hence explaining the slightly larger photocurrent observed for LTAY at the OCP (Table 4.3).

For CdS, on the contrary, all the lighter photo-generated $h^+$ are most likely capable of reaching the surface of the grains without the need for an external electric field. Hence the high $I_{ph}$ at the OCP, in agreement with the documented instability for this pigment in paintings,[39,259] and the lack of a significant dependency on the potential applied at the WE. The slightly higher increase in $I_{ph}$ observed under green laser illumination compared to blue laser illumination for CdS is related to the fact that green light is absorbed less efficiently by the semiconductor. The $e^-$/$h^+$ pairs are therefore formed deeper in the semiconductor. Here the separation of the photo-generated free charges is less efficient, due to the lower influence of the electric field present only in the superficial space-charge layer, and therefore the recombination is more probable (Figure 4.6b).[55] When a positive over-potential is applied at the WE, however, the thickness of the space-charge

140

layer is increased.[291] This makes the separation of the $e^-/h^+$ pairs generated by the absorption of green light more efficient, leading to the relative $I_{ph}$ increase observed experimentally.

## 4.4 Conclusions

The multi-faceted analytical and computational approach described in this chapter allowed to unravel the material properties behind the stability of lead pyroantimonate yellow pigments. First, meaningful insights were obtained on the intrinsic instability of stoichiometric $Pb_2Sb_2O_7$ in the cubic pyrochlore structure. This confirms that the latter formula, extensively employed to describe the pyrochlore pigment commonly known as Naples Yellow, is not correct. Since accurately understanding the material composition is the first fundamental step for conservation, this information is crucial.

The presence of a diverse range of substitutions in the lattice of both natural and synthetic lead pyroantimonates supports our findings. As shown in the present work, in fact, substitutions taking place both at the A and B sites of this pyrochlore lead to similar changes in its stoichiometry and electronic properties, ultimately stabilizing the pigment in a cubic structure. While substitutions at the octahedral sites are well documented, however, the effects of A-site substitutions are not yet studied in the literature. For the first time, our results demonstrate that the partial substitution of $Pb^{2+}$ by $Na^+$ in the A sites of the pyrochlore allows to stabilize the cubic lead antimonate mixed oxide. No evidence of the presence of Na in paintings and historical samples of Naples yellow is reported in literature, however this element is too light to be detected with the non-invasive p-XRF or MA-XRF instruments often used to perform the analysis. As a next step, the laboratory analysis of paint microsamples is being planned in order to prove the presence of Na in historical Naples Yellow samples. Being able to confirm the link between the historical synthesis processes and the presence of different substituents in the pigment structure could represent an extremely useful tool for the attribution and authentication of historical paintings.

Furthermore, this study unraveled fundamental information on the optoelectronic properties of lead pyroantimonates. The experimental and computational results, in fact, confirmed the hypothesis of a semiconducting nature for this class of pigments. However, the absorption of visible light by these semiconductors does not trigger self-

corrosion mechanisms or catalytic degradation of the organic binding medium in contact with them. This behavior is the result of a combination of poor light absorption properties and low minority carrier (h$^+$) mobility, preventing potential h$^+$-mediated (self-)oxidation reactions from taking place at the surface of the pigment grains. This confirms that the extreme stability of this family of yellow pigments is the result of intrinsic material properties, hence not depending on the medium in which the pigment is embedded (e.g. insulating glassy matrix in glass objects rather than siccative oil in easel paintings). This is in agreement with the information available in literature about the extreme stability of this family of pigments in different media.

The results presented in this chapter represent a fundamental step towards a better understanding of the complex material properties and photochemistry of artists' pigments and of pyrochlore mixed oxides in general. Given the extraordinarily wide range of fields in which these mixed oxides find application, a better understanding of the effect of lattice substitutions on their optoelectronic properties is of capital importance. In addition, the methodology described in this study can potentially be used to probe the material properties of any semiconducting pigment in powder form, with applications also beyond the field of conservation science and cultural heritage.

## 4.5  Supplementary information
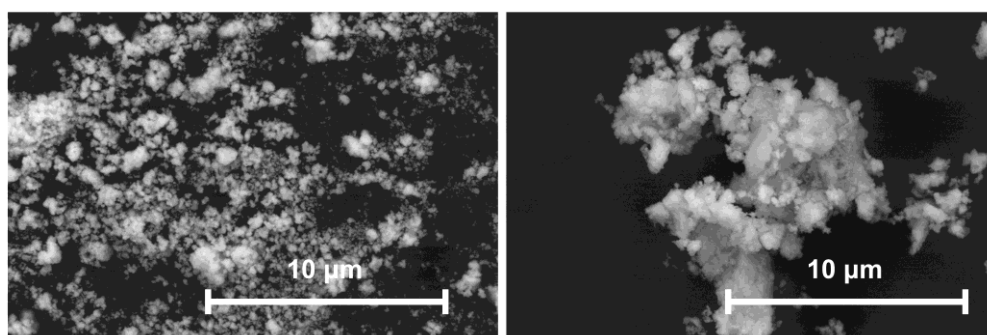


*Figure S4.1_SEM backscattered electron image (BEI) of the powder samples: a) LTAY; b) LAY.*

*Table S4.1_SEM-EDX results for the LAY and LTAY sample.*

| LAY | Na | Pb | Sb | Na + Pb |
|---|---|---|---|---|
| Average (wt%) | 3.0±1.6 | 49.9±4.9 | 42.8±4.7 | 45.8±5.6 |
| Average (mol) | 0.13±0.07 | 0.24±0.02 | 0.35±0.04 | 0.37±0.07 |
| mol/mol$_{Sb}$ | 0.37±0.18 | 0.69±0.08 | - | 1.06±0.15 |

| LTAY | Pb | Sn | Sb | Sn + Sb |
|---|---|---|---|---|
| Average (wt%) | 61.3±1.4 | 17.8±2.3 | 20.6±1.2 | 38.4±1.4 |
| Average (mol) | 0.30±0.01 | 0.15±0.02 | 0.17±0.01 | 0.32±0.01 |
| mol/mol$_{Pb}$ | - | 0.51±0.09 | 0.57±0.03 | 1.08±0.07 |



a)

Pb poor (-7.13,0,0)   $\Delta\mu_{Pb}$   Pb/Sb rich-O poor (0,0,-2.04)

$Sb_2O_3$

(-1.10,-1.92,-1.18) ← B   PbO
(-3.45,-3.68,0) ←

$O$ rich   C

D   A   $\Delta\mu_{Sb}$
(-1.70,-3.43,-0.57)
(-2.84,-4.28,0) ←   $PbO_2$

A: $\Delta\mu_{Na} \in$ [-4.11, -2.53]
B: $\Delta\mu_{Na} \in$ [-3.76, -2.20]
C: $\Delta\mu_{Na} \in$ [-5.50, -3.99]
D: $\Delta\mu_{Na} \in$ [-4.96, -3.34]

(0,-7.13,0) Sb poor
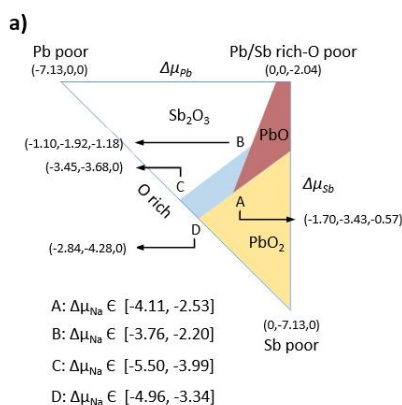
b)

| Compound | $\Delta H_f$ (eV) | Source |
|---|---|---|
| $PbO_2$ | -2.8447 | NIST |
| PbO | -2.2740 | NIST |
| $Sb_2O_3$ | -7.3559 | Wikipedia |
| $Na_2O$ | -4.3115 | Aspiala et al. |
| NaCl | -4.2610 | NIST |

c)

| Compound (*) | $a$ (Å) | $E_g$ (eV) | $E_f$ (eV) |
|---|---|---|---|
| $Pb_2Sb_2O_{6.5}$ | 10.8706 (PBE) | Metal | -0.1844 |
| $Na_{0.5}Pb_{1.5}Sb_2O_7$ | 10.7194 (PBE) | Metal | 0.4834 |
| $Na_{0.5}Pb_{1.5}Sb_2O_{6.5}$ | 10.7194 (PBE) | Metal | -0.3303 |
| $Na_{0.5}Pb_{1.5}Sb_2O_{6.75}$ | 10.5041 (HSE) | 0.5557 (opt) 0.4152 (fund) | -1.4431 |
| $NaPbSb_2O_7$ | 10.5647 (PBE) | Metal | 0.8858 |
| $NaPbSb_2O_{6.5}$ | 10.3996 (HSE) | 2.2759 (opt) 1.9582 (fund) | -1.6232 |
| $Na_{1.5}Pb_{0.5}Sb_2O_7$ | 10.4731 (PBE) | Metal | 2.9092 |
| $Na_{1.5}Pb_{0.5}Sb_2O_{6.5}$ | 10.4731 (PBE) | Metal | 2.3627 |
| $Na_{1.5}Pb_{0.5}Sb_2O_{6.25}$ | 10.3344 (HSE) | 2.2325 (opt) 2.0898 (fund) | 0.2633 |

(§) For point A with $\Delta\mu_{Na}$ = -3.32 eV
(*) $Na_2Sb_2O_6$ exists in the pyrochlore structure with a lattice constant $a$=10.2 Å (www.aflowlib.org)

*Figure S4.2_a) Stability triangle for the phases involved in this study. The light blue-gray area indicates the chemical potential ranges for which $Pb_2Sb_2O_7$ is thermodynamically stable against precipitation of the competing oxides in the triangle. In these areas $Na_{0.5}Pb_{1.5}Sb_2O_{6.5}$ and $NaPbSb_2O_{6.5}$ will have a lower formation energy than $Pb_2Sb_2O_7$ in sufficiently Na-poor conditions that nor $Na_2O$ or NaCl precipitate. The interval of Na chemical potentials for which this occurs at the vertices of the blue-gray area are indicated in the figure (all energies in eV). b) Experimental enthalpies of formation used in the calculations. c) Calculated formation energies, lattice parameters and band gaps for chemical potentials corresponding to point "A" in figure (a), as an example.*

143
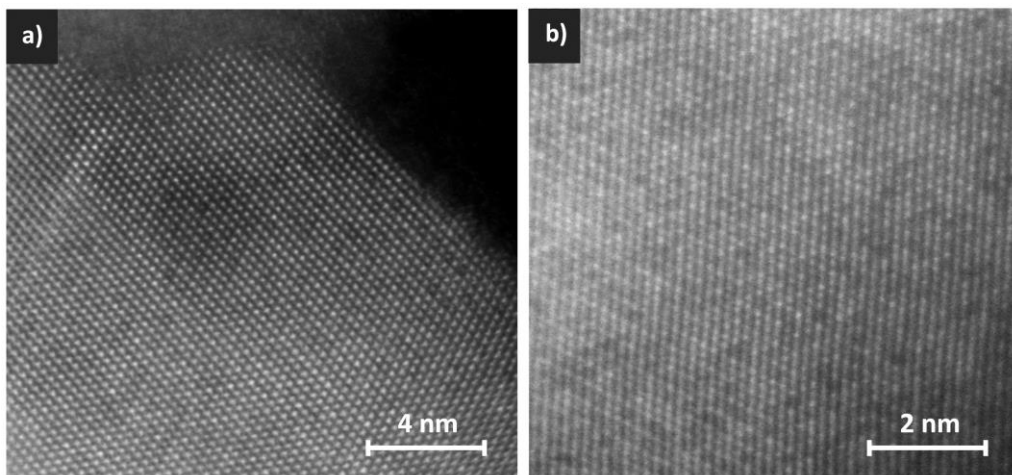
*Figure S4.3_High-resolution STEM-HAADF Z-contrast image of the two pyrochlore phases in the LAY sample: a) $Na_{0.5}Pb_{1.5}Sb_2O_{6.5}$ along [141] zone axis and b) $NaPbSb_2O_{6.5}$ along [011] zone axis. The atomic columns showing darker contrast are assigned to be Na rich (Pb deficient). As expected, the density of these darker columns is higher in $NaPbSb_2O_{6.5}$.*
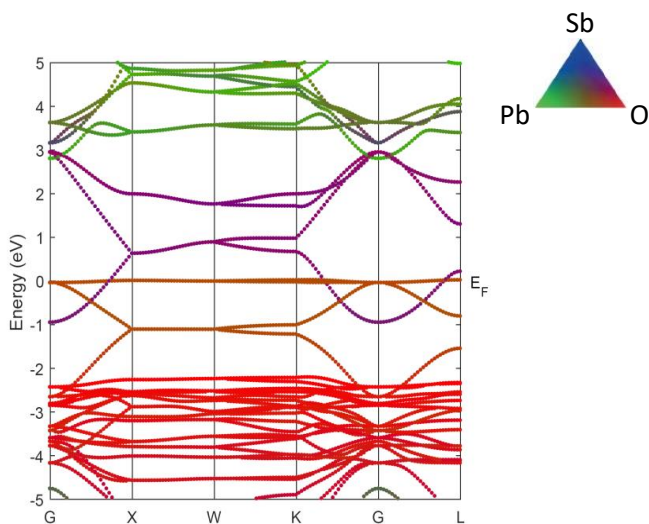


*Figure S4.4_Computed band structure for $Pb_2Sb_2O_7$ in a pyrochlore structure. The presence of highly localized states at the Fermi level suggests an intrinsic structural instability for this compound.*
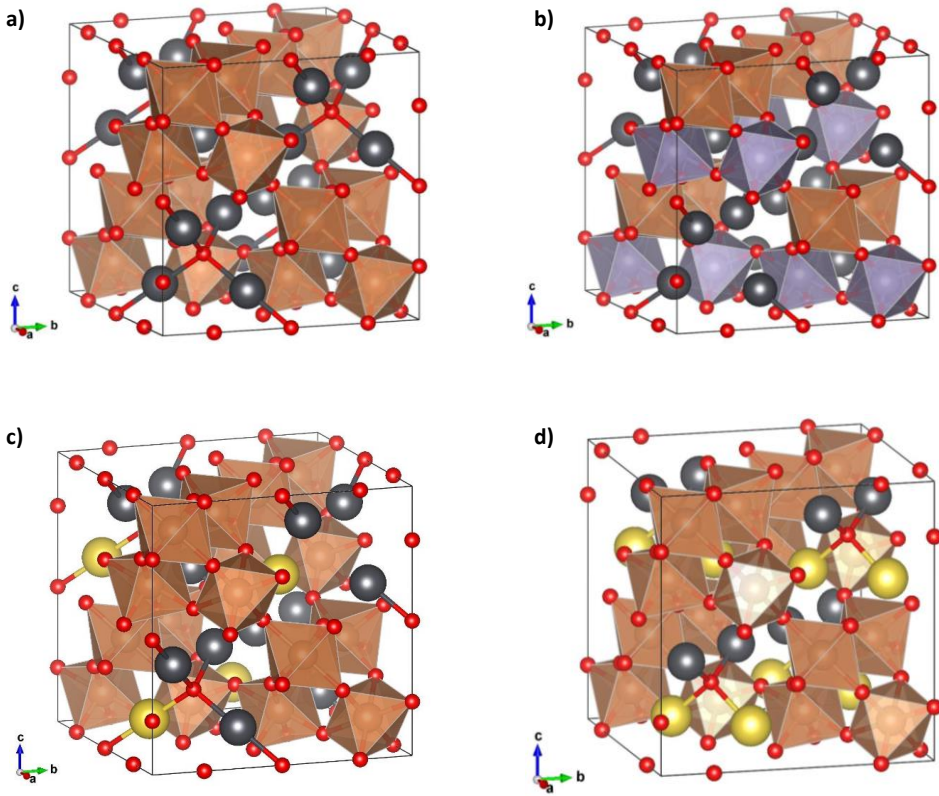
*Figure S4.5_Computed crystalline structure for a) $Pb_2Sb_2O_7$, b) $Pb_2SbSnO_{6.5}$, c) $Na_{0.5}Pb_{1.5}Sb_2O_{6.75}$, d) $NaPbSb_2O_{6.5}$. The spheres represent single atoms in the structure: grey = Pb, brown = Sb, purple = Sn, yellow = Na and red = O.*
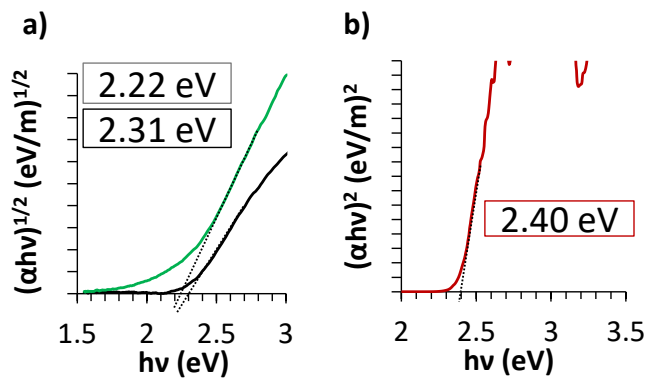


*Figure S4.6_Tauc plots with calculated band gap sizes for the indirect semiconductors LAY and LTAY (a) and for the direct semiconductor CdS (b). Green = LTAY, Black = LAY, Red = CdS.*
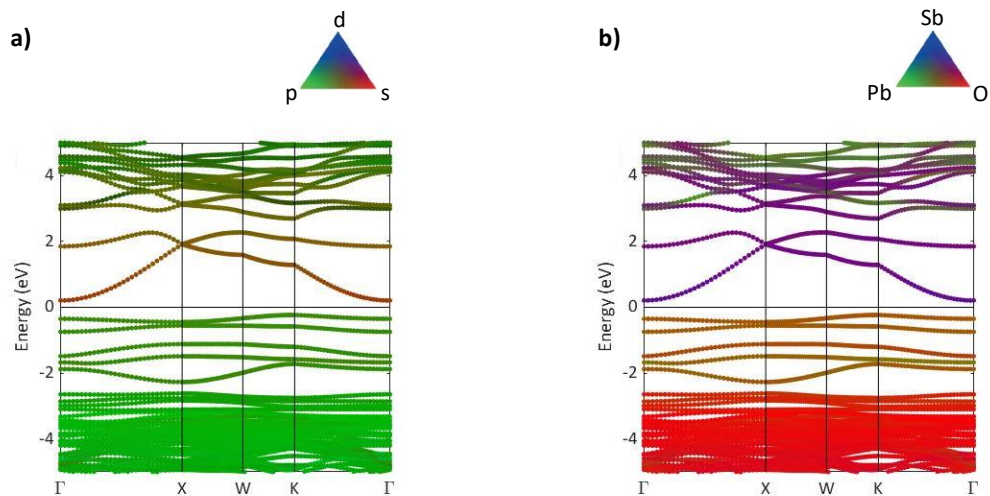
*Figure S4.7_Computed band character for Na$_{0.5}$Pb$_{1.5}$Sb$_2$O$_{6.75}$ with respect to a) angular momentum and b) atomic species. Na relative contribution to the band character is negligible and therefore it is not shown in (b).*
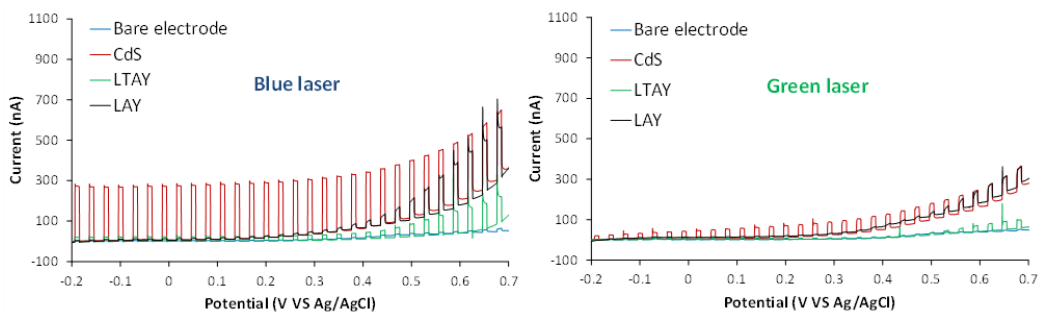


*Figure S4.8_Linear sweep voltammetry under light chopped illumination conditions. Scan rate = 0.5 mV/s; electrolyte = 1mM NaCl. Results with blue and green laser for the pigments in analysis.*
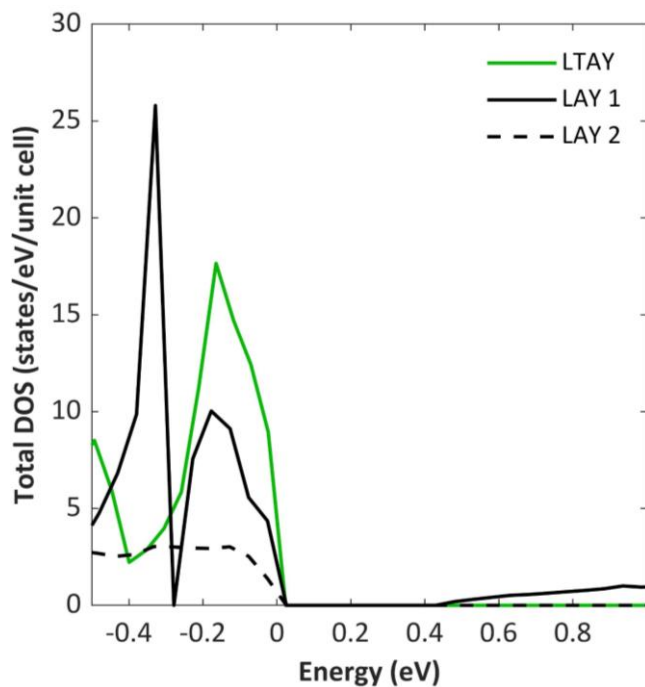
*Figure S4.9_Computed total density of states near the valence band maximum for the pyrochlore phases considered.*

# |5

## [Part 1]

# Geranium lake pigments: the role of the synthesis on the structure and composition

**V. Beltran\*, A. Marchetti\*, S. De Meyer, G. Nuyts, K. De Wael**

**\* Contributed equally**

# Abstract

In this section of this doctoral thesis, the focus is shifted to the study of a different family of artists' pigments: the Geranium lake pigments. The reason to study these pigments lies in their intrinsic instability and, in particular, in their tendency to fade upon light exposure. Such a behaviour results in significant chromatic alterations for the paintings where these pigments are employed, with severe consequences on the value (well beyond the mere economic meaning of the word) of the work of art. In the past years, attempts have been made to understand the reactivity and decipher the degradation mechanism of these pigments. However, despite great efforts, a lack of agreement still exists in the literature on this topic.

In a strive to make clarity in this rather complex field of research, in this chapter we take a step back, trying to first understand what kind of link might exist between synthesis conditions, composition and reactivity of these pigments. Our hypothesis, in fact, is that the lack of agreement in the literature could be a result of the reactivity often being studied for pigments synthesized in different conditions. While a similar overall composition and behaviour for these differently-synthesized pigments is assumed, and used as a base to draw interstudy comparisons, it is however not demonstrated. In Chapter 5, therefore, we systematically study the effect of changing the synthesis conditions first on the structure and composition of the pigments (First part of the chapter) and then on their reactivity (Second part of the chapter).

From a chemical point of view, Geranium lake pigments are metallic complexes of the synthetic dye eosin Y. Given the application of such complexes in a wide variety of fields, including photovoltaics and photocatalysis, understanding the effect of the synthesis conditions on their structure and composition hold relevance well-beyond the field of conservation science.

In particular, eosin Y complexes in Geranium lake pigments are normally Al- or Pb-based. Therefore, the first part of this chapter presents a thorough investigation of the structure and composition of in-house synthesized lake pigments containing these two metals, by FTIR, XRPD and Raman spectroscopy. The results clearly show changes in the coordination mode of the Pb complexes depending on the synthesis protocol, while the structure of Al complexes remains stable. In both cases, the formation of by-products during the synthesis is also demonstrated here for the first time (with their nature and

amount depending on the synthesis protocol). Additionally, a detailed band assignment of the FTIR and Raman spectra of eosin Y and Pb and Al complexes is described, providing novel insights on the interaction between the metallic ion and the xanthene moiety (chromophore). Such a thorough interpretation of the vibrational spectra holds great relevance for the analysis of historical paintings where eosin Y is bonded to metallic ions, but also for the study of other eosin Y-based materials finding application in different fields. Furthermore, this deep understanding of the FTIR spectra of Geranium lakes is also exploited, in the second part of this chapter, to better understand the reactivity of these pigments.

## 5.1 Introduction

In virtue of its extraordinary photochemical properties, eosin Y (2′,4′,5′,7′-tetrabromofluorescein) has been traditionally used as a phosphorescent probe or photosensitizer.[292,293] Lately, this specific xanthene dye characterized by a vibrant red colour, is gaining attention due to its capacity to form complexes with metallic elements, finding applications in many different fields such as drugs detection,[294,295] dye sensitized solar cells[296–298] or artists' pigments.[299,300]

Eosin Y complexes used as pigments in paintings are better known as Geranium lakes. They were synthesized for the first time in the 19th century and, according to literature, they typically include Pb or Al ions (Pb-lakes and Al-lakes respectively). Thanks to their extraordinarily intense red hue, they rapidly gained popularity as artists' pigments, finding their way into the palette of great masters such as Vincent Van Gogh and Paul Gauguin.[17,23,301–303] However, when exposed to the environment, the vivid red tone of the Geranium lakes tends to fade, leaving a greyish material behind.[16,304,305] Such a degradation may lead to severe changes in the appearance of paintings, with cultural, societal and economic implications as a result. Understanding how these pigments degrade is the first capital step towards defining the appropriate measures to protect these masterpieces, thus a task of maximum priority.

Although previous studies provided valuable insights about the degradation reactions, there are still open questions regarding the precise reactivity of Geranium lakes and the factors influencing it.[306–308] One of the reasons for such discrepancies might be linked to differences in composition caused by changes in the synthesis of these pigments. Thus, deciphering the link between synthesis and composition of these pigments is essential to allow a reliable comparison between published data and future studies.

To synthesize Geranium lakes, a solution of dianionic eosin Y is prepared and mixed with a metallic salt to precipitate the complex. This protocol is generally followed, with some of the experimental parameters, in particular the pH of the initial solution and the amount of metallic salt added, changing from one paper to another.[308–311] These changes are introduced in spite of the fact that an influence of pH and metal concentration on the nature of the synthesized products can be reasonably expected. Eosin Y is, in fact, a polyprotic acid (one phenolic group and one carboxylic group where $pK_{a\text{-COOH}} > pK_{a\text{-OH}}$),[312] hence the protolytic species present in the solution are strongly influenced by the pH.

Additionally, it should be also kept in mind that different tautomers can be found for each protolytic specie. The main tautomers are described in Figure 5.1.[312] In principle, each protolytic specie may form different types of intermolecular bonds with the metallic ions, ultimately leading to different products. In addition, changes in pH may also lead to the formation of by-products. Excess Pb and Al ions can react with hydroxyl ions leading to the formation of precipitates, finally resulting in the contamination of the pigment and influencing the overall reactivity. The extent and nature of this contamination is evidently linked not only to the pH, but also to the amount of metal ions in solution. According to the literature, the stability of the complexes is linked to the photosensitizing properties of the precursor dye and to the lifetime/reactivity of its excited state.[293,307] Such properties are typically affected by the microenvironment of the photosensitizer.[313] Hence, it is likely that the changes in the structure of the complex and the overall composition of the pigment (i.e. presence of by-products formed during the synthesis) play a role in its stability.

Previous research has given valuable insights on the chemical nature of Geranium lakes depending on the type (Pb or Al) and number (one or two) of metallic salts used, elucidating the formation of a bond between the carboxylic acid group of eosin Y and the metal ion.[314] However, no systematic study exists on the effect of different synthesis conditions on the eosin Y-metal coordination and the overall chemical composition including the presence of by-products. A correlation between changes in the synthesis method and the composition of Geranium lakes has been previously hypothesized[315] but not yet proven.

A thorough characterization of the eosin Y-metal coordination and of the by-products formed during Geranium lakes synthesis under different conditions is therefore a first crucial step towards a better understanding the eosin complexes reactivity. To allow the analysis of a wide range of compounds and their inter- and intramolecular interactions, Fourier transform infrared (FTIR) spectroscopy is first addressed in this chapter. The interpretation of FTIR spectra can be complex in molecules such as eosin Y and Geranium lakes due to the presence of several bands, sometimes overlapping. To overcome this limitation, this research started with a detailed assignment of the FTIR bands to determine the spectral markers of each molecule. Such fundamental task was performed through the comparison of eosin Y, Al-lakes and Pb-lakes with molecules having similar structures, as well as with a range of reaction products appositely synthesized by modifying specific functional groups in the molecules in exam. FTIR spectra have been complemented with Raman spectroscopy, allowing to corroborate the assignment

proposed. Based on this meticulous assignment, a systematic study of the spectral changes associated with differences in the synthesis conditions was performed, focusing in particular on bands shifts and on the identification of by-products.

In general, differences in the behaviour of Pb-lakes and Al-lakes are observed, with the former being much more sensitive to modifications of the synthesis protocol than the latter. Furthermore, the presence of Pb- or Al-containing by-products in the synthesized pigments is demonstrated for the first time, as well as their correlation with the synthesis protocol. In particular, lead carbonates were formed in Pb-lakes and amorphous basic aluminium was formed in Al-lakes. These products could alter the reactivity of the pigment, in particular when mixed with a binding media that contains fatty acids (such as drying oils), due to the formation of metal soaps, potentially compromising the integrity of paintings.[54] Additionally, the proposed assignment of the FTIR and Raman bands from eosin Y and Geranium lakes spectra provides a fundamental reference for their identification in heritage objects, as well as for the monitoring of possible modifications in their structure. The accurate characterization of the eosin Y complexes and by-products in Geranium lakes discussed in this study also allowed to unravel the existence of an interaction between the metal ion and the phenoxide ion, and thus the xanthene moiety, likely playing a role in the reactivity of the complexes. This is a fundamental insight for their conservation in paintings, but relevant also for any other research field in which eosin Y complexes are employed.

## 5.2  Materials and methods

### 5.2.1   Reagents

To perform the band assignment, the spectrum of pure eosin Y (Sigma Aldrich, ~99% purity, ref. E4009) was compared to that of rhodamine B (Sigma Aldrich, ≥95%, ref. R6626) and fluorescein (J&K Scientific, 95%, ref. 916551).

To prepare the complexes (Figure 5.5, Figure 5.6 and Figure 5.7), pure eosin Y was used. Solid eosin Y was solubilized in a solution of NaOH (Sigma Aldrich, 98%, ref. S5881) prepared at pH=12. If necessary, additional NaOH or an acid ($H_2SO_4$ (Sigma Aldrich, 99.999%, ref. 339741) for the syntheses of Al-lakes and $CH_3COOH$ (Sigma Aldrich,

≥99.7%, ref. 695092) for the syntheses of Pb-lakes) was added until reaching the pH required (pH$_i$). Afterwards, the metallic salt was slowly added to the solution to form the complex. For Pb-lakes, Pb(COOCH$_3$)$_2$·3H$_2$O (Fluka, ref. 32306) was employed. For Al-lakes the results obtained with AlCl$_3$·6H$_2$O (Alfa Aesar, 99%, ref. A14437) and Al$_2$(SO$_4$)$_3$·18 H$_2$O (Sigma Aldrich, ≥98%, ref. 237086) were compared. Additional synthesis protocols were tested (Figure S5.6 and Figure S5.7) using eosin Y disodium salt (Sigma Aldrich, ≥85 % ref. E6003). The specific conditions used in each case are mentioned in the literature cited therein.

### 5.2.2   FTIR spectroscopy

FTIR spectra were collected with a spectrometer Bruker Alpha II equipped with a DTGS detector. Measurements were performed in transmission mode using KBr (Sigma Aldrich, FTIR grade, ref. 221864) pellets. A total of 128 scans was accumulated in each sample, using a resolution of 4 cm$^{-1}$ and a wavenumber range between 4000 to 400 cm$^{-1}$. All spectra showed were not corrected in order to avoid any kind of distortion.

### 5.2.3   Raman spectroscopy

Raman spectra (Figure 5.2, Figure 5.4 and Figure 5.5) were collected with the micro-Raman spectrometer InVia Renishaw equipped with a CCD detector. Measurements were performed with a 785 nm laser and a 50x/NA 0.5 magnification objective. For each spectra 50 seconds measurements were accumulated during 4 acquisitions. The energy used was 1% to avoid sample degradation. All spectra showed were not corrected in order to avoid any kind of distortion.

The Raman spectra of the Pb by-products showed a broad band from fluorescence, therefore the Bruker Bravo PSSERS spectrometer (Bruker Optik GMBH, Ettlingen, Germany) was used (Figure 5.8). This device is equipped with two lasers (785 and 853 nm) with sequentially shifted excitation to suppress fluorescence. Laser power level and time cannot be adjusted, but they are reported to be <100 mW and less than 1 min for a single analysis. Spectral range is 300–3200 cm$^{-1}$ at 10–12 cm$^{-1}$ resolution.

### 5.2.4   X-Ray powder diffraction

The X-ray powder diffraction (XRPD) measurements were performed in transmission mode using a focused (0.3 mm x 0.3 mm) monochromatic Ag-Kα X-ray source (22 keV) operated at 50 kV and 0.88 mA while the emerging diffraction signals were collected with a PILATUS 200K detector. Multiple points on the powder surface were measured with an exposure time of 10 s per point. Calibration and integration of the diffraction signals was performed using the XRPDUA software package.[211]

# 5.3   Results and discussion

### 5.3.1   Foundations of a robust FTIR and Raman analysis

Eosin Y and the corresponding Pb and Al complexes present FTIR and Raman spectra with several bands in overlapping spectral regions. Nonetheless, a reliable band assignment for Pb-lakes and Al-lakes is required in order to obtain novel insights about their structure and its changes depending on the synthesis conditions.

The first step to determine the band assignment of Geranium lakes includes the in-depth interpretation of the FTIR and Raman spectra from eosin Y, since its molecular structure is well known. In solid state, eosin Y exists in two forms: lactone and quinoid (Figure 5.1) (the presence of the zwitterionic form is almost negligible[312]). These forms share many functionalities, namely the xanthene rings, the hydroxyl and the bromine groups, while they only differ in the structure of the carboxylic group. Pure solid eosin Y is composed mainly of lactone form with small amounts of quinoid form,[316,317] while eosin Y complexes present only the quinoid form since the metal is bonded through the carboxylic acid group.[314] Therefore, in order to compare the spectra of eosin Y and Geranium lakes, it is necessary to discriminate the bands specific to the lactone and quinoid forms from the bands of the shared structures.
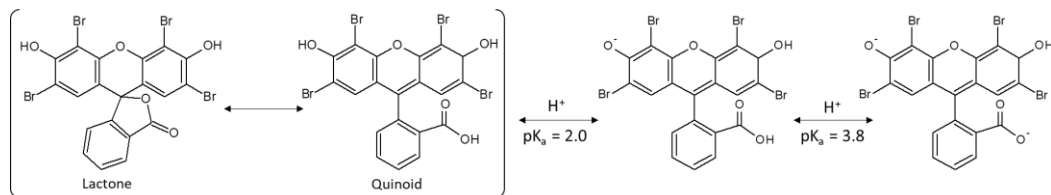
*Figure 5.1_Main tautomers and pKa of eosin Y.*

## 5.3.2   Analysis of the shared structures between quinoid and lactone forms

In order to study the bands associated with the functionalities present in both quinoid and lactone forms, the spectrum of eosin Y was compared to rhodamine B and fluorescein (Figure 5.2). Fluorescein can be found in different forms: lactone, quinoid and zwitterionic, that can be distinguished by their colour and their specific markers in the spectra (Figure S5.1). In this case the quinoid form was used, which is characterized by a strong red colour (unlike the zwitterionic form or the lactone form) and the lack of the bands related to lactone or carboxylate groups.[318]
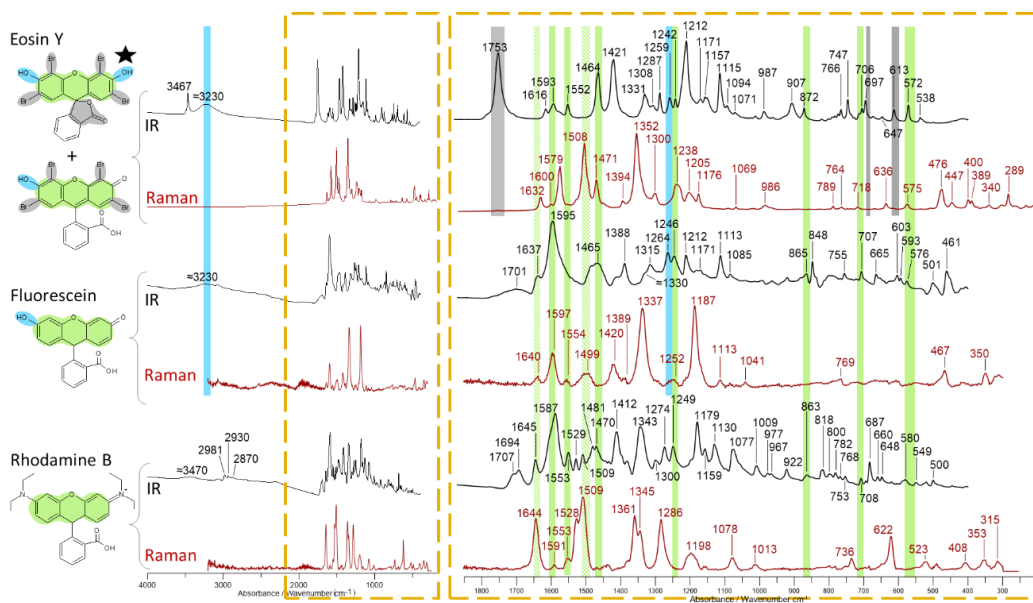


*Figure 5.2_Comparison of the IR and Raman spectra of different xanthene dyes eosin Y, fluorescein and rhodamine B. The structure of each compound is showed at the left, the star indicates the predominant form in eosin Y. The shared structures are marked in pink, green and blue. The structures only present in eosin Y are marked in grey. FTIR spectra is plotted in black lines, Raman spectra in dark red, a magnification of the region marked in orange is displayed at the right. The bands related to each structure are marked with the same colour (full areas for FTIR bands, striped areas for Raman bands).*

All molecules have a xanthene group (Figure 5.2, structure highlighted in green), hence the bands that are present in all three spectra are linked to this functionality. The bands found only in the eosin Y and fluorescein spectra are probably linked to the hydroxyl, only found in these molecules (Figure 5.2, structure highlighted in blue). Finally, the bands only found in the spectrum of eosin Y are related to the structures present just in this molecule (Figure 5.2, structure highlighted in grey). The comparison of Raman and FTIR spectra, which have different active vibrations, helped to verify the proposed assignment.

The xanthene moiety (Figure 5.2, structure marked in green) has aromatic groups and an ether. Regarding the aromatic groups, the C=C stretchings were identified in the region between 1650 to 1450 $cm^{-1}$, specifically the bands at ≈1590, ≈1553 and ≈1465 $cm^{-1}$ (more intense in the FTIR spectra but in some cases also visible in the Raman spectra) and at ≈1640 and ≈1505 $cm^{-1}$ (more intense in the Raman spectra but in some cases also visible in the FTIR spectra). The C-O-C stretching of the ether group is most probably associated to the band at ≈1245 $cm^{-1}$, only noticeable in the FTIR spectra. Three additional bands at ≈865, ≈706 and ≈575 $cm^{-1}$ are present in the spectra of all the three compounds, related to skeletal vibrations of the shared structure.[319,320] Indeed, similar bands also appear in the spectra of rhodamine 6G, having the same xanthene moiety.[321] These assignments agrees with previous studies based on computational chemistry.[322,323]

Previous research has linked the small bands at ≈1330, 1171 and 1113 $cm^{-1}$ in the fluorescein spectra, with similar relative intensity, and only noticeable in the FTIR spectrum, to the xanthene moiety.[318,324,325] In the spectra of eosin Y and rhodamine B, bands in similar regions can be observed too, associated to the same functional group. The band shifts observed in each spectrum (1331-1330-1343 $cm^{-1}$; 1171-1171-1179 $cm^{-1}$; 1115-1113-1130 $cm^{-1}$) can be explained by the different substituents of the xanthene in each molecule.

The bands related to the hydroxyl group (Figure 5.2, structures marked in blue) appear at ≈3230 $cm^{-1}$, linked to the O-H stretching, and at ≈1260 $cm^{-1}$, linked to the C-O stretching / O-H deformation. Both bands are only present in the FTIR spectra of eosin Y and fluorescein since this Raman vibration is weak. However, some differences can be noticed in the O-H stretching region: the band from fluorescein is very broad and there is an additional peak at 3467 $cm^{-1}$ in the spectra of eosin Y. The broader band of fluorescein is explained by the presence of two types of –OH (hydroxyls and carboxylic

158

groups), each one forming hydrogen bonds between them as well as with the ketone group: this wide range of interactions broadens the band. On the other hand, eosin Y has only one type of –OH (hydroxyls) which, in addition, are less prone to form hydrogen bonds due to the steric hindrance caused by the adjacent Br atoms. For this reason, the band of bonded –OH (3230 cm$^{-1}$) is lower and narrower and there is also a peak at 3467 cm$^{-1}$ which is probably associated to the single-hydrogen bridges, that tend to appear in this region.[326]

Finally, there are a few bands found only in the spectra of eosin Y (Figure 5.2, structures marked in grey). The clearest example is located at 1753 cm$^{-1}$, related to the C=O stretching of the lactone group.[319,320] Despite fluorescein and rhodamine B also containing carboxylic groups, the band related to the C=O stretching is expected to appear at a much lower wavenumbers, overlapped with the bands of aromatics. This agrees with the higher intensity of the bands at 1597 and 1587 cm$^{-1}$ in the spectra of fluorescein and rhodamine B respectively, compared to the other bands related to the C=C stretching of the aromatic groups. The decrease of the wavenumber is explained by the conjugation of the C=O bonds and the higher number of intermolecular bonds of fluorescein and rhodamine B compared to eosin Y, whose –OH are less available as a result of the steric hindrance due to the Br atoms. Both effects contribute to decrease the wavenumber of the carbonyl peak.[319] Additionally, there are two bands at 697 and 613 cm$^{-1}$, probably related to the C-Br stretching. The fact that these two bands are also present in the FTIR spectra of 2,6-dibromophenol, that contains similar C-Br bonds, supports this hypothesis.[327]

### 5.3.3   Discrimination of the bands specific to quinoid and lactone forms

In order to discriminate the bands related to lactone and quinoid forms, eosin Y was mixed with different solvents in order to modify the carboxylic group, monitoring the reactions by FTIR spectroscopy (Figure 5.3). Raman spectroscopy was not used here since most of the vibrations related to the expected changes are not Raman active.[319,320] In detail, pure eosin Y was treated with ethanol (Figure 5.3a) and with acetone (Figure 5.3b) to alter the lactone group. Additionally, eosin Y was mixed with water and filtered to isolate the non-soluble fraction, corresponding to the weakly-polar lactone form (Figure 5.3c). The spectra of the modified compounds were compared to pure eosin Y (i.e. mainly lactone form with small amounts of quinoid form) (Figure 5.3d).

The expected reactivity was verified by focusing on the spectral region corresponding to the C=O stretching, where the changes are clear since there are no overlaps with bands related to other functional groups. In particular, when the lactone group (Figure 5.3, structure highlighted in green) is modified (spectra 3a and 3b), the intensity of the corresponding band centred at 1753 cm$^{-1}$, decreases compared to pure eosin Y (spectrum 3d). After the reaction with ethanol (spectrum 3a) where the opening of the lactone and the esterification of the carboxylic acid (Figure 5.3, structure highlighted in grey) is expected, the band at 1753 cm$^{-1}$ is broader. This is explained by the formation of the ester group, whose C=O stretching typically appears around ≈1730 cm$^{-1}$.[319,320] After the reaction with acetone (spectrum 3b), where the formation of the quinoid form is expected, two shoulders at ≈1703 and 1717 cm$^{-1}$ appear. This change is related to the occurrence of the carboxylic group, whose C=O stretching typically appears around ≈1700 cm$^{-1}$ (Figure 5.3, structure highlighted in brown), and the ketone, whose C=O stretching appears normally at ≈1717 cm$^{-1}$ (Figure 5.3, structure highlighted in pink).[319,320] The ketone band is probably present also in the spectrum 3a, but it is hidden by other more intense bands.

As it can be noticed, the C=O stretching related to the –COOH group from the quinoid form of eosin Y appears at higher wavenumber than fluorescein and rhodamine B (Figure 5.2). Despite the C=O from all three molecules being conjugated, eosin Y cannot form as many hydrogen bonds as fluorescein and rhodamine B due to the steric hindrance of the –OH and ketone groups, which explains the higher wavenumber from the eosin Y band.[319,320] Conversely, the band at 1753 cm$^{-1}$ in spectrum 3c (pure lactone form) is very narrow. This can be explained by the presence of only one type of C=O. In spectrum 3d (pure eosin Y), the band at 1753 cm$^{-1}$ is broader than in 3c because pure eosin Y contains mainly lactone form but also small amounts of quinoid form: quinoid form includes the C=O from both the carboxylic group and the ketone, so the related C=O stretching bands overlap with the band at 1753 cm$^{-1}$ making it broader.

Having confirmed the expected reactivity of eosin Y treated with different solvents by the band at 1753 cm$^{-1}$, the additional bands associated to these molecular changes could be identified. In particular, the bands in the region below 1600 cm$^{-1}$, typically more overlapped, are I) C-O stretching / O-H deformation of the carboxylic groups present in quinoid form, II) C=C stretching of the C=C bonds that appear in the quinoid form and III) bands linked to the hydroxyl group that appear mostly in the lactone form.

I) Regarding the carboxylic groups, spectra 3a and 3b show a decrease of the relative intensity of the band at ≈1212 cm⁻¹ compared to other bands that do not change between lactone and quinoid form, such as the ones at 1467 and 1422 cm⁻¹. This indicates the relationship of this band with the lactone form (Figure 5.3, structures highlighted in green), probably C-O st / O-H deformation of the lactone group. Indeed, this band is very small in fluorescein, where the lactone form is minor, and it is absent in rhodamine B, where no lactones are present, which can be deduced by their strong colour[318,328] (Figure 5.2). Similarly, an increase of the shoulder at ≈1185 and ≈1171 cm⁻¹ can be noticed (spectra 3a and 3b respectively), most likely related to the same type of vibrations but for the ester group (Figure 5.3, structure highlighted in grey) and the carboxylic acid (Figure 5.3, structure highlighted in brown) formed.[319,320]
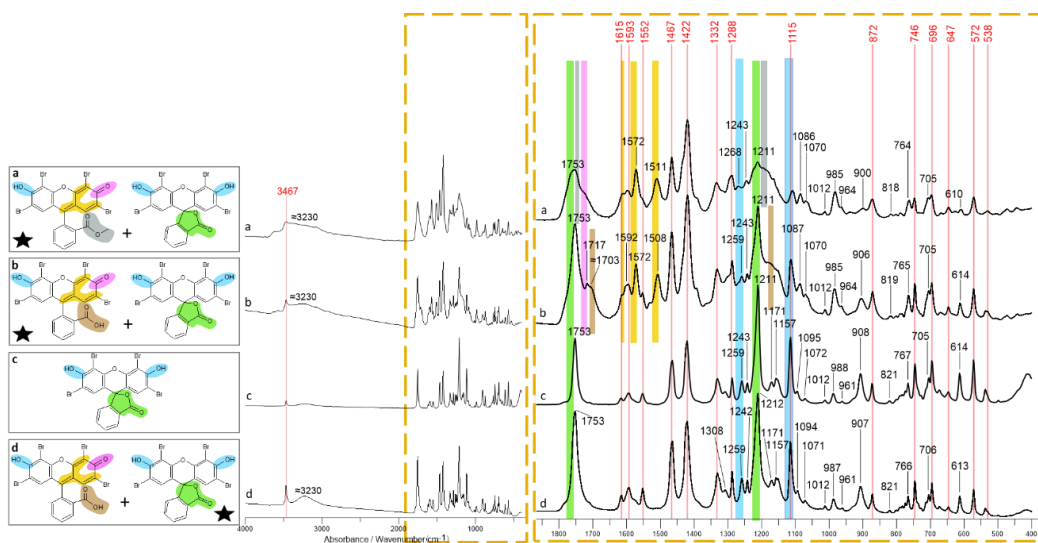


*Figure 5.3_Reactivity of eosin Y with different solvents followed by FTIR spectroscopy. The structure(s) of each sample is showed at the left a) eosin Y after reacting with ethanol, b) eosin Y after reacting with acetone, c) fraction of eosin Y not soluble in water, d) eosin Y. The predominant molecule in each case is marked with a star. The shared structures have been marked in the same colors that the associated bands in the spectra. A magnification of the spectral region marked in orange is displayed at the right, the bands written in red are present in all the samples.*

II) Regarding the C=C bonds (Figure 5.3, structures highlighted in yellow), spectra 3a and 3b show an increase of the bands at 1602, 1572 and ≈1510 cm⁻¹, presumably related to the C=C stretching of the new C=C bonds formed.

III) Regarding the hydroxyl groups (Figure 5.3, structures highlighted in blue), the band at 1259 cm⁻¹, previously related to the –OH group, slightly decreases in spectra 3a and

161

3b. Since the proportion of –OH is lower in the quinoid structure (main form in spectra 3a and 3b), such a decrease is in good agreement with the band assignment formerly stablished. In a similar fashion, a decrease of the band at 1115 cm$^{-1}$ in spectra 3a and 3b is also noticeable, that could be explained by the contribution of the -OH group to this band.

During the experiments of Figure 5.3 no changes in the ether, the skeletal vibrations and the C-Br bonds are expected. As it can be seen, the bands previously associated to these functional groups are present in all the spectra (although some of them are now overlapped with neighbouring bands), which corroborates the stablished band assignment.

### 5.3.4    Band assignment proposed for eosin Y and Geranium lakes

The results of the experimental approach previously discussed (Figures 5.2 and Figure 5.3) complemented with minor literature data,[319,320] allowed to propose a novel band assignment for the FTIR and Raman spectra of eosin Y. This exhaustive interpretation is displayed in Figure 5.4, (experimental assignments in blue, assignments from literature in green).
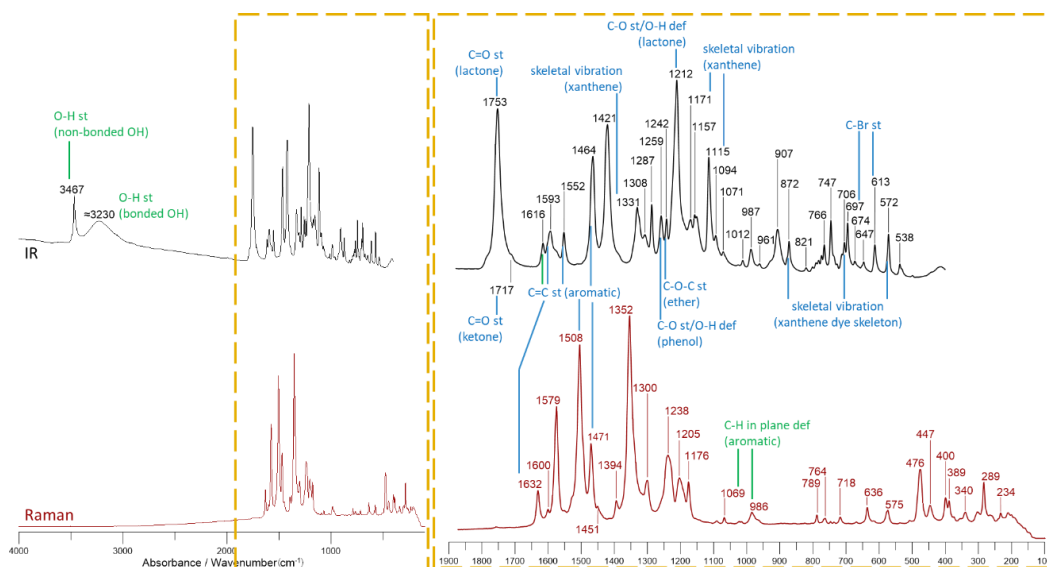


*Figure 5.4_Eosin Y Raman and FTIR spectra with the proposed band assignment. Blue assignments are obtained from the comparisons of Figure 5.2 and Figure 5.3. Green assignments are obtained from the literature. A magnification of the spectral region marked in orange is displayed at the right.*

Based on the band assignment of eosin Y and the bands related to its quinoid form, an assignment for the FTIR and Raman spectra of Geranium lakes complexes is also proposed (Figure 5.5). $Al_2(SO_4)_3$ was used in particular to synthesize the Al-lakes, previous studies have reported indistinctively the use of $Al_2(SO_4)_3$[314] and $AlCl_3$,[309,329] indeed the FTIR and Raman spectra obtained for both compounds showed no significant differences (Figure S5.2). The lakes were obtained at $pH_i$=10 and 0.8 g of reagent $(Pb(COOCH_3)_2)$ for Pb-lake and $pH_i$=12.2 and 0.8 g of reagent $(AlCl_3)$ for Al-lake in order to decrease the presence of by-products that may interfere with the interpretation of the FTIR spectra. However, the effect of these parameters will be discussed in the following sections. The spectra of the lakes were compared to eosin Y disodium salt, obtained from the solution of eosin Y before adding the metallic salt.

The first noticeable change in the FTIR spectra of both synthesized lakes and eosin Y disodium salt (Figure 5.5) is the decreasing/lack of the bands at 1753 and 1212 cm$^{-1}$ related to lactone, due to the presence of the carboxylate group. This change confirms the relationship between these bands and the lactone group. Nevertheless, a small peak at 1753 cm$^{-1}$ is still noticeable in the spectra of Pb-lake and Al-lake, demonstrating the presence of small amounts of eosin Y in lactone form in the products.

Compared to the eosin Y FTIR spectra, two new peaks at ≈1555 and ≈1445 cm$^{-1}$ can be observed. These are probably linked to the C=O stretching, asymmetric and symmetric respectively, of the newly-formed carboxylate group. These bands are broad due to the overlapping with other smaller peaks from the C=C aromatic groups at ≈1570, ≈1510 and ≈1466 cm$^{-1}$ previously mentioned. The presence of the C=C bands in the FTIR spectra is confirmed by the Raman spectra (Figure 5.5, red lines), where the C=O stretching vibrations are not active, and by their presence in the FTIR spectra a and b from Figure 5.3, related to the quinoid form of eosin Y. Previous works assigned other bands to the C=O stretching of the carboxylate group based on theoretical models,[330] however carboxylate frequencies are influenced by many factors therefore they difficult to predict.[331] Furthermore, the attribution of the ≈1555 and ≈1445 cm$^{-1}$ to the carboxylate group is additionally supported by three evidences: I) these vibrations are not active in Raman, and no bands can be detected at these frequencies in the Raman spectra, II) small shifts can be seen in the bands when different metals are bonded to eosin Y, which is explained by the differences in the electronegativity of the metallic ions and in the type of coordination between the metal and the ligand and III) the same carboxylate bands have been detected at similar frequencies (1600-1560 and 1400-1430 cm$^{-1}$) in the spectra of zwitterionic fluorescein.[318]
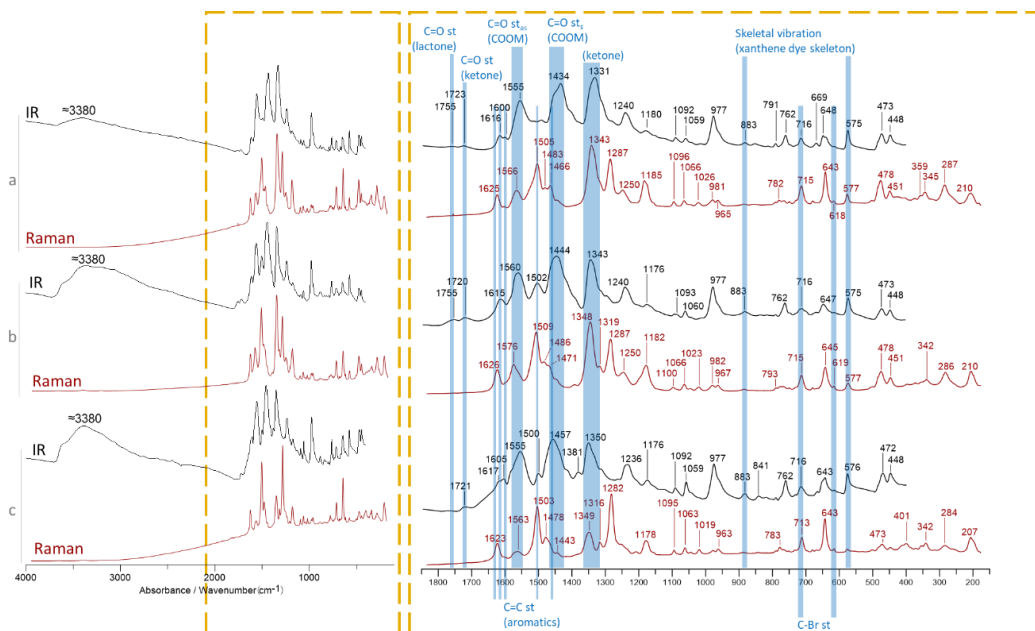
*Figure 5.5_Raman and FTIR spectra and proposed band assignment for a) Pb-lake, b) Al-lake and c) disodium salt of eosin Y. A magnification of the spectral region marked in orange is displayed at the right.*

Another intense band, present in all the FTIR spectra of Figure 5.5, is the one at ≈1340 cm⁻¹. In addition, small shifts in the position of this band are noticeable for the different compounds (1331, 1343 and 1350 cm⁻¹), in the same direction and with similar magnitude as the ones observed in the C=O symmetric stretching of carboxylates (1434, 1444, 1457 cm⁻¹ respectively). Consequently, we propose to assign this band to the ketone interconverted with the deprotonated hydroxyl from the xanthene group (phenoxide ion), which is interacting with the metallic ion of the complex causing those small shifts depending on the electronegativity of the metal. The nature of the interaction between phenoxide ion and the metallic ion is not certain, one hypothesis is the formation of a metallic chelate, whose asymmetric and symmetric stretching would fall between 1608-1524 cm⁻¹ and 1390-1309 cm⁻¹ respectively.[332] Thus, the asymmetric stretching would be overlapped and only the symmetric stretching could be distinguished. As it has been previously mentioned (Figure 5.2), this vibration would overlap the minor peak related to the xanthene group at 1340 cm⁻¹. However, the contribution of the xanthene is expected to be very small here since, as it has been

previously noticed, its intensity is similar to the other bands related to this group at ≈1176 and ≈1115 cm$^{-1}$, which in this case are very low.

The assignment of the ≈1340 cm$^{-1}$ band to the phenoxide ion interacting with the metallic ion is supported by three evidences, namely I) the presence of a similar band in the FTIR spectra of deprotonated fluorescein, which has been assigned to the oxygenated groups from the xanthene moiety,[318,324] II) the FTIR spectra of eosin B disodium salt (which contains Br and –NO$_2$ substituents in the xanthene rings[308]): the additional –NO$_2$ group is expected to create an steric impediment that decreases the interactions of phenoxide ion-metal, therefore the band has lower intensity and III) the interaction phenoxide ion-metal has been already detected in eosin Y adsorbed on titania.[333]

The interaction metal ion-phenoxide ion, and thus with the xanthene chromophore of the eosin Y molecule, implies a potential influence of the metal on the properties of the fundamental and excited states of the complex. Such an interaction is in agreement with the differences in colour experimentally observed between Pb- and Al-lakes (Figure S5.3 and previous works[314,329]). Given the close connection between light absorption, photosensitizing properties and stability of Geranium lakes, this evidence might also help explaining the differences in reactivity reported in literature for different eosin Y complexes.[307,329,334] On the other hand, the spectra of the synthesized products allow to corroborate some band assignments previously proposed related to I) the aromatic groups (≈1616, ≈1600 and ≈1500 cm$^{-1}$), the skeletal vibrations (≈880, ≈715 and ≈575 cm$^{-1}$) and the C-Br bonds (≈613 cm$^{-1}$) in the FTIR spectra and II) the aromatic groups (≈1625, ≈1505 and ≈1470 cm$^{-1}$) in the Raman spectra. These groups are present in all mentioned compounds, so the fact that these bands are present in all spectra confirms the band assignment proposed.

The FTIR and Raman spectral markers of eosin Y and lakes are summarized in Table 5.1. As it can be seen, both techniques allow the discrimination of eosin Y from the synthesized compounds. On the contrary, the Raman spectra from Al-lake, Pb-lake and eosin Y disodium salt are very similar, therefore FTIR spectroscopy is a more suitable technique to distinguish them.

Table 5.1_Specific markers of each compound in the FTIR and Raman spectra. The numbers in italics correspond to the precise values of these bands in previous works: a[314], b[335], c[308], d[330], e[336] and f[337].

| Eosin Y | | Disodium salt of eosin Y | | Pb-lake | | Al-lake | | Assignment |
|---|---|---|---|---|---|---|---|---|
| FTIR | Raman | FTIR | Raman | FTIR | Raman | FTIR | Raman | |
| 1753 *1750 a* *1753 b* *1754 d* *1747 e* | | | | | | | | C=O st (lactone) |
| | | 1457 *1453 a* *1455 c* *1458 f* | | 1444 | | 1434 | | C=O st$_s$ (carboxylate) |
| | | 1350 *1352 c* *1350 f* | | 1343 | | 1331 | | *probably related to ketone* |
| | | | 1282 | | 1287 | | 1287 | Skeletal vibration |
| 1211 *1209 a* *1215 d* | | | | | | | | C-O st/O-H def (lactone) |
| | 1205 | | | | | | | Skeletal vibration |
| 1115 *1115 a* *1113 e* | | | | | | | | Skeletal vibration (xanthene) |
| 907 *906 e* | | | | | | | | Skeletal vibration (xanthene) |
| | | 472 *469 c* *470 f* | | 473 | | 473 | | Skeletal vibration |
| | | 448 *447 f* | | 448 | | 448 | | Skeletal vibration |
| | 400 *400 e* | | 400 | | | | | Skeletal vibration |
| | 390 | | | | | | | Skeletal vibration |

### 5.3.5 Characterization of Geranium lakes synthesized following different protocols

Pb-lakes and Al-lakes are traditionally synthesized by first preparing a solution of dianionic eosin Y where the metallic salt is then added.[308–311] For each type of lake, the synthesis was repeated changing either I) the pH of the solution before adding the metallic salt ($pH_i$) with a fixed amount of metallic salt or II) the amount of metallic salt added with a fixed $pH_i$. Since the pH affects the protolytic species of eosin Y present in the solution and the formation of by-products, the pH after the addition of the metallic salt was also measured ($pH_f$). The obtained Geranium lakes were analysed by means of FTIR spectroscopy following the band assignment previously proposed. Raman spectroscopy was not considered here since the changes are linked to the carboxylate group, for which the vibrations are more active in the FTIR spectra. This allowed to systematically investigate potential changes in the lakes structure. The yield was calculated according to the molecular formula previously proposed[314] considering eosin Y as the limiting reagent. The obtained values are >100% meaning that the molecular formulas used do not reflect the exact composition of the samples: since no other molecular formulas have been proposed, these results have been displayed for the sake of comparison and labelled as "% of Obtained Product" (%OP).

It should be pointed out that, instead of using only one type of metallic salt, some historical recipes include another type of inorganic component in the synthesis (previous works[309,311,314] and references cited therein), that could be also coordinated to the eosin Y molecule forming so called geranium bimetallic lakes, i.e. eosin Y coordinated to two types of metallic ions. However, since the previous analysis of the pigments produced following such recipes showed that eosin Y is coordinated to only one type of metal atom,[314] geranium bimetallic lakes will not be considered in this study.

### 5.3.6 Synthesis of Pb-lakes

The results of the synthesis of Pb-lakes are displayed in Figure 5.6. The FTIR spectra of the obtained products show some variations (Figure 5.6, left side). On one hand, some products show a shoulder at ≈1450 $cm^{-1}$ in the band at ≈1437 $cm^{-1}$, previously associated to the C=O symmetric stretching from the carboxylate group. Previous reports,[338] have stablished a relationship between the position of the bands related to C=O symmetric

and asymmetric stretching and the type of metal-carboxylate coordination. Specifically, if the distance between both bands in the complex is similar to the ionic compound (in this case the disodium salt of eosin Y, Figure 5.6c), the complex has bidentate bridging coordination, a bigger distance indicates a unidentate coordination and a smaller distance a bidentate chelating coordination. Therefore, since the C=O asymmetric stretching does not change (band at 1555 $cm^{-1}$), the peak at 1437 $cm^{-1}$ is expected to be related to unidentate coordination and the shoulder at ≈1450 $cm^{-1}$ suggests the formation of bidentate bridging coordination. The band at ≈1335 $cm^{-1}$ (related to the phenoxide ion) shows shifts similar to the ones observed in the carboxylate group, i.e. a shoulder at 1344 $cm^{-1}$. This agrees with the hypothesis of a phenoxide ion-metal interactions previously mentioned: indeed, if this interaction takes place, a different coordination of the carboxylate-metal would affect the bands related to the phenoxide ion. Thus, the FTIR spectra highlight a clear link between the coordination of the Pb-lakes and the synthesis conditions. If a larger amount of $Pb(COOCH_3)_2$ is used, the proportion of bidentate bridging coordinated complexes is higher, probably explained by the greater number of $Pb^{2+}$ ions available in the solution. In a similar fashion, a higher $pH_i$ leads to a bigger proportion of bidentate bridging coordinated complexes, most likely because the proportion of eosin Y totally deprotonated is larger, so it has more electrons available to form more bonds with the metal.

The presence of by-products is linked to the shoulder at ≈1407 $cm^{-1}$ since this band does not appear in the spectra of eosin Y, related compounds (Figure 5.4 and Figure 5.5) or in the spectra of the metallic salts used for the synthesis (Figure S5.4). The amount of by-products formed strongly depends on the amount of metallic salt added, but also on the $pH_f$ of the synthesis. This is due to the fact that the solubility of Pb salts is higher at lower pH,[339,340] so the by-product formed is re-solubilized if the $pH_f$ is low enough.

As it can be seen, the $pH_f$ changes depending on the synthesis conditions (Figure 5.6, plots at the right). In general, when the metallic salt is added, in parallel to the formation of the eosin Y complex a reaction between $OH^-$ and $Pb^{2+}$ takes place, leading to the precipitation of by-products and causing a diminution of the pH. Hence, when the same amount of metallic salt is added, a lower $pH_i$ results in a lower $pH_f$. Consequently, the amount of by-product is smaller because it starts to solubilize (Figure 5.6, green spectra, the peak at ≈1407 $cm^{-1}$ related to the by-product decreases). Similarly, higher amounts of $Pb(COOCH_3)_2$ (Figure 5.6, orange spectra) result in lower $pH_f$, but also in a higher concentration of $Pb^{2+}$ ions. Thus, the effect of the solubilisation of the by-product at low pH is compensated by the larger amount of by-product formed due to the higher amount

168

of $Pb^{2+}$ ions, consequently the final amount is analogous (peak at ≈1407 $cm^{-1}$ with similar intensity).



*Figure 5.6_Synthesis of Pb-lake depending on the $pH_i$ and the amount of $Pb(COOCH_3)_2$. Left: spectra of the compounds obtained with each type of synthesis, a magnification of the spectral region marked in yellow have been displayed. The %OP of each reaction is presented in the bar plot at the right, using the chemical formula previously published.[314] Right: variations of the $pH_f$ depending on the synthesis conditions. Top (green line): $pH_f$ with different $pH_i$ and $Pb(COOCH_3)_2$=0.8g, bottom (orange line): $pH_f$ with different amount of $Pb(COOCH_3)_2$ and $pH_i$=12. The conditions that increase the proportion of bidentate bridging coordination are marked with an arrow.*

It may seem that a low $pH_f$ is more convenient since this leads to a low amount of by-products, so the obtained pigment is purer. However, it should be kept in mind that at low $pH_f$, eosin Y starts to protonate. The fraction of protonated eosin Y is too low to be detected in the FTIR spectra, however, it can be seen that at low $pH_f$ the supernatant shows an orange tone (Figure S5.5), associated to the presence of eosin Y. In any case, the $pH_f$ does not decrease below 6-5.8 in all studied conditions, which is explained by the equilibrium established by the by-products formed and the solubility of $Pb^{2+}$ which increases at low pH.[339,340] Interestingly, the %OP of the Pb-lake synthesis (Figure 5.6, barplot) exceeds 100% in all cases, explained by the presence of the by-product and the

type of carboxylate-metal coordination. In fact, a bidentate bridging coordination translates into one atom of Pb per each ligand of eosin Y, which increases the total molecular weight compared to the previous formula.[314] Consequently, a higher %OP is observed in the compounds for which the spectra shows a bidentate bridging coordination.

Finally, other types of synthesis reported in the literature, with small additional variations in the procedure, were reproduced to verify if the results fit the trends previously observed (Figure S5.6).[314] These syntheses start from a $Pb(COOCH_3)_2$ solution ($pH_i$ =6.1), where eosin Y disodium salt is added, and from an eosin Y disodium salt solution ($pH_i$ =6.5), where the metallic salt is added. In the latter, two different amounts of $Pb(COOCH_3)_2$ were used to verify its influence. As it can be noticed, the predominant form is the unidentate coordination, probably because the $pH_i$ is too low and thus the proportion of deprotonated eosin Y is limited. Therefore, the effect of pH is crucial: even when adding high amounts of $Pb(COOCH_3)_2$, in fact, the proportion of bidentate bridging coordination is lower compare to unidentate. Additionally, a synthesis at a very low $pH_f$ was also tested (spectrum d, Figure S5.6), by adding $CH_3COOCH_3$ to the final solution. As it can be seen, the predominant coordination mode is unidentate. Eosin Y is surely mixed with the obtained pigment but, unlike for Al-lakes, the bands cannot be seen in the spectra, due to the higher molar absorptivity of Pb-lakes.

### 5.3.7 Synthesis of Al-lakes

The results of the synthesis of Al-lakes are displayed in Figure 5.7. The plots at the right, showing the $pH_f$ depending on the synthesis conditions, present the same trends seen for the Pb-lakes (Figure 5.6), i.e. the $pH_f$ is lower when $pH_i$ is lower or when higher amounts of $Al_2(SO_4)_3$ are used. Like in the synthesis of Pb-lakes, this is probably explained by the formation of a by-product of $OH^-$ and $Al^{3+}$. However, the range of $pH_f$ obtained in the synthesis of Al-lakes, $pH_f \approx 3.7$, is lower and the range is narrower than in Pb-lake, which can be explained by the lower solubility of the $Al^{3+}$ salts[341] compared to $Pb^{2+}$ salts.[339] Due to the lower $pH_f$, a higher formation of protonated eosin Y is expected, which agrees with the colour of the supernatants observed in all the performed experiments (Figure S5.5).
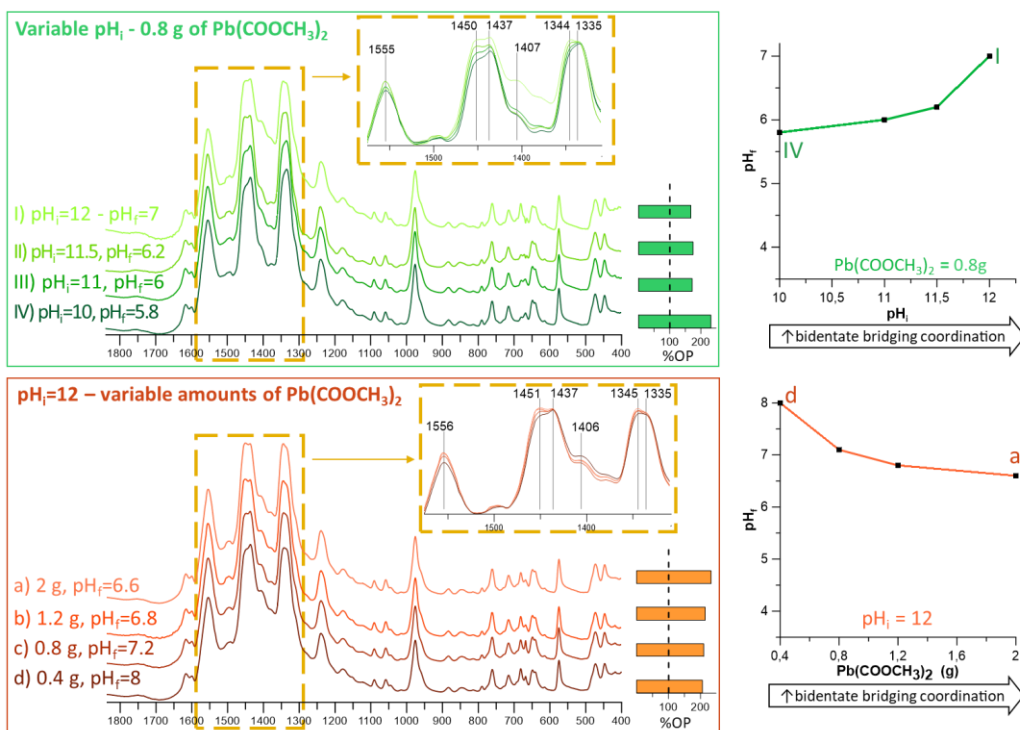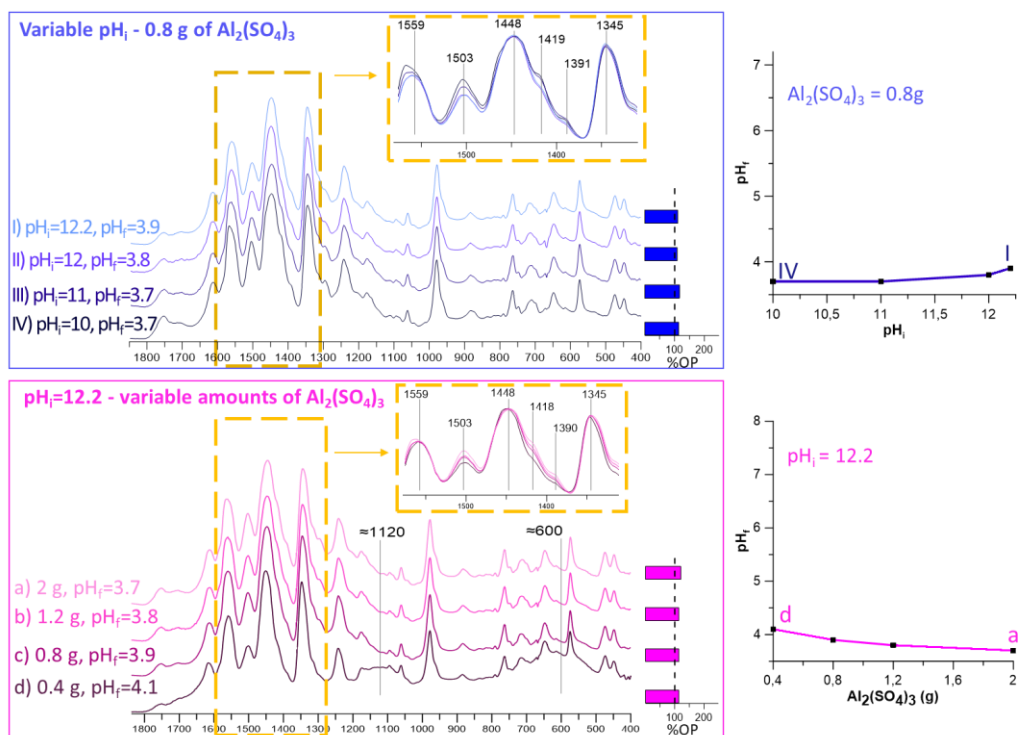
*Figure 5.7_Synthesis of Al-lake depending on the pH$_i$ and the amount of Al$_2$(SO$_4$)$_3$. Left: spectra of the compounds obtained with each type of synthesis using the same color code, a magnification of the spectral region marked in yellow have been displayed. The %OP of each reaction is presented In the bar plot at the right, using the chemical formula previously published.[314] Right: variations of the pHf depending on the synthesis conditions. Top (blue line): pH$_f$ with different pH$_i$ and Al$_2$(SO$_4$)$_3$ =0.8g, bottom (pink line): pH$_f$ with different amount of Al$_2$(SO$_4$)$_3$ and pH$_i$=12.2.*

Regarding the characterization of the obtained products by FTIR spectroscopy (Figure 5.7, right side) no shifts can be seen in the position of the bands related to the carboxylate group, therefore the metal-carboxylate coordination does not change depending on the pH$_f$ in this case. Comparing the position of these bands with the Pb-complex and the disodium salt of eosin Y, it can be assumed that the main metal-carboxylate coordination of Al-lakes is bidentate bridging. However, since the band at 1448 cm$^{-1}$ is quite broad, it is feasible that other coordination modes exist in lower proportions and that the associated bands are overlapped with the one at 1448 cm$^{-1}$. Besides the carboxylate bands, additional variations can be noticed in other regions, namely I) the increase of the bands at 1753, 1503, 1205 and 1115 cm$^{-1}$ and the shoulders at ≈1570, 1418 and 1390 cm$^{-1}$ at low pH$_f$, that can be related to the growing amount of protonated (i.e. non-complexed) eosin Y, and II) the increase of broad bands at ≈1120

171

and ≈600 cm$^{-1}$ at high pH$_f$, probably associated to the presence of by-products of Al$^{3+}$. Likewise Pb-lakes, at low pH$_f$ a lower amount of by-product and a higher amount of protonated eosin Y are generated. When it comes to the %OP of the synthesis of Al-lake (Figure 5.7, barplot at the right), it can also be observed that it is higher than 100%. Similarly to Pb-lakes, this can be explained by the presence of by-products and by the bidentate bridging coordination between the carboxylate and the metal, that would increase the molecular weight of the lake. Compared to the Pb-lake, the %OP is smaller due to the lower atomic weight of Al compared to Pb.

Additional experiments were also performed in order to verify the effect of further small variations in the synthesis protocol observed in the literature (Figure S5.7).[314] In the same fashion of Pb-lakes, the conditions tested include starting the synthesis with a Al$_2$(SO$_4$)$_3$ solution (pH$_i$ =3.3), where eosin Y disodium salt is added, or with an eosin Y disodium salt solution (pH$_i$ =6.5), where the metallic salt is added. In the latter, two different amounts of Al$_2$(SO$_4$)$_3$ were tested. As it can be seen, also in this case the coordination of eosin Y-metal does not change. Indeed, the FTIR spectra seem very similar to the ones obtained in Figure 5.7 with similar pH$_f$, meaning that Al-lakes form the bidentate bridging coordination even when the proportion of deprotonated eosin Y is relatively low and independently of the amount of metallic salt used. However, the proportion of eosin Y increases dramatically at low pH$_f$ affecting severely the purity of the obtained lake.

In conclusion, the carboxylate-metal coordination in Al-lakes is mostly bidentate bridging, while the proportion of unidentate or bidentate bridging coordination in Pb-lakes depends on the synthesis conditions. For the first time, the formation of by-products in both types of lakes is demonstrated: for Pb-lakes the amount of by-products decreases at low pH$_f$ due to the increase of their solubility in these conditions. In the case of Al-lakes, the by-products formed are less soluble and their amount is significant even at the lowest pH$_f$ tested. Additionally, protonated eosin Y is also found mixed with the obtained lakes when the pH$_f$ is low enough: its characteristic colour is noticeable in the supernatant at pH$_f$ <6 and its specific bands are distinguishable in the FTIR spectra at pH$_f$ <4. The different coordination modes of Pb-lakes may lead to differences in their reactivity, as it has been previously demonstrated in other type of complexes.[342,343] Additionally, the presence of by-products and eosin Y may also affect their chemical behaviour, especially since eosin Y degrades fast under specific conditions.[293]

Consequently, the type of synthesis of Geranium lakes may significantly affect their stability.

### 5.3.8   Characterization of the by-products depending on the synthesis method

The analysis of the FTIR spectra of Geranium lakes allowed to link some of the bands to the co-precipitation of by-products during the synthesis. The characterization of such by-products is of great importance, since they might affect the purity of the pigments and, thus, their reactivity.

The behaviour of the metal solutions was separately investigated to characterize the by-products formed. In detail, the same conditions used to synthesize Al- and Pb-lake were reproduced without the presence of eosin Y in order to study the by-products formed depending on the pH. The obtained products were characterized by XRPD, FTIR and Raman spectroscopy.

The by-products generated by Pb salts are displayed in Figure 5.8. Two different products were detected depending on the $pH_f$: at $pH_f$ >11 a pale yellow precipitate is formed, and at 11>$pH_f$ >7 the precipitate is white. Below pH=7 the precipitate starts to re-dissolve. At both pH, the FTIR (Figure 5.8, black lines) and Raman (Figure 5.8, red lines) spectra show the spectral markers of lead (II) carbonate.[344] In particular, the FTIR spectra of pH=8.2 suggests the presence of plumbonacrite ($Pb_5(CO_3)_3O(OH)_2$), due to the presence of a band at 3430 and 865 cm$^{-1}$ related to more than one site of OH$^-$ and CO$_3^{2-}$, respectively, in the structure of the lead (II) carbonate. The presence of plumbonacrite is confirmed by the XRPD data (Figure 5.8, green line), although the XRPD shows also an unidentified crystalline compound in the by-product at pH=11.7. On the other hand, the XRPD analysis of the previously synthesized Pb-lakes (Figure 5.6) shows the presence of another type of lead (II) carbonate, specifically hydrocerussite ($Pb_3(CO_3)_2(OH)_2$) (Figure S5.8). This difference is probably explained by the lower amount of Pb$^{2+}$ ions available during the synthesis, since they are partially complexed to form the Pb-lake. The generated by-product re-dissolved completely at pH<6.

The by-products generated by Al salts are displayed in Figure 5.9. In this case, all precipitates are white but different spectral features are observed at different $pH_f$. The FTIR spectra of the product obtained at $pH_f$ =9.1 shows the presence of bands related to amorphous basic aluminum carbonate,[345] possibly dawsonite.[346] At $pH_f$ = 6.7 the

173

spectrum is similar but the proportion of carbonate groups is lower since the related bands (1528 and 1418 cm$^{-1}$) are less intense. Finally, at pH$_f$ =3.5, the bands related to – OH groups (3450 and 1650 cm$^{-1}$) are higher, indicating a higher proportion of this functionality. According to the obtained spectra, the presence of basic aluminium sulphates at pH$_f$ = 6.7 and pH$_f$ = 3.5 is feasible.[347] In this case, the XRPD diffractogram show no bands, in agreement with the amorphous nature of the generated by-products, and the Raman spectra shows a broad band related to fluorescence, typically seen in aluminium compounds. The generated by-product was insoluble at the lowest pH tested (pH=3.5). The different solubility of the by-products agrees with the different pH$_f$ ranges observed for Pb-lakes and Al-lakes.
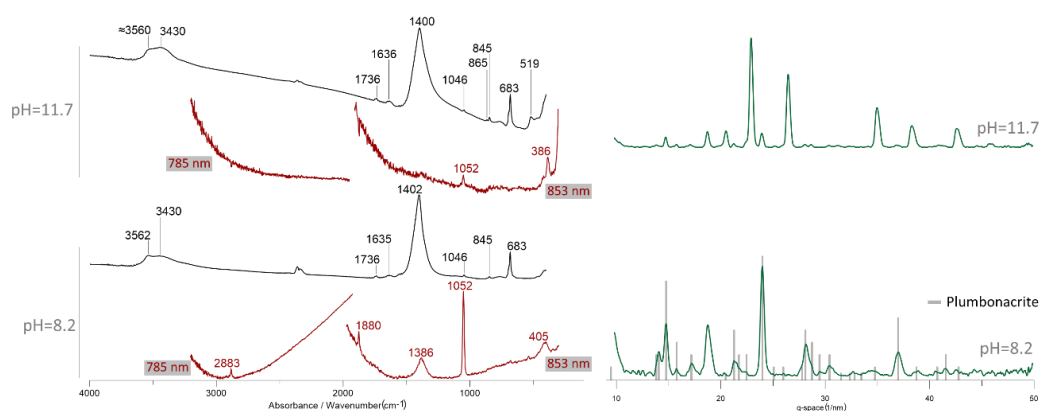


*Figure 5.8_Spectra of the by-products obtained in the synthesis of Pb-lake at different pH (11.7 and 8.2). Left: FTIR spectra are plotted in balck and Raman spectra in red (in order to avoid the fluorescence, two wavelenghts were used, 785 nm and 853 nm). Right: XRD diffractograms are plotted in green compared to the reference spectra of plumbonacrite (grey lines).*

The presence of Pb and Al compounds can play an important role in the reactivity of the pigments used in oil paintings. Lead carbonates are known to react with fatty acids from the binding media to produce lead soaps, the formation of Al soaps has also been observed.[53,105,348,349] Metal soaps are associated with the formation of protrusions and cracks in the paintings.[54] Thus, a higher proportion of these compounds would cause a higher damage to the paintings, that should not be confused with the reactivity of Geranium lakes themselves. Furthermore, the presence of white by-products mixed with the complexes might affect their long-term stability due to the scattering of the light, increasing their tendency to fade. Lead carbonates mixed in the paint film, in particular, have been found to promote such fading processes.[329]

Additionally, lead carbonates have been used in historical paintings as a white pigment, also in combination with Geranium lakes.[17,302] Knowing that such compounds could also exist as impurities in the pigments is of great importance to accurately interpret and reconstruct the formulation of historical paints. This is a relevant information to understand the artistic choices and the painting technique of the artists who used these pigments, allowing to perform more accurate authentication and attribution of paintings.
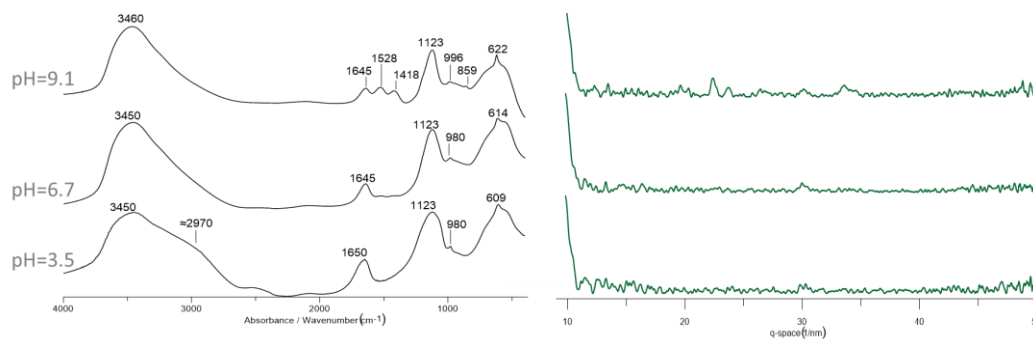


*Figure 5.9_Left: FTIR spectra of the by-products obtained in the synthesis of Al-lake at different pH (9.1, 6.7 and 3.5). Right: XRD diffractograms (plotted in green).*

## 5.4 Conclusions

This chapter presented a thorough investigation of the structure and composition of eosin Y complexes based on Al and Pb, by FTIR and Raman spectroscopies and complementary techniques, with a particular focus on the effect of changes in the synthesis conditions. In the first place, the results further the understanding of the eosin Y-metal coordination with Al and Pb, showing a clear link between changes in the synthesis conditions and changes in such coordination. In detail, Pb-lakes show an eosin Y-metal unidentate or a bidentate bridging coordination depending on $pH_i$ and amount of metallic salt used. Al-lakes, on the other hand, present mostly a bidentate bridging coordination in all the synthesized products, nonetheless lower amounts of unidentate and bidentate chelating coordination might also be present, as suggested by the broad C=O symmetric stretching band. Furthermore, an additional interaction between the metal ion and the phenoxide ion, and thus the xanthene moiety (chromophore), is proposed for all the complexes. This interaction is of capital importance since it implies

a potential influence of the metal ion on the properties of the fundamental and excited states of the complexes, ultimately determining their reactivity. In addition, the evidence for a chromophore-metal interaction presented in this study supports the literature findings on the differences in colour and in reactivity for Al- and Pb-lakes.

In both cases, the synthesized lakes also contain by-products mixed with the eosin Y complexes. Such by-products are detected and identified here for the first time. In detail, lead carbonates are observed in Pb-lake samples when the $pH_f$ is higher than 6. Below this value, lead carbonates are not present due to their solubility at low pH, however eosin Y starts to protonate and is found in the pigment powder. In the case of Al-lakes, amorphous basic aluminium carbonate was identified, with variable proportions of carbonate and OH groups. Since the $pH_f$ is low, around 3, the amount of eosin Y mixed with the synthesized lake is higher than for the Pb-lakes. Consequently, the Geranium lake pigments generated by the synthesis methods studied will always contain impurities.

Additionally, a detailed band assignment of the FTIR and Raman spectra of eosin Y and Pb and Al-based Geranium lakes has been described. This band assignment has the potential to become a reference to better understand and monitor molecular alterations during the degradation of Geranium lakes and eosin Y complexes in general, as well as to more easily distinguish these molecules in unknown samples. This is of great importance not only for the analysis of historical paintings, but also for the study of any other material containing eosin Y bonded to metallic ions. Particularly, in all the applications in which the nature of the interaction between eosin Y and a metal/metal oxide surface could completely change the outcome of a photochemical process, such as dye-sensitized solar cells, removal of dyes from wastewater, or photocatalysis. The accurate characterization of the eosin Y complexes and by-products discussed in this study will ultimately help to understand their reactivity.

# 5.5 Supplementary information
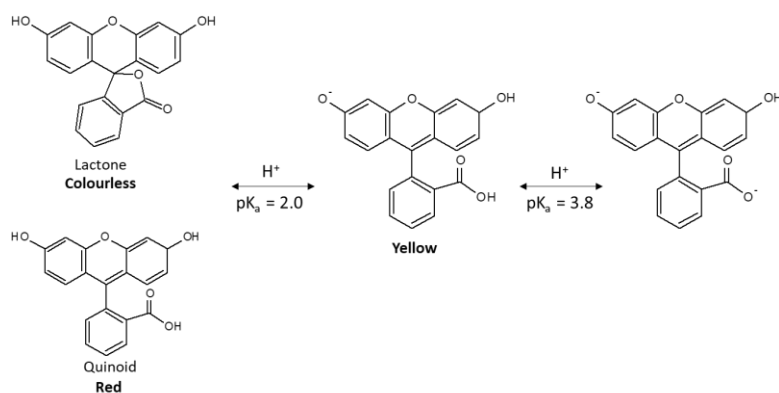


*Figure S5.1_Main tautomers and pKa of fluorescein. The colors mentioned are based on previous literature.*[318]
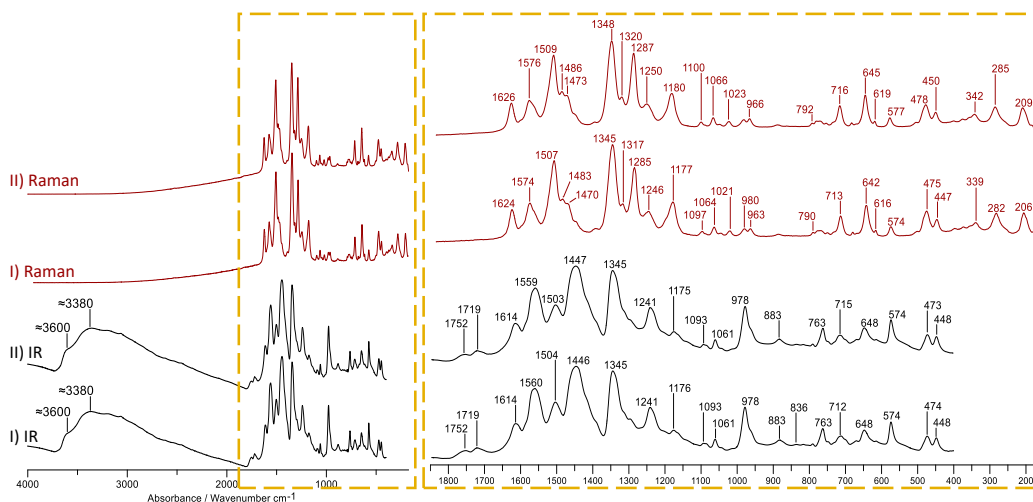


*Figure S5.2_Raman and FTIR spectra of aluminum based Geranium lakes prepared with I) Al$_2$(SO$_4$)$_3$ and II) AlCl$_3$. A magnification of the spectral region marked in yellow is shown on the right.*

| Pb-lake | Al-lake |
|---|---|
| pH$_i$ = 12 | pH$_i$ = 12 |
| 0.8 g Pb(Ac)$_2$ | 0.8 g Al$_2$(SO$_4$)$_3$ |
| pH$_f$ = 4.6 | pH$_f$ = 3.9 |
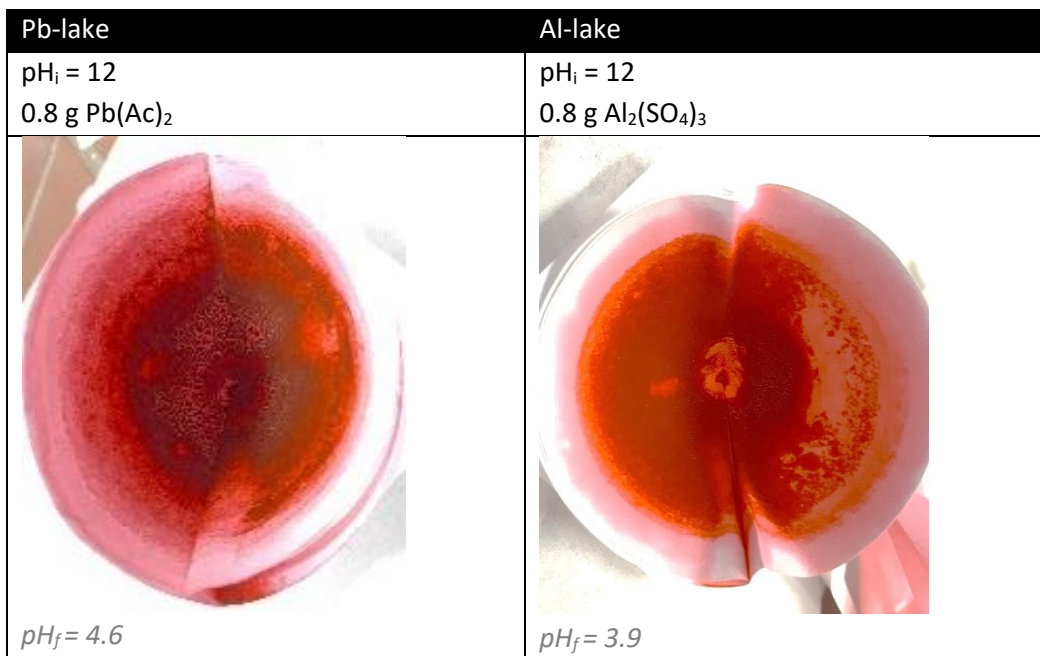
Figure S5.3_Color of Pb-lake and Al-lake obtained at similar synthesis conditions.
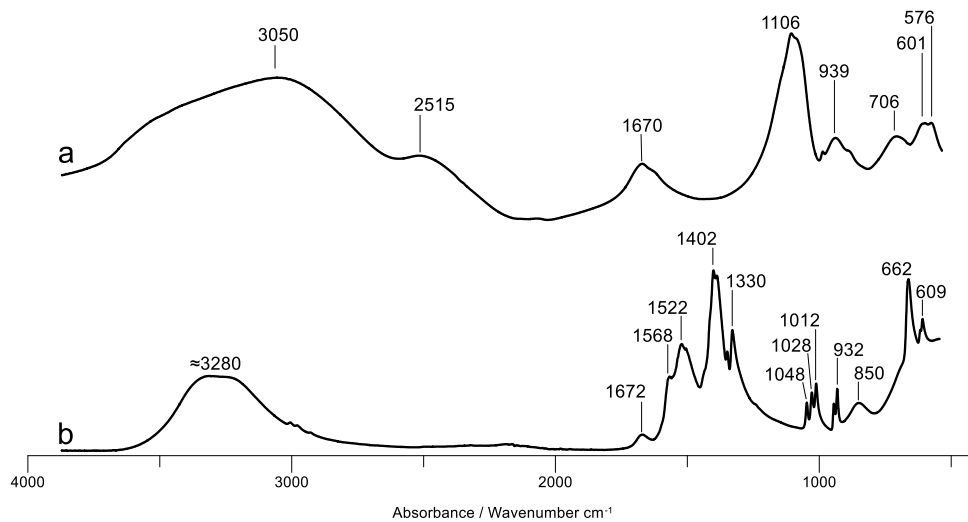


Figure S5.4_FTIR spectra of the metallic salts used to prepare the complexes a) Al$_2$(SO$_4$)$_3$ and b) Pb(COOCH$_3$)$_2$.
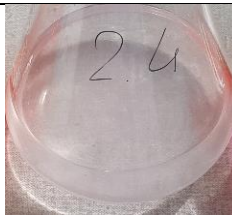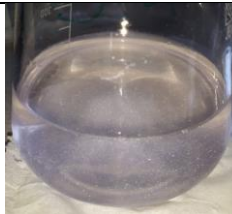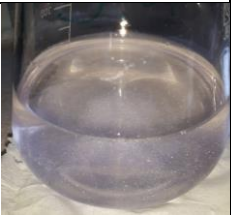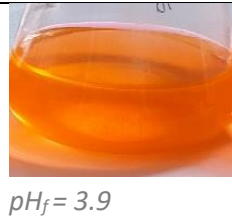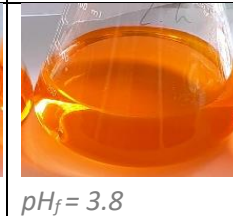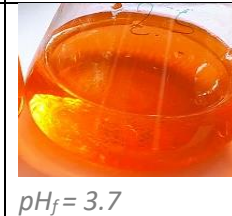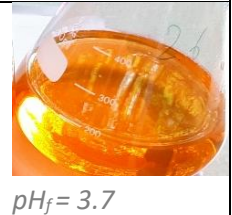
*Figure S5.5_Filtered supernatant of Pb-lake and Al-lake synthesis depending on the conditions.*
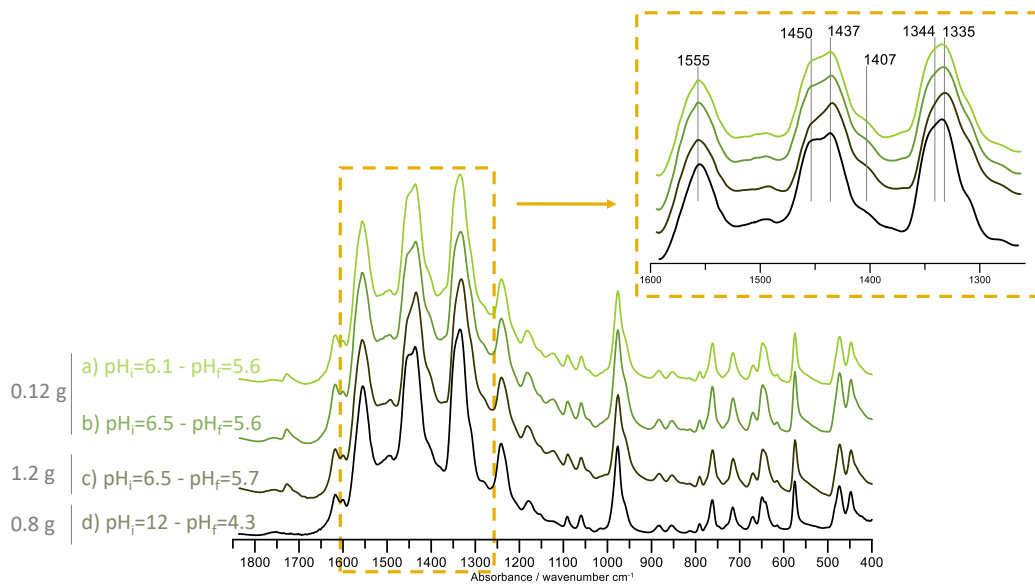
*Figure S5.6_FTIR spectra of the Pb-lakes obtained at other type of conditions. A magnification of the spectral region marked in yellow is displayed.*
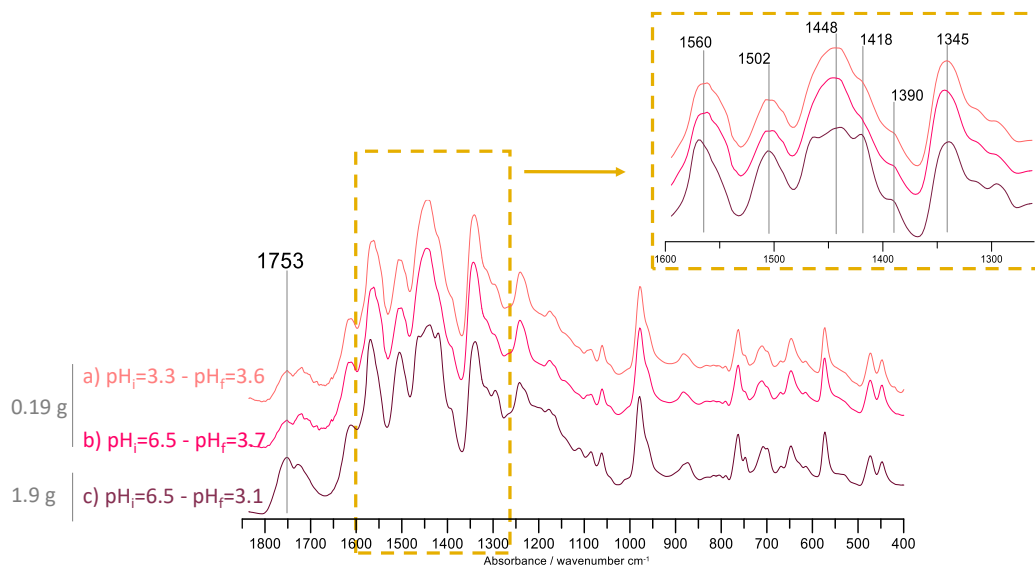


*Figure S5.7_FTIR spectra of the Al-lakes obtained at other type of conditions. A magnification of the spectral region marked in yellow is displayed.*
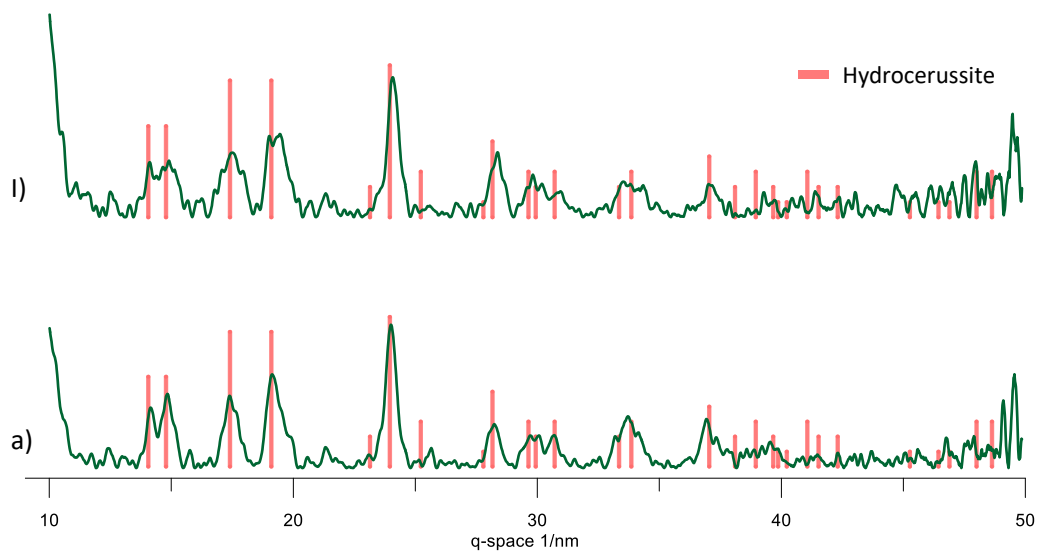
*Figure S5.8_XRD diffractograms of the Pb-lakes synthesized in Figure 5.6 corresponding to spectra I) and a). The graphs have been compared to reference spectra of hydrocerussite (pink lines).*

# |5

## [Part 2]

Preliminary results on the reactivity of the synthesized Geranium lake pigments

# Abstract

In this second part of the chapter, preliminary information is obtained on the relationship between the synthesis-induced differences in composition just observed for Geranium lakes and their reactivity. The study of the natural ageing of some of the Geranium lake samples previously synthesized, chosen on the basis of significant differences in composition, is first presented. The molecular transformations associated with the degradation in natural light and dark conditions are monitored by means of FTIR, basing the interpretation of the spectral changes on the thorough band-assignment introduced in the first part of the chapter. Although not conclusive, these first results already highlight the fundamental role played by the amount and type of by-products in the pigments on their ageing kinetics. In addition, preliminary insights on the solubility of the eosin Y-based complexes in contact with aqueous electrolyte solutions, potentially relevant to understand their reactivity in paintings, are also presented.

# 5.6 Natural ageing of Al- and Pb-based Geranium lake samples

As mentioned in the first part of this chapter, open questions still remain when it comes to the reactivity of Geranium lakes and the factors influencing it.[306–308] One of the reasons explaining the discrepancies in the results in literature, could be traced back to the different synthesis conditions, leading to pigments with different composition in different studies. A different composition alone, however, does not always necessarily translate into different reactivities and fading kinetics. In order to verify if the differences in composition observed in the pigments, synthesized in the first part of this chapter, could lead to a difference in the degradation, the ageing of a selection of pigments was studied by means of FTIR spectroscopy. This selection includes Pb-lakes and Al-lakes synthesized following different protocols, which were demonstrated to influence the chemical composition of the obtained pigment.

The in-depth interpretation of the FTIR spectra of Geranium lakes presented in the first part of this chapter served as a reference to monitor the molecular changes associated with the degradation. Raman spectroscopy was not employed in this case, since the previous results showed that this technique is less sensitive to changes in the coordination mode of Geranium lakes.

Despite the fact that previous studies on the degradation of eosin Y-based pigments focused on the accelerated ageing by means of light,[307,329] here the study of the natural ageing is proposed. Previous papers have in fact showed that differences may exist in the effects of these two different types of ageing.[350,351] This might be explained by the fact that accelerated ageing cannot reproduce some of the phenomena observed during natural ageing, for instance the migration and aggregation of compounds, which can potentially influence the specific degradation processes. Thus, the study of the natural ageing of Geranium lakes is expected to provide a more complete understanding of their reactivity.

Given the known influence of visible light on the degradation of Geranium lakes,[302,307] the pigments in analysis were aged both in dark and light conditions. In order to reproduce the ageing conditions in a museum environment, the samples were kept indoors at room conditions (1 atm, 20 °C). As a comparison, pure eosin Y was also aged in the same conditions of the synthesized lakes.

## 5.6.1   Samples and ageing conditions

The Geranium lake samples to be naturally aged were selected based on the results of the synthesis and characterization described in the first part of this chapter. In particular, synthesis conditions leading to differences in the chemical composition of the final pigment were chosen. For Pb-lakes, whose composition is strongly influenced by the synthesis conditions, three different samples (Pb1, Pb2 and Pb3) produced with increasing amounts of metallic salt and $pH_i$ were considered. For Al-lakes, less dramatically influenced by the synthesis protocol, two synthesis conditions with different $pH_i$ and amounts of metallic salt were chosen (Al1 and Al2). The synthesis conditions are summarized in Table 5.2.

*Table 5.2_Synthesis conditions of the synthesized Pb and Al lakes exposed to natural ageing.*

| Sample name | Metal salt [g] | $pH_i$ | $pH_f$ | %OP |
|:-----------:|:--------------:|:------:|:------:|:---:|
| Pb1 | $Pb(COOCH_3)_2$ [0.12] | 6.5 | 5.6 | 116% |
| Pb2 | $Pb(COOCH_3)_2$ [0.8] | 10 | 5.8 | 168% |
| Pb3 | $Pb(COOCH_3)_2$ [2.0] | 12 | 6.6 | 206% |
| Al1 | $Al_2(SO_4)_3$ [0.4] | 12.2 | 4.1 | 114% |
| Al2 | $Al_2(SO_4)_3$ [0.8] | 10 | 3.7 | 111% |

The spectra of the analyzed Geranium lakes, before ageing, are displayed in Figure 5.10. Following the trends observed in the first part of this chapter, Pb-lakes show increasing amounts of lead carbonate when higher $pH_i$ and more metal salt are employed. This can be clearly noticed by the increase in the signal at 682 $cm^{-1}$ (C-O stretching of $CO_3^{-2}$), which is not overlapped by other bands and reaches a maximum in sample Pb3. Additionally, changes in the proportion of bidentate bridging coordination (shoulder at ≈1454 $cm^{-1}$) compared to unidentate coordination (≈1435 $cm^{-1}$) are also observed, with the Pb3 lake showing the highest contribution of the bidentate one. On the other hand, the slight increase in the shoulders at 1756 and 1429 $cm^{-1}$ in Al2 compared to Al1, indicates the presence of a slightly higher content of eosin Y as a by-product in Al2.
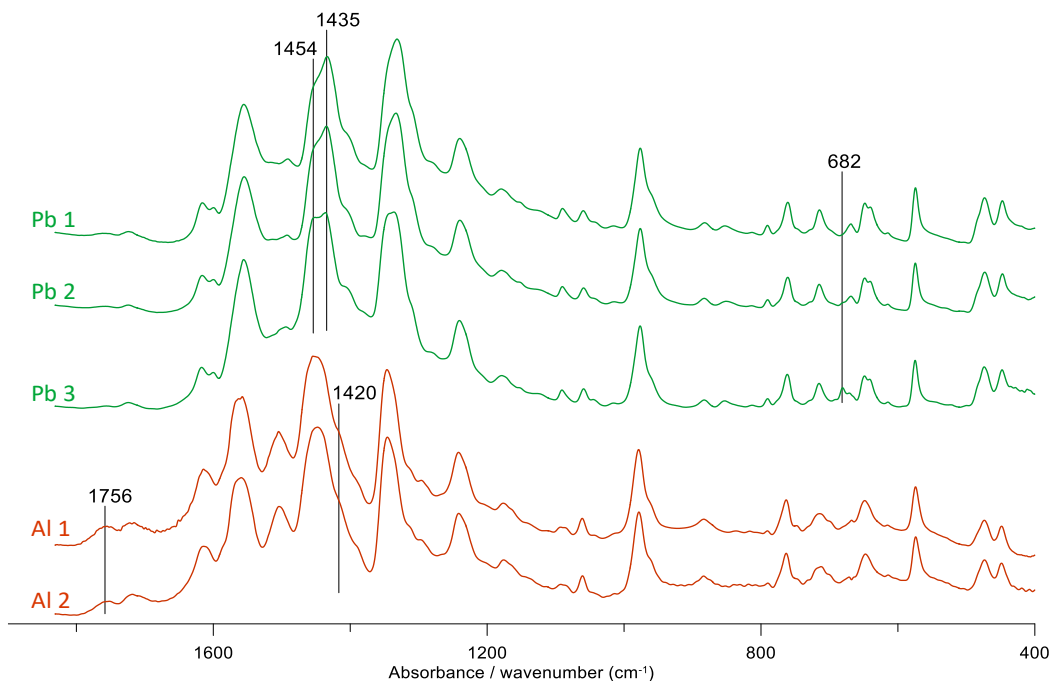
*Figure 5.10_FTIR spectra of the Geranium lake samples considered before the ageing. Green: Pb-lakes. Red: Al-lakes.*

The single Geranium lake samples were mixed with KBr, pressed into pellets and deposited on a glass surface for natural ageing. The degradation was monitored by means of FTIR over a period of 14 to 16 months. The experimental conditions for the analysis of the pellets were the same as described in the first part of this chapter (5.2 Materials and methods).

## 5.6.2   Data processing

The analysis of the collected FTIR spectra lead to the detection of spectral markers of the degradation of Geranium lakes. In order to compare the degradation rate of each compound, kinetic plots were prepared by calculating the intensity of those spectral markers in each spectrum. In order to do so, the single FTIR spectra had to be first baseline corrected and normalized. The data processing was performed with the OPUS software (Bruker) and strongly relied on the insights obtained in the first part of the

187

chapter on the FTIR spectra of Geranium lakes. The experimental parameters are the same for all the samples, in order to ensure the comparability of the datasets.

The baseline correction was performed by selecting four constant points for all the spectra and applying the concave rubberband correction method. The number of points was minimized in order to avoid a distortion of the spectra that may interfere with the interpretation. The selected points are in regions were no bands have been previously detected, in particular: 3990, 2500, 1900 and 490 cm$^{-1}$.

In order to normalize the spectra, a reference band (or spectral range) remaining constant during the ageing (meaning that the related functional groups are not altered) had to be selected. For the eosin-based lakes, the most intense bands are the ones associated to the symmetric and asymmetric stretching of the carboxylate group. These band are expected to change during the ageing only if 1) the lakes are protonated and the COO-Metal bond is broken (which has not been previously reported) or 2) if changes take place in the coordination of the metal complex. In this second case, however, the changes in coordination would alter significantly the band of the C=O symmetric stretching (1450 cm$^{-1}$), but not the one of the C=O asymmetric stretching (1555 cm$^{-1}$) (as shown in the first part of this chapter). It is also true, however, that this second band overlaps with another band at 1555 cm$^{-1}$ related to aromatics which, although small, might be altered during the degradation. Since changes in the molecular structure affecting this band would, most likely, affect also the other bands related with the ring stretchings of the aromatic rings (1616 and 1590 cm$^{-1}$), the eventual instability of this band can be verified. For these reasons, the band at 1555 cm$^{-1}$ was employed as a reference in the normalization of all the spectra.

Finally, the intensity of each band was calculated by drawing a baseline between the valleys of the peak: the precise wavenumber was calculated by means of the second derivative.

### 5.6.3   Preliminary results

In order to interpret the changes in the spectra of Geranium lakes, eosin Y was also aged in the same conditions, since the two compounds present several common features in their structure.

188

The results of the natural ageing of eosin are shown in Figure 5.11. As it can be noticed, the variations associated with the ageing are localized in specific parts of the spectra. In particular, an increase in two shoulders at 3150 and 1384 cm$^{-1}$ is observed. Among them, the band at 1384 cm$^{-1}$ could be attributed to the absorption of $CO_2$, however this explanation should be discarded since the other spectral markers of this compound, for instance the peaks at 2430 and 2400 cm$^{-1}$ are not present. According to the spectral range[319,320] and the elemental composition of the molecule, the band at 1384 cm$^{-1}$ may be related to the formation of C-O bonds (C-O deformation). This vibration is also present in C=O groups, but their presence can be discarded due to the lack of additional bands in the region of 1800-1700 cm$^{-1}$ related to the C=O stretching. In the same fashion, $CH_3$ groups could be considered since they include a vibration in this spectral region (C-H deformation), however their presence is less probable as it would also imply the increase of the C-H stretching around 2900 cm$^{-1}$, which is not noticeable. On the other hand, the band at 3150 cm$^{-1}$ could be related to the formation of –OH groups (O-H stretching). Hence, the hypotheses that may be drawn are related to the formation of alcohols, either by the hydrolysis of the ether in the xanthene moiety or by the oxidation of a double bond.
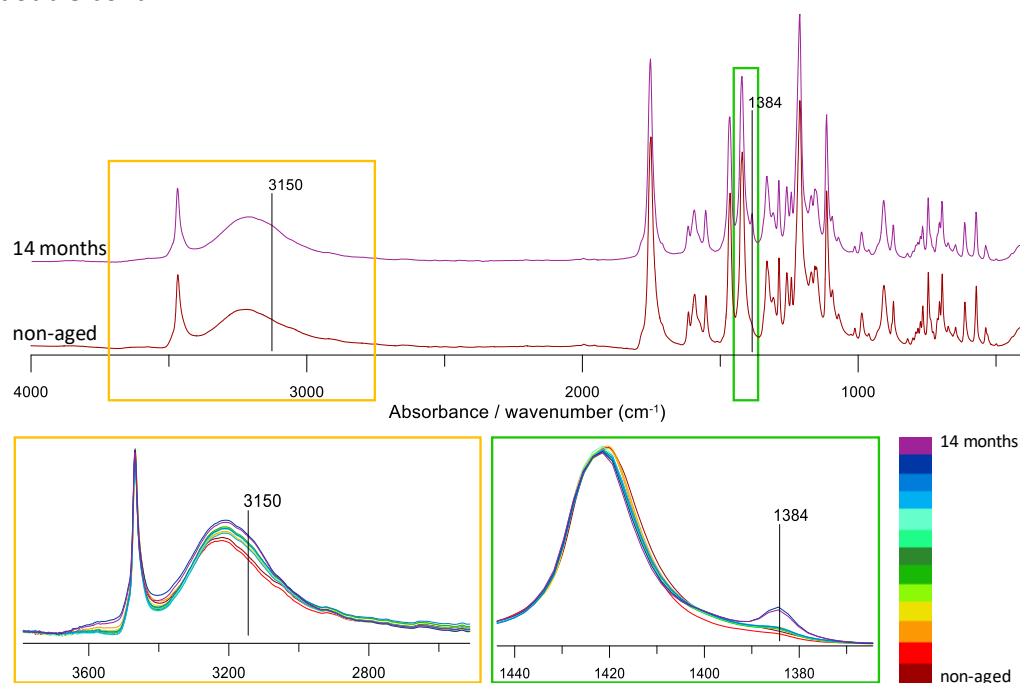


*Figure 5.11_Natural ageing of eosin Y exposed to light. Top: FTIR spectra of non-aged eosin Y compared to eosin Y aged for 14 months. Bottom: magnification of the spectral regions where the main changes were detected.*

It should be noticed that the changes in the spectra previously mentioned appear also in the samples aged in a dark environment, but the increasing of the bands is less obvious. Indeed, a significant effect of light can be clearly seen in the kinetic plots displayed in Figure 5.12 (the complete spectra are shown in Figure S5.9). The fact that the ageing is induced by light matches with the previous literature on eosin Y fading.[293]
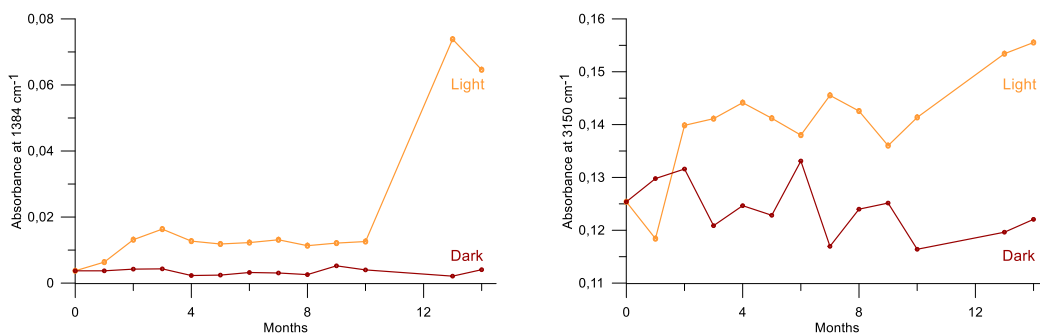


*Figure 5.12_Changes in the intensity of the bands associated to eosin Y degradation during ageing in light (orange) and dark (red). Left: absorbance of the 1384 cm$^{-1}$ band. Right: absorbance of the 3150 cm$^{-1}$ band.*

After studying the ageing of eosin Y, the changes occurring in the spectra of the Geranium lake pigments during the ageing were investigated starting from the Pb-lakes. The results of the natural ageing of Pb1 are displayed in Figure 5.13. Three types of changes can be noticed in the collected data: I) alterations in the bands associated to the coordination mode ($\approx$1450 and $\approx$1350 cm$^{-1}$), II) increase of the bands at $\approx$3350 and $\approx$1630 cm$^{-1}$ related to the water adsorption due to the polar nature of the lakes and III) increase of the same bands observed during eosin Y ageing, namely $\approx$3150 and $\approx$1380 cm$^{-1}$.

In the first place, clear changes in the coordination mode can be observed already in the first weeks of ageing. In particular, a bidentate bridging coordination becomes predominant, although most probably a fraction of unidentate coordination remains since the peak is relatively broad. This change can be explained by the rearrangement and migration of the lake molecules during ageing. Based on this evidence, it can be assumed that the differences in coordination modes observed in pigments synthesized in different conditions will likely not play a role in the degradation, since the rearrangements of the structure will anyway tend to converge to a bidentate bridging coordination.
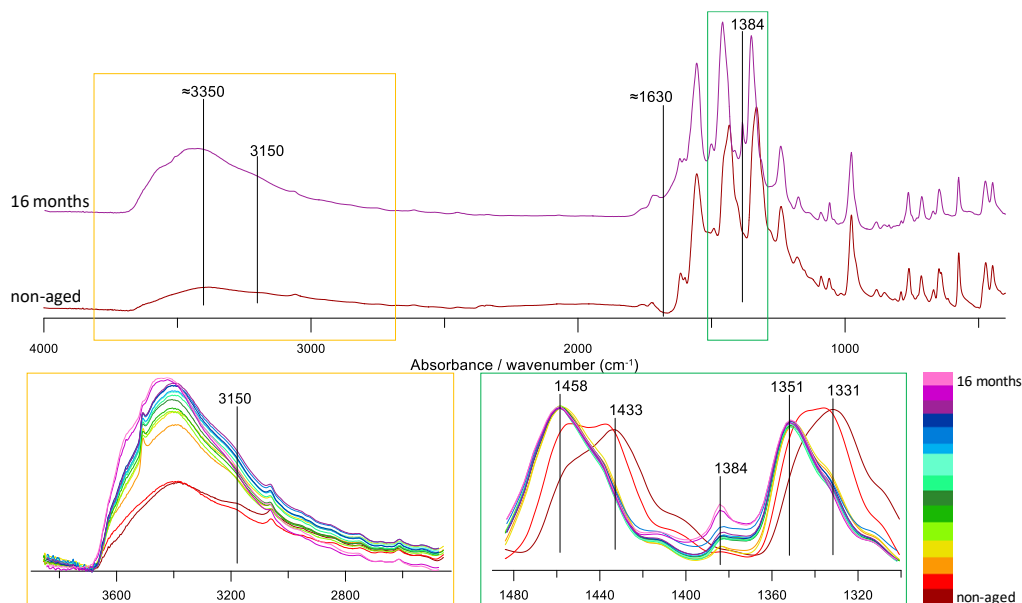
*Figure 5.13_Natural ageing of Pb1 exposed to light. Top: FTIR spectra of non-aged Pb1 compared to Pb1 aged for 16 months. Bottom: magnification of the spectral regions where the main changes were detected.*

In addition, the increase with ageing of the same bands previously associated with the ageing of eosin Y, implies that the degradation of the pigments is linked to the shared structure between the two molecules and, therefore, not to the bond with the metal ion nor to the quinoid structure. In particular, the increase in the bands at 3150 and 1384 cm$^{-1}$ could be assigned to the hydrolysis of the ether in the xanthene moiety, as previously suggested to explain the ageing of eosin Y. Although only preliminary, this seems like a plausible conclusion, since it is in agreement with results previously reported for the artificial ageing of Geranium lakes[307] and would also explain, due to the breakdown of the xanthene moiety (i.e. the chromophore), the well-known tendency to fade of this family of pigments.

The molecular changes observed for Pb1 during the natural ageing in a dark environment, as well as the changes in all the other synthesized Pb-lakes, are very similar. The degradation rates, on the contrary, differ significantly. This is clearly illustrated in Figure 5.14.

191
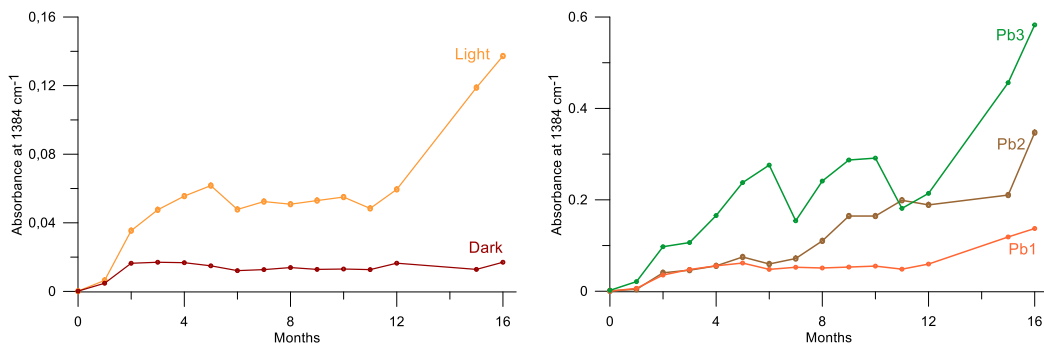
*Figure 5.14_Changes in the intensity of the band at 1384 cm$^{-1}$ during the ageing for different Pb lakes. Left: Pb1 in light (orange) and dark (red). Right: Pb1-3 in light.*

In the first place, the central role played by light on the degradation of Geranium lake pigments is confirmed. As shown in Figure 5.14 (left), in fact, the increase in the intensity of the band at 1384 cm$^{-1}$ is much slower in the dark also for the lake samples. This is in agreement with the hypothesis, advanced in the literature, of visible light causing the fading of Geranium lake pigments due to the break-down of the chromophore (i.e. the xanthene group).[307]

In addition, clear differences can be also noted in the light-induced degradation rates of Pb-lakes obtained with different synthesis protocols. This is shown in Figure 5.14 (right), where the increase in the intensity of the peak at 1384 cm$^{-1}$ appears much slower in Pb1 than in Pb2 and, especially, Pb3. Interestingly, this trend clearly reflects the amount of lead carbonate present as a by-product in the samples. The pigments showing the fastest degradation rates, in fact, are also the ones with a more evident contribution of Pb-carbonate in the initial FTIR spectrum (Figure 5.10). This evidence is extremely relevant for conservation purposes, since it suggests that the presence of Pb-carbonate by-products, strongly dependent on the synthesis conditions, could negatively affect the stability of Pb-based Geranium lake pigments.

The study of the ageing of Al-based Geranium lake pigments highlighted strong similarities with the Pb-lakes (Figure 5.15). In particular, although no changes in the coordination mode were detected in this case, the same increase in the bands at 3150 and 1384 cm$^{-1}$, previously tentatively linked to the breakdown of the xanthene moiety, was observed. Additionally, the increase of the water adsorption is also noticeable by the increase of the regions at 3350 and 1360 cm$^{-1}$.
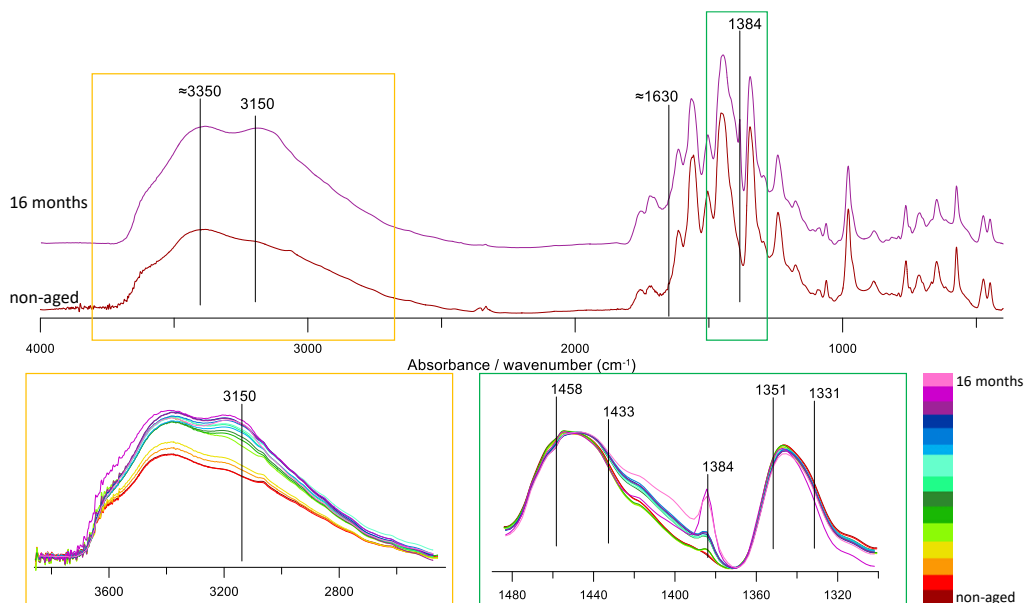
*Figure 5.15_Natural ageing of Al1 exposed to light. Top: FTIR spectra of non-aged Al1 compared to Al1 aged for 16 months. Bottom: magnification of the spectral regions where the main changes were detected.*

Furthermore, a certain influence of the synthesis method on the degradation rate was observed also in this case. In particular, Al1 showed a more significant increase in the intensity of the band at 1384 cm$^{-1}$ during ageing compared to Al2 (Figure 5.16). It should be remarked that the content of eosin Y is higher in Al1, meaning that this by-product of the synthesis might help to slow down the degradation rate of the pigment.
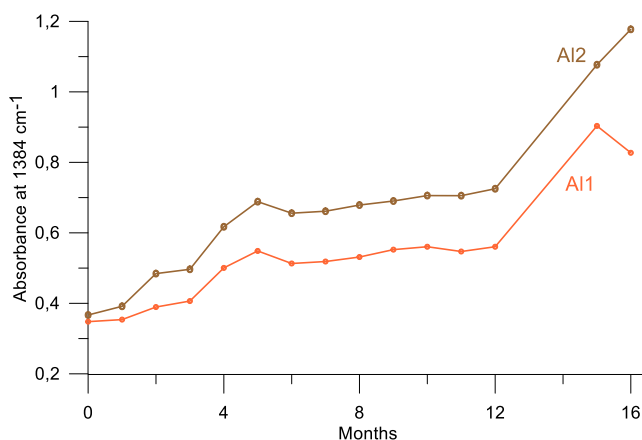


*Figure 5.16_Light-induced degradation of Al-lakes: increase in the intensity of the band at 1384 cm$^{-1}$ during ageing in light.*

193

### 5.6.4 Conclusions and future perspectives

In conclusion, these preliminary results clearly highlight the link existing between the synthesis protocols of Geranium lake pigments and their degradation kinetics. In particular, it was demonstrated that the amount of carbonate by-products in Pb-lakes and of non-complexed eosin Y in Al-lakes can affect the reactivity of the final products. On the other hand, the differences in the coordination mode observed in the synthesized Pb-lakes do not affect the degradation, since all the pigments considered tend to rearrange and converge to a bidentate bridging coordination during the first stages of the ageing. This evidence should raise awareness in the field on the capital importance of employing the same synthesis method(s) in order to ensure the inter comparability of degradation studies. Hopefully, a greater attention to this parameter will finally lead to an agreement in the literature on the degradation mechanism of these pigments in paintings.

Additionally, the presented results demonstrated the suitability of FTIR spectroscopy for the study of the degradation of Geranium lakes. Since previous studies focused on the accelerated ageing of these pigments by means of light, the next step will be to monitor also this type of degradation by means of FTIR, providing a more complete understanding of the pigments' reactivity. Furthermore, this work will be complemented by the study of the degradation of Geranium lakes in the presence of other painting materials, in order to obtain a full comprehension of their reactivity in historical paintings.

# 5.7 Preliminary insights into the solubility of Geranium lake pigments

The photo-reactivity of pigments in painting is often associated to the contact with moisture and electrolytes, e.g. due to the condensation of atmospheric moisture and solubilization of deposited PM or soluble by-products.[43,64,109] Even though the pigment particles are normally embedded in a protective binding medium film, in fact, small amounts of aqueous solutions can penetrate into the paint layers during their ageing (e.g. for siccative oils, due to the formation of cracks and the increase in the polarity of the medium.[64,352,353] Once in contact with the pigments particles, these electrolytic

solutions can catalyse redox reactions, triggering the degradation of the paint components.[258] Furthermore, the presence of moisture can also lead to the solubilization and migration of soluble species, whether intrinsic to the painting or products of degradation, through the paint layers.[354,355]

Geranium lake pigments are the product of a complexation and precipitation reaction taking place in an aqueous environment. In principle, when in contact with an aqueous solution, these complexes could be partially re-solubilized until reaching an equilibrium condition. This solubilization could influence the overall reactivity of the pigments and, in principle, cause their migration and/or favour the (photo)chemical reactions responsible for their fading in paintings. Moreover, the risk for contact with atmospheric moisture could be extremized by the hygroscopicity observed for the Geranium lake pigments during their natural ageing (Figure 5.13 and Figure 5.15). Nonetheless, in the literature no information is available on the behaviour of Geranium lakes in contact with water-based solutions.

For these reasons, in this last section of chapter 5 some preliminary tests on the solubility of these complexes are presented. The pigments were first suspended in a water based electrolytic solution for a period of 24 hours in the dark. The supernatant was then characterized by means of ATR-FTIR and UV-Vis absorption spectroscopy.

## 5.7.1   Materials and methods

The in-house synthesized Geranium lake samples Pb2 an Al2 (Table 5.2) were considered in these preliminary tests. Eosin Y in lactone form (Sigma Aldrich, ~99% purity, ref. E4009) and eosin Y disodium salt (Sigma Aldrich, ≥85 % ref. E6003) were also analyzed as reference compounds.

50 mg of the powdered pigments were mixed in the dark over a period of 24 hours with six different aqueous solutions: 1) distilled water; 2) distilled water with 0.1M NaCl; 3) 0.02M Na phosphate buffer (PBS) at pH 5.8; 4) 0.02M PBS at pH 7; 5) 0.02M PBS at pH 7 with 0.1M NaCl; 6) 0.02M Na borate buffer at pH 8. The resulting solution was then centrifuged and the supernatant separated, filtered (0.2 μm PTFE syringe filter) and analyzed.

The UV-Vis absorption spectra of the solutions were determined with an AvaSpec-ULS2048CL-EVO spectrometer. The spectral range 250-900 nm was considered and the spectra were collected with an integration time of 2 ms and averaged over 1000 acquisitions. The spectra were normalized based on the intensity of the absorption maximum in order to be qualitatively compared.

The solution FTIR spectra of the supernatant were collected with a spectrometer Bruker Alpha II equipped with a DTGS detector and a diamond ATR accessory. A total of 128 scans were accumulated in each sample, using a resolution of 4 $cm^{-1}$ and a wavenumber range from 4000 to 400 $cm^{-1}$. Given the large contribution of water and buffer solutions in the FTIR spectra of the samples (Figure 5.17), a blank spectrum was collected for all the water-based solutions considered and subtracted from the spectra of the corresponding samples. The background subtraction was performed with the software Omnic 9.2 (Thermo Fisher Scientific).
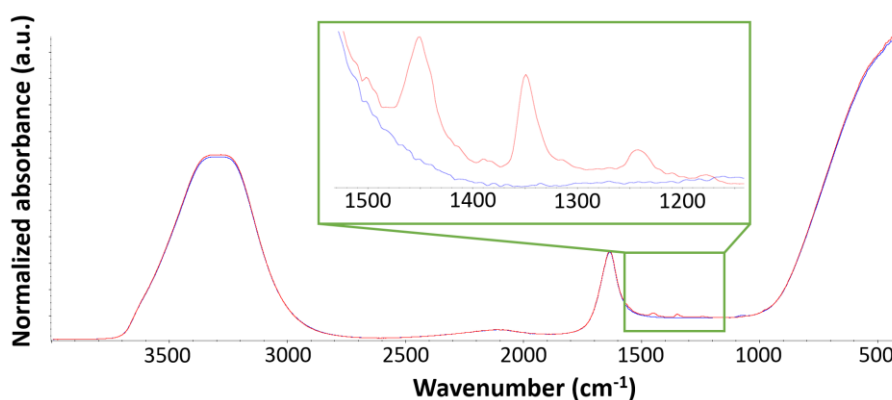


*Figure 5.17_Raw ATR-FTIR spectrum of the extract of the Al-lake sample in PBS at pH7: sample (red) and PBS background (blue). A magnification of the spectral region marked in green is displayed.*

### 5.7.2 Preliminary results

In the first place, the visual observation of the solutions after 24 hours of contact with the solid shows the clear presence of colored products in solution (Figure 5.18). Nonetheless, a large amount of solid remains present, suggesting that only a fraction of the pigment might be solubilized. The only exception is the eosin disodium reference salt, known to be readily soluble in aqueous solutions

For eosin Y (lactone) and the Geranium lake samples, it is interesting to notice how the color appears more intense in the electrolyte-containing solutions than in distilled water. This might suggest an influence of the ionic strength of the solution and/or the presence of buffering agents on the interaction with the pigments.
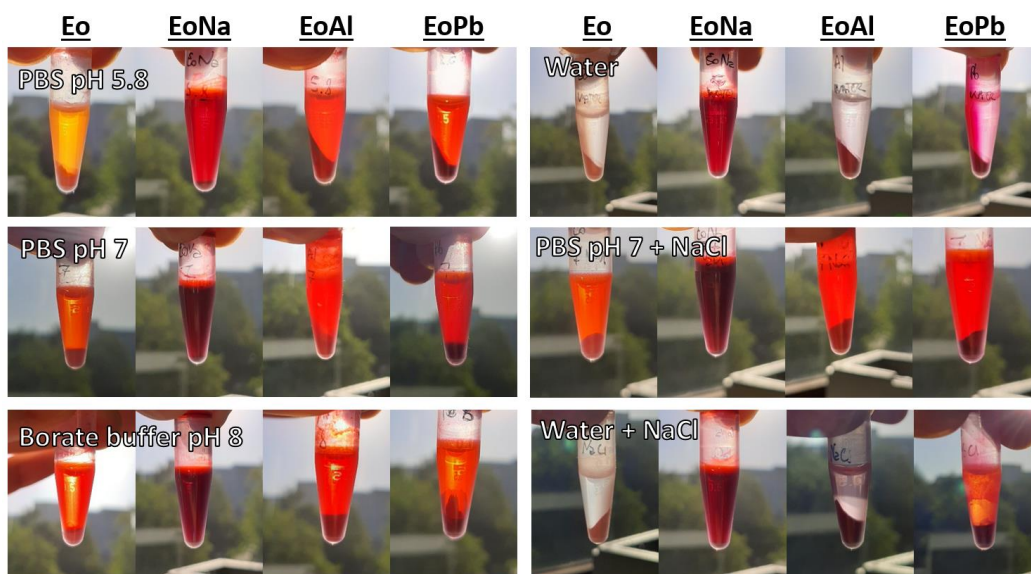


*Figure 5.18_Visual appearance of the samples after 24 hours of contact with different aqueous solutions: eosin Y (Eo), eosin disodium salt (EoNa), Al-lake (EoAl) and Pb-lake (EoPb).*

The nature of the products in solution was investigated by means of UV-Vis absorption and ATR-FTIR spectroscopies. Due to the low concentration of products in solution in distilled water, below the detection limit of the techniques, no further characterization could be performed on these samples.

The UV-Vis results (Figure 5.19) confirmed the presence of colored species in solution showing a major absorption band at ≈517 nm and a shoulder at ≈490 nm. These spectral features match the absorption spectrum of eosin Y in solution, with the main feature corresponding to the absorption of the chromophore, the substituted xanthene responsible for the red color, and the shoulder being ascribed to the dimerization of the dye in solution.[356] Remarkably, the same optical properties are observed for all the samples in a specific solution, which suggests a similar chemical nature for the solubilized products. This hypothesis was verified by means of ATR-FTIR spectroscopy analysis in solution.
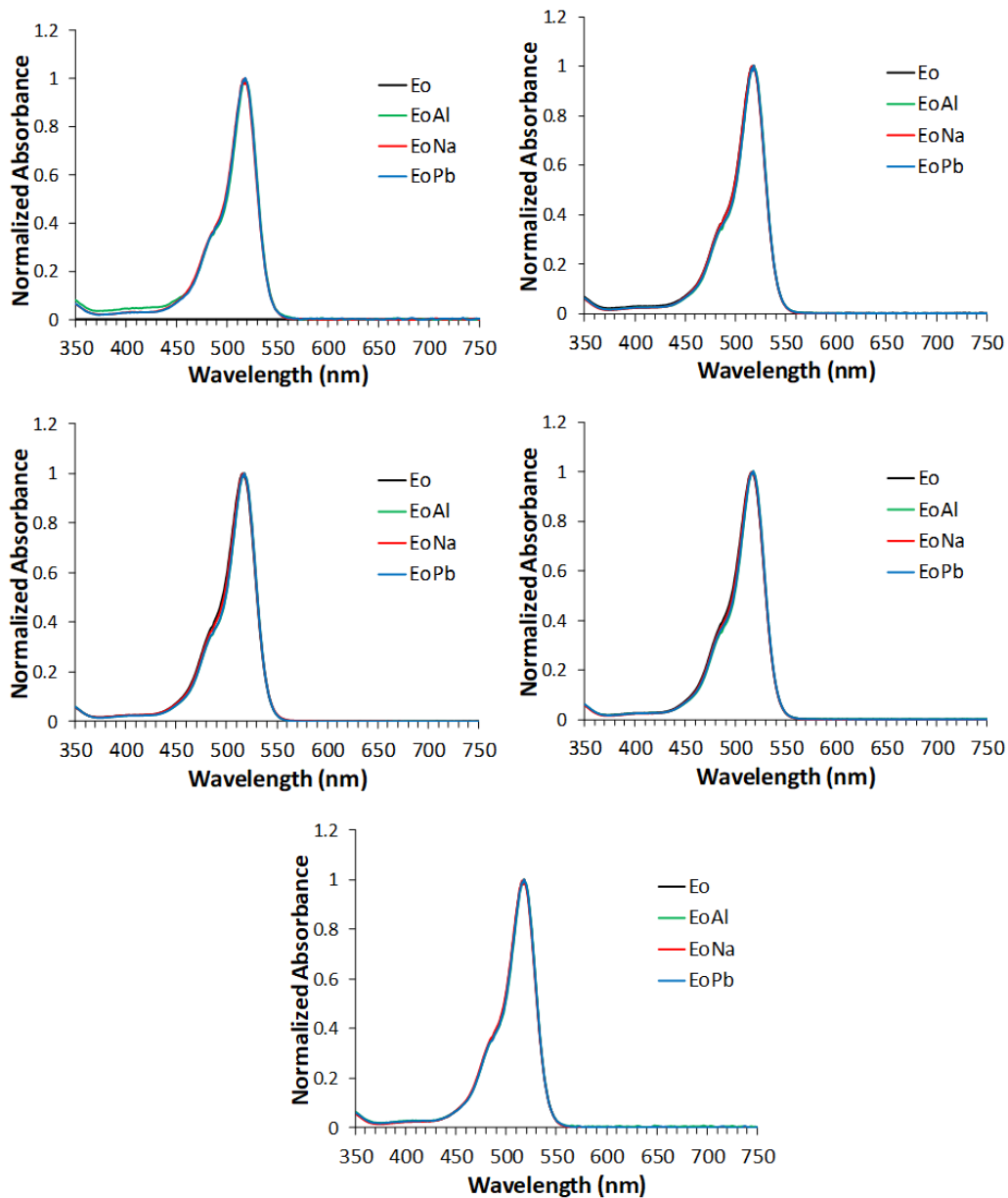
*Figure 5.19_Normalized UV-Vis absorption spectra of the soluble fraction of eosin Y (Eo), eosin disodium salt (EoNa), Al-lake (EoAl) and Pb-lake (EoPb) in a) 0.1M NaCl, b) PBS pH5.8, c) PBS pH7, d) PBS pH7 + 0.1M NaCl, e) borate buffer pH8.*

The results, shown in Figure 5.20, confirmed the similarity of these species also from a molecular point of view. The region of the spectrum between 1600 and 1200 cm$^{-1}$ is

considered in particular, due to the lower contribution of the medium and the presence of intense peaks from the species in solution (Figure 5.17).
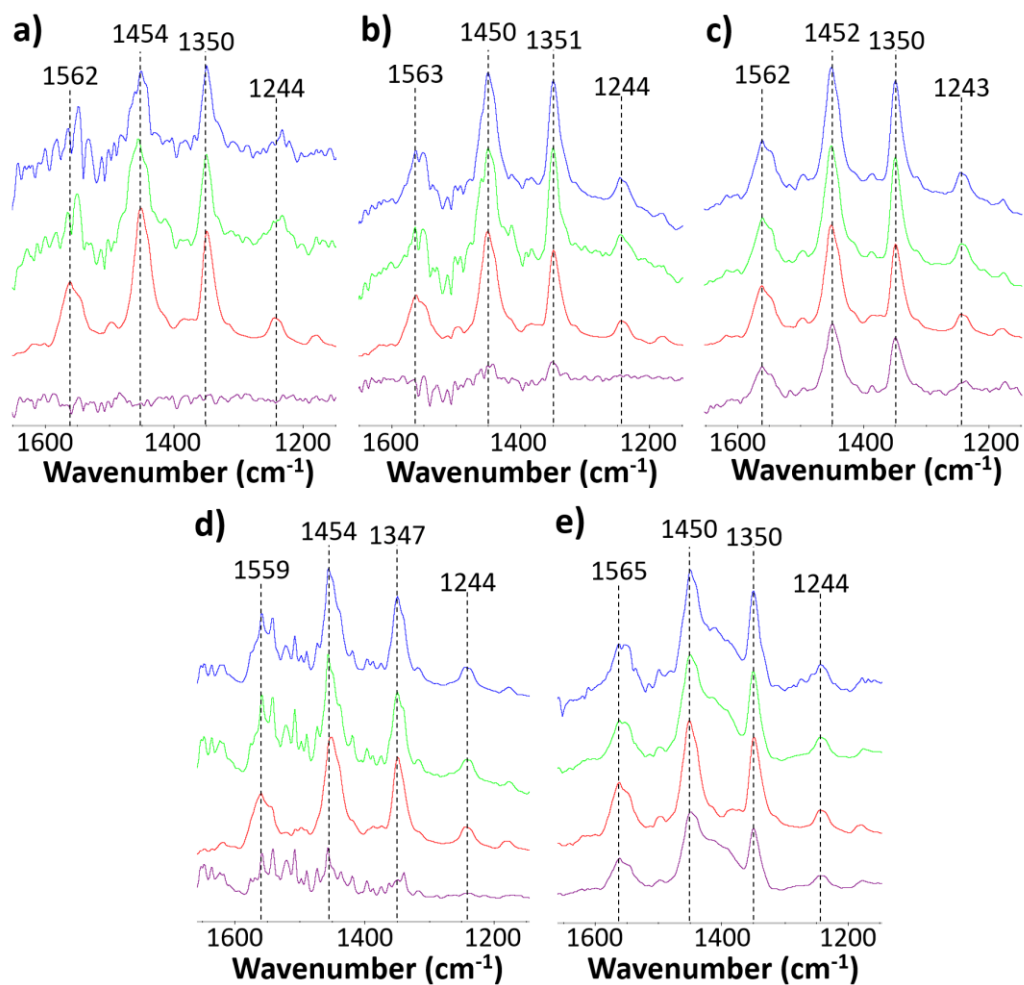


*Figure 5.18_Background subtracted ATR-FTIR absorption spectra of the soluble fraction of eosin Y (purple), eosin disodium salt (red), Al-lake (green) and Pb-lake (blue) in a) 0.1M NaCl, b) PBS pH5.8, c) PBS pH7, d) PBS pH7 + 0.1M NaCl, e) borate buffer pH8.*

In this range, four main characteristic features are observed in the FTIR spectra collected (Figure 5.20), namely at ≈1560, ≈1450, ≈1350 and ≈1244 cm$^{-1}$. Since these features are clearly present in the spectrum of solubilized eosin disodium salt, known to be ionic in nature and to dissociate into eosin Y dianion and Na$^+$ cations in water, and based on the

thorough interpretation of the FTIR spectra of eosin Y-based compounds presented in the first part of this chapter, these vibrations are traced to the presence of deprotonated eosin Y in solution (dianion). In particular, these features are assigned to asymmetric ($\approx$1560 cm$^{-1}$) and symmetric ($\approx$1450 cm$^{-1}$) C=O stretching of the deprotonated carboxylate, to the stretching of the ketone interconverted with the deprotonated hydroxyl from the xanthene group (phenoxide ion) ($\approx$1350 cm$^{-1}$) and to the C-O-C stretching of the ether group in the xanthene ($\approx$1244 cm$^{-1}$). In the first part of this chapter, the position of the peaks at 1450 and 1350 cm$^{-1}$ has been shown to be strongly dependent on the environment of the carboxylic group and the phenoxide ion, and in particular on the presence of metal ions interacting with these groups. The fact that no significant change in the position of these peaks is observed for different samples (i.e. different metals) in the same aqueous conditions, strongly supports the full dissociation of the metal complexes in solution into eosin Y dianion and metal cations. The shoulder observed at $\approx$1400 cm$^{-1}$ in the spectra recorded in borate buffer at pH 8 (Figure 5.20e) is due to a residual contribution of the buffer (Figure S5.10). The small signals observed in general for eosin Y are related to the low solubility of the lactone form in water (as already shown in the first part of Chapter 5).

### 5.7.3   Conclusions and future perspectives

In conclusion, the preliminary tests conducted in this final section of the chapter allowed to obtain some first relevant insights into the solubility of Geranium lake pigments.
In detail, the results showed how Pb- and Al-based complexes of eosin Y can dissociate when in contact with aqueous electrolyte solutions. The formation of dianionic eosin Y, confirmed by UV-Vis and ATR-FTIR spectroscopies by comparison with reference compounds, is particularly relevant. The deprotonated eosin Y, in fact, is a well-known photosensitizer and it is easily photo-oxidized in aerated aqueous solutions.[356–358] Its possible formation due to the contact between moisture and pigment particles in paintings, therefore, could in principle be linked to the poor photostability of Geranium lakes. Furthermore, the solubilization and migration of eosin Y dianion in the paint layers could lead to further interactions between these and other species in the paintings, ultimately resulting in an increased instability. For example, such a process could play a role in the enchanced fadeing observed for eosin-based pigments when mixed with semiconductors in paintings (e.g. due to migration, adsorption on the surface and interaction with the semiconducting particles).[306,334]

In order to obtain a clearer picture of the factors influencing the solubility of Geranium lake pigments, further studies will be performed. In particular, the effect played by the nature of the electrolyte on the solubility of the eosin Y-complexes will have to be thoroughly investigated. Quantitative solubility studies for Geranium lake pigments obtained with different synthesis methods will also be performed, with the final aim of investigating a possible link between the solubility and the differences in the ageing kinetics observed for these species.

## 5.8  Supplementary information
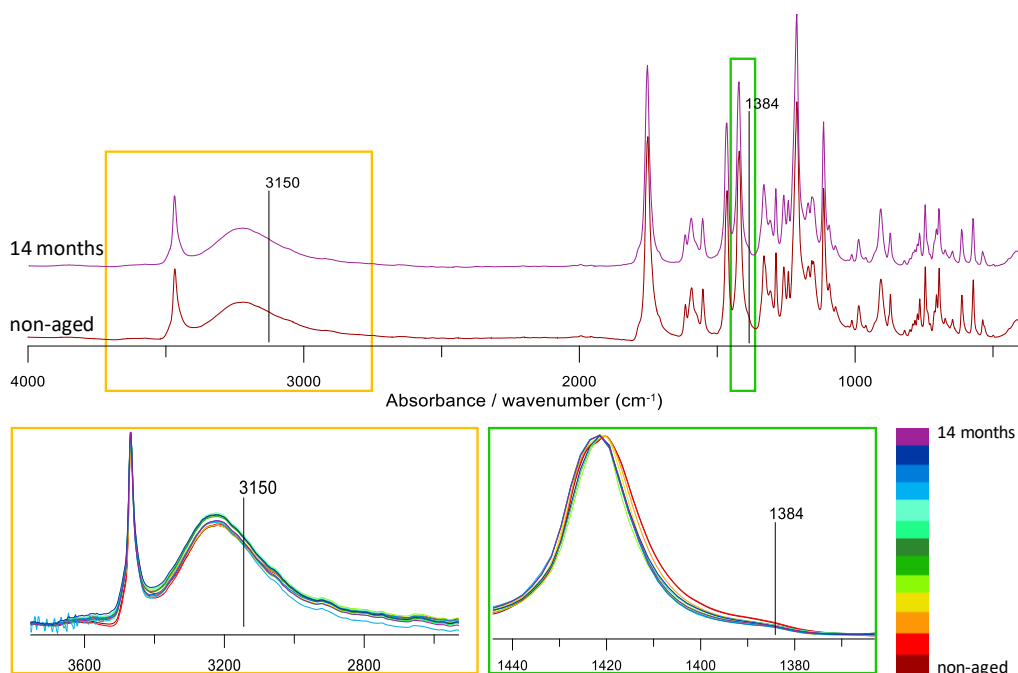


*Figure S5.9_Natural ageing of eosin Y in a dark environment. Top: FTIR spectra of non-aged aged eosin Y compared to eosin Y aged for 14 months. Bottom: magnification of the spectral regions where the main changes were detected.*
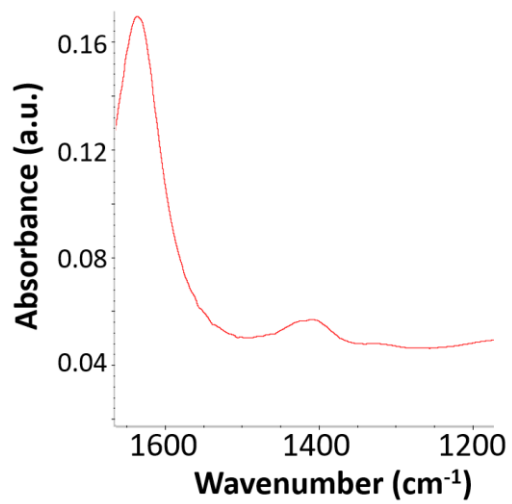
*Figure S5.10_ATR-FTIR spectrum of the region of interest for 0.02M borate buffer at pH8. A peak is visible at 1409 cm$^{-1}$.*

# |6

High-resolution analysis of historical paintings by means of optical-photothermal infrared (O-PTIR) spectroscopy: identification of micrometric organic particles in *L'Arlésienne (portrait of Madame Ginoux)* by Van Gogh

**V. Beltran\*, A. Marchetti\*, G. Nuyts, M. Leeuwestein, C. Sandt, F. Borondics, K. De Wael**

**\* Contributed equally**

# Abstract

One of the most challenging aspects of the analysis of Geranium lake pigments is their identification in paint samples. Their detection is, in fact, often complicated by the poor conservation state of these pigments in paintings and by the fact that they were often employed in very small amounts in the first place, due to their extremely intense color. For these reasons, micrometric red particles are often all that remains in Geranium lake-containing paintings. This poses extreme analytical challenges, in particular when it comes to the molecular characterization of such particles in heterogenous and microscopic paint samples.

In this chapter, the potential of the recently developed optical photo-thermal IR (O-PTIR) spectroscopy to overcome these challenges and achieve the non-contact sub-micron molecular imaging of a paint microsample is tested. Based also on the promising results obtained with this technique on glass and metal samples in chapter 3, a fragment from Van Gogh's painting *L'Arlésienne (portrait of Madame Ginoux)* is analyzed, in an attempt to chemically characterize a series of micrometric red organic particles found in the paint layers. The striking results obtained on this very small and challenging fragment, including the detection of Geranium lakes in the paint layers, failed with other state-of-the-art techniques (SR-μ-FTIR and μ-Raman spectroscopy), clearly highlight the great potential of this method for heritage applications. Moreover, although no sample preparation is inherently necessary for O-PTIR, the technique proved highly efficient for the analysis of thin sections of embedded painting fragments. The suitability of this sample preparation for O-PTIR analysis underlines the compatibility of this technique with other commonly employed high-resolution characterization methods, hence opening to the possibility of a full integration of O-PTIR in multitechnique studies of cultural heritage objects.

# 6.1  Introduction

The composition of cultural heritage objects tends to be highly heterogeneous. In addition to the main compounds, there are often materials present in a very low proportion which can be either intrinsic to the artworks[359–362] or that can be traced back to the ageing of the object.[363,364]

These minor components are often detected in samples from cultural heritage objects in the form of micrometric particles, sometimes <10 μm. Such particles can be related to the physical properties of the object (such as the color of specific regions)[364–366] or to specific degradation processes (such as the migration and aggregation of molecules).[54,105] The characterization of these species is therefore a fundamental requirement in order to understand the composition and physical properties of the object and/or to decipher possible degradation reactions, helping to find the appropriate conservation treatments to avoid bigger damages.

Unfortunately, the identification of these micrometric particles can be extremely complex due to I) the wide diversity of materials present in the sample, including organic and inorganic materials with low and high molecular weight, II) the low proportion of particles compared to other materials of the painting and III) the limited amount of sample available for the analysis. Previous studies have shown the potential of high-resolution techniques such as X-rays based methods to characterize inorganic particles.[367,368] Nonetheless, there are still open questions regarding the most suitable method for the discrimination of the organic ones. For this purpose, former research applied micro Fourier Transform Infrared (μ-FTIR) spectroscopy and μ-Raman spectroscopy, that provide information on the molecular structure as well as the spatial distribution of the compounds. However, the resolution of μ–FTIR spectroscopy is low: the minimum size achievable is restricted by the diffraction limit to 5-10 $\mu m^2$ depending on the wavelength, consequently the bands of the spectral markers of the particles are often too low to be unequivocally detected.[369] On the other hand, Raman spectroscopy can reach a higher resolution (≥2 $\mu m^2$), but it is often limited by the presence of fluorescence and the potential damage that might be caused on sensitive materials.[370–372] Lately, photothermal induced resonance (PTIR) has been applied to the analysis of paintings[105,106]: this technique uses an atomic force microscope (AFM) coupled to infrared spectroscopy providing a resolution up to 20 nm (size of the cantilever), which has been proved to successfully characterize organic materials in painting samples.[105,106]

However, this technique requires a continuous contact between the cantilever and the sample surface. In the case of painting fragments, this requirement is problematic due to brittleness of the materials: on one hand, during the handling of the samples small particles are often detached, these crumbles can remain on the surface disturbing the path of the cantilever and producing interferences in the collected data. On the other hand, the crumbliness of the materials makes it difficult to have a totally flat surface, with imperfections (detached particles, cracks or protrusions) that can alter the path of the cantilever and may lead to the damage of the thin section or the cantilever tip.

In this chapter, we investigate for the first time the potential of optical-photothermal infrared (O-PTIR) spectroscopy for the analysis of micrometric organic particles in historical paintings. O-PTIR is a recently developed technique based on the thermal expansion of the sample induced by the irradiation with an IR laser, which is then measured using a visible probe laser. Thus, the spatial resolution is determined by the dimension of the visible laser, overcoming the diffraction limit that defines the resolution achievable by traditional FTIR spectroscopy. Besides its high resolution, typically well below 1 μm, O-PTIR measurements do not require a contact with the sample, avoiding the interferences with the detached particles or potential damages to the analyzed fragment. Moreover, the collected spectra are comparable to transmission FTIR measurements, allowing the comparison between the collected data and the extensive literature on FTIR spectroscopy applied to cultural heritage materials.[104,373,374] The technique was applied, in particular, to the identification of some micrometric red particles (≤2 μm diameter, Figure 6.1) observed in the paint layers of the painting *L'Arlésienne (portrait of Madame Ginoux)* by Vincent Van Gogh (Figure 1.10). The results obtained demonstrate the potential of O-PTIR for the molecular characterization of small painting fragments and the identification of micrometric organic particles. With the suitable sample preparation, in fact, O-PTIR provided high-resolution data on the particles and the painting stratigraphy in a non-destructive manner. Based on these results, it is therefore demonstrated that O-PTIR is a powerful technique that can be efficiently integrated in multitechnique studies, thus helping to complement and extend the information provided by other analytical methods.

## 6.2  Materials and methods

### 6.2.1   Sample preparation

The sample was extracted from the Vincent van Gogh's *painting L'Arlésienne (portrait of Madame Ginoux)* (February 1890, oil on canvas, Kröller-Müller Museum [KM 110.202/F541]), from a region where a pink colour could be observed. The fragments were embedded in epoxy resin (Resineco, ref TR KIT). Thin sections of 2 µm thickness were cut with a ultramicrotome Leica EM UC6 equipped with a diamond knife Diatome Histo at 45° (Leica, HI 7177). The thin sections were then deposited on pellets made with KBr (Sigma Aldrich, 221864-M FT-IR grade).

### 6.2.2   O-PTIR

O-PTIR measurements (spectra and images) were collected on the mIRage Infrared Microscope (Photothermal Spectroscopy Corp.). Spectra were collected in reflection mode, 2 cm$^{-1}$ spectral data point spacing, through a 40x, 0.78 NA, 8 mm working distance Schwarzschild objective. The pump IR source was a pulsed, tunable four-stage QCL device, scanning from 800 to 1900 cm$^{-1}$. The probe was a CW 532 nm visible variable power laser. To obtain a good signal-to-noise ratio to interpret the spectral difference, 20 scans spectra were averaged at each point. The maps shown in Figure 6.2 were obtained with a spatial resolution of 450x450 nm$^2$.

### 6.2.3   SEM-EDX

The samples were examined with a Field Emission Gun – Environmental Scanning Electron Microscope (FEG-ESEM) equipped with an Energy Dispersive X-Ray (EDX) detector (FEI Quanta 250, USA; at AXES and EMAT research groups, University of Antwerp), using an accelerating voltage of 20kV, a take-off angle of 30°, a working distance of 10 mm and a sample chamber pressure of $10^{-4}$ Pa. Imaging was performed based upon secondary electrons (SE) and back-scattered electrons (BSE). Elemental maps with a pixel size of 0.2 µm and a dwell time of 2.25 ms/pixel were collected using a beam current of ~0.5 nA. In order to remove the contribution of the underlying KBr pellet, EDX spectra were also recorded using an accelerating voltage of 10kV. Spectra

were acquired, using a beam current of ~0.5 nA and a dwell time of 60 s per spectrum.  A spectrum of the resin was recorded to prove that there is no contribution of the pellet.

## 6.2.4   SR-μ-FTIR

SR-μ-FTIR measurements were performed in SMIS beamline at Synchrotron Soleil (France) using a Thermo Fischer NEXUS FTIR spectrometer Nicolet 5700 attached to a microscope Continuum XL. Samples were analysed in transmission mode accumulating 256 scans at 4 cm$^{-1}$ spectral resolution, the wavenumber range is between 4000 to 800 cm$^{-1}$. Maps were collected with an aperture of 10x10 μm$^2$ and a step of 5 μm.

## 6.2.5   SR-μ-FTIR and O-PTIR data treatment

SR-μ-FTIR and O-PTIR data were treated using the Quasar 1.0.0 software.[209,210] The spectra shown in Figure 6.2, Figure 6.4, Figure 6.5 and Figure 6.7 have been normalized by the min-max method using the most intense band. To ensure a fair comparison, no smoothing, baseline correction or any other adjustment have been applied to the spectra. Spectral maps were generated by plotting the integrated area of selected peaks with a linear baseline computed using two wavenumbers at the feet of the peak.

## 6.2.6   μ-Raman spectroscopy

Raman spectroscopy measurements were performed by means of a Xplora Plus Microscope (Horiba) with a 100mW 785 nm laser, considering the effective range of 150-1000 cm$^{-1}$. At each point, five accumulations were collected during 10 seconds each one. The spectra presented have not been corrected in order to avoid any kind of distortion.

## 6.2.7   OM

Optical Microscopy (OM) of thin sections has been performed with a microscope Nikon Eclipse LV100 in dark field mode.

# 6.3 Results and discussion

## 6.3.1 Potential of O-PTIR for the stratigraphic characterization of historical paintings

The sample selected for these experiments comes from the historical painting *L'Arlésienne (portrait of Madame Ginoux)* by Van Gogh (Figure 1.10). Due to the high historical and artistic value of this painting, the extracted fragment is very small, ≈200x200x25 µm³ (Figure 6.1, top). As it can be seen in the thin section displayed on Figure 6.1 (bottom), the stratigraphy consists of a bottom layer with the canvas fibers (≈10-20 µm thickness), a thin white ground layer (≈10 µm thickness) and finally a thin top paint layer with red particles (≈10 µm thickness). The presence of such thin layers, already noticed in other works from the same painter,[17,375] poses great challenges for the characterization of the stratigraphy.
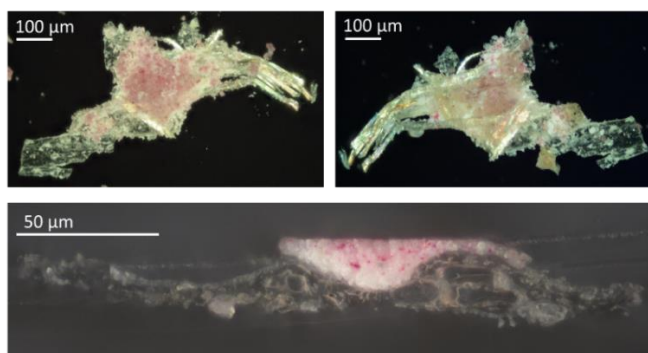


*Figure 6.1_Fragment of Van Gogh L'Arlésienne (portrait of Madame Ginoux) selected for the analysis. Top: fragment before embedding (front and back). Bottom: thin section of the embedded fragment.*

In order to verify the potential of O-PTIR for the analysis of paint fragments, it is essential to compare it with existing and established methods. In this case, the samples have been analyzed by µ-FTIR spectroscopy coupled to Synchrotron Radiation (SR-µ-FTIR spectroscopy): this technique provides a high resolution with a high signal-to-noise ratio and, for these reasons, it is widely employed for the molecular characterization of thin paint layers.[376,377] The SR-µ-FTIR spectroscopy measurements have been performed in transmission mode, which provides the best spectral resolution, with a straight baseline and a reduced possible influence of spectral artifacts. The obtained results have been compared to O-PTIR, in order to verify the potential and the possible constraints of this

technique. The same thin section was analyzed with both methods, in order to ensure the comparability of the datasets (Figure 6.2).
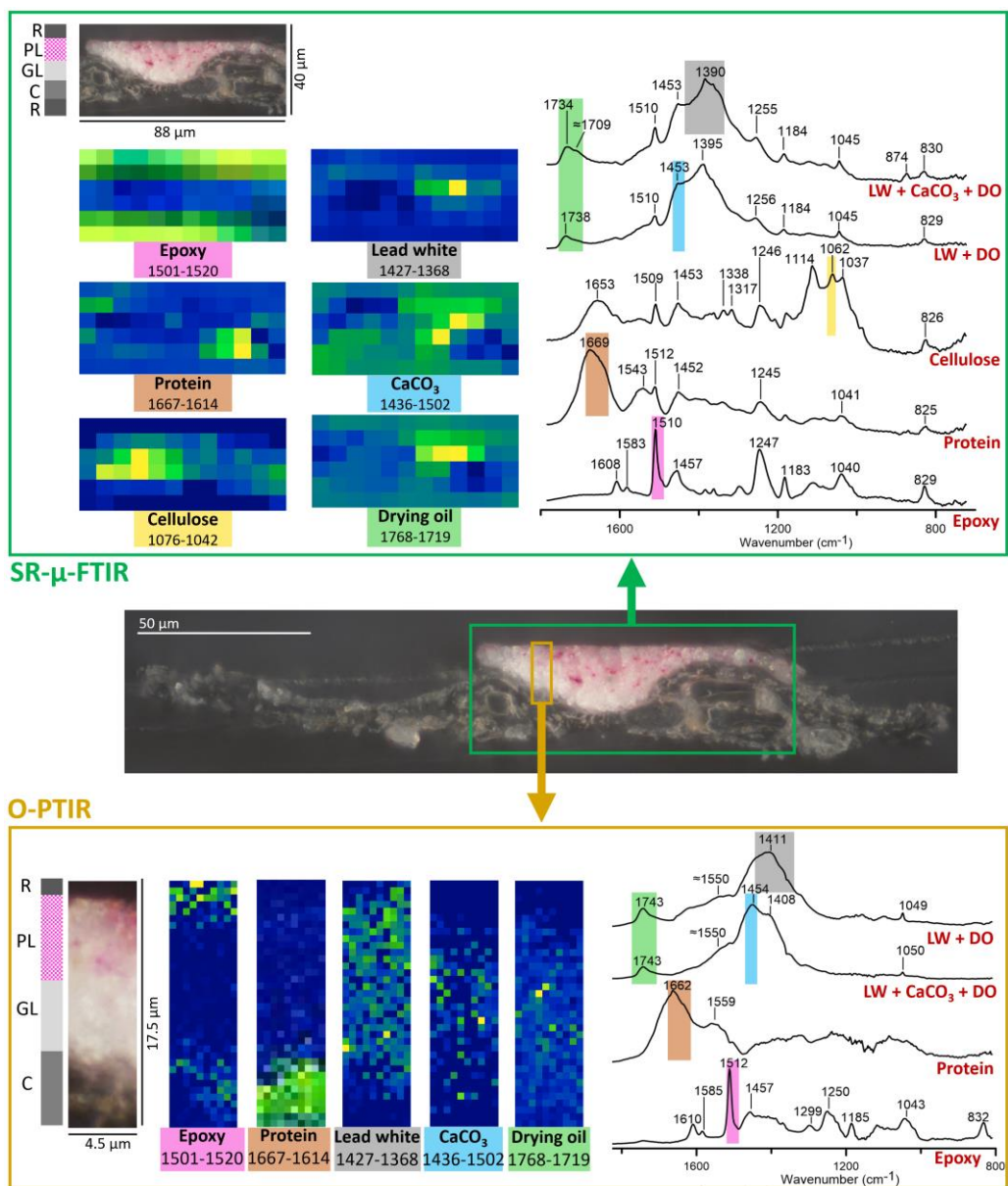


*Figure 6.2_Analysis of the stratigraphy by SR-μ-FTIR and O-PTIR. Top: SR-μ-FTIR results of the area marked in green in the analyzed thin section displayed in the middle. Bottom: O-PTIR results of the area marked in yellow in the analyzed thin section. In each analyzed area a scheme of the stratigraphy is displayed (C: canvas, GL: ground layer, PL: paint layer, R: embedding resin) as well as the integration maps of the spectral regions corresponding to the specific compounds found in the sample and a representative spectrum of each material (LW: lead white, DO: drying oil).*

The results obtained by SR-μ-FTIR spectroscopy are displayed in Figure 6.2 (top). Overall, the spectra are characterized by the high spectral quality (high signal to noise ratio and straight baseline) typical of SR-μ-FTIR. Among the collected data, five main types of spectra have been distinguished (Figure 6.2, top right corner, the full range of the spectra is displayed in Figure S6.1). The main pigment identified is lead white ($2PbCO_3 \cdot Pb(OH)_2$ / $PbCO_3$), whose markers can be seen at ≈1390 and 1045 cm$^{-1}$ (asymmetric and symmetric C-O stretching vibrations of $CO_3^{2-}$ anions respectively[344]). Additionally, there are smaller amounts of $CaCO_3$, which is detected by the shoulder at 1453 and the small band at 874 cm$^{-1}$ (C-O stretching and bending of the $CO_3^{2-}$ anions respectively[378]). The band at ≈1734 cm$^{-1}$ is probably associated to the presence of a drying oil, which was most likely used as a binder. In some regions, this band shows a shoulder at ≈1709 cm$^{-1}$ corresponding to the hydrolysis of the esters from the drying oil, which is a degradation reaction linked to its ageing. The presence of Pb and Ca has been confirmed by SEM-EDX, agreeing with the identification of lead white and $CaCO_3$ (Figure 6.3). These painting materials have been previously identified in other paintings by the same artist.[23,302,379,380]
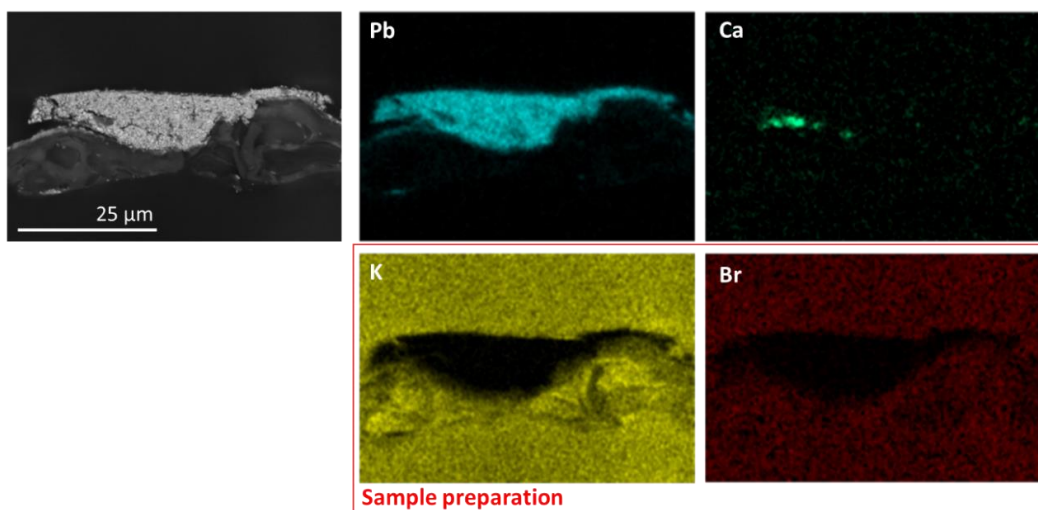


*Figure 6.3_SEM-EDX analysis of the thin section displayed in Figure 6.2. Left: BSE image. Right: elemental distribution maps. The elements marked in red are related to the KBr pellet where the sample is deposited.*

In addition, some spectra correspond to the presence of a protein (bands at ≈1660 and 1543 cm$^{-1}$, related to amide I and amide II respectively[381]) and cellulose (bands at 1114, 1062 and 1037 cm$^{-1}$, related to the C-O bending of the skeletal vibration of carbohydrates rings, HCHOH deformation and the skeletal vibration of the carbohydrate rings[382]). These

compounds are related to the support of the painting, in this case a canvas coated with a sizing,[383] with the cellulose being linked to the textile fibers and the protein to the animal glue used as an adhesive. Finally, the spectra of the epoxy resin used to embed the sample can also be discriminated. It should be mentioned that the most intense bands (1512 cm$^{-1}$ related to the C=C stretching of the aromatic groups and at 1247 cm$^{-1}$ related to the C-O deformation[384]) are also noticeable in the other displayed SR-μ-FTIR spectra: this is probably explained by the infiltration of the embedding resin into the sample during its preparation.

Compared to SR-μ-FTIR, the spectra collected by O-PTIR (Figure 6.2, bottom right corner) display similar spectral features, allowing to discriminate most of the compounds previously mentioned. No band shifts are observed between both techniques and the relative intensities of the bands are similar: this can be clearly seen in the spectra of the epoxy resin, which is the only homogeneous compound (the fluctuations in the other spectra may be explained by the different composition of the precise analyzed spot).

Furthermore, O-PTIR spectra do not always show the bands related to the embedding medium, contrarily to SR-μ-FTIR. Since the analyzed thin section is the same in both techniques, this difference is probably explained by the size of the analyzed area in each technique. The spot size of SR-μ-FTIR is large compared to the size of the sample, consequently the analyzed areas usually include regions outside the paint fragment, where there is only embedding medium, or regions close to the edge of the sample, where the embedding medium has infiltrated. Hence, the bands of epoxy resin appear in all the collected spectra. In an opposite fashion, the smaller spot size of O-PTIR allows to select areas far away from the edge of the sample, providing spectra not overlapped with the epoxy bands.

The lack of the epoxy bands in the spectra helps to avoid their overlapping with the signal from other compounds, preventing the loss of spectral features and potentially allowing a more efficient discrimination of the different components. Consequently, the O-PTIR data are extremely useful for the analysis of highly heterogeneous samples, often the case for painting cross sections. Indeed, a shoulder at ≈1550 cm$^{-1}$ is noticeable in the O-PTIR spectra, probably related to the presence of metal carboxylates.[54] In the SR-μ-FTIR data, this shoulder is overlapped with the band at ≈1510 cm$^{-1}$ from epoxy resin, therefore the presence of metal carboxylates is less obvious.

The spectral markers of the identified compounds were integrated in order to obtain the spatial distribution of each substance (Figure 6.2, top and bottom left corners), the position of the displayed spectra in the integration maps is shown in Figure S6.2. Due to the lower resolution, SR-μ-FTIR maps are much less detailed, providing only the main distribution of the compounds: epoxy resin around the sample, protein and cellulose at the bottom of the stratigraphy and $CaCO_3$, lead white and drying oil in the ground and paint layers. On the contrary, the maps calculated from O-PTIR spectra allowed to distinguish also the variations of the composition across the thin layers of the stratigraphy: the ground layer is composed mainly of drying oil and lead white, while the paint layer contains drying oil, lead white and $CaCO_3$. Specifically, $CaCO_3$ is distributed mainly in the middle of the stratigraphy. This distribution is in agreement with the results obtained by SEM-EDX (Figure 6.3).

A consequence of the higher resolution of O-PTIR is the length of the measurements. Since the number of acquired spectra is larger, the required time for the analysis is much longer. In this case, the area analyzed by SR-μ-FTIR spectroscopy is 88x40 $\mu m^2$ (Figure 6.2, top) and took ≈3 hours, while the area analyzed by O-PTIR is 4.5x17.5 $\mu m^2$ (Figure 6.2, bottom) and took ≈10 hours. The slower data collection implies that the maps should be smaller and, hence, less representative. In this case, for instance, cellulose was not detected by O-PTIR. In addition, it should be remarked that the signal-to-noise ratio is slightly lower in O-PTIR compared to SR-μ-FTIR. In the higher range of the O-PTIR spectra the noise level is still low, although subtle features such as the shoulder at ≈1710 $cm^{-1}$ related to the degradation of the drying oil cannot be appreciated. However, the noise is more evident at lower wavenumbers: for instance, the band at 874 $cm^{-1}$ related to $CaCO_3$ cannot be distinguished in O-PTIR. Consequently, the highest potential of O-PTIR is achieved when this technique is implemented in a multianalytical approach, complementing its high resolution with faster or more sensitive techniques.

In conclusion, these results confirm the suitability of O-PTIR for the high-resolution analysis of the stratigraphy of historical paintings. The obtained spectra are comparable to the ones obtained by SR-μ-FTIR allowing to identify the same type of compounds. Despite the lower signal-to noise ration of O-PTIR compared to SR-μ-FTIR, the smaller spot size provides spectra which are less overlapped, helping to better discriminate the compounds present in the sample. This higher spatial resolution offers accurate information on the distribution of materials, helping to better characterize the techniques used to produce the painting as well as its conservation state. It is clear that

such information can have great relevance for the analysis and conservation of historical paintings.

Moreover, the results also demonstrated the great advantages of the preparation of thin sections for the analysis by O-PTIR. Although such a thin sample is not necessary for O-PTIR (technically, no sample preparation is needed), the preparation of thin sections allows the compatibility of the obtained dataset with other complementary techniques, such as transmission SR-μ-FTIR spectroscopy and SEM-EDX, but also Raman spectroscopy or SR-μ-XRD,[384,385] meaning that these techniques are fully compatible and can be implemented in the same multi-analytical approach.

### 6.3.2 Application of O-PTIR for the identification of micrometric Geranium lake particles

In the paint layer of the sample, small red particles of ≤2 μm diameter can also be observed (Figure 6.1). Their characterization is extremely relevant, since it can provide information on the source of the pink color of the sampled area of the painting. However, the analysis of these particles is challenging due to their small size and the presence of additional compounds in the same layer.

Indeed, the analysis by SR-μ-FTIR spectroscopy (Figure 6.2) did not provide any spectral marker that may be related to this pigment, most probably due to the low spatial resolution of the technique. The size of the particles is in fact very small in comparison to the size of the analyzed spot, so the spectral markers are hidden below the spectra of the main compounds, whose bands cover broad spectral regions. Consequently, there are no noticeable bands that could be attributed to the material used as a red pigment.

In order to improve the resolution, μ-Raman spectroscopy was also tested (Figure 6.4). The spectra collected around one of the red particles show the characteristic bands from lead white at 1048 and 104 cm$^{-1}$ as well as a group of bands around ≈200 cm$^{-1}$ probably related to the degradation products resulting from lead white.[386] Moreover, a group of low-intensity bands can be seen at ≈1430, ≈1307 and ≈1249 cm$^{-1}$ (Figure 6.4, bands marked in red). These bands are in a spectral region where some of the main signals of Geranium lake pigments appear, as it can be seen in the reference spectrum (Figure 6.4, spectrum in red), meaning that the presence of these pigments is compatible with the

216

results. However, the bands are low, broad and the maximums are slightly shifted compared to the reference. Moreover, in the same region the signals of other lake pigments employed by the same artist could be also present, such as cochineal.[17,302,387] Therefore, the identification of the type of red pigment cannot be unambiguously concluded based on these experimental results.
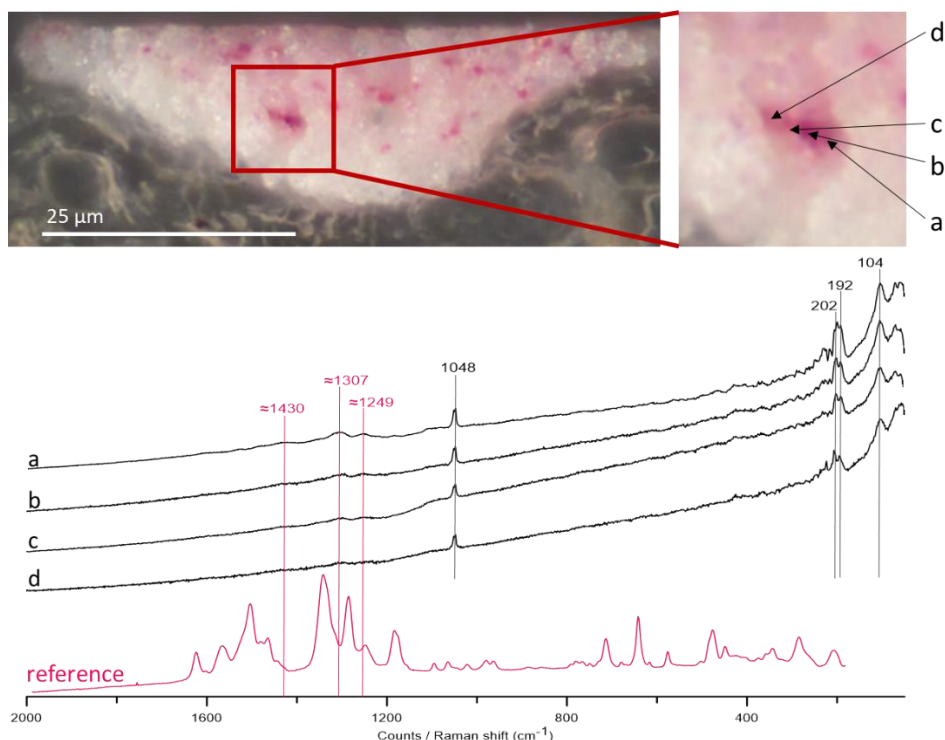


*Figure 6.4_Characterization of a red particle by μ-Raman spectroscopy. Top: particle selected for the analysis (left) and its magnification with the analyzed points in evidence, a-d (right). Bottom: Raman spectra collected at each point compared to a reference of freshly synthesized Geranium lake (red line, synthesis conditions described in Chapter 5 part 1, Figure 5.6, sample III). The peaks marked in red are presumably associated to Geranium lakes.*

Interestingly, the application of O-PTIR made it possible to overcome the limitations previously encountered with both SR-μ-FTIR and μ-Raman spectroscopies. This novel technique, in fact, allowed to unequivocally identify the red particles in exam as a type of Geranium lake pigment (Figure 6.5). The collected spectra (Figure 6.5, spectra in black) clearly show a good match with a reference spectrum obtained with the same technique (Figure 6.5, spectrum in red) for a Geranium lake reference pigment (Pb-lake, synthesis conditions described in Chapter 5 part 1, Figure 5.6, sample III). In particular, the bands

observed can be ascribed to the carboxylate group (≈1550 and ≈1460 cm$^{-1}$) and to the xanthene and ketone groups (≈1605, ≈1351 and ≈1254 cm$^{-1}$) of the eosin-metal complex (Chapter 5, Figure 5.5). It should be remarked that the spectra include also the bands from the other compounds of the painting previously detected: among them, lead white and lead carboxylates show bands at ≈1450 and ≈1550 cm$^{-1}$ that overlap with the peaks of Geranium lakes, producing slight shifts in the bands. These shifts hinder the identification of the exact type of Geranium lake (Al- or Pb-based) on the basis of these vibrational data (as described in the systematic study presented in Chapter 5). Nonetheless, the low intensity of the band at 1045 cm$^{-1}$, related to lead white, and the lack of an intense band at 1400, where lead carboxylates normally have a main signal, suggest that the intensity of the peaks related to both substances is low enough to still be able to confidently detect the presence of a generic Geranium lake pigment. It should be also mentioned that the minimum at 1359 cm$^{-1}$ is probably an instrumental artifact linked to the chip transitions of the laser (Figure S6.3), however, this does not affect the presence of a clear shoulder at 1351 cm$^{-1}$ linked to the composition of the sample. The fact that this shoulder and also the shoulder at 1605 cm$^{-1}$ cannot be assigned to any other compound previously detected in the sample, and that the obtained spectra are clearly different from the IR spectrum of cochineal lakes,[388,389] unequivocally confirms the presence of Geranium lakes in the painting in exam. Due to the overlap with the bands from other compounds it is not possible to map the distribution of Geranium lakes in the sample. Nonetheless, the selected spectra are located in the pink paint layer, clearly highlighting the link between the presence of Geranium lakes and the color of the paint film.

The use of Geranium lakes has been previously observed in other paintings by Van Gogh.[17,301,302,380,390] The presence of this family of pigments is normally deduced from the detection of Br in red colored areas, however the identification of the pigment molecules is difficult since they are normally mixed with drying oil containing similar functional groups, namely carboxyls, carbonyls and C=C bonds. In the case of the painting in analysis, the detection is even more challenging due to the co-presence in the same paint layer of lead white, lead carboxylates and CaCO$_3$, whose intense bands at ≈1400, ≈1550 and ≈1450 cm$^{-1}$ respectively overlap with Geranium lakes. Hence, the molecular detection of Geranium lakes proves the great potential of O-PTIR for the analysis of micro- and nano-heterogeneities, even in adverse conditions.
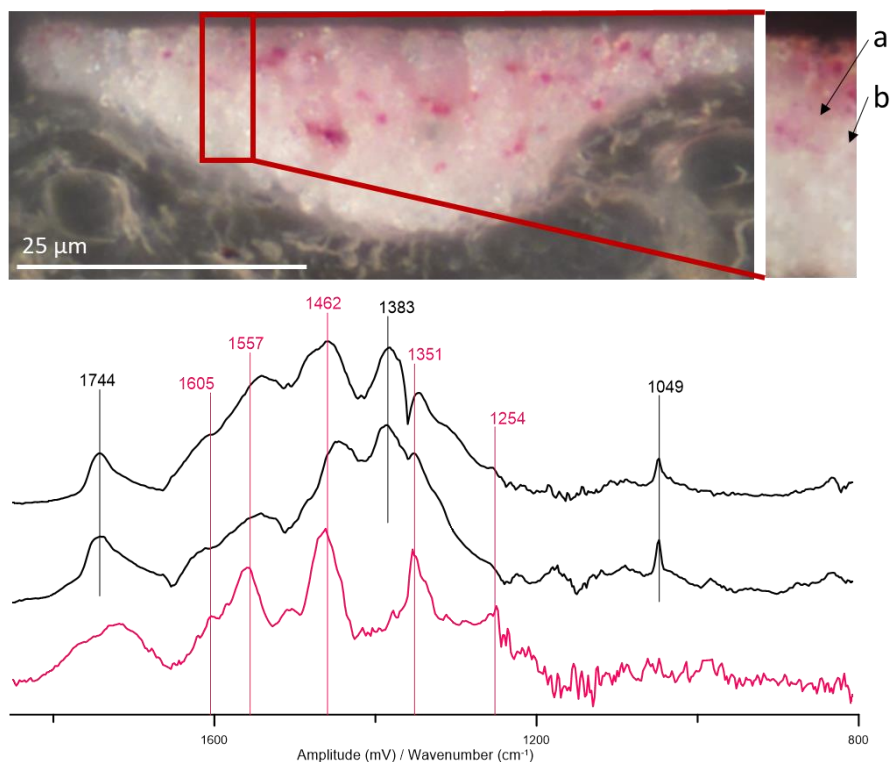
*Figure 6.5_Characterization of the red particles by O-PTIR spectroscopy. Top: region selected for the analysis (left) and its magnification with the analyzed points in evidence, a-b (right). Bottom: O-PTIR spectra collected at each point and reference spectrum of freshly synthesized Geranium lake (synthesis conditions described in Chapter 5 part 1, Figure 5.6, sample III) obtained with the same technique (red). The peaks marked in red correspond to Geranium lakes.*

In order to corroborate this interpretation, the same sample was analyzed by SEM-EDX (Figure 6.6) using a low energy (10 KeV) in order to decrease the penetration in the sample and thus avoid the interference from the KBr pellet used as the sample holder. Due to the low amount of pigment it has not been possible to map the presence of Br. Nonetheless, it is noticeable that the spectrum collected in the paint layer shows the presence of small amounts of Br (Figure 6.6c), while this element cannot be found in the ground layer (Figure 6.6b) or in the embedding medium (Figure 6.6a). Therefore, the presence of Br is specifically linked to the pink paint layer, which is in agreement with the presence of Geranium lakes in the painting.
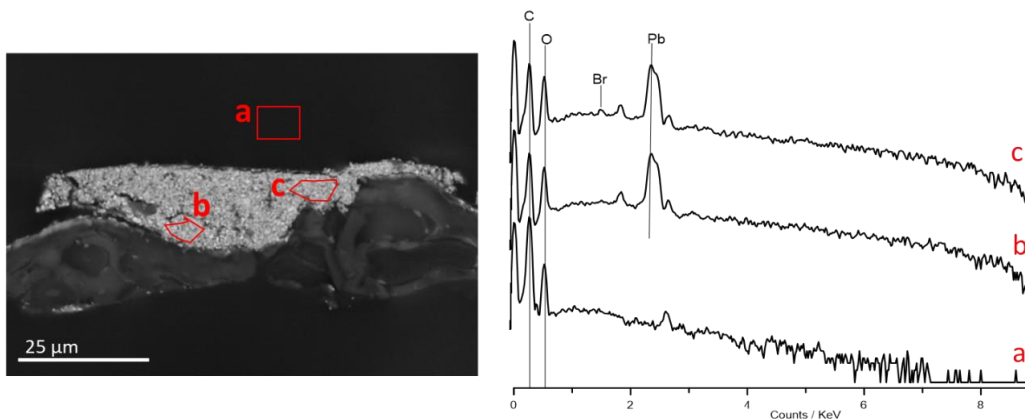
*Figure 6.6_Characterization of the paint layer by SEM-EDX. BSE image (left), the regions marked in red correspond to the areas where the EDX spectra (right) were collected. Specifically: a) embedding medium, b) ground layer and c) paint layer.*

Since Geranium lake pigments are well known to degrade in the presence of visible light,[302,307] it is important to verify if the visible laser used by O-PTIR could causes any damage to the sample, potentially hampering further analysis by other techniques. This eventuality was tested by collecting a series of replicate O-PTIR analyses on the same spot of a reference sample (Figure 6.7). The results show that the final spectrum obtained after 22 repetitions (Figure 6.7, $t_f$) is very similar to the initial one (Figure 6.7, $t_0$), hence proving that O-PTIR has not caused a noticeable damage to this sensitive material. For this reason, the technique can be considered as non-destructive for the type of materials considered in this study.
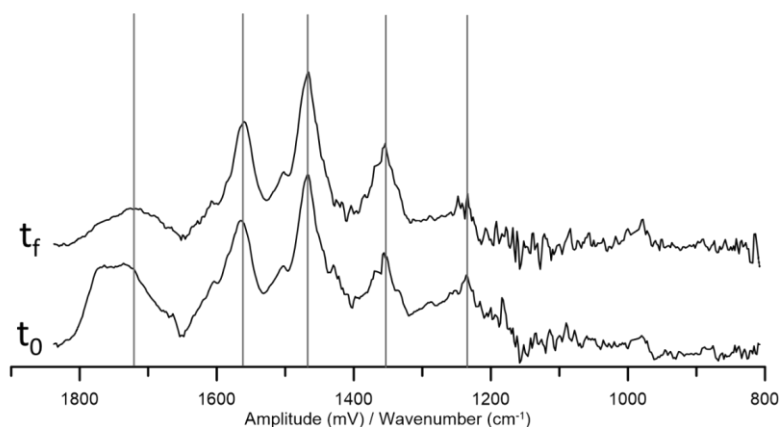


*Figure 6.7_Study of the potential radiation damage on Geranium lakes during O-PTIR analysis. Initial spectrum ($t_0$) compared to the spectrum after being irradiated during 22 consecutive accumulations ($t_f$).*

# 6.4  Conclusions

In this study, the application of O-PTIR spectroscopy to the analysis of micrometric organic particles in historical paintings is presented for the first time. This technique allowed to non-destructively identify the red particles present in a small fragment of the Van Gogh painting *L'Arlésienne (portrait of Madame Ginoux)* as Geranium lake pigments. Due to the limited size of the particles and the presence of additional compounds, the other analytical techniques tested, namely SR-μ-FTIR and μ-Raman spectroscopy, were not able to unambiguously identify these species.

The high spatial resolution offered by O-PTIR, which pushes the boundaries of traditional molecular spectroscopy by overcoming the diffraction limits of traditional FTIR, presents great advantages for the analysis of paintings and heritage objects in general. This allows, in fact, the high-resolution chemical characterization of the stratigraphy, even when only micrometric fragments are available. In particular, the results of this study demonstrated how O-PTIR does not only provide less overlapped spectra, helping to identify micro- and nano-heterogeneities in the samples, but also allows to decrease the size of the samples needed for the analysis. This presents clear advantages for the study and preservation of cultural heritage, maximizing the obtainable information while minimizing the sampling of the objects. Moreover, although no sample preparation is inherently necessary for O-PTIR, the technique appeared highly efficient for the analysis of thin sections of embedded painting fragments. The suitability of this sample preparation for O-PTIR analysis highlights the compatibility of this technique with other commonly employed high-resolution characterization methods, hence opening to the possibility of a full integration of O-PTIR in multitechnique studies of cultural heritage objects.

## 6.5 Supplementary information
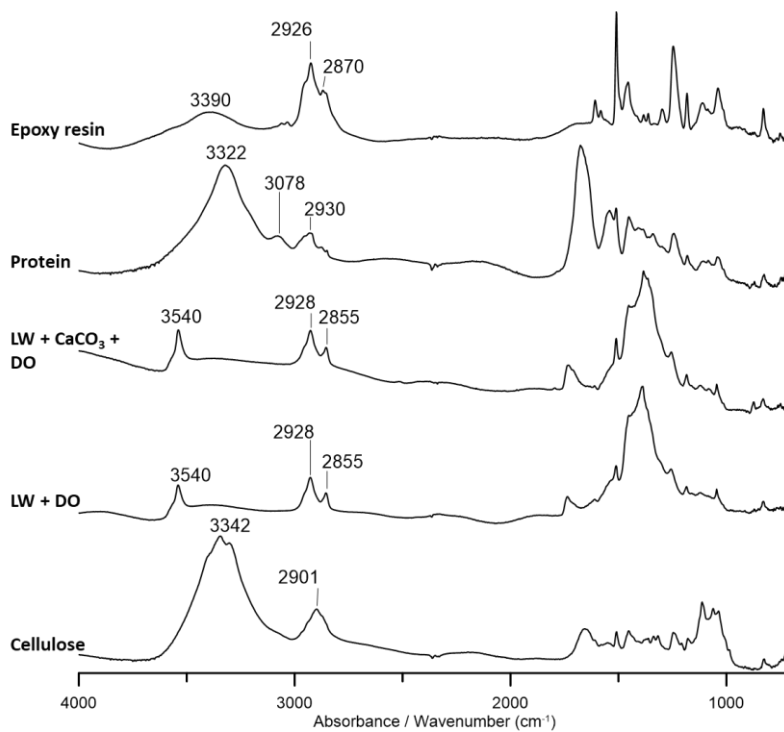


*Figure S6.1_Full range of the SR-μ-FTIR spectra shown in Figure 6.2.*
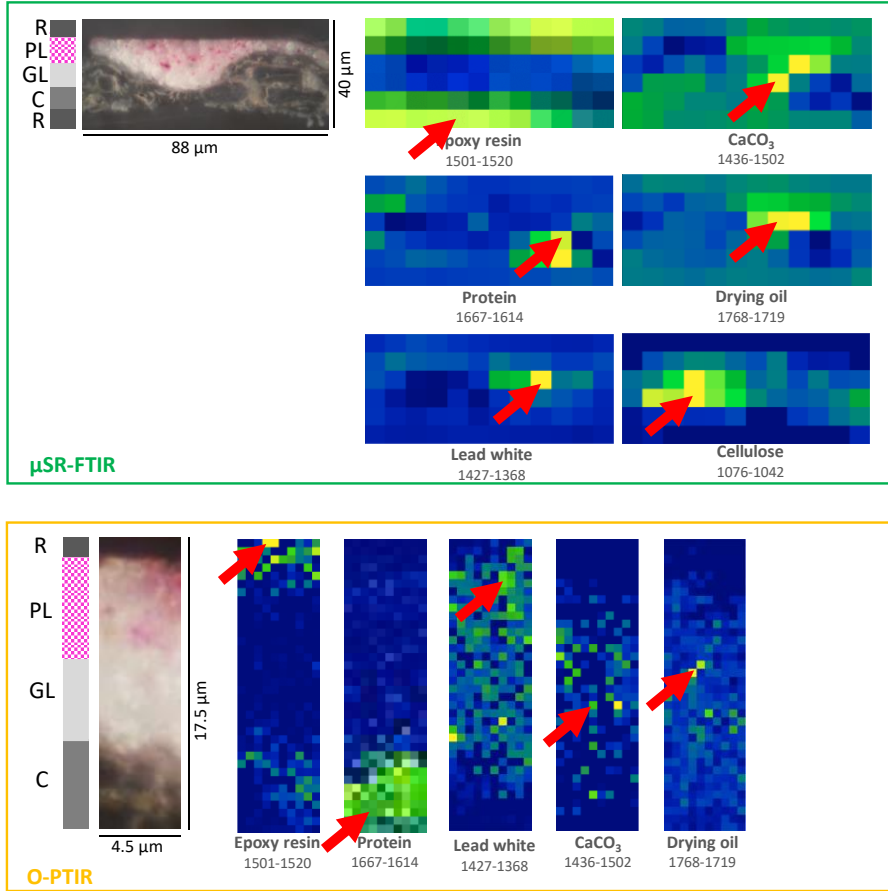
*Figure S6.2_Position of the spectra displayed in Figure 6.2.*
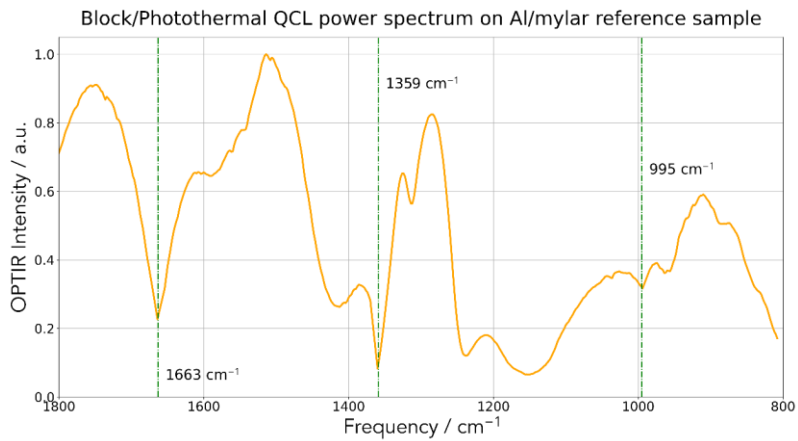


*Figure S6.3_Spectrum of the laser power used in the O-PTIR measured with the background sample (aluminized mylar).*

# Indoor environmental quality index for conservation environments: the importance of including particulate matter

**A. Marchetti\*, S. Pilehvar\*, L. 't Hart\*, D. Leyva Pernia, O. Voet, W. Anaf, G. Nuyts, E. Otten, S. Demeyer, O. Schalm, K. De Wael**

**\* Contributed equally**

# Abstract

It is commonly known that the conservation state of works of arts exhibited inside museums is strongly influenced by the indoor environmental quality (IEQ). Heritage institutions traditionally record and evaluate their IEQ by monitoring temperature, relative humidity, and -more rarely- light. However, smart use of technology enables monitoring other parameters that give a more complete insight in environmental 'air aggressiveness'. One of this parameters is particulate matter (PM) and especially its concentration, size distribution and chemical composition.

In this chapter, a selection of data sets are presented which were obtained in a measuring campaign performed in the War Heritage Institute in Brussels, Belgium. A continuous monitoring of PM concentration with a light scattering based particle counter was performed. In addition the daily mass concentration and size distribution of airborne PM was monitored by means of Harvard impactors. The chemical composition of sampled PM was inferred from the results of XRF and IC analysis. The insights from these datasets are combined with the results of traditional environmental monitoring (temperature, relative humidity and light intensity), and assessed against the recommended guidelines for conservation environments. By using an integrated approach based on the calculation of an IEQ-index, a straightforward methodology is introduced to evaluate and visualize the IEQ including also continuous PM monitoring. It is clear from the results of this study how including PM in IEQ analysis allows to identify potential risks for museum collections that remain invisible when only traditional parameters are considered.

# 7.1 Introduction

In order to protect and conserve the relics of human history, it is important to address the environmental factors that may cause damage to museum collections and cultural heritage in general. Consequently, continuous indoor environmental quality (IEQ) measurements are a prerequisite to evaluate best practices in an exhibition or storage environment.

Currently, the continuous evaluation of conservation environments is usually based on physical parameters only, such as temperature, relative humidity and the intensity of visible (Vis) and ultraviolet (UV) light.[74,75,391–397] It is generally accepted that these parameters pose the largest threat towards hygroscopic and light sensitive objects, influencing also the conservation of general collections.[398] Several commercial systems are available on the market to monitor these physical parameters. However, deterioration is also influenced by gaseous pollutants and particulate matter (PM).[64,79,85,92,93,399] A large number of studies taking into account the average levels of these pollutants in conservation environments has been published through the years.[77,91,99,215,400–407] However, only in few cases a continuous monitoring was performed.[408–411] This can be explained for gaseous pollutants by the lack of suitable sensors for a continuous and sensitive monitoring. The commercially available sensors for common pollutants such as $O_3$, $NO_2$, $SO_2$, $H_2S$, formaldehyde and acetic acid[412–421] are usually created for industrial applications and present limit of detections higher than the recommended levels in conservation environments.[63] On the other hand, PM can rather easily be continuously monitored using airborne particle counters based on light scattering principles. Both precise and accurate sensors created for clean rooms monitoring and inexpensive sensors for home or office applications exist.[119,422,423] However, these systems are not yet employed to their full potential in cultural heritage. In this section of this PhD work, a system is presented that enables the continuous monitoring of temperature (ºC), relative humidity (%), illuminance of visible light (lux), UV light intensity ($mW/m^2$) and PM concentration (number of particles/$m^3$) in a simultaneous and synchronous way. Extended measuring campaigns were performed at two locations in the former Royal Museum of the Armed Forces and of Military History, or shorter Royal Military Museum, in Brussels, Belgium. The Royal Military Museum is integrated in the War Heritage Institute (WHI) since May 1$^{st}$ 2017.[424] Since the risk associated with the presence of airborne PM in conservation environments strongly depends on the concentration and aerodynamic dimension of the particles,[77,425] but also

on their chemical composition,[11,64,399] the continuous monitoring is supplemented by an in depth chemical analysis of PM. The total mass concentration and chemical composition of fine ($PM_1$, $PM_{2.5}$) and coarse particles ($PM_{10}$) is analyzed. This qualitative and quantitative analysis of PM allows to register sudden changes of the indoor environmental quality which are invisible with physical parameters. The available guidelines for conservation environments are then used to calculate an IEQ-index[426] by combining the information of temperature, relative humidity and light exposure with that of PM. No univocal guideline has been found in literature prescribing an optimal PM concentration for conservation environments expressed in number of particles per unit volume. A mass per unit volume threshold is therefore considered and converted into number of particles/$m^3$ values on the basis of site-specific empirical correlations. Taking into account the extreme variety of objects exposed in the museum, the ASHRAE maximum limit for general collection of 10 µg/$m^3$ for $PM_{2.5}$ is applied.[74]

This first part of chapter 7 discusses in detail how and why continuous PM data should be included in indoor environmental quality studies. The versatile methodology discussed can be applied to the monitoring of the environmental quality in different types of indoor conservation environment. When the main concern is directed towards objects or materials with more specific needs, potentially dangerous conditions can be promptly recognized by simply changing the threshold values applied in the calculation of the IEQ-index.

# 7.2  Materials and methods

## 7.2.1  Sampling locations and campaigns

The Royal Military Museum is located in the Parc du Cinquantenaire area in the city center of Brussels in Belgium (50°50'29.4"N 4°23'31.6"E). The building dates from the end of the 19th century. The collections of the Royal Military Museum, now integral part of the War Heritage Institute (WHI), illustrate ten centuries of military history ranging from medieval times up until this day. The more than 125,000 objects include amongst others uniforms and headgear, edged weapons and firearms but also paintings and sculptures, medals and music instruments. The museum building even houses airplanes, armored vehicles and artillery. The collections consist of an extremely wide range of

materials. The museum occupies five large exhibition galleries covering approximately 40,000 m$^2$.

First, measurements were performed in one location from April 11 to April 24 in 2016, followed by a period in a second place from April 25 to May 9 in 2016. The first location is the central storage facility situated underground (further indicated as 'storage'), the second location is the Historic Gallery, situated at the ground level of the Army museum and further indicated in the text as 'gallery' (Figure 7.1).



*Figure 7.1_Images of the sampling locations: the 'Historic Gallery' and the central alley of the storage facility with indication of the sampling unit (white box).*

The collection stored in the storage is a mixed collection, including paintings, textiles, leather, metal, stone and ceramic objects. The measuring equipment was located in the central alley of the storage. This space is equipped with a HVAC-system with two different types of filters (TL7U600 class F7 and TM9U600 class F9, AL-KO KOBER SE, Germany) to control environmental conditions and PM levels. The storage is located above a highway tunnel and indirectly connected to it through a shared emergency exit. This connection could negatively affect the IEQ in this environment, potentially causing high levels of gaseous pollutants and particulate matter.

The gallery was inaugurated in 1923 and is dedicated to the Belgian army between 1831 and 1914. It houses a collection consisting of hundreds of oil paintings on canvas, uniforms, flags, weapons and musical instruments. The gallery has a large roof with a skylight that enables direct sunlight entering (Figure 7.1), causing a severe temperature increase on sunny days. In winter period the gallery is heated but no cooling nor humidity control are installed. This strongly influences the thermo-hygrometric conditions for the collection. The gallery is not equipped with an air filtering system, which also might affect

the PM levels. The objects are exhibited on the walls and in oaken display cases originating from the early 20th century. This type of display cases has a high air exchange rate, allowing infiltration of dust.[89,427]

The very different environmental conditions in the two locations do not allow to obtain an overview of the conservation conditions in the whole museum, but represent an ideal context for testing the methodology discussed in this work. The "controlled" environment in the storage and the "uncontrolled' environment in the gallery, in fact, ideally represent the two extremes of the possible range of conditions that can be found in this conservation environment.

## 7.2.2 Monitoring of environmental parameters (temperature, relative humidity, Vis and UV light, $CO_2$)

The monitoring of environmental parameters was performed with a frequency of 15 minutes during the sampling campaigns. For simplicity, and to underline the difference between these monitoring techniques and other PM sampling methods used, this "semi-continuous" monitoring will be referred to as "continuous" throughout the rest of this chapter. Well-calibrated, commercial off-the-shelf sensors were connected to a multi-purpose data logger (DataTaker DT85, Thermo Fischer scientific, Australia).[428] Data was available online using a 4G network. Temperature, relative humidity and carbon dioxide ($CO_2$) were measured with a GMW90 sensor (Vaisala, Finland),[429] while the intensity of visible and UV light were measured with the sensors SKL310[430] and SKU421[431] (Skye Instruments, UK). For the light sensors, the orientation and distance from the light source have a substantial impact on the intensity. The sensors were placed in a vertical position to simulate vertically stored objects (e.g., paintings). To monitor the real light exposure, the sensors should be placed next to the object of interest. The monitoring unit and its sensors were placed on a table at a height of 1.10 m. This corresponds with the average height of the lower edge of exhibited paintings.[432]

## 7.2.3 Sampling and analysis of particulate matter

PM was monitored with a frequency of 15 minutes by means of a Lighthouse Handheld 3016-IAQ continuous air particle counter (Lighthouse Worldwide Solutions, USA).[433] This

device is designed to respect the ISO 21501-4 directives in terms of accuracy and precision for the measurement of size and concentration of particles suspended in air. Particles in the range of 0.3 μm – 10 μm are resolved into 6 particle size channels. Black carbon was continuously monitored using a Portable Aethalometer® Model AE42 (Magee Scientific Corporation, USA).[434] The concentration is deduced from the absorption of an 880 nm light bundle, black carbon being the only aerosol component that significantly absorbs at this wavelength.

The monitoring campaign was supplemented by an in-depth analysis of PM mass. Different fractions of particulate matter ($PM_1$, $PM_{2.5}$, $PM_{10}$) were sampled with 3 different Harvard-type impactors (MS&T area sampler, Air Diagnostics and Engineering Inc., USA).[116] $PM_{2.5}$ and $PM_{10}$ were collected on mixed cellulose ester filters (SKC MCE 0.45 μm 225-1914, SKC Limited, UK), $PM_1$ on Teflon membrane filters (Pall 7227 TK15-G3M 37MM, Pallflex® Air Monitoring Filters, PALL Life Sciences, USA). All the fractions of PM were sampled for 24 hours, for the period of two consecutive weeks during each sampling campaign. The pumping units connected to Harvard impactors worked with the flow rate of 10 L/min for $PM_{2.5}$ and $PM_{10}$ and with the flow rate of 23 L/min for $PM_1$. Changes in the average flowrate were monitored by means of a rotameter model P equipped with a 044-14-N tube (Aalborg Instruments & Controls, USA). Outliers based on the flowrate were identified with the interquartile range method and excluded from further considerations. The filters were weighed before and after sampling to obtain the mass of collected matter and calculate PM concentrations in μg per unit volume of sampled air. The gravimetric analysis was performed on an analytical microbalance MT5 (Mettler, USA) with capacity: 5.1 g, readability: 0.001 mg, repeatability: 0.0008 mg and linearity: 0.004 mg.

The elemental composition of the different fractions of PM was determined using a energy-dispersive X-ray fluorescence spectrometer (EDXRF-Epsilon 5, PANalytical, The Netherlands), equipped with a Gd X-ray tube (600W, 100 kV and 24 mA). Three different sets of settings were used to cover the entire range of elements of interest. Na, Mg, Al, Si, P, S, Cl, K and Ca concentrations were determined by using a Ti secondary target with an operating voltage, current and measuring time of respectively 25 kV, 24 mA and 500 s. Ti, Cr, Mn, Fe, Co, Ni, Cu, Zn and Ba concentrations were determined using a Ge secondary target ( 75 kV; 8 mA; 1500 s). Finally a Mo secondary target (100 kV; 6 mA; 1500 s) was used to determine the As, Se, Br, Sr, Zr and Pb concentrations. Then, the water-soluble fraction was ultrasonically leached in 8 mL of Milli-Q water allowing a quantitative analysis of positive and negative ions by means of ion chromatography

(Metrohm 883 basic IC plus, Switzerland). Metrosep C 6 -150/4.0 column was used for the analysis of cations, Metrosep Asupp5 – 250/4.0 for the analysis of anions.

On the basis of x-ray fluorescence (XRF) and ion chromatography (IC) results the relative amounts of soil dust, sea salts, ammonium salts and mineral salts (soluble fraction of soil dust) in the different PM fractions was estimated. The method used is described in detail by Anaf et al..[99]

## 7.2.4   Data evaluation

Eventual anomalies and sudden perturbations of single parameters are thoroughly investigated in order to identify and interpret situations of potential risk for the museum objects. To deepen the understanding on the causes of anomalous behaviors the data obtained in the different indoor locations are assessed against the outdoor values for the corresponding period.

The assessment of the IEQ is performed using an IEQ-index that combines the measurement data of temperature, relative humidity, visible light, UV, and $PM_{2.5}$ into a simpler magnitude representing the degree of air aggressiveness for collections.[426] This index is calculated based on thresholds already applied and well recognized by the cultural heritage conservation community; the ASHRAE standards for 'Museums, Libraries, and Archives' for temperature, relative humidity, and $PM_{2.5}$ [74], and the Thomson standards for visible light and UV.[1]

The ASHRAE standards propose a set of five control classes depending on the potential risk for a collection under specific thermo-hygrometric conditions (Table 7.1). These classes vary from situations with the lowest possible risk for most objects (class AA) to a considerably high risk of damage for most of the artefacts (class D). The specific IEQ-index for temperature and relative humidity is defined by associating each of the aforementioned classes to a numerical value in each data point. The index range from 100 to 0, as it covers the situations from the lowest to the highest risk of degradation or damage. Consequently, class AA corresponds to the maximum IEQ-index=100, A to IEQ-index=80, B to IEQ-index=60, C to IEQ-index=40, and D to IEQ-index=20. Below class D (relative humidity larger than 75%) the IEQ-index will reach the minimum value of 0.

*Table 7.1_Overview of the ASHRAE standards for temperature and relive humidity[74] and their correspondence to the IEQ-index.*

| ASHRAE Class | | Temperature | Relative Humidity | Remarks |
|---|---|---|---|---|
| Class AA<br><br>IEQ-index=100 | | 15-25°C<br>Short fluctuations: ±2°C.<br>Seasonal adjustments: ±5°C | 50%<br>Short fluctuations: ± 5%. No seasonal adjustments. | No risk of mechanical damage to most artefacts and paintings. |
| Class A<br><br>IEQ-index=80 | As | 15-25°C<br>Short fluctuations: ±2°C.<br>Seasonal adjustments: +5°C -10°C | 40-60%<br>Short fluctuations: ± 5%. Seasonal adjustments: ±10% | Small risk of mechanical damage to high vulnerability artefacts; no mechanical risk to most artefacts, paintings, photographs, and books. |
| | A | | Short fluctuations: ± 10%. Seasonal adjustments: No variation. | |
| Class B<br><br>IEQ-index=60 | | 15-25°C<br>Short fluctuations: ±5°C.<br>Seasonal adjustments: ±10°C but <30°C | 40-60%<br>Short fluctuations: ± 10%. Seasonal adjustments: ±10% | Moderate risk of mechanical damage to high-vulnerability artefacts; tiny risk to most paintings and photographs and no risk to most artefacts and books. |
| Class C<br><br>IEQ-index=40 | | <30°C | 25-75% | High risk of mechanical damage to high vulnerability artefacts; moderate risk to most paintings, photographs, and tiny risk to most artefacts and books. |
| Class D<br><br>IEQ-index=20 | | | ≤75% | High risk of sudden or cumulative mechanical damage to most artefacts and paintings due to low humidity fracture, but high humidity delamination and deformations. Mold growth and rapid corrosion avoided. |

The index for light and PM is evaluated based on the maximum allowed thresholds available in literature for general collections (not particularly sensible objects). The thresholds applied for light are 200 lux for visible light illuminance and 75 μW/lm (=15 mW/m$^2$) for UV.[1] For particulate matter the guideline applied is 10 μg/m$^3$ of $PM_{2.5}$.[74] The behavior of the IEQ-index for light and PM differs from the one of temperature and relative humidity due to the specific characteristics of these thresholds. Now the values equal or below the thresholds are considered acceptable (IEQ-index=100) and those above would imply IEQ-index=0; without any gradual transition between the two categories.

The general IEQ-index in each data-point is set by the lowest value of the parameter-specific indexes in that point. For example, a situation where it was measured a temperature of 20°C, with a short time fluctuation of ±2°C and seasonal adjustment of ±5°C, a relative humidity of 50%, short fluctuations of ±5% relative humidity, no seasonal adjustment, and UV of 16 mW/m$^2$ would translate in IEQ-index(temperature, relative humidity)=100, IEQ-index(UV)=0, and consequently IEQ-index=0.

In order to facilitate the visualization, the evolution of the IEQ-index through time is represented by a colour map with a fixed scale of colours. The scale varies from red to blue conforming the index varies from 0 to 100. The IEQ-index calculation and graphical representation was performed using MATLAB R2017a (The MathWorks, Inc., 2017).

## 7.3  Results and discussion

First, a traditional interpretation of the environmental data is presented. The thermo-hygrometric data and light values recorded in the storage are compared with the gallery. Subsequently, a diverse range of PM monitoring techniques are evaluated. Finally, in order to investigate the effect of the inclusion of particulate matter in indoor environmental quality monitoring, the IEQ-index is calculated for traditional environmental parameters both including and not including PM.

### 7.3.1 Environmental parameters (T, RH, Vis and UV light, $CO_2$).

The collected data streams are visualized using graphs (Figure 7.2). The information in the graphs is enhanced by adding a coloured zone that denote the acceptable range as defined by ASHRAE guidelines[74] for temperature and relative humidity and by Thomson[1] for Vis and UV light intensity. ASHRAE classes take into account also short time fluctuations, in this case only the absolute limit values for temperature and relative humidity for classes As, A and B (from no risk to moderate risk only for high-vulnerability artefacts) are represented in the graph.

Figure 7.2a shows the temperature trend at the two selected locations. The temperature in the storage is very stable due to the controlled environment, with a minor daily difference of ±0.3 °C. The gallery experiences more extreme daily temperature differences of ±3.7 °C. Figure 7.2b shows the relative humidity trends in both environments. The relative humidity in the storage is more stable compared to the gallery. Moreover, the average relative humidity is 47%, close to the 50% average recommended by ASHRAE.[74] The relative humidity in the gallery on the other hand drops below 40% with an average of 30%, close to the lowest limit (25%) of ASHRAE class C (high risk for sensible objects and moderate to tiny risk for all other hygroscopic artefacts).[74] The presence of daily fluctuations of ±8% also increases the risk of damage towards high vulnerability artefacts.[74] The stabilizing effect of the HVAC in the storage is clearly visible in the temperature and relative humidity gradient in contrast to the uncontrolled environment in the gallery.

Figure 7.2c and d show the light evolution of Vis and UV respectively. In the storage, visible light is originating from artificial lights with an intensity of 450 lux when switched on, zero when switched off. This light source emits 14.8 mW/m$^2$ UV on average. The artificial light level, significantly higher than the maximum suggested threshold value of 200 lux, leads to the exposure of the collection to potentially endangering conditions on a daily basis. UV levels are extremely close to the threshold. Even though these values are not strictly exceeding the recommended limit in this case, it is anyway important to remember that it is advised to keep UV radiation as low as possible.[1] A further risk for the stored objects comes from the fact that lights in the storage remain switched on for long periods also during the night. This depends on security reasons connected to an increased terror threat after the 2016 Brussels bombings, unfortunately causing the unnecessary exposure of the objects to potentially dangerous levels of light. However, by simply changing the type of lamps installed, this danger can be easily averted. In the

gallery high values for illuminance and UV are reached during day time, with peaks above the suggested thresholds on a daily basis. An increase in the maximum Vis light is observed after 3/05, from an average of 514 lux to an average of 1039 lux. Temperature also presents a growing trend in the same days, from an average maximum of 21 ºC (before 3/05) to an average maximum of 28 ºC (after 3/05). The higher temperatures observed when more light is entering the building from the windows underlines the central role played by direct sunlight on the indoor environmental quality.

To get an idea about human activity in the indoor environment, the $CO_2$ level was monitored (Figure 7.2e). In the storage, the $CO_2$ average level rises during weekdays but significantly decreases in the weekends (highlighted days in Figure 2). On the contrary, in the gallery the $CO_2$ level variation is more irregular and no clear distinctions are present between weekdays and weekends. This depends on the presence of visitors in the museum also in the weekends, but also on the variation of outdoor levels of the gas. As an example, on May 1st the level of $CO_2$ is extremely low compared to the previous days in the gallery, while on May 2nd an absolute maximum is observed. On both days the museum was closed to visitors, but on May 1st the outdoor level of $CO_2$ is around the average for the period of analysis, while on May 2nd one of the highest values for whole 2016 was registered in the surroundings of the museum (data from IRCELINE, monitoring stations 41WOL1 and 41002).[435] The rate at which the $CO_2$ level decreases when people are not present in the environment is linked to the air exchange rate between indoor and outdoor.[436] The drop in concentration observed every night in the gallery appears to be much faster than the slow decrease registered in the storage, leading to the conclusion that the air exchange rate in the former is higher than in the latter. To our knowledge a threshold for $CO_2$ levels in generic collections is still not defined, the concentrations observed in both environments remain anyway well below the threshold for humans of 1000 ppm.[74]
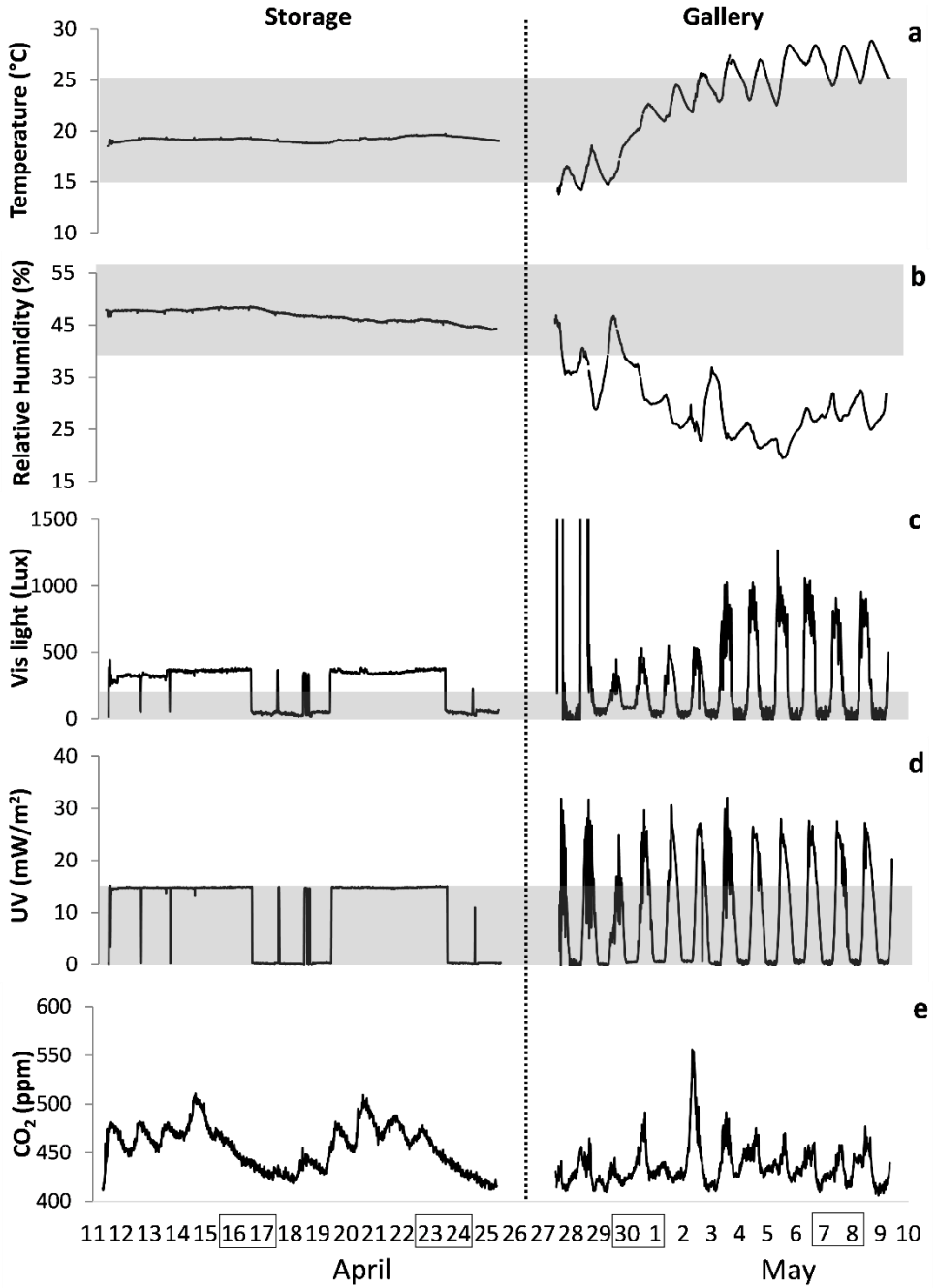
*Figure 7.2_Physical parameters continuous monitoring in storage and gallery: a) temperature, b) relative humidity, c) Vis light illuminance and d) UV light intensity, e) $CO_2$ concentration. Grey areas represent the suggested range for general collections.*

According to the guidelines for the traditionally monitored parameters, the storage is on average better suited for preserving general collections compared to the gallery, strongly influenced by the outdoor environment. In general, the variations observed are mainly connected to day/night cycles, without allowing to clearly identify specific events.

## 7.3.2   Average amounts of airborne particulate matter

The deposition of particulate matter on cultural heritage materials has been proven to represent a concrete risk for their conservation.[64,85,92,399] PM transport and deposition mechanisms are strictly linked to concentration and aerodynamic dimension of the particles, practically deciding the fate of the suspended matter.[77,425] The threats associated with the presence of airborne PM in conservation environments therefore strongly depend on these factors.[64]

Daily measurements of particulate matter over a period of two weeks were performed in storage and gallery via traditional Harvard impactors. Figure 7.3 shows the average concentrations of $PM_1$, $PM_{2.5}$, and $PM_{10}$ for both locations. The average PM values in the storage are lower compared to the gallery. As it is clear from Figure 7.3, the PM concentration in the gallery reaches the outdoor levels of the corresponding PM fraction, confirming the close interaction with the outdoor environment. Also the average particle size distribution in the gallery matches the one outside, with similar percentages of $PM_{10-2.5}$ (31%, 39%), $PM_{2.5-1}$ (36%, 31%) and $PM_1$ (33%, 30%) in the total $PM_{10}$ mass. The storage room is more protected from the outdoor environment, filtering particles and especially the coarse fraction. On average, in fact, $PM_{10-2.5}$ represents only 7% of the total $PM_{10}$ mass in the storage, while $PM_{2.5-1}$ and $PM_1$ respectively represent 56% and 37%. The HVAC system installed in the storage is responsible both for the general lower PM content and for the different size distribution observed in this room. A very similar situation to the one registered in this HVAC controlled environment is observed by Ligocki et al.[91] in three different museums where filtering HVAC systems are installed. Also in this case very similar concentrations of $PM_{2.5}$ and $PM_{10}$ are observed, showing the strong influence of air filtering systems in terms of coarse fraction reduction.
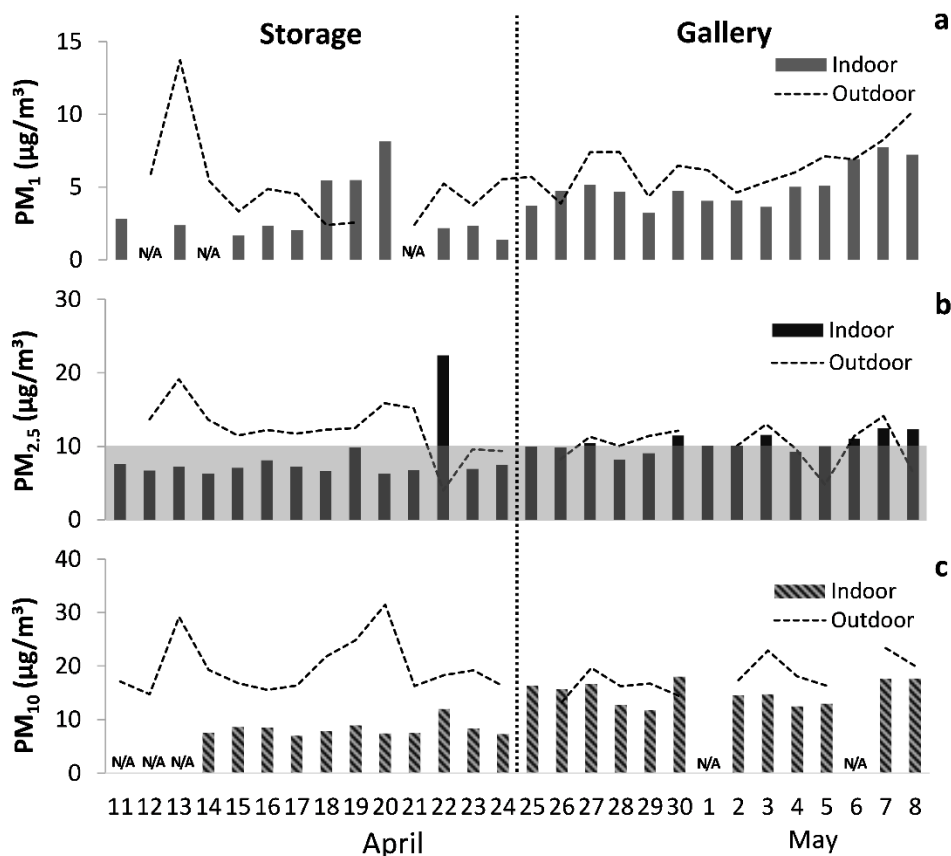
*Figure 7.3_Daily average of a) PM$_1$, b) PM$_{2.5}$ and c) PM$_{10}$ measurements in storage and gallery. The grey area represents the ASHRAE suggested maximum concentration for PM$_{2.5}$ in general collections.[74] N/A= data not available (flow rate outliers).*

Indoor to outdoor ratios (I/O) of mass concentrations of PM$_1$, PM$_{2.5}$ and PM$_{10}$ were calculated for both locations (Figure 7.4). In the storage, the values observed are significantly lower than unity, except for some higher I/O values for fine PM at specific days. On the other hand, in the gallery the values for I/O ratios are closer to unity, indicating a high natural ventilation rate. This behavior appears very similar to the one observed by Ligocki et al.,[91] with close to unity I/O ratios in two historical buildings not equipped with PM filtration systems (Sepulveda House and Southwest Museum, Los Angeles) and significantly lower values in HVAC-equipped museums (J. Paul Getty Museum, Malibu; Norton Simon Museum, Pasadena; Huntington Library, San Marino). This difference between storage and gallery underlines the close contact between the

latter and the outdoor environment, causing the variability in PM values to depend mainly on factors such as wind speed, wind direction and road traffic outside the museum. On the contrary, given the higher average level of protection from the outdoor environment observed in the storage, the presence of peaks can be attributed to indoor human activities. In detail, some extreme sudden variations from a quite constant trend are present on April 18, 19 and 22. Indoor, the temperature and relative humidity are mildly disturbed on those days and the $CO_2$ levels are slightly higher compared to the other days, evidence that suggests the presence of people in the storage. During this week the floor of the storage was treated with a sealant and a number of objects were moved. These activities might have caused the increase in fine PM, exposing the collection to a potential threat undetectable by monitoring only conventional parameters. The monitoring of PM therefore constitutes an important tool for the assessment of the real risk level the stored objects are exposed to.
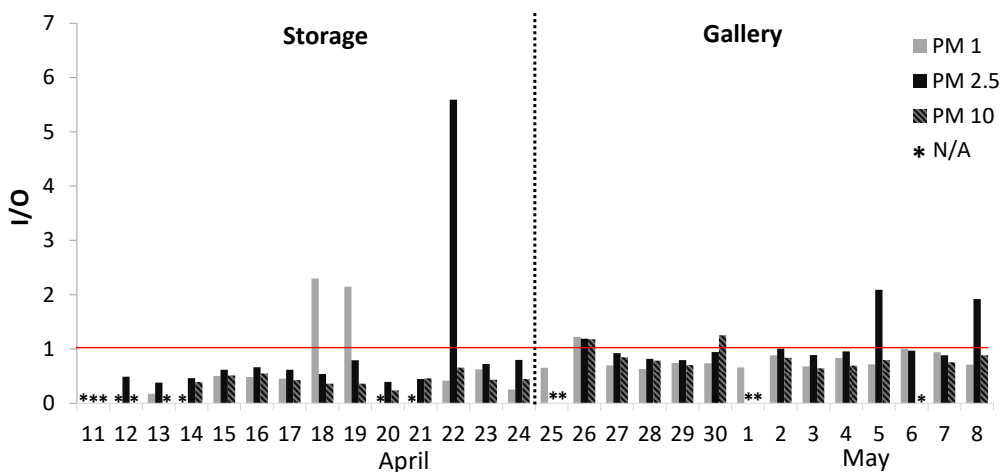


*Figure 7.4_Indoor/outdoor (I/O) ratios for $PM_1$, $PM_{2.5}$ and $PM_{10}$ concentration in storage and gallery. N/A=data not available (flow rate outliers).*

### 7.3.3   Average chemical composition of particulate matter.

The potential risk associated with airborne particulate strongly depends also on the chemical composition of the deposited material.[11,64,72,77,85,259,399] In particular, the presence of airborne soil dust and black carbon has been linked to the soiling of works of art. The deposition of these particles on the surface of museum objects can lead to

240

the building up of dark deposits, which are difficult, expensive and often even impossible to remove safely.[64,77,85] Other types of inorganic particles, such as ammonium salts, sea salts and Fe-rich particles, can also pose a chemical hazard to specific materials.[11,72,259,399] In this section the reconstruction of the abundances of different particle types in different PM fractions is introduced.

First, the abundances of soil dust, sea salts, ammonium salts and mineral salts (soluble fraction of soil dust) in the different locations are calculated. The daily average results of the analysis of black carbon are also included in the chemical reconstruction of PM mass. Since in general both primary and secondary soot particles fall into the submicron size fraction,[437,438] all the observed black carbon is considered to be part of $PM_1$. Black carbon was not analyzed in the outdoor environment, therefore IRCELINE values (monitoring station 41R001)[439] are used in order to allow a comparison. Considering the difference in position between museum and monitoring station these values are only an approximation of the real values.[112]

The total inorganic and black carbon mass obtained from these results represents only a limited part of the total PM mass collected. This is due to the presence of organic dust and aerosol-associated water.[91,99] In the storage, in particular, the unexplained mass accounts for over 90% of the total mass on average, with higher values in the fine fraction than in the coarse (Table 7.2). The low air exchange rate and the HVAC filtration system account for the extremely high content of organic aerosols in this environment.[91] On the other hand, in the gallery the percentage of unknown mass is lower, with a total average close to the one observed for the outdoor environment. Also in this case the values are higher for the fine fraction than for the coarse fraction. When compared to the outdoor results, the amount of unknown mass in the gallery appears slightly higher in all fractions. This suggests the presence of indoor sources of organic dust. The chemical composition of this fraction in museum environments has been linked before to the shedding of particles by visitors and to maintenance operations, such as vacuum cleaning and floor waxing.[91] In order to have a complete vision of the indoor environmental quality in the museum, the nature of this organic fraction should be further investigated both in the storage and in the gallery.

The results for the chemical reconstruction of the inorganic fraction of $PM_{10-2.5}$, $PM_{2.5-1}$ and $PM_1$ are presented in Figure 7.5, 7.6 and 7.7. Soil dust and all other species considered are present in much lower concentrations in the storage than in the gallery, reflecting the trend observed for the total PM amount. The relatively high

concentrations of inorganic PM and black carbon in the gallery compared to the storage confirms the important influence of the outdoor environment on the IEQ for this room. This close relation between the two environments is supported by the distribution of the single species in the different fractions. In particular, the fine fraction is mainly composed of ammonium salts and black carbon, with small amounts of sea salts in the $PM_{2.5-1}$ fraction in both environments. In the same way, the coarse fraction contains soil dust, sea salts and mineral salts mainly. Soil dust is often carried indoor from the outside through shoes, in particular when outdoor relative humidity is high, and resuspended by human activities.[99,440] A significant difference is observed only for the sea salts concentration, much lower in the gallery than outdoor. Black carbon concentration is also lower indoor, but the different location of museum and IRCELINE monitoring station could have influenced these results.

*Table 7.2_Percentage of unexplained mass in different PM fractions in storage, gallery and outdoor.*

|  | $PM_1$ | $PM_{2.5-1}$ | $PM_{10-2.5}$ |
|---|---|---|---|
| Storage | 96.7±0.9% | 99.8±0.1% | 93.5±4.5% |
| Gallery | 71±7% | 81±9% | 55±20% |
| Outdoor | 50±11% | 68±8% | 44±14% |

On the other hand, in the storage the very small portion of mass identified consists mainly of black carbon, ammonium salts and soil dust in the fine fraction and almost exclusively of soil dust in the coarse fraction. The relatively high content of soil dust is connected to the presence of people in the environment, while the other inorganic particles concentrations are efficiently reduced by the HVAC system installed.[91] The level of soil dust appears to be relatively high compared to the other species also in the fine fraction. The absolute concentration in $PM_1$ and $PM_{2.5-1}$ remains anyway low compared to the one observed for the coarse fraction, where soil dust is usually more abundant.[437] The chemical composition of PM observed in the storage confirms the similarity between this environment and the HVAC-equipped museums studied by Ligocki et al.[91] In both cases in fact extremely high percentages of organic matter and an inorganic fraction dominated by soil dust were observed.
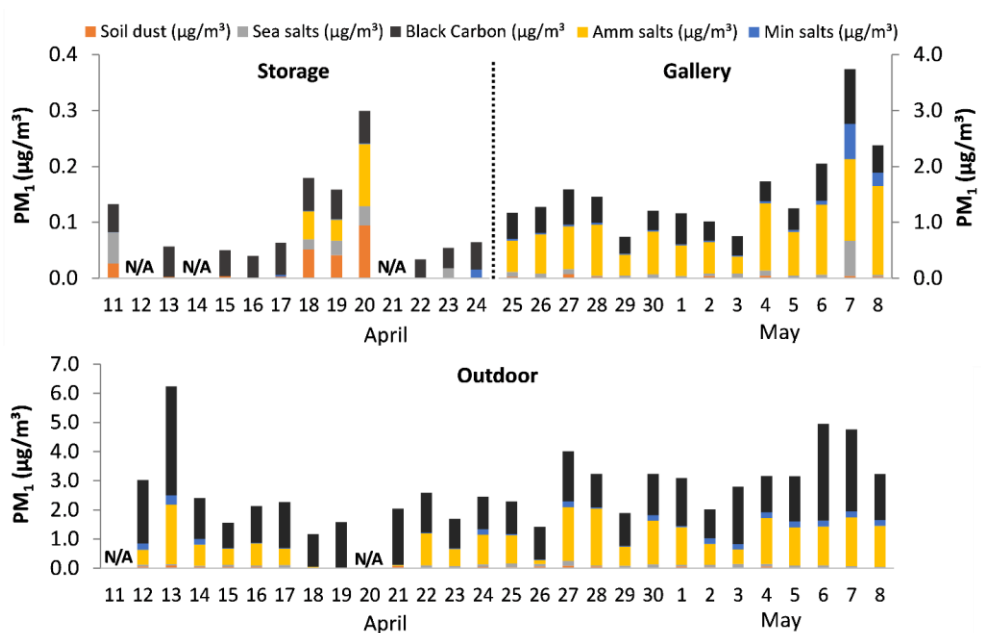
*Figure 7.5_Daily composition of the airborne inorganic fraction of $PM_1$. N/A= data not available (flow rate outliers).*
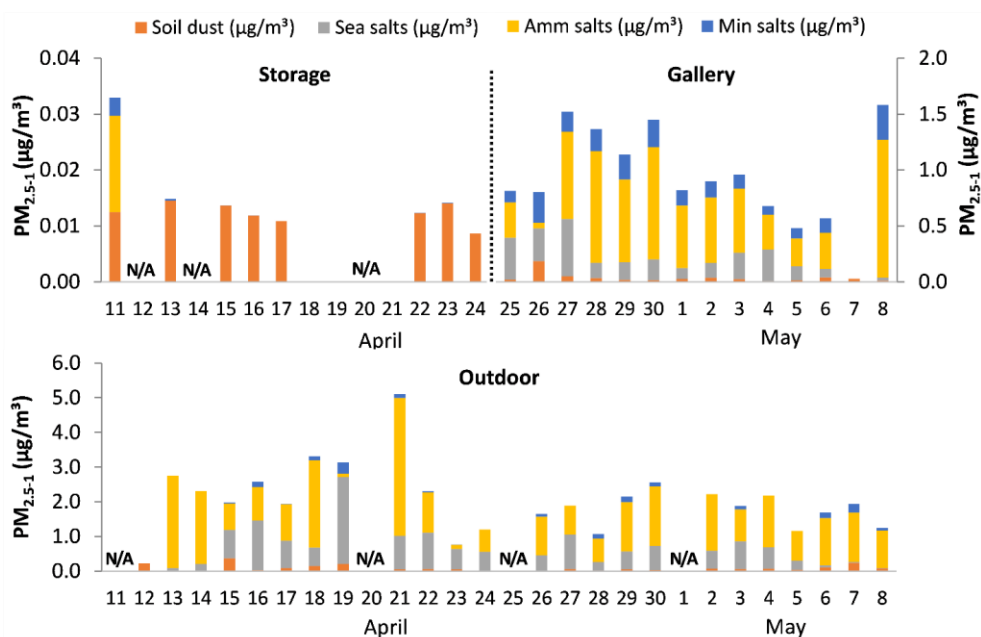


*Figure 7.6_Daily composition of the airborne inorganic fraction of $PM_{2.5-1}$. N/A= data not available (flow rate outliers).*

243
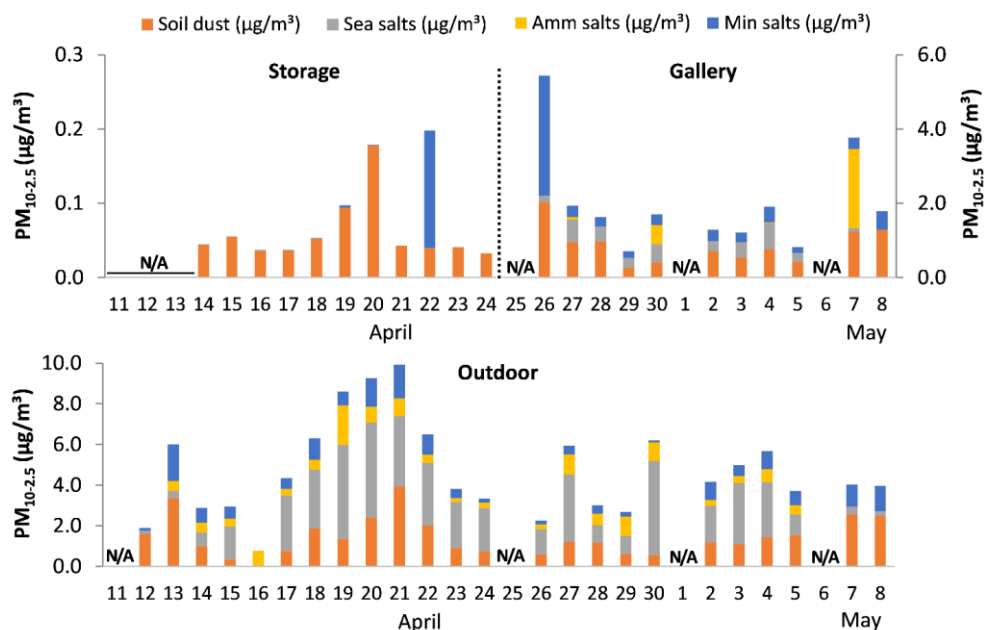
*Figure 7.7_Daily composition of the airborne inorganic fraction of PM$_{10-2.5}$. N/A= data not available (flow rate outliers).*

In order to further explore the origin of the inorganic aerosols observed inside the museum, Indoor/Outdoor (I/O) PM ratios are calculated. In Figure 7.8 and 7.9, the average daily indoor to outdoor ratios of soil dust, sea salts, ammonium salts and mineral salts in PM$_1$, PM$_{2.5}$ and PM$_{10}$ are presented. As expected, in the well-insulated and well-controlled storage the ratios are significantly lower than 1 on average. This value is exceeded only in precise events and only for certain species in the fine fraction. In particular an ammonium concentration slightly higher than the outdoor level on 18/04 (I/O=1.2) is observed, together with an important soil dust enrichment on 18 and 19/04 (I/O=13.5 and 12.8 respectively). This peak of material corresponds to the days in which a new floor sealant was applied in the storage, probably causing the resuspension of important amounts of particulate matter. The increase registered in the soil dust ratios is more drastic than the one for ammonium salts on these days. The very low concentration of soil dust in outdoor PM$_1$ accounts for the relative difference observed for the two species. It is not clear if the event was caused directly by the sealing intervention or if the fine particulate suspension was caused by the movement of the stored objects. What is certain is that this perturbation of the preexistent equilibrium condition represents a potential risk for the stored objects, emphasizing the importance of including PM in the monitoring of indoor environmental quality.
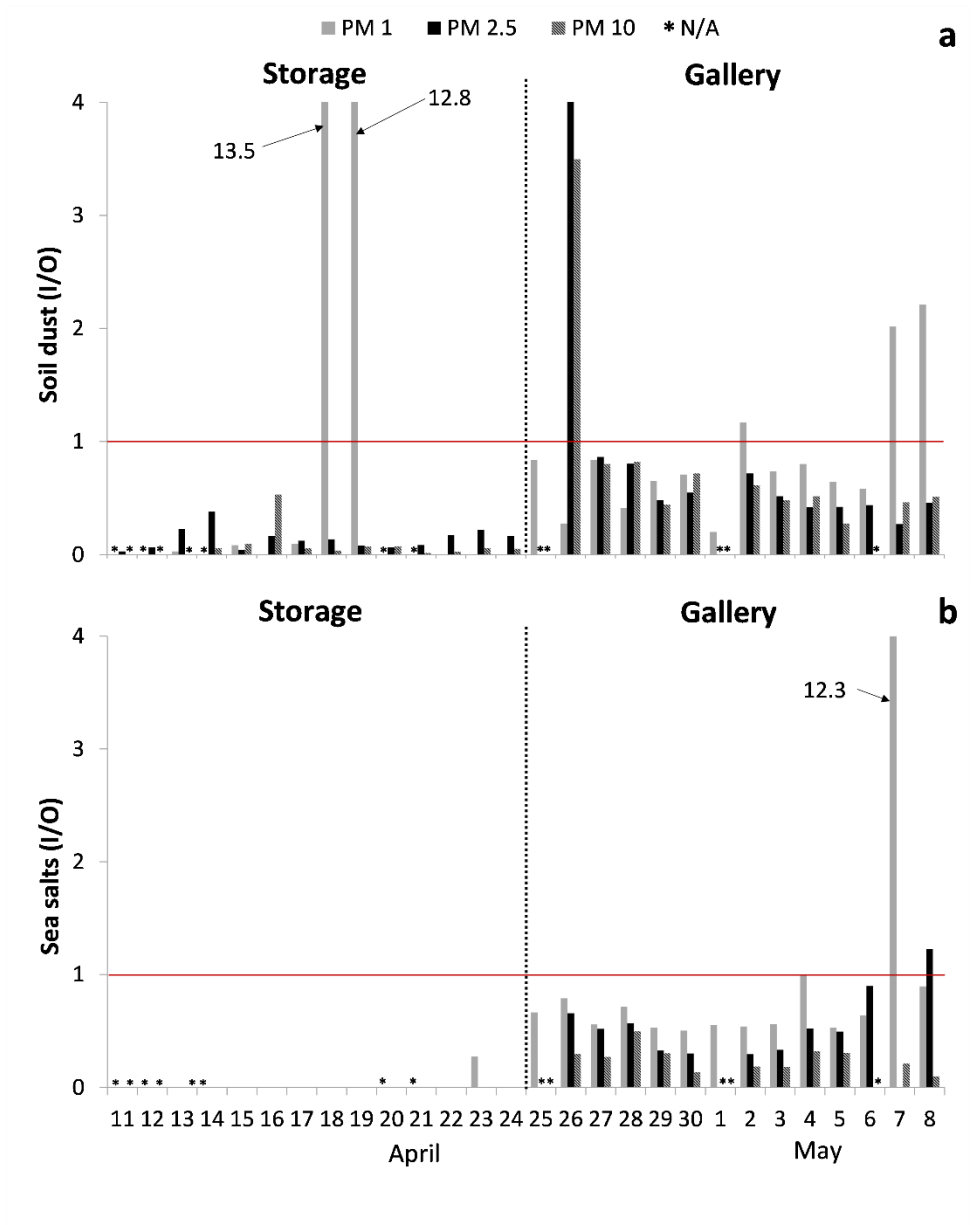
*Figure 7.8_Indoor/outdoor (I/O) ratios for a) soil dust and b) sea salts in PM$_{10}$, PM$_{2.5}$ and PM$_1$. N/A=data not available (flow rate outliers).*
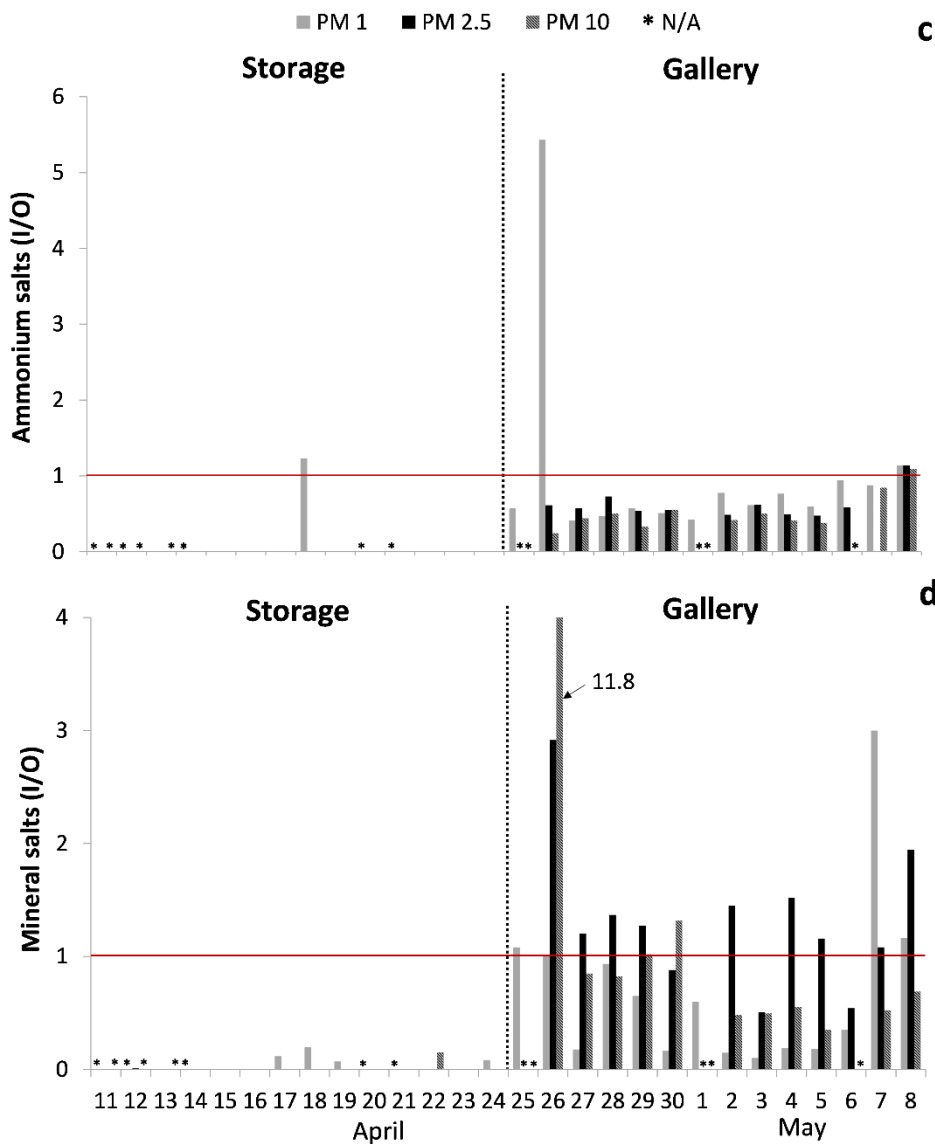
*Figure 7.9_Indoor/outdoor (I/O) ratios for c) ammonium salts and d) mineral salts in $PM_{10}$, $PM_{2.5}$ and $PM_1$. N/A=data not available (flow rate outliers).*

In the gallery the situation appears different, with ratios generally closer to 1 for all the fractions. In particular, the ratios for the fine fraction tend to be higher than the ratios for $PM_{10}$. This evidence is connected to the fact that $PM_1$ usually infiltrates more efficiently than the other fractions through the building shell.[77] In detail, soil dust

246

presents ratios on average slightly lower than 1, but significantly higher than 1 on 26/04 for $PM_{10}$ and $PM_{2.5}$ and on 7 and 8/05 for $PM_1$. Sea salts seem to enter less efficiently or to be less resuspended in the exhibition environment than soil dust, presenting lower I/O ratios especially for $PM_{10}$. The introduction of soil dust through the shoes of visitors accounts for this difference in behavior.[99] A single higher ratio can be noticed on 7/05 only for $PM_1$. Ammonium salts present a similar behavior to the one observed for soil dust. The ratios in the gallery are in general smaller than 1 while one single enrichment is present on 26/04 for $PM_1$. Mineral salts are characterized by generally higher and extremely variable ratios; on average lower than 1 for $PM_1$ and $PM_{10}$ and slightly higher for $PM_{2.5}$. Particularly high mineral salt I/O ratios in the gallery are present on 26/04 for $PM_{2.5}$ and $PM_{10}$ and on 7/05 for $PM_1$. Generally speaking this situation confirms the dominant outdoor influence on the environmental quality of the gallery, with variations associated only to single discrete events the causes of which are difficult to identify. Knowing the type and dimension of the inorganic particles suspended in the gallery during these events can be an important tool for defining the best conservation strategies for the objects.

Indoor/Outdoor ratios were calculated also for black carbon (Figure 7.10). The observed values remain approximately stable in both locations throughout the whole sampling period, with an average ratio of 0.04±0.01 in the storage and 0.31±0.08 in the gallery. The low average ratios confirm the absence of indoor sources. As a consequence, the closer contact of the gallery with the outside accounts for the 10 times higher ratios registered in this environment compared to the storage. Since elemental carbon enters the atmosphere mainly through incomplete combustion of fossil fuels and biomass,[438] the black carbon observed inside the museum is mostly produced by outdoor traffic. From this point of view, it is interesting to notice how the levels of elemental carbon in the storage are relatively low, even though this environment is indirectly connected to a highway tunnel. The efficiency of the storage insulation in preventing the contamination even from submicron sized outdoor particles is therefore confirmed. The role played by the filtration system in this case is probably secondary to the one played by the underground location of the storage. The black carbon I/O ratios appear in fact from 2 to 10 times lower than the ones observed in HVAC-equipped museums by Ligocki et al., a difference that cannot be explained by a higher filtration efficiency given the state-of-the art quality of the systems installed in these museums and the lower efficiency of filters in removing submicron particles.[91]
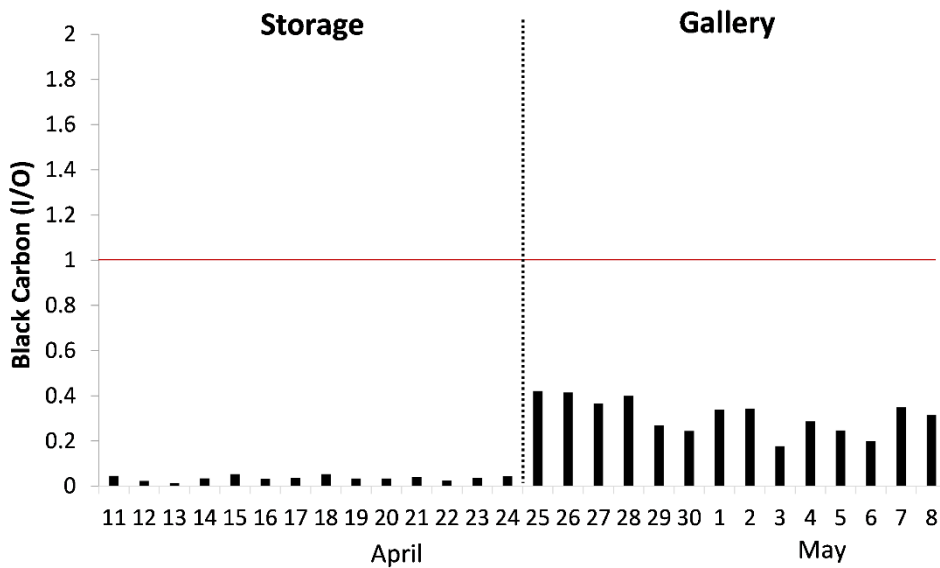
*Figure 7.10_Indoor/outdoor (I/O) daily average ratios for black carbon in storage and gallery.*

### 7.3.4 Continuous monitoring of PM$_{2.5}$

The indoor concentration of PM$_{2.5}$ in terms of number of particles per unit volume was continuously determined by means of Lighthouse Handheld 3016-IAQ particle counter. Continuous measurements allow to obtain much more detailed information about short-time PM variations than daily average measurements. This makes it easier to identify sudden risks for museum collections as well as to reconstruct the sources of PM enrichments. An example is given in Figure 7.11, where the continuous data registered with the particle counter are compared to their daily average. Due to a malfunctioning during the measurements the data from 21/04 23:15 to 26/04 10:15 are missing.
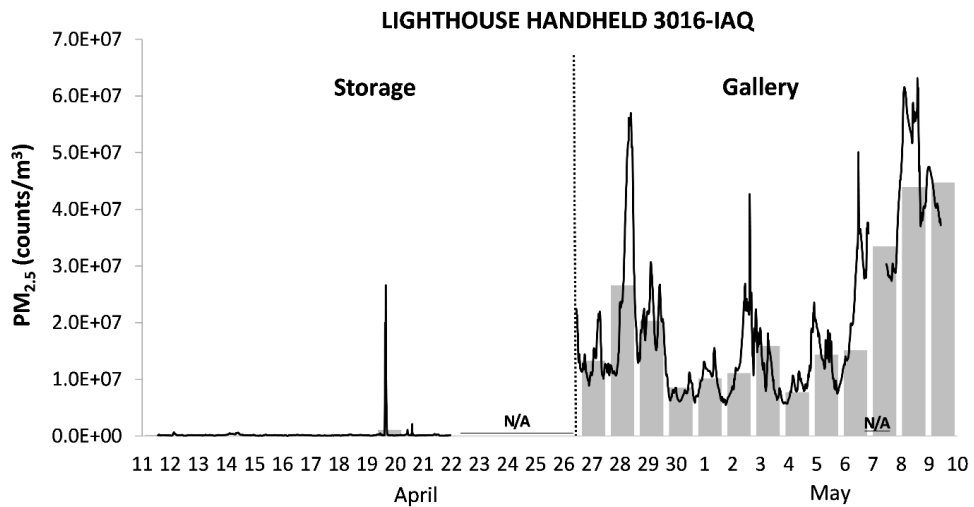
*Figure 7.11_Comparison between continuous monitoring and daily averages of PM$_{2.5}$ with Lighthouse Handheld 3016-IAQ particle counter. N/A=data not available*

Before being able to implement the IEQ-index with continuous PM data, it is necessary to convert the PM$_{2.5}$ threshold value for general collections ($\mu g/m^3$)[74] into an average number of particles/$m^3$. For this reason, the daily average of Lighthouse results is compared with the mass data from Harvard impactors. Different results were obtained for the two different environments, with higher correlation in the storage (r=0.84) than in the gallery (r=0.57). In Figure 7.12 the centered daily average concentrations (Average=0, Standard deviation=1) for storage and gallery are presented. Because of the different correlation obtained, the standardization of the data was performed separately for the two sets. The better correlation observed for the storage is clear from the figure. This behavior is likely caused by the uncontrolled environmental conditions observed in the gallery, closer to an outdoor environment than to an indoor one. The response of light scattering based particle counters is a function not only of particle size, but also of particle refractive index and shape. In an outdoor-like environment particulate matter can present widely differing morphologies and chemical compositions, potentially causing changes in both optical properties and density.[441] These factors lead to the poor correlation between particle counts and mass measurements observed in the gallery. For this reason, the calculation of a PM threshold expressed in counts/$m^3$ in this environment is not feasible without introducing a substantial uncertainty. This makes it impossible to implement the IEQ-index with continuous PM data in a simple and accurate way. On the contrary, in the storage the good insulation from the outdoor

environment and the HVAC system installed grant a significant stability both from a physical and chemical point of view. These conditions produce the good correlation observed in this environment, allowing to convert the $PM_{2.5}$ maximum threshold for general collections (10 $\mu g/m^3$)[74] into a site-specific counts/$m^3$ PM limit value. In this specific case this mass threshold was chosen, but any threshold value can be selected according to the specific needs of the collection considered.
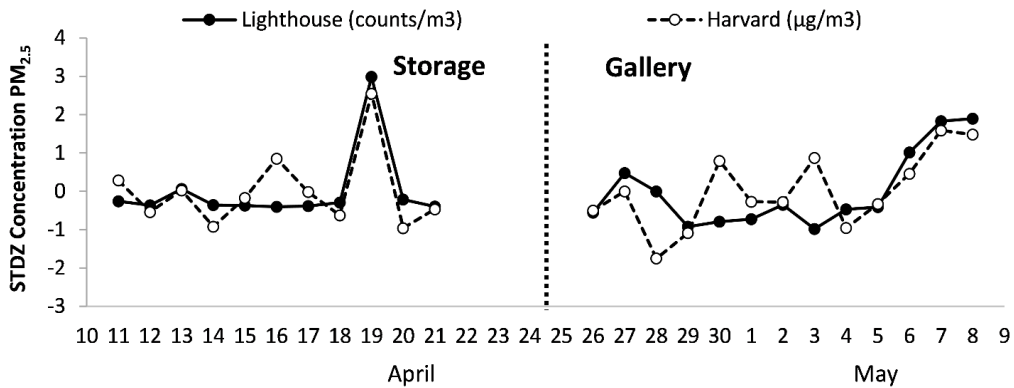


*Figure 7.12_Comparison between the standardized daily concentrations of $PM_{2.5}$ obtained by Lighthouse particle counter and Harvard impactor. The data from the two locations are standardized separately.*

The result of the threshold conversion for the storage is 901043±171674 counts/$m^3$. Given the significant standard error of regression, to prevent the underestimation of possible risks for the collection the greatest lower bound of the range of calculated values is considered. In other words, the difference between the average counts/$m^3$ calculated threshold and the standard error of regression is determined. The resulting value of 729369 counts/$m^3$ is then used as final $PM_{2.5}$ threshold. By applying this approximated limit value to the continuous $PM_{2.5}$ data collected with Lighthouse, it is possible to include PM concentrations in the calculation of the IEQ-index. In this way, a continuous estimate of the risk associated to indoor PM levels can be taken into account when monitoring the environmental quality in an indoor location. The use of continuous PM data for the calculation of the IEQ allows to identify short time events and potentially dangerous situations for the collection, deepening the understanding of the conservation conditions. By using only the daily averages these events may remain hidden, in particular in a relatively clean environment such as the storage.

Further studies will be necessary to better understand the factors influencing the correlation between particle counters response and mass measurements, and consequently the range of applicability of this methodology. At this stage, the successive step has been to try to simplify and reduce the cost of this approach by substituting the expensive Lighthouse device with a low-cost laser particle counter. Different devices suggested for home or office applications are commercially available, but their effective precision and accuracy are still a matter of debate[119,423] and will have to be preventively tested. Efforts in this direction are presented in the second part of this chapter.

### 7.3.5    IEQ-index

To visualize the evolution in time of the indoor environmental quality, the IEQ-index method[426] is applied to the continuous data of the traditional environmental parameters and PM. In Figure 7.13 the environmental data are presented in terms of IEQ analysis with colour coding. This intuitive representation allows a fast evaluation of the indoor environmental quality compared to the selected threshold values. The first two bars in Figure 7.13a represent general IEQ indexes for the collection. In order to underline the effect of including PM analysis in the study of indoor environmental quality, these general indexes are calculated both including and not including particulate matter. In these bars, a specific time instant corresponds to the lowest IEQ value in that instant for the parameter-specific IEQ components. Therefore, red areas indicate that one or more parameters are potentially posing a threat to the objects. The separate bars per parameter (Figure 7.13b,c,d,e) allow to identify which parameter should be improved. Since the implementation of the index with continuous PM data was not possible in the gallery, an average IEQ-index is calculated by including the daily measurement of PM mass with Harvard impactors in this location. The inclusion of average values is not ideal and leads to a loss of short-term information, but it is sufficient to clearly visualize the strong influence of the inclusion of PM on indoor environmental quality evaluation.

Generally speaking, the IEQ analysis highlights the presence of different conservation conditions in the two environments. In the gallery, in particular, the important outdoor influence causes the IEQ to assume very low values for all the considered parameters. This situation exposes the whole collection to a high risk of deterioration and damage. A better insulation of the building and the installation of a HVAC system capable of controlling temperature, relative humidity and PM infiltration rate would significantly improve the conservation conditions. Unfortunately, the dimension of the gallery makes

this type of intervention expensive and complicated. The risk associated with temperature and illumination can be anyway partially contained by limiting the access of direct sunlight (e.g. by covering with reflecting materials the southern facing side of the roof).

On the other hand, in the storage low IEQ values are limited to light intensity and single PM events. Light sensitive objects should therefore not be stored in this room without accurately protecting them by covering and/or without preventively changing the light source to a lower intensity LED light.

The inclusion of $PM_{2.5}$ in the general IEQ index leads to different results for storage and gallery. In the storage, in fact, the inclusion of PM data does not cause visible changes. However, when considering the single IEQ bar for PM, the presence of potentially dangerous peaks of particulate can be observed on the days in which a floor sealant was applied in the room. Therefore, this data representation allows the museum personnel to easily recognize potential threats and to understand their possible causes. The detailed analysis of PM supporting the continuous monitoring and IEQ-index calculation allows to estimate more accurately the real risk on the basis of the type of particles observed. In this case a specific analysis of the organic fraction of PM would be also necessary. The information obtained should anyway lead to the development of safety measures to prevent high PM levels when maintenance operations are performed or to preventively protect the objects if this is not possible.

On the contrary, in the gallery the inclusion of discrete $PM_{2.5}$ data in the general IEQ index leads to a significant change in the results. The collection appears in fact to be under a constant threat when also PM is considered, even in periods in which only short events are taking place according to traditional environmental parameters. The introduction of this additional information underlines the importance of including PM data in IEQ studies. Without considering this parameter the collection would be considered safe, even in moments when PM levels could potentially endanger it. Nevertheless, the impossibility of implementing continuous PM measurements in the IEQ for this location strongly limits the amount of information obtainable with this method. The development of a methodology that can be applied even on the monitoring of uncontrolled environments is therefore of capital importance for the future.
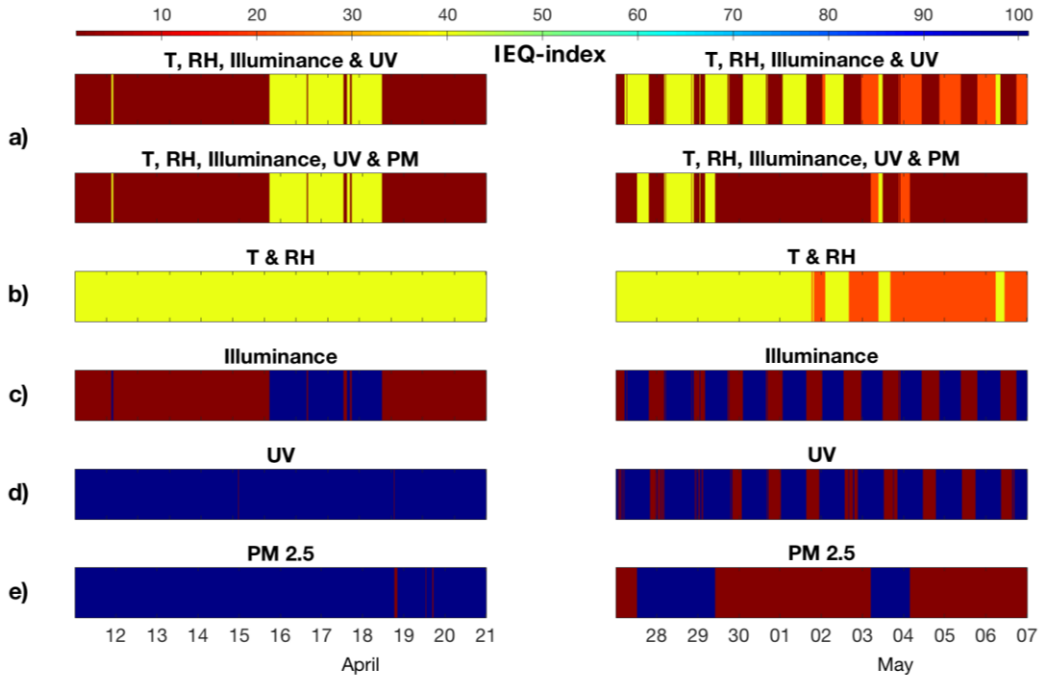
*Figure 7.13_Representation of the IEQ-index[74] in storage (11/04/2016-21/04/2016) and gallery (27/04/2016-7/05/2016) using colour codes (red=higher risk for the collection, blue=lower risk): a) general indexes calculated combining all the considered parameters, PM included and excluded; b) temperature (T) and relative humidity (RH) combined, c) Vis light illuminance, d) intensity of UV radiation, e) PM$_{2.5}$ Lighthouse data (storage) and Harvard impactors data (gallery).*

## 7.4  Conclusions

The present study showed how particulate matter is present in conservation environments in concentrations that can significantly and suddenly vary with time. The presence of sudden events could not be identified by temperature, relative humidity and light monitoring, suggesting the presence of many more risks for museum collections that remain invisible when only traditional parameters are considered. For this reason, it is important to include a continuous monitoring of PM concentration in the evaluation of indoor environmental quality. The methodology discussed in this work allows to implement PM concentrations in the IEQ-index calculation, easily recognizing potentially dangerous conditions for the collections. After recognizing in which periods the collection was at risk, one can further analyze the graphs and understand which parameters need to be improved. When it comes to PM, the chemical characterization of the particulate helps to deeper understand the real risk for the objects and the

reasons behind sudden increases in concentration. The implementation of PM in the IEQ calculation was not possible in uncontrolled environments, therefore the proposed method still needs to be perfected. However, reliable results were obtained when stable environmental conditions and a good insulation from the outdoor environment were granted (ideal conditions for a conservation environment). In conclusion, these results show why and how IEQ calculation methods should be discussed and implemented, not only in terms of PM levels. This, in fact, is not the only potentially endangering parameter excluded from traditional continuous IEQ monitoring. Also the inclusion of continuous data for gaseous pollutants, now hindered by the sensitivity of commercially available sensors, could allow to identify further threats to indoor cultural heritage.

# |7

## [Part 2]

Field testing of low-cost sensors for the monitoring of PM and gaseous pollutants for heritage applications

**A. Marchetti, W. Anaf, A. Cabal, J. Callier, O. Voet, P. Van Espen, O. Schalm, K. De Wael**

# Abstract

In the first part of this chapter, we demonstrated how relevant the implementation of the continuous monitoring of pollutants in IEQ studies can be in order to visualize potential conservation hazards. However, some important obstacles remain on the way for pollutants continuous monitoring to become a routine operation in conservation environments. One of the main limitations to this approach is the high price of well-calibrated monitoring devices (as opposed to T, RH and light sensors).

Recent technological advancements made possible the development of a growing number of small, easy-to-use and low-cost sensors for the monitoring of PM and gaseous pollutants in industrial contexts and households. The possibility of characterizing the IEQ with high temporal resolution, along with the small size and low cost of those sensors, make them extremely appealing for the application in conservation environments. However, due to the frequent lack of detailed quantitative specifications, the independent field testing of these sensors is an essential prerequisite for the application to their full potential.

In this study, five low-cost systems were tested in the context of a 7-months long monitoring campaign in the St. Martin's church in Aalst, Belgium. The performances of two low-cost PM sensors (Dylos DC1100-Pro and Shinyei PPD20V) were evaluated by comparison with a more expensive and well-calibrated Lighthouse Handheld 3016-IAQ particle counter. Preliminary results on the performances of three gas sensors by Alphasense (NO2-A43F, OX-A431 and PID-AH2) were also obtained by comparison with the weekly data collected by means of Radiello® passive samplers. The differential response of the sensors on different climatic conditions and perturbation events was investigated. Generally speaking, the low-cost sensors tested showed extremely promising results, with advantages and disadvantages that are thoroughly discussed in this section of the thesis. The data presented ultimately demonstrate that a critical approach towards the choice and use of commercial sensors for gaseous and particulate pollutants in cultural heritage applications is fundamental.

## 7.5  Introduction

It is widely acknowledged that the conservation state of works of arts is strongly influenced by the quality of their preservation conditions. When it comes to indoor cultural heritage, the overall environmental quality is ideally evaluated by considering both physical (e.g. temperature, relative humidity, intensity of visible light) and chemical parameters (e.g. concentration of gaseous pollutants and airborne particulate matter - PM).[74,75,92,93,215,394,396–398] While several low-cost and relatively easy-to-use commercial systems are commonly used to monitor physical parameters with high-time resolution (seconds or minutes), discrete methods (days or weeks of sampling time) are traditionally employed for chemical pollutants (i.e. diffusive samplers for gas pollutants, impactors for PM sampling).[77,215,400–402,405,407] However, by studying only average concentrations of pollutants, a large part of the information on short-time variations and sudden decreases in the indoor environmental quality (IEQ) are lost (as demonstrated in the first part of this chapter). The loss of this information results in knowledge gaps on the real risk cultural heritage materials are exposed to, hindering the recognition of the hazards causing an inferior IEQ and impeding the deployment of adequate preventive conservation measurements.

Small, easy-to-use and low-cost sensors represent the future of IEQ monitoring.[442] New technologies allow improvements in the development of smaller and more affordable sensors for the monitoring of PM and gaseous pollutants.[114,115] Even though these solutions are usually not appositely designed for the application in museums and conservation environments, the small size and low cost make them extremely appealing. A large number of these new commercial sensors are continuously being produced and often commercialized without providing detailed quantitative specifications (e.g. the effect of T, RH, particle size distribution, PM concentration on the performance of the sensor) which are fundamental to define the applicability in a specific environment.[115] For this reason, the independent testing of low-cost PM and gas sensors both in controlled laboratory conditions and on the field is a crucial step towards the application to their full potential.[443] A large number of studies tackled this issue in the past few years,[114,115,119,120,423,443–460] but the questions about the reliability of these sensors for the application in different types of environments have only been partially answered.[115]

This study contributes to the general need for information on the performances of commercial sensors for gaseous pollutants and PM, in order to fully understand their

advantages and limitations. Given the particular lack of information about low-cost PM and gas sensors in historical buildings and conservation environments, we tested two optical particle counters (OPC) and three gas sensors during a 7-months long monitoring campaign in the St. Martin's church in Aalst, Belgium. The poor insulation of the historical building, together with the carrying out of construction and restoration works both inside and outside the church, allowed to test the sensors in a wide range of environmental conditions (e.g. high to low values of both temperature and relative humidity, dust events, infiltration of outdoor gaseous pollutants).

# 7.6 Materials and methods

## 7.6.1 Experimental design

The field performances of two low-cost PM monitors and three low-cost continuous gas sensors were evaluated against reference methods. All the sensors were connected to a multi-purpose data logger (DataTaker DT85, Thermo Fischer scientific, USA), together with a GMW90 sensor for temperature and relative humidity (Vaisala, Finland). Temperature, relative humidity, airborne PM levels (particles/unit volume) and gas pollutants concentrations (ppb of $NO_2$, $O_3$, VOCs-volatile organic compounds) were measured in phase with a 15-minutes frequency.

The responses of the PM sensors Dylos DC1100-Pro (Dylos Corporation, USA) and Shinyei PPD20V (SHINYEI Technology, Japan) were set against the high-time resolution data collected with a Lighthouse Handheld 3016-IAQ particle counter (Lighthouse Worldwide Solutions, USA). The well-calibrated Lighthouse particle counter is considered as the reference device. Due to the saturation of the internal HEPA filter, the reference counter had to be switched off and sent back to the producer for maintenance for approximately 1 month (15/05/2018 – 21/06/2018) during the measuring campaign (12/2017 – 07/2018).

The preliminary results of the gas sensors NO2-A43F ($NO_2$), OX-A431 ($O_3$) and PID-AH2 (VOCs) (Alphasense, UK) were compared to the average weekly data collected by means of Radiello® passive samplers (Fondazione Salvatore Maugeri, Italy). The Radiello® analysis of VOCs focused on seven volatile compounds that can be considered as markers

for different VOCs sources inside and outside the church (wooden furniture: α-pinene,[461] acetic and formic acid;[63] traffic: toluene;[462] polyethylene plastic used for temporary protection of the church interior: 2-ethyl-1-hexanol;[463] industry: ethanol and ethylacetate[464]). The analysis of gaseous pollutants with Radiello® passive samplers is a well-established method and is considered in this study as the reference measurement. Given the relatively high cost of these samplers, only a preliminary investigation was conducted over a period of 6 weeks (21/12/2017–6/02/2018).

## 7.6.2   PM sensors

All the PM sensors considered are optical particle counters (OPC, Section 1.4.6 of this thesis). In general, different sensors employ slightly different technical solutions to measure the PM concentration over time. Table 7.3 gives an overview of the technical specifications of the particle counters considered.

Most OPC perform a size discrimination of the airborne particles based on their scattering properties. In addition, some commercial particle counters allow to obtain information on PM mass concentrations ($\mu g/m^3$). However, although number of particles (calculated from light scattering) and PM mass are intuitively related, the nature of this relationship is strongly affected by some properties that can vary over time, such as the chemical composition, the density, the shape and the optical properties of the aerosol.[118–121]

The **Shinyei PPD20V**, further referred to as the Shinyei, is a simple low-cost sensor for the measurement of PM levels. Only a limited number of recent studies focused on the performances of Shinyei particle counters.[114,120,444,456–460] Of these studies, most did not consider the PPD20V sensor used in the present work (only[114,456]), but the very similar PPD42V.[120,444,457–460] All these publications tried to correlate the response of the counters with PM mass measurements. In these studies Shinyei PPD20V generally performs poorly (good correlation observed only for high concentrations in one out of three locations by Johnson et al.[456]), but no real information on how the counter would perform when compared with other particle counting monitors is collected. The only different study from this point of view is the one by Prabakar et al.,[444] evaluating the performances of a Shinyei PPD42V against a Dylos 1100-Pro. A good correlation is observed between the daily average of the sensors outputs ($R^2 \approx 0.81$), but no

information on short-time variations and no comparison with a well-calibrated certified method is presented.

The **Dylos DC1100-Pro**, here called the Dylos, is a low-cost sensor designed for the monitoring of PM levels in offices and homes. More information is available in literature on the performances of Dylos particle counters,[119,423,444–451,465] but only few of these studies focused on the Dylos DC1100-Pro.[119,444] As for the Shinyei, most of the published works compare the output of the counters with $PM_{2.5}$ mass concentration results from reference methods. The work by Prabakar et al.[444] is one of the few studies considering the direct response of this counter, but here, as previously mentioned, Dylos is used as a reference to evaluate the performances of a second monitor. In another study by Manikonda et al.,[119] the number of particles detected by Dylos is compared both with mass measurements and with reference particle number concentrations in controlled laboratory conditions. In this last study, different correlations are observed depending on the type of particles considered ($R^2$ from 0.67 to 0.99). To the authors' best knowledge, no field study on the comparison between the direct output of Dylos 1100-pro and a reference particle counter has been performed. In literature, Dylos particle counters are often used to obtain information on the mass concentration of airborne PM. In this study, the algorithm described in the context of the project "Air Quality Sensor Network for Philadelphia" of Drexel University[466] was applied for the conversion of particle counts into mass data. A more detailed description is given in the supporting information (Section 7.10.1).

The more expensive **Lighthouse Handheld 3016-IAQ** air particle counter (further indicated as the Lighthouse) was used as a reference. This monitor is designed to respect the ISO 21501-4 directives in terms of accuracy and precision for the measurement of size and concentration of particles suspended in air. Many examples of the application of this OPC in various indoor environments are available in literature.[422,467–477] In addition, the Lighthouse instrument calculates $PM_{2.5}$ concentration in µg/m$^3$ as a direct mass output during the measurement. More information on the formula employed by the instrument for the conversion is given in the supporting information (Section 7.10.2). The direct mass concentration output of Lighthouse was used as a reference in the comparison with the Dylos mass data.

*Table 7.3_Overview of the specifications of the three OPC used in this study, as found in the technical sheets of the devices.*

| Specifics | Shinyei PPD20V | Dylos DC1100-Pro | Lighthouse Handheld 3016-IAQ |
|---|---|---|---|
| Price | c. $120 | c. $600 | c. $4500 |
| Dimension | 8x6x2 cm | 18x11x8 cm | 22x13x6 cm |
| Light source | Infrared light-emitting diode | Red laser diode (650 nm) | Red laser diode |
| Internal optics | Plastic focusing lens | None | Multiple collection optics |
| Detector | Photo-diode. c. 45° from light source | Photo-diode. 90° from light source | Photo-diode. Non-specified position |
| Air sampling | Convective (small 0.25 W resistor) | Mechanical (low pressure computer fan) | Mechanical (Vacuum pump) |
| Level of sound | None | Fan makes some noise | Pump makes noise |
| Size discrimination | c. >1 μm | >0.5 μm (Fine channel) >2.5 μm (Coarse channel) | >0.3 μm, >0.5 μm, >1 μm, >2.5 μm, >5 μm, >10 μm |
| Counting accuracy | Not specified | Not specified | 50% >0.3 μm 100% >0.45 μm |
| Maximum PM concentration | $3.0*10^7$ particles/m3 | Not specified | $1.4*10^8$ particles/m3 |
| Output | Analog voltage (c. #particles/unit volume) | #particles/0.01ft3 | #particles/m3 |
| Direct PM mass output | No | No | Yes |

### 7.6.3 Gas sensors and Radiello® passive samplers

The NO2-A43F $NO_2$ sensor and OX-A431 $O_3$ sensor by Alphasense (Table 7.4) are both electrochemical sensors based on a 4-electrode cell. Detailed information on the working principle of these sensors can be found on Alphasense website.[478] Alphasense provides several formulas to calculate the gas concentration from the measured signals (voltages), leading to significantly different results and creating an overall confusion. This problem is addressed more in detail in the supporting information (Section 7.10.3), where more information on how the gas concentrations were calculated from the voltage outputs can be found as well. Only few recent articles studied the response of these sensors[114,443,479–484] and to our knowledge no test in a historical building was performed. In general, the correlation observed between these sensors and reference

263

methods appears to be extremely variable. In addition, the response seems to be affected by cross-sensitivity problems and by a certain influence of relative humidity.[443]

*Table 7.4_Overview of the specifications of the three gas sensors considered in this study, as found in the technical sheets of the devices.*

| Specifics | NO2-A43F | OX-A431 | PID-AH2 |
|---|---|---|---|
| Price | c. $ 150 | c. $ 150 | c. $ 400 |
| Dimension | 2 cm Ø x 2 cm | 2 cm Ø x 2 cm | 2 cm Ø x 2 cm |
| Type of sensor | Electrochemical | Electrochemical | PID (UV lamp = 10.6 eV) |
| Analyte | NO2 | NO2+O3 | VOCs (non-selective) |
| Cross-sensitivity | NO (strong +), H2S (weak -), SO2 (weak +) | NO (strong +), H2S (weak -), SO2 (weak -) | Non specified |
| LOD | Non specified | Non specified | 1 ppb isobutylene |
| Linearity range | 0 - 20 ppm | 0 - 20 ppm | 1 ppb - 50 ppm isobutylene |
| Output | ppb (calculated from voltage) | ppb (calculated from voltage) | voltage (α total VOCs) |
| Level of sound | None | None | None |

The **PID-AH2 sensor** measures all volatile organic compounds (VOCs) in air by photoionisation detection (PID). Detailed information on the working principle of this sensor can be found on Alphasense website.[478] No information could be found in literature on the application of this specific sensor for the monitoring of VOCs levels in indoor environments. Only the older model of this sensor (PID-AH), found recent application both as a detector for gas chromatography[485,486] as well as in the environmental monitoring of specific compounds.[487,488] However, the performances of the sensor have not been discussed in detail yet.

As a reference, $O_3$, $NO_2$ and VOCs environmental concentrations were determined by means of **Radiello® diffusive samplers** (Fondazione Salvatore Maugeri, Italy). This sampling method is widely tested, commonly used and trusted for the quantification of gaseous pollutants both in indoor and outdoor environments (here reported some review articles and recent studies,[489–494] more can be found on Radiello website[117]).

These passive samplers allow an easy and noiseless sampling but are relatively expensive and require an extended sampling period. More information on the working principle of the diffusion tubes and on the experimental procedures employed for the quantification of the different analytes is reported in the supporting information (Section 7.10.4).

### 7.6.4   Study location

The results discussed below were collected over a period of approximately seven months (December 2017-July 2018) in the St. Martin's church in Aalst, Belgium. The multi-sensor tool, together with all other devices and samplers previously described, were located at the organ loft at a height of around 7 meters (Figure 7.14b).

The St. Martin's church, prime example of late Brabant Gothic style, was built over a period of 180 years from 1480 onwards. This extremely voluminous building hosts a large and diverse collection of work of arts by Flemish painters and sculptors, including "The Pestlijders" by Peter Paul Rubens. The church is located in the very city center of the city of Aalst (50°56'16"N 4°02'28"E), a small center (80.000 inhabitants) less than 30 kilometers north-west of Brussels. Therefore, the location is a typical urban environment, with the possible additional influence of industrial sites located in the immediate proximity (Tereos Starch & Sweeteners: wheat starch plant, Combined Heat Power plant and bioethanol facility) (Figure 7.14a).
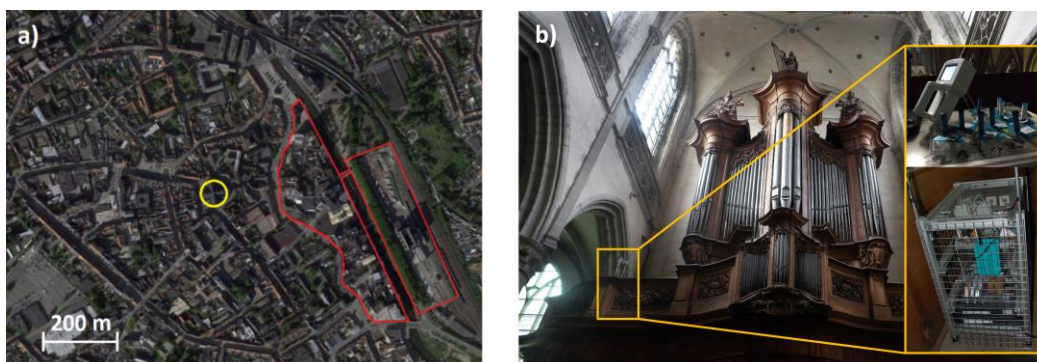


*Figure 7.14_a) Satellite image of the city center of Aalst, Belgium. The St. Martin's church is indicated by the yellow circle and the industrial production site of Tereos Starch & Sweeteners by the red area. b) Monitoring unit and sampling location.*

In this type of environment, several outdoor and indoor pollution sources can exist that might affect the overall IEQ. Given the presence of large and non-well-insulated doors in the building, PM (both fine and coarse) and gases directly or indirectly produced by the outdoor traffic, household heating or industry may easily enter the building.[77,78,464,465] Indoor PM sources, such as the presence of visitors (coarse fraction) and the burning of candles (fine fraction), have been found to have a significant influence on the indoor environmental quality of churches,[465,495] and will likely be relevant also in this case. In addition, the church underwent a series of building and restoration works during the sampling campaign that might have significantly affected the IEQ. Such extreme events during the sampling campaign allowed the authors to test their sensors in a wide range of environmental conditions.

## 7.7 Results and discussion for the PM sensors

### 7.7.1 Concentration time series

A first comparison of the raw data of the three different particle counters showed clearly non-random distributions and similar concentration trends. As illustrated in Figure 7.15, a time shift between Dylos and the other two sensors was observed, as well as a clear loss of sensitivity for the Lighthouse particle counter over time.
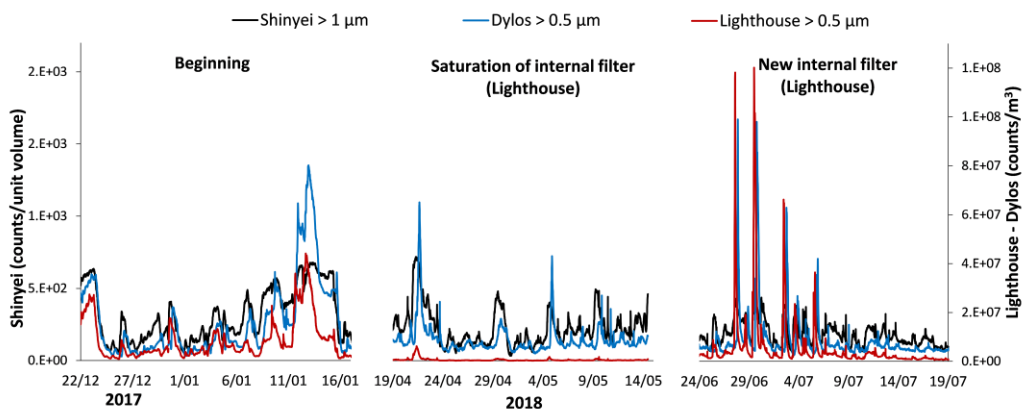


*Figure 7.15_Concentration time-series data for the three particle counters (smaller channel for Lighthouse and Dylos) over three periods of approximately one month each: at the beginning of the campaign, immediately before changing the internal HEPA filter of Lighthouse and immediately after that.*

With regards to the time shift, the Dylos counter showed an average delay of 6 hours and 45 minutes (± 45 minutes) compared to both Lighthouse and Shinyei. Of the two previous works considering Dylos DC1100-Pro, Prabakar et al.[444] studied only daily averages of the data, potentially not being able to notice short time shifts, while Manikonda et al.[119] considered higher time resolutions but still did not observe any delay. No clear correlation could be observed between the magnitude of the irregular delay and other parameters such as time, temperature, relative humidity and absolute PM concentration ($|r|<0.3$, Table S7.5). No clear explanation can therefore be found for the presence of this delay. In order to allow the comparison of the concentration values registered by the three sensors, the average time shift of Dylos was corrected (i.e. the data was shifted backwards of 6 h and 45 min).

On the other hand, the loss of sensitivity of Lighthouse showed an exponential dependency from time. The decrease in the signal observed is a consequence of the instrumental design of the monitor. The internal HEPA filter, in fact, gets slowly saturated after a sampling time in an environment characterized by intense dust events (such as the church during restoration works). A correction for the sensitivity loss was performed during the data analysis. More details are given in the supporting information (section 7.10.6).

## 7.7.2   Accuracy fine fraction

The accuracy of the tested low-cost sensors was evaluated by direct comparison with the PM reference data (Lighthouse corrected for the sensitivity drift). In the first place, the particle number concentrations registered by Shinyei and Dylos (fine channel) were set against the results for the reference Lighthouse>0.5 µm channel. Then the relative error (RERR) was calculated according to Equation 7.1, and the correlation between its magnitude and parameters such as temperature, relative humidity and absolute PM levels was investigated in order to verify the possible influence of environmental parameters on the differential response between sensors.

$$RERR = \frac{PM_{Measured} - PM_{Reference}}{PM_{Reference}} \tag{7.1}$$

Where $RERR$ is the relative error at a specific time t, $PM_{Measured}$ is the PM concentration registered by the low-cost counter considered at the time t and $PM_{Reference}$ is the concentration registered by Lighthouse at the time t.

In the scatter plots in Figure 7.16 it clearly appears how a generally good correlation between the instrumental responses can be observed. The main difference between the two low-cost sensors lies in the nature of this correlation. Dylos, in fact, presents a linear correlation with the Lighthouse data, with an angular coefficient relatively close to the unity. The average ratio Dylos/Lighthouse=0.71±0.26 reflects the high similarity between the results of the two particle counters.
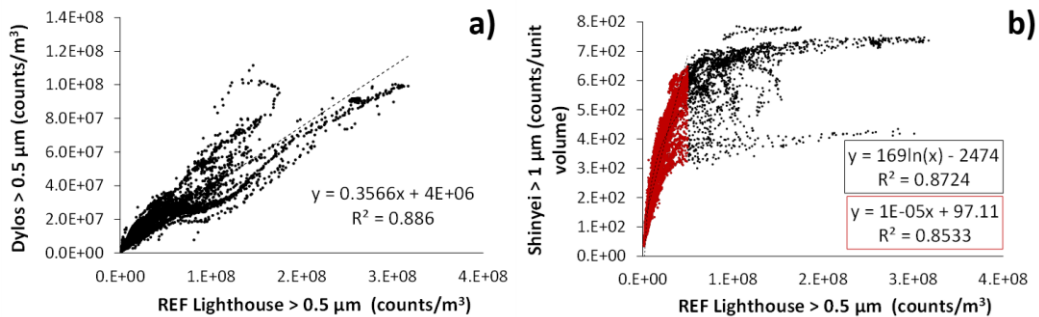


*Figure 7.16_Comparison between the concentration data measured by the tested sensors and the reference PM data (Lighthouse>0.5 μm corrected for the sensitivity drift): a) Lighthouse VS Dylos>0.5 μm, linear fit; b) Lighthouse VS Shinyei, exponential fit; in red Lighthouse below 5.0\*10^7 particles/m³ VS Shinyei, linear fit.*

On the contrary, Shinyei data show a clear deviation from linearity at high PM concentrations (the best fit for the experimental data is a logarithmic function). The direct link between the underestimation of the PM levels by Shinyei and the absolute PM concentration in the environment is confirmed by the relatively high negative correlation coefficient observed between RERR and the PM reference (Table 7.5). The tendency of Shinyei to systematically underestimate the real concentration for high PM levels is the consequence of a saturation of the counter, meaning that most of the particles present are not converted into a visible signal above a certain PM concentration. This drawback of the instrumental design is mentioned by the manufacturer itself, indicating a nominal upper limit of the linearity range of $3.0*10^7$ particles/m³.[496] The response plateau showed by Shinyei is located at approximately 700 counts/m³, corresponding to a PM concentration of $≈4.0/5.0*10^7$ particles/m³

268

(Lighthouse reference data) and being therefore in good agreement with the nominal limit mentioned by the manufacturer. Up to this concentration, the Shinyei shows a good linear correlation with the reference data (Figure 7.16b).

*Table 7.5_Correlation between the relative error (RERR) of Shinyei (set against Lighthouse reference data>0.5 μm) and time, temperature (T), relative humidity (RH), size distribution (fraction of PM larger than 1, 2.5, 5 and 10 μm) and total concentration of PM > 0.5 μm.*

| SHINYEI | Time | T | Lighthouse 0.5-1/0.5 | Lighthouse 0.5-2.5/0.5 |
|---|---|---|---|---|
| Pearson's r | 0.01 | 0.02 | -0.16 | -0.10 |
| p value | 0.03 | 0.03 | 0.00 | 0.00 |
| | RH | Lighthouse>0.5 | Lighthouse 0.5-5/0.5 | Lighthouse 0.5-10/0.5 |
| Pearson's r | -0.01 | -0.71 | 0.05 | 0.05 |
| p value | 0.24 | 0.00 | 0.00 | 0.00 |

The absence of a correlation between the relative error of Shinyei and the registered temperature is particularly interesting. The convective flow that the low-cost counter exploit to draw particles into the scattering chamber, in fact, is supposed to be influenced by the ambient temperature, being dependent on the temperature gradient. Most likely, the temperature changes observed in the church (6-28˚C) are not extreme enough to cause a visible effect. A similar behavior is reported by Holstius et al.,[457] who found no temperature effect on the experimental output of a Shinyei PPD42V (same sampling mechanism as the PPD20V) during mild temperature changes (20-30˚C). Only in more extreme temperature conditions (Min=-3.5˚C), a temperature dependency was observed for this particle counter by Gao et al..[459]

In terms of absolute response, the values registered by Shinyei are much lower than the reference values (Average Shinyei/Lighthouse=$2.1*10^{-5}\pm0.7*10^{-5}$). The huge difference in sensitivity is related to the fact that the low-cost counter gives a response in terms of analog voltage changes and not directly in terms of number of particles per cubic meter. According to the manufacturer the two properties are directly proportional (and the experimental data seem to confirm this suggestion), but the proportionality coefficient is not further expressed. The low response of Shinyei is therefore probably related to the

presence of a low proportionality coefficient linking the registered changes in voltage and the number of airborne particles.

For Dylos, on the other hand, only a limited correlation was observed between the RERR and the absolute PM concentration (Table 7.6). The absence of a clear significant correlation of the error with all the considered parameters does not allow to identify one specific mechanism. In general, the different design and components of the instruments can be considered responsible for the slightly different behavior. The presence of an irregular time shift between the two counters likely plays a role in the loss of correlation as well. It is anyway interesting to notice how changes in the size distribution of the airborne particulate matter do not seem to affect the accuracy of the response of the counters.

*Table 7.6_Correlation between the relative error (RERR) of Dylos > 0.5 µm (set against Lighthouse reference data) and time, temperature (T), relative humidity (RH), size distribution (fraction of PM larger than 1, 2.5, 5 and 10 µm) and total concentration of PM > 0.5 µm.*

| DYLOS | Time | T | Lighthouse 0.5-1/0.5 | Lighthouse 0.5-2.5/0.5 |
|---|---|---|---|---|
| Pearson's r | 0.33 | 0.31 | -0.22 | -0.22 |
| p value | 0.03 | 0.03 | <0.01 | <0.01 |
| | RH | Lighthouse>0.5 | Lighthouse 0.5-5/0.5 | Lighthouse 0.5-10/0.5 |
| Pearson's r | 0.06 | -0.46 | -0.10 | -0.08 |
| p value | 0.24 | <0.01 | <0.01 | <0.01 |

### 7.7.3   Accuracy coarse fraction

At this point, in order to test the accuracy of Dylos also in counting coarse particles, the data of the >2.5 µm channel of this counter were set against the reference Lighthouse>2.5 µm channel. In a similar fashion as for the finer particles channel, the relative error was calculated (Equation 7.1) and its dependency on various environmental parameters was investigated.

The results are extremely similar to the ones previously observed for the fine fraction, with a good linear correlation with the Lighthouse reference data and a slope relatively close to the unity (Figure 7.17). The average Dylos/Lighthouse ratio=0.72±0.25 is extremely similar to the one already observed for the finer size channel (0.71±0.26). The performance of Dylos in terms of accuracy is therefore comparable for the two fractions. Furthermore, the good correlation observed for both size channels means that the scattering-based size discrimination of the low-cost counter is comparable to the one of the more expensive Lighthouse.
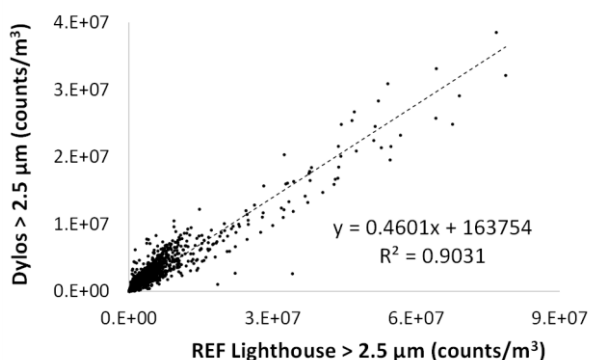


*Figure 7.17_ Comparison between Dylos and Lighthouse corrected coarse fraction data (>2.5 µm). In evidence the linear best fit.*

Also in the case of the coarse fraction there seems to be no univocal factor behind the deviation from linearity of the counter (Table 7.7). A partial role could be played by time, temperature and relative humidity (all factors correlated with each other) but the coefficients are too small to truly recognize an interdependency. A certain influence of relative humidity on the light scattering properties of the particles could be expected,[497] especially when it comes to hygroscopic species such as coarse salt particles and to extreme RH changes like the ones observed in the church (25-90%). If the reference counters algorithm actually corrects for changes in the relative humidity (it is not mentioned by the producer but the counter has an integrated sensor for T and RH), changes in RH could actually justify a loss of correlation.[454] However, a correlation factor of 0.51 ($r^2$=0.26) alone is not enough to explain the mechanism behind the discrepancies between Dylos and Lighthouse results.

*Table 7.7_Correlation between the relative error (RERR) of Dylos > 2.5 µm (set against Lighthouse reference data) and time, temperature (T), relative humidity (RH), size distribution (fraction of PM larger than 5 and 10 µm) and total concentration of PM > 2.5 µm.*

| DYLOS | Time | T | Lighthouse 2.5-5/2.5 |
|---|---|---|---|
| Pearson's r | -0.50 | -0.55 | 0.21 |
| p value | 0.03 | 0.03 | <0.01 |
| | **RH** | **Lighthouse>2.5** | **Lighthouse 2.5-10/2.5** |
| Pearson's r | 0.51 | -0.41 | 0.16 |
| p value | <0.01 | <0.01 | <0.01 |

### 7.7.4 Mass results comparison

In a similar fashion as previously observed for the particle number concentration results, the relative accuracy of the PM mass values obtained with Dylos was evaluated by comparison with the Lighthouse's mass results. In the case of PM mass results, however, it is impossible to objectively define which one of the counters is giving the best estimate of the real $PM_{2.5}$ concentration. The Lighthouse instrument, in fact, only respects specific regulations concerning particle counting, and not mass measurements. In addition, the principle the particle counters are based on is different than the one of the instruments measuring the mass of specific PM fractions. The counters, in fact, separate the particles into size channels based on their optical properties, and therefore on the basis of an "optical" diameter. This property is certainly related to the aerodynamic diameter used to define the different PM class of particles, but the two dimensions does not necessarily coincide.[115,441]

In Figure 7.18, the scatter plot of the $PM_{0.5-2.5}$ mass data is presented. For continuity, a "relative error" of Dylos compared to Lighthouse was calculated (Equation 7.1) also in this case, but the meaning here is that of a relative difference between values rather than a real error against a reference. A certain linear interdependency is present between the two datasets, but the correlation appears to be much lower than previously observed for the particles number data. Another interesting difference is the module of the slope of the linear fit, much lower now than in the previous cases. Even though the starting particle number data are extremely similar in terms of both relative and absolute

272

values, the two approaches lead to significantly different $PM_{0.5-2.5}$ mass results. This type of result did not come unexpectedly, given the different starting assumptions made in the two cases and the apparent absence of a humidity correction factor in the Lighthouse algorithm. However, RH does not seem to play a role in the deviation from linearity (Table 7.8).
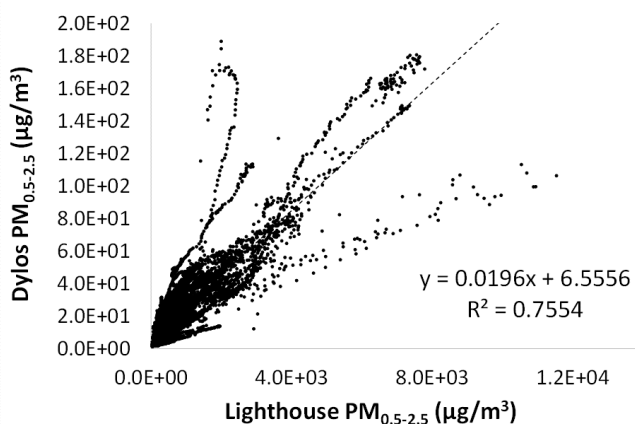


*Figure 7.18_Comparison between Dylos and Lighthouse corrected coarse fraction data (>2.5 μm). In evidence the linear best fit.*

*Table 7.8_Correlation between the relative error (RERR) of Dylos $PM_{0.5-2.5}$ mass results (set against Lighthouse $PM_{0.5-2.5}$ mass data) and time, temperature (T), relative humidity (RH) and total concentration of $PM_{0.5-2.5}$.*

| DYLOS | Time | T | RH | Lighthouse $PM_{0.5-2.5}$ |
|---|---|---|---|---|
| Pearson's r | 0.35 | 0.35 | -0.08 | -0.35 |
| p value | <0.01 | 0.03 | <0.01 | <0.01 |

In conclusion, the lack of a good correspondence between the mass measurements of the two counters constitutes a solid warning on the highly approximate nature of these results. In this case, the values measured by Lighthouse appear too high to be accurate. The concentrations measured by Dylos are still extremely high, in particular for a conservation environment (up to 20-fold the highest suggested ASHRAE threshold for general collections[74]), but surely more realistic. The advertised possibility of using these optical particle counters as PM mass monitors might be extremely temping for conservators, given the opportunity to directly compare high-time resolution data with

literature thresholds (as of today, no PM thresholds for conservation environments expressed in terms of particle number concentration has been defined). The new results presented here help understanding how different counters and different assumptions made in the conversion of particle counts into mass values can lead to completely different results, making any interpretation potentially misleading.

# 7.8 Preliminary results for the gas sensors

## 7.8.1 Reference data (Radiello®)

Over the six weeks of analysis relatively low concentrations of gaseous pollutants were observed. This is particularly true for $O_3$, where 4 out of 6 total measurements showed results below the limit of detection indicated by the manufacturer (2ppb for one week of exposure).[117] Due to the low concentrations, most of the triplicate analysis (5 out of 6) presented a relative standard deviation higher than the 7% indicated by the manufacturer (between 12 and 25%). The low concentrations are good news from the point of view of the conservation of the work of arts present in the church,[63] but they make the comparison with the continuous sensor extremely difficult and subject to a high uncertainty.

$NO_2$ levels, on the other hand, were always higher than the limit of detection indicated by the manufacturer (1ppb for one week of exposure)[117] but lower than the suggested threshold for conservation environments.[63] The higher concentrations translated into more precise results (relative standard deviation between 6 and 8%), allowing a more efficient comparison with the electrochemical sensor.

The analysis of VOCs proved the presence of extremely low concentrations in this environment. The only gas considered showing values always higher than the experimental LOD was toluene, for all the other six gases only 8 triplicate measurements showed meaningful values (1 acetic acid, 1 ethanol, 1 ethyl acetate, 3 α-pinene, 2 2-ethyl-1-hexanol, none formic acid). The reference concentrations can be found summarized in Table S7.6.

## 7.8.2   Sensors response

The concentration time series obtained with the gas sensors tested over the seven months of sampling are shown in Figure 7.19. It is immediately clear how the data appear very noisy, to the point that for the VOCs sensor PID-AH2 no features can be clearly distinguished (a part for an unexplained gradual decrease of the experimental noise in March-April). The lack of a clear signal is likely a result of the very low VOCs levels in the environment (as demonstrated by the reference measurements).
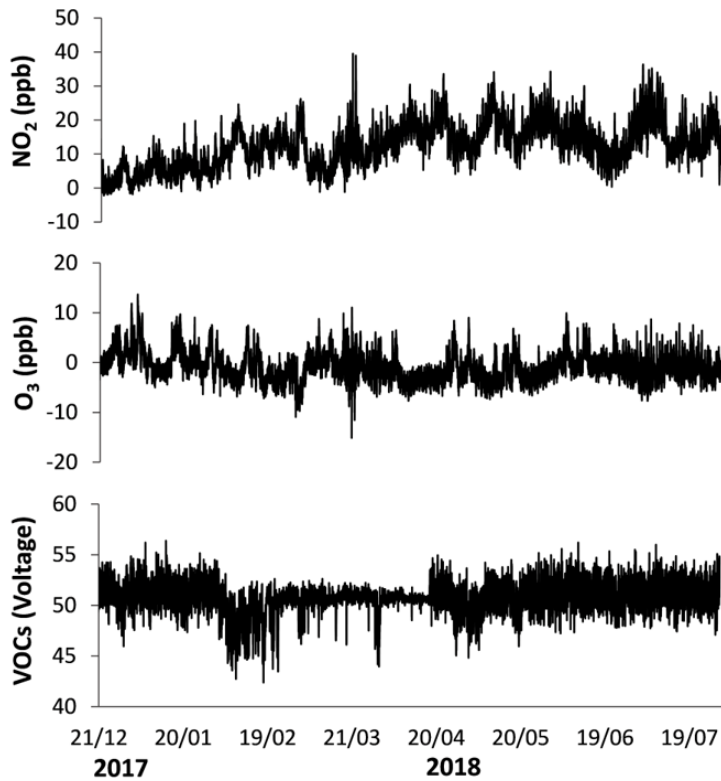


*Figure 7.19_Concentration time series over the whole sampling campaign for the low-cost gas sensors considered.*

In a different fashion, the $NO_2$ and $O_3$ sensors showed a clearly non-random response, which allowed to calculate corresponding concentration values. However, as clearly visible in Figure 7.19, negative concentrations were often obtained. This is especially the case for the $O_3$ sensor, showing concentration values below zero in over 50% of the collected data points (median=-0.2 ppb). The $NO_2$ sensor, on the contrary, returns

negative concentrations only less than 2% of the time. The presence of this large amount of physically impossible concentration values for $O_3$ is likely a consequence of the methodology used to quantify the concentration. The cross sensitivity of the sensor for $NO_2$, in fact, makes it necessary to calculate and subtract the contribution of this gas from the final signal. This additional data treatment introduces extra uncertainty and, potentially, systematic errors affecting the accuracy of the results.

### 7.8.3 Average weekly accuracy

After studying the concentration trends over the whole sampling period, the weekly average sensors' data for a period of 6 weeks were compared with the reference Radiello® results in order to obtain preliminary information on the sensors' accuracy (Figure 7.20). The error bars in Figure 7.20 represent the standard deviation of the three replicate measurements for Radiello.



a)
y = 0.8409x + 0.4801
$R^2 = 0.9186$
x=y

b)
y = 0.8977x - 0.4558
$R^2 = 0.5939$
x=y
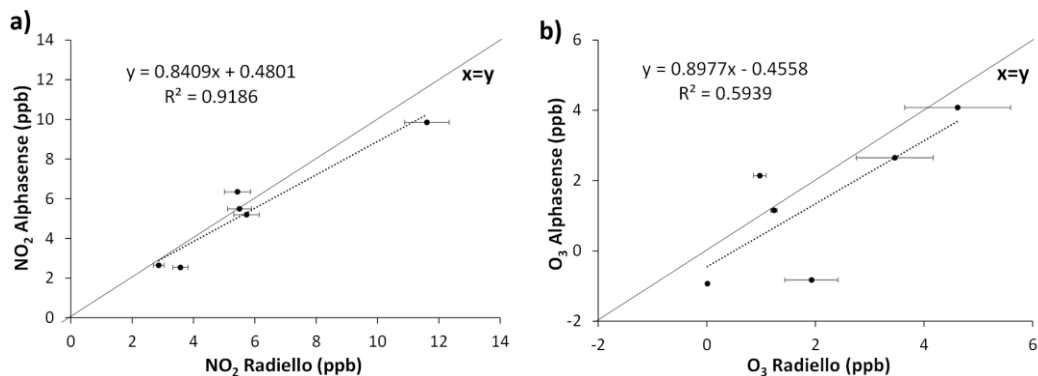
*Figure 7.20_ Comparison between the weekly average concentrations of $NO_2$ (a) and $O_3$ (b) registered by Alphasense and Radiello.*

The results for $NO_2$ present a promising linear correlation, with a slope extremely close to the unity (Figure 7.20a). This indicates a good average accuracy for the NO2-A43F sensor. The $O_3$ sensor, on the contrary, showed a much lower correlation, although the slope of the linear best fit remains close to one. The lower correlation between the response of the sensor and the reference values is probably a consequence of the lower environmental concentration for this gas in the church. This translated into both higher uncertainty for the reference measurements and higher noise influence on the sensors output.

276

# 7.9 Conclusions

### 7.9.1 PM sensors

The two low-cost PM sensors tested in this study showed a generally accurate response when compared to a reference particle counter. These positive results translate into a great potential for the application of these sensors in the IEQ monitoring of churches and historical buildings in general. Since some drawbacks were also observed, it is fundamental to be well-aware of the presence of both advantages and disadvantages when one specific sensor is selected. Positive and negative characteristics of all the sensors considered are summarized in Table 7.9.

In detail, the **Dylos DC1100-Pro** showed high accuracy and sensitivity in comparison with the reference counter for both size channels. The main drawback observed for this monitor was the presence of an irregular time delay when compared with Lighthouse. It was not possible to identify any clear correlation between the size of the delay and any of the experimental properties measured. This could constitute a problem when a high time resolution is needed in order to understand the causes behind a specific PM event. In general, however, the agreement observed between the two counters in an extremely wide concentration range ($1.3*10^6$-$3.2*10^8$ particles/m$^3$), together with the absence of changes in sensitivity over time and in a wide T and RH range, make Dylos a good candidate for the monitoring of PM levels in historical buildings even for long periods. Pairing a low-cost Shinyei to the Dylos could be sufficient to verify the presence of large time shifts in the data, being this second sensor not affected by time delays.

In addition to the absence of time shifts, the **Shinyei PPD20V** showed no clear negative effect of T and RH on the sensor's response, contrarily to what expected given the convective nature of the air stream entering the counter. However, the Shinyei also systematically underestimates high environmental PM concentrations. From a practical point of view, this could lead to a wrong perception of the real risk artistic objects are exposed to, due to an underestimation of the severity of the most intense PM events. Furthermore, the sensor's output is not directly expressed in terms of number of particles/m$^3$, making the cross calibration with a well-calibrated monitor necessary to obtain information on the absolute PM concentrations. In general, the response of Shinyei could be considered reliable for environmental concentrations of particles larger than 0.5 μm below $5.0*10^7$ particles/m$^3$. If detecting the presence and the magnitude of

intense PM events is the aim of the study, however, relying on Shinyei PPD20V alone could lead to significant errors. The use in combination with a second different sensor, such as Dylos 1100-pro, could allow to both calibrate the Shinyei and detect deviations from a linear response at high concentrations, while at the same time recognizing possible time delays in the Dylos' response.

Even the reference **Lighthouse Handheld 3016-IAQ**, in any case too expensive to be used for routine PM monitoring in historical buildings, showed important limitations for the application in this type of environment. When high PM concentrations are present even for short periods of time, in fact, the internal HEPA filter tends to get saturated in a matter of few weeks. This leads to a decrease in the true sampling rate of the instrument, resulting in an underestimation of the PM concentration close to 50% after only 3 weeks and reaching 90% approximately 3 months from the starting of the measurement. Changing the internal filter allows to restore an ideal response, but any intense PM event can trigger again an exponential decrease in sensitivity with time. These results should suggest caution in the employment of this monitor for periods longer than 2-3 weeks in environments characterized by high-PM events, even short in time (few hours).

In conclusion, the synergic use of Dylos and Shinyei could represent the best solution for the monitoring of PM particles number concentration in an historical building potentially subject to intense PM events. The combined use of these sensors could in fact allow to both calibrate the Shinyei and detect deviations from a linear response at high concentrations (with Dylos), while at the same time recognizing possible time delays in the Dylos response (with Shinyei). This relatively low-cost solution (≈700$) did not show any loss of sensitivity problems over the 7 months of sampling, overcoming even the limits of the more expensive Lighthouse unit (≈4500$). Given the positive results obtained in this study, it could be now interesting to test these sensors in a "cleaner" environment (e.g. a museum with state-of-the-art air filtering systems), pushing the low-cost sensors towards their limit of detection. Furthermore, even though counters like Dylos and Lighthouse allow to obtain direct PM mass data ($\mu g/m^3$), the large experimental difference observed between the counters should be a reminder of how highly approximated these results are. Different assumptions about the mass, shape, density and optical properties of the measured particles, in fact, lead to significant mass differences even when the starting particle number data are similar. Extreme caution should therefore be exercised when using PM mass data directly obtained from optical particle counters.

*Table 7.9_Summary of the advantages and disadvantages of the PM sensors considered in this study. The information in bold is directly derived from the comparative study.*

| PM | Advantages | Disadvantages |
|---|---|---|
| **Dylos DC1100-Pro** | - Low-cost (≈600$)<br>- Relatively small (18x11x8 cm)<br>- 2 different size channels<br>- Can be connected to a data logger<br>- **High sensitivity and accuracy**<br>- **Wide linearity range**<br>- **No obvious influence of T and RH on the response** | - **Irregular time delay in the response**<br>- **Slight underestimation of PM concentrations (71%±26% of the real value)** |
| **Shinyei PPD20V** | - Low-cost (≈120$)<br>- Small (8x6x2 cm)<br>- Can be connected to a data logger<br>- **Immediate response (no experimental time delay)**<br>- **Linear response to PM for low concentrations (up to approx. 5.0*107 particles>0.5 µm/m3)**<br>- **No influence of T and RH on the response** | - Approximate cut-off size (<1 µm)<br>- No size discrimination<br>- **Deviation from linearity at high PM concentrations (underestimation)**<br>- **Need for a cross-calibration with a well calibrated monitor to obtain absolute PM concentrations** |
| **Lighthouse 3016-IAQ** | - Relatively small (22x13x6 cm)<br>- 6 size channels<br>- Accurately calibrated according to ISO regulations (100% counting efficiency for particles >0.45 µm) | - High-cost (≈4500$)<br>- Need to manually save the data (3000 memory slots)<br>- **Sensitivity drift in high PM environments** |

## 7.9.2  Gas sensors

The positive and negative characteristics emerged from the preliminary testing of the three low-cost gas sensors are summarized in Table 7.10. The **NO2-A43F** $NO_2$ sensor by Alphasense showed a promising linear response when compared with reference Radiello data ($R^2$=0.92, slope=0.84). Given the relatively small amount of data points available, further studies should be conducted to confirm these results. The correlation observed, together with the relatively low influence of random noise on the instrumental output, are nonetheless very positive results regarding the reliability and average weekly

accuracy of the Alphasense NO$_2$ sensor. Studies on the accuracy of the data at high time resolution will be also a necessary step towards the exploitation of these gas sensors to their full potential in conservation environments.

Table 7.10_Summary of the advantages and disadvantages of the methods for the study of gaseous pollutants. In bold the information directly derived from this preliminary comparative study.

| GASEOUS POLLUTANTS | Advantages | Disadvantages |
|---|---|---|
| **NO2-A43F (NO$_2$)** | - Low-cost (≈150$)<br>- Small (2Φx2 cm)<br>- Can be connected to a data logger<br>- **Good linear response and accuracy with NO$_2$ weekly average concentrations** | - **Multiple protocols to convert sensor response into concentration values (might introduce errors)** |
| **OX-A431 (O$_3$)** | - Low-cost (≈150$)<br>- Small (2Φx2 cm)<br>- Can be connected to a data logger<br>- **Approximately linear response even at low O3 concentrations (weekly average)** | - **Multiple protocols to convert sensor response into concentration values (might introduce errors)**<br>- **Underestimation of the real concentration for low PM levels (negative output)** |
| **PID-AH2 (VOCs)** | - Low-cost (≈400)<br>- Small (2Φx2 cm)<br>- Can be connected to a data logger | - **No visible signal in these experimental conditions (low environmental VOCs concentration)** |
| **RADIELLO®** | - Small tube (8x8x6 cm)<br>- Widely tested and employed<br>- Accurate and precise | - Relatively expensive (≈350$ for a package of 20)<br>- Long sampling time (days/weeks)<br>- Cartridges must be stored in a fridge<br>- Labour intensive processing in well-equipped lab |

The low environmental concentrations of O$_3$ caused problems both to the **OX-A431** Alphasense sensor and to the Radiello passive samplers. In the first case a general underestimation of the real concentration for low O$_3$ levels was observed, resulting in negative concentration values. In the case of Radiello, high levels of standard deviation

were observed for most of the data points. This situation resulted into a worse, but still promising, linear correlation between sensor's output and reference concentrations ($R^2$=0.60). Since the concentrations observed are below the LOD of the reference method, however, more laboratory and field studies need to be performed in order to obtain more meaningful data.

The raw output of the **PID-AH2** Alphasense sensor for the analysis of total VOCs appeared dominated by the presence of random noise. No meaningful signal could be isolated. The extremely low environmental concentrations of VOCs in the church are likely responsible for this poor performance. In conclusion, despite the promising results, much more laboratory and field testing will be necessary before being able to exploit these gas sensors to their full potential in cultural heritage applications.

# 7.10 Supplementary information

## 7.10.1 Particle counts to mass conversion (Dylos)

In literature, Dylos particle counters are often used to obtain information on the mass concentration of airborne PM through assumptions and approximations. However, the manufacturer only presents an approximate conversion chart taped on the back of the instrument itself (Table S7.1).

*Table S7.1_Chart taped on the back of the Dylos DC1100-Pro: indoor environmental quality (IEQ) based on PM levels (for households) and number of particles to mass concentration conversion.*

| IEQ | Number of particles (counts/ft³) | PM mass (µg/m³) |
|---|---|---|
| Bad | > 7000 | > 47 |
| Mediocre | 5000 - 7000 | 33 - 47 |
| Acceptable | 3000 - 5000 | 20 - 33 |
| Good | 1000 - 3000 | 7 - 20 |
| Very good | < 1000 | < 7 |

In order to obtain $PM_{2.5}$ mass concentrations, Dylos tech support suggested to divide the difference between the raw counts for the two size channels (>0.5µm - >2.5µm) by 100, but also advised us to consider the results as nothing more than a crude approximation.

The results calculated in this way did not match the tabulated values showed in Table S1. In this study, a more complex algorithm for the conversion of Dylos DC1100-Pro or DC1700 data into mass measurements, described in the context of the project "Air Quality Sensor Network for Philadelphia" of Drexel University,[466] was used. The complete formula, based on general assumptions on particles size and density based on the research of Lee et al.[498] and Tittarelli et al.[499] and taking into account also a humidity correction factor, is:

$$PM_{0.5-2.5} \left(\frac{\mu g}{m^3}\right) = n \times m \times 3531.5 \times RH \times$$

Where n is the number of particles larger than 0.5 μm measured by the Dylos (counts/0.01ft³), m is the average particle mass calculated from average volume and density (assumed to be $5.89*10^{-7}$ μg ), RH is the experimental relative humidity (%) and ε is a tabulated humidity correction factor.[466] The results calculated with this formula perfectly match the conversion values mentioned in Table S7.1.

The empirical relationships observed by Semple et al.[447] and Han et al.[449] are sometimes also used in literature to derive mass concentration from raw Dylos data.[423,500] Given the site specificity of these models we decided to not consider them in this study. A more accurate algorithm taking into account changes in density and refraction index of particles was developed by Northcross et al..[445] However, this option requires a custom modification of the monitor and additional analysis on the composition and properties of PM, which defeats the purpose of this study to test low cost and easy to use solutions to directly monitor PM levels.

## 7.10.2  Particle mass measurements (Lighthouse)

According to the manufacturer, the conversion of number of particles in the single size channels into PM mass concentrations by the Lighthouse Handheld 3016-IAQ air particle counter is based on the following equation:

$$PM \left(\frac{\mu g}{m^3}\right) = \frac{\pi}{6} \times d^3 \times \delta \times \alpha \times n \times 10^{-4}$$

Where d is the minimum diameter of the particles in the size channel considered (µm), δ is the average particle density (assumed to be 1.5 g/cm³), α is the absorption coefficient (assumed to be 1) and n is the concentration in number of particles registered by the instrument in the size channel considered (counts/ft³). This equation assumes the particles to behave, from an optical point of view, as white Teflon spheres with uniform density and constant radius.

The results manually calculated with the suggested formula, however, did not match the direct mass output of the instrument, showing an approximately linear relationship ($R^2$=0.995) with a slope of $1.2*10^{-3}$ (Figure S7.1). The non-perfectly linear relationship indicates that some non-constant factor is responsible for the observed mismatch. The direct mass concentration output of the instrument (and not the calculated values) was used for the comparison with the Dylos counter since those values are the ones most likely used for further interpretation by the average user of the counter.
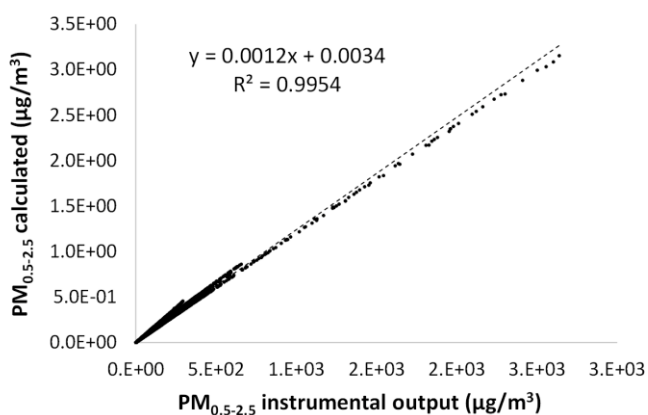


*Figure S7.1_Comparison between the direct mass concentration output and the calculated concentration values for Lighthouse. A slight difference between the theoretically coincident datasets can be observed.*

### 7.10.3 Calculation of $NO_2$ and $O_3$ concentrations from the raw output of the low-cost sensors

According to the manufacturer (Alphasense), the voltage generated by the gas sensors $V_{gas}$ due to the gas can be calculated using four different algorithms. All the algorithms introduce temperature-dependent correction factors: $n_T$, $k_T$, $k'_T$ or $k''_T$.

$$V_{gas} = (V_{WE} - V_{0,WE}) - n_T \times (V_{AE} - V_{0,AE})$$
$$V_{gas} = (V_{WE} - V_{0,WE}) - k_T \times (V_{0,WE}/V_{0,AE}) \times (V_{AE} - V_{0,AE})$$
$$V_{gas} = (V_{WE} - V_{0,WE}) - (V_{0,WE} - V_{0,AE}) - k'_T \times (V_{AE} - V_{0,AE})$$
$$V_{gas} = (V_{WE} - V_{0,WE}) - V_{0,WE} - k''_T$$

Where $V_{WE}$ and $V_{AE}$ are the measured voltages of working electrode (WE) and auxiliary electrode (AE), and $V_{0,WE}$ and $V_{0,AE}$ are the "zero" voltages of WE and AE. The temperature-dependent correction factors, as well as zero voltages and sensitivities are described for each sensor in an accompanying certificate. The suggested algorithms for both A type and B type sensors are given in Table S7.2. The relevant tabulated values used in the calculation of $V_{gas}$ for the two sensors used in this study are listed in table S7.3 and S7.4.

From the voltage generated by the gas $V_{gas}$ the corresponding gas concentration $C_{gas}$ in ppb can be calculated with:

$$C_{gas} = \frac{V_{gas}}{S_{gas}}$$

where $S_{gas}$ is the WE sensitivity given as mV/ppb and tabulated in Table S7.3. The gas sensor OX-A431 detects both ozone and nitrogen dioxide ($V_{gas} = V_{O3+NO2}$). The gas sensor NO2-A43F measures only nitrogen dioxide. Ozone concentration can be calculated using the sensors together. The sensitivity of the OX-A431 towards $NO_2$ $S_{NO2}$ is given in the accompanying certificate (Table S7.4).

$$C_{O3} = \frac{V_{O3+NO2} - S_{NO2} \times C_{NO2}}{S_{O3+NO2}}$$

*Table S7.2_Suggested algorithms for all the A type and B type gas sensors by Alphasense.*

|  | Suggested algorithm | | Alternative algorithm | |
|---|---|---|---|---|
|  | A-type | B-type | A-type | B-type |
| CO | 1 | 1 | 4 | 2 |
| **NO2** | **1** | 1 | **3** | 3 |
| **OX** | **3** | 1 | **1** | 3 |
| H2S | 2 | 1 | 1 | 2 |
| SO2 | 4 | 4 | 1 or 3 | 1 or 2 |
| NO | 3 | 2 | 4 | 3 |

*Table S7.3_Look-up table for the temperature correction factors for the sensors considered in this study (suggested algorithms).*

| Sensor | Algorithm | Factor | -30°C | -20°C | -10°C | 0°C | 10°C | 20°C | 30°C | 40°C | 50°C |
|---|---|---|---|---|---|---|---|---|---|---|---|
| NO2-A4 | 1 | nT | 0.8 | 0.8 | 1.0 | 1.2 | 1.6 | 1.8 | 1.9 | 2.5 | 3.6 |
| | 3 | k'T | 0.2 | 0.2 | 0.2 | 0.2 | 0.7 | 1.0 | 1.3 | 2.1 | 3.5 |
| OX-A4 | 1 | nT | 1.0 | 1.2 | 1.2 | 1.6 | 1.7 | 2.0 | 2.1 | 3. | 4.6 |
| | 3 | k'T | 0.1 | 0.1 | 0.2 | 0.3 | 0.7 | 1.0 | 1.7 | 3.0 | 4.0 |

*Table S7.4_Technical specifications of the sensors considered (from Alphasense).*

| Variables in mV | Symbol | NO2 A43F | OX-A431 |
|---|---|---|---|
| **WE electronic zero** | $V_{0,WE}$ | **295** | **407** |
| WE sensor zero at 23°C | | 10 | 0 |
| **AE electronic zero** | $V_{0,AE}$ | **300** | **401** |
| AE sensor zero at 23°C | | 2 | 1 |
| **WE sensitivity (mv/ppb)** | $S_{gas}$ | **0.211** | **0.369** |
| **Sensitivity NO₂ (mV/ppb)** | $S_{NO2}$ | **0.211** | **0.246** |

Both the recommended algorithms for the two sensors considered in this study were tested. The results are shown in Figure S7.2.
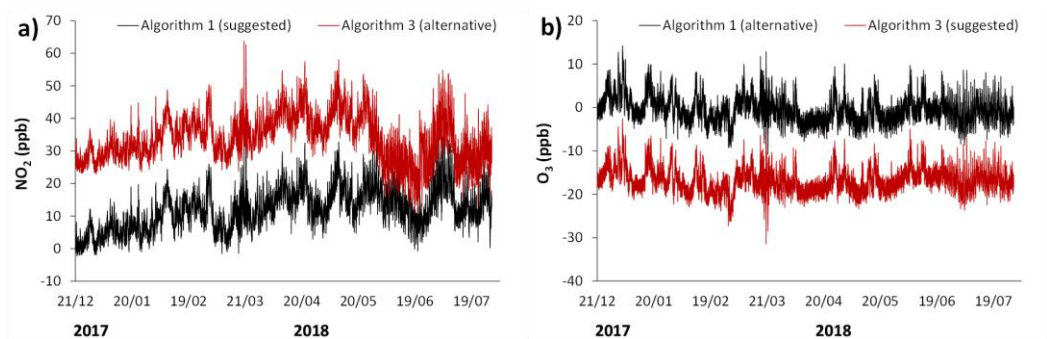


*Figure S7.2_Technical Gas concentration time series (ppb) calculated from the voltage output of the sensors according to the algorithms suggested by Alphasense. a) NO2-A4 and b) OX-A4.*

For the NO2-A4 sensor, the $NO_2$ concentrations calculated according to algorithm 1 were considered (as recommended by the manufacturer) in the successive steps of the study. For the OX-A4 sensor, on the contrary, the algorithm suggested by Alphasense (number 3) resulted in a predominantly negative concentration output. For this reason, the results of algorithm 1 for this sensor were used in the successive steps of the study.

### 7.10.4  Radiello®: experimental procedure

The gaseous analyte diffuses inside a microporous polyethylene body and it is then selectively adsorbed on a chemisorbing cartridge. Following Radiello directives a 4,4'-dipyridylethylene coated silica gel cartridge was selected for $O_3$, a triethanolamine (TEA) coated microporous polyethylene cartridge for $NO_2$, a stainless steel cartridge packed with activated carbon for VOCs. In addition, acetic and formic acids were analysed using the same TEA coated cartridge used for $NO_2$. The exposure of 4,4'-dipyridylethylene to ozone and water leads to the formation of 4-pyridaldehyde. This is consequently condensed through reaction with 3-methyl-2-benzothiazolinone hydrazone (MTBH) obtaining a yellow colored azide solution. The $O_3$ average concentration in the sampling period is hence determined by means of UV-Vis spectrometry (azide absorbance at 430 nm). $NO_2$ is selectively adsorbed on the TEA coating as nitrite anion. The contamination from particulate matter is prevented by the external diffusive body. The anions are then extracted in 5 ml of Milli-Q water for one hour and then analyzed with ion chromatography (IC). Acetic and formic acids concentrations were calculated from the acetate and formate content in this same extraction. The applied method is described in detail by Kontozova-Deutsch et al..[501] The carbon disulfide displacement extraction and FID gas chromatography analysis of VOCs were performed by the Environmental Research Centre of Padua of the Fondazione Salvatore Maugeri – IRCCS.

The analyses were conducted in triplicates and the results presented in the form of average and standard deviation between the three measurements. For every batch of cartridges, two units were left unexposed (kept in the original packaging in the darkness) and analyzed as experimental blanks (in total two batches and four blanks per cartridge type).

## 7.10.5  Time-shift in PM monitoring (Dylos)

Table S7.5_Correlation between the magnitude of the time shift between Dylos and Lighthouse and other experimental parameters.

| | Time | T (°C) | RH (%) | Dylos > 0.5 μm | Lighthouse > 0.5 μm |
|---|---|---|---|---|---|
| **Pearson's r** | 0.19 | 0.14 | -0.12 | -0.27 | -0.30 |
| **p value** | 0.15 | 0.29 | 0.36 | 0.04 | 0.02 |

## 7.10.6  Correction of sensitivity drift (Lighthouse)
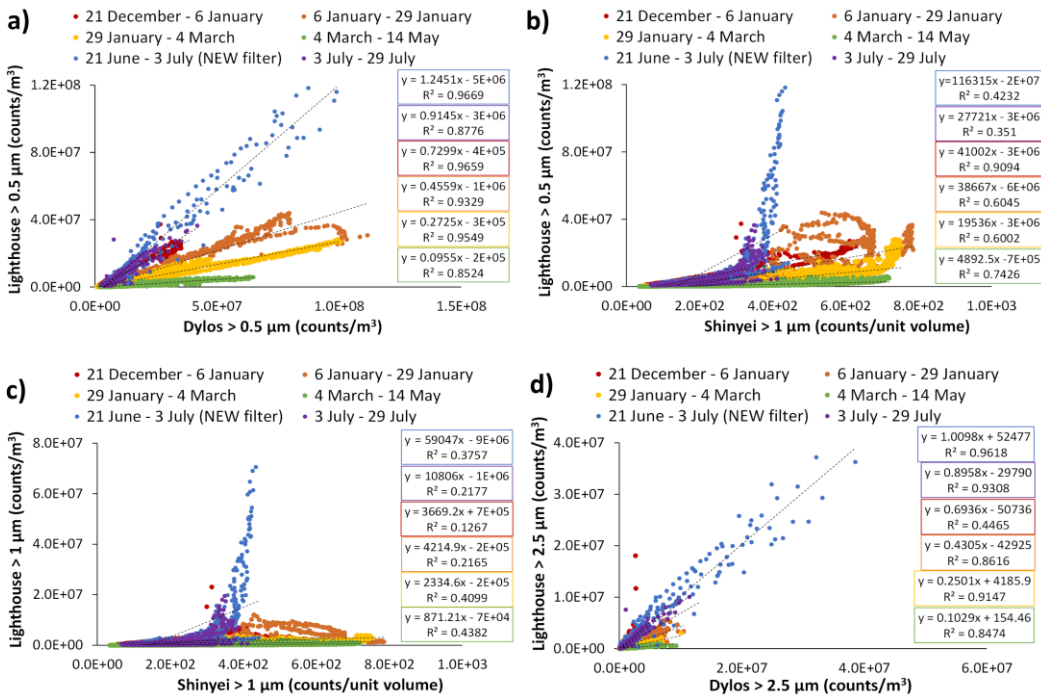


*Figure S7.3_Comparison between the raw data of the tested sensors and the reference counter: a) Lighthouse>0.5 μm VS Dylos>0.5 μm; b) Lighthouse>0.5 μm VS Shinyei; c) Lighthouse>1 μm VS Shinyei; d) Lighthouse>2.5 μm VS Dylos>2.5 μm. In evidence the decrease of the slope of the linear correlation over time due to the loss of sensitivity of Lighthouse.*

In order to proceed with the study, the Lighthouse data were corrected for the loss of sensitivity by quantifying its dependency from time (by comparison with Dylos). The

choice of using the Dylos and not the Shinyei counter for the correction of the sensitivity drift of the Lighthouse is based on the empirical evidence of a linear correlation (with a slope decreasing with time) between the first and the latter (Figure S7.3a). Shinyei, on the other hand, does not show a clear linear correlation with the reference particle counter (Figure S7.3b,c), both when considering the size channel corresponding to the nominal cut-off size (>1 µm) and when considering also smaller particles (>0.5 µm). In this regards, it is particularly interesting to notice how the response of Shinyei seems to correlate better with the smaller Lighthouse channel, indicating a real cut-off size probably smaller than the nominal one[496] (Figure S7.3b,c).
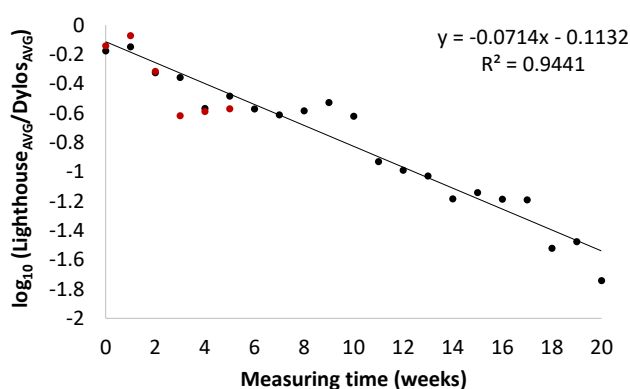


*Figure S7.4_Linear decrease of the logarithm of Lighthouse/Dylos weekly average ratio (>0.5 µm) due to the loss of sensitivity of Lighthouse over time. Black: original filter; red: new filter.*

In Figure S7.4, the logarithm of the ratio of the average weekly concentration registered by Lighthouse and Dylos is plotted against time. The decrease observed is a consequence of the saturation of the internal HEPA filter of Lighthouse, leading to a loss of sensitivity. In order to proceed with the study, the sensitivity drift of this counter was corrected by defining and ideal average Lighthouse/Dylos ratio (average weekly Lighthouse/Dylos ratio for the first two weeks of measurement and the first two weeks after replacing the internal filter) and correcting the experimental ratios for the linear decay of $\log_{10}$(Lighthouse/Dylos) with time. The corrected Lighthouse response was then finally calculated from the corrected experimental ratio at a given time. The resulting response was assumed to be the best representation of the real PM concentration in the environment and it was therefore used as a reference in the evaluation of the performances of the low-cost particle counters.

The same approach was used for the sensitivity drift correction of both Lighthouse >0.5 µm and Lighthouse>2.5 µm data (Figure S7.3d), which were then used as PM reference for the comparison with Shinyei and Dylos fine channel (>0.5 µm) and with Dylos coarse channel (>2.5 µm) respectively.

### 7.10.7 Radiello® VOCs results

*Table 7.6_Average weekly concentration (µg/m³) and standard deviation (3 measurements) of VOCs measured by means of Radiello® diffusive samplers. The experimental limit of detection (LOD=3\*standard deviation of the blanks) in µg/m³ is also reported for the different compounds.*

| Start date | Form Ac | Stdev | Acetic Ac | Stdev | Ethanol | Stdev | Ethyl Acetate | Stdev |
|---|---|---|---|---|---|---|---|---|
| 21/12 | <LOD | | <LOD | | <LOD | | <LOD | - |
| 30/12 | <LOD | | <LOD | | <LOD | | <LOD | - |
| 8/01 | <LOD | | <LOD | | <LOD | | 0.722 | 11% |
| 15/01 | <LOD | | <LOD | | <LOD | | <LOD | - |
| 23/01 | 8.57 | | 35.14 | 18% | 0.77 | - | 0.854 | - |
| 30/01 | 13.00 | | 34.76 | 22% | 2.08 | 9% | 0.339 | 11% |
| LOD | 3.71 | | 9.58 | | 0.67 | | 0.311 | |

| | Toluene | Stdev | α-pinene | Stdev | 2-ethyl 1-hexanol | Stdev | |
|---|---|---|---|---|---|---|---|
| 21/12 | 0.52 | 17% | 0.16 | 21% | 1.09 | 14% | |
| 30/12 | 0.30 | 8% | <LOD | | 0.22 | 13% | |
| 8/01 | 1.72 | 8% | 0.37 | 8% | <LOD | - | |
| 15/01 | 0.70 | 19% | <LOD | | <LOD | - | |
| 23/01 | 1.01 | 50% | <LOD | | <LOD | - | |
| 30/01 | 1.03 | 35% | 0.32 | 8% | <LOD | - | |
| LOD | 0.20 | | 0.10 | | 0.12 | | |

*\*red=only 1/3 measurements > LOD; orange=only 2/3 measurements > LOD*

**|8**

Conclusions and outlook

This doctoral thesis was centered on the application of a wide range of analytical strategies to explore different aspects of the complex and multifaceted issue of the conservation of tangible cultural heritage. By starting from the fundamental concept of the intrinsic materiality of heritage objects, and with the final aim of preventive conservation in mind, specific case studies and un-answered research questions were tackled, in an attempt to fill some of the relevant knowledge gaps remaining in this extremely wide field of research. Since the conservation and degradation of cultural heritage are two faces of the same coin, this attempt translated into a strive to deepen the understanding of the two main actors playing a role in the degradation processes: the object and its conservation environment.

In detail, in this PhD work a selection of unexplained material-environment interactions was considered, from cases in which well-studied materials do not behave as expected, to specific materials whose properties are still not univocally understood. In addition, in the final steps of this research, the focus was shifted from the material-environment interaction to the analytical characterization of specific materials and to the monitoring of the conservation environment, testing innovative analytical strategies and methodological approaches in order to overcome existing limitations.


**Enclosed gardens**

The first case study considered is represented by a series of historical heritage objects: the enclosed gardens of Mechelen (Museum Hof Van Busleyden). Five of these shrines, in the occasion of their restoration, were the subject of a detailed analytical investigation within the ArtGarden project (KIK-IRPA, University of Antwerp, KU Leuven). In the context of this PhD work, novel insights on specific material-environment and material-material(-environment) interactions were obtained, through the application of multiple analytical methods.

One of the features that first caught the eye of the conservators working on the enclosed gardens was how hundreds of round and leaf-shaped metallic sequins appeared extremely shiny, in contrast to the high degree of degradation observed for other pieces and materials. An in-depth chemical, morphological and metallographic characterization of these objects revealed the reason for their extraordinary stability to be a combination of high-quality materials (i.e. medium Zn content, low impurities) and optimal surface properties (i.e. low roughness and homogenous micromorphology), ultimately emphasizing the central role of the manufacturing process on the long-term behavior of

historical brass. Finally, this section of this doctoral thesis showed how brass can still present unaltered aesthetical properties after a five-century long exposure to the environment, even when the Zinc content is above the arbitrary 15% limit that conventionally defines alloys at high risk of dezincification. Such information, holding a clear relevance well beyond the field of conservation science and cultural heritage, represents a significant step towards a deeper understanding of the long-term behavior of α-brass in an indoor environment.

At this stage, further relevant information could be obtained by systematic reactivity studies aiming at a more quantitative understanding of the link between surface roughness and micromorphology and the degradation of brass. The use of electrochemical methods (e.g. electrochemical impedance spectroscopy or corrosion measurements) and/or the artificial ageing of mock-up brass objects, for example, could certainly lead to relevant outcomes for conservation purposes (and not only).

After confirming the extraordinary stability of the metallic sequins in the enclosed gardens and the tarnishing (but not corrosion nor loss of structural properties) of the metallic wires, the attention was focused on a very small selection of metallic objects (sequins and wires) appearing completely corroded. Such a severe corrosion, with complete loss of structural properties, arose in fact surprise given the "mild" nature of the environment represented by the enclosed gardens (indoor and partially enclosed) and the striking contrast with the exceptional preservation state previously described. Understanding what kind of interaction caused such a severe form of degradation was of foremost importance for conservation purposes, in order to highlight potential future risks for the remaining brass objects. The thorough observation of the corroded objects and their surroundings allowed to tentatively trace back the corrosion to a possible interaction between the metal and some weathered glass beads. The two materials were probably in close contact but, given the extreme corrosion and loss of structural properties of the metallic elements, the original position was not always certain.

In order to verify this hypothesis, in Chapter 3 of this PhD work a selection of analytical methods was employed to identify markers of glass-induced metal corrosion on the surface of both metal and glass objects. The complex three-dimensional geometry and limited amount of degradation products on the surface of the glass beads, made necessary the application of novel or not routinely employed characterization methods (such as O-PTIR and μ-CT). The proposed multi-analytical approach allowed to unequivocally recognize glass-induced metal corrosion processes as the main cause for

the severe corrosion of the selected brass objects in the enclosed gardens. The presence and distribution of basic copper formate and mixed K, Zn salts on the surface of both glass and metal, in fact, confirmed the initial hypothesis of a chemical interaction at the glass/metal interface driven by the formation of K-rich alkaline liquid films on the surface of the weathered potash glass in analysis. This clearly indicates how, even objects normally extraordinarily stable in indoor environmental conditions, can completely corrode when their (micro-)environment is modified.

For the purpose of conservation, conditions of T and RH potentially resulting in moisture condensation on the surface of glass should be avoided in the future. A particular focus should be also kept on the evolution of the conservation state of brass objects in the proximity of potash glass decorative elements in the enclosed gardens. Moreover, the results of this study also allowed to obtain first clear insights into the huge potential for the application of novel O-PTIR spectroscopy for the non-invasive molecular characterization of cultural heritage objects.

**Pigment (in)stability and reactivity**
Chapter 4 and Chapter 5 studied the (photo-)reactivity of two different families of pigments, putting particular emphasis on the role played by chemical composition and structural properties on their overall stability.

*Naples Yellow and lead tin antimonate yellow*
The pyroantimonate pigments Naples Yellow and lead tin antimonate yellow are recognized as some of the most stable synthetic yellow pigments in the history of art. However, this exceptional light-fastness is in contrast with experimental evidence suggesting that this class of mixed oxides is of semiconducting nature. Semiconductors are, in fact, often associated to instability in paintings, in particular in the presence of light, moisture and soluble particulate matter (PM).

By means of a combined multi-faceted analytical and computational approach (photo-electrochemical measurements, UV-Vis diffuse reflectance spectroscopy, STEM-EDS, STEM-HAADF and density functional theory calculations), both the semiconducting nature and the lightfastness of these pigments was demonstrated. Poor optical absorption and minority carrier mobility were identified as the main properties responsible for the observed stability. The role of lattice substitutions on the overall properties of the pigments was evaluated in particular, obtaining novel crucial insights

into the role played by Na atoms in the stabilization of the otherwise intrinsically unstable $Pb_2Sb_2O_7$ pyrochlore. The results of this work ultimately represent a fundamental step towards a better understanding of the complex material properties and photochemistry of artists' pigments and of pyrochlore mixed oxides in general. Given the extraordinarily wide range of fields in which these mixed oxides find application, a better understanding of the effect of lattice substitutions on their optoelectronic properties is of capital importance.

As a next step, the laboratory analysis of microsamples of historical paintings would be relevant in order to better characterize the lattice substitutions eventually present in historical Naples Yellow samples (and in particular the presence of Na). Being able to confirm the link between the historical synthesis processes and the presence of different substituents in the pigment structure could represent an extremely useful tool for the attribution and authentication of historical paintings. In addition, the combined analytical and computational approach described in this section of the PhD can potentially be used to probe the material properties of any semiconducting pigment in powder form, with applications also beyond the field of conservation science and cultural heritage.

*Geranium lakes*
The name Geranium lake refers to a family of red metal-organic pigments based on metal complexes (normally Al or Pb) of the synthetic dye eosin Y. One of the most characteristic features of these materials is their intrinsic instability and their tendency to fade upon exposure to the environmental agents, and in particular to light. Such a degradation may lead to severe changes in the appearance of paintings, with grave cultural, societal and economic implications as a result. In Chapter 5, the effect of different synthesis conditions on the overall composition of Geranium lake pigments (Al- or Pb-based), and in particular on the structure of the eosin Y-metal complexes and on the formation of byproducts, was systematically investigated. The natural ageing of the powdered pigments obtained with different synthesis methods was then monitored, with the aim of identifying possible differences in their behavior.

The first fundamental outcome of this study was a detailed band assignment of the FTIR and Raman spectra of eosin Y and Pb and Al complexes, relevant both for the characterization of eosin Y-based species (in paintings as well as in several other fields) and for the monitoring of the molecular changes induced by the degradation of Geranium lake pigments. On this basis, the experimental results clearly showed changes

in the structural properties and chemical composition of the pigments depending on the synthesis protocol. In particular, the coordination mode of the carboxylate moiety of the Pb complexes appears extremely sensitive to the pH and amount of reagents in the synthesis, while the structure of Al complexes remains more stable. Additional fundamental insights into the eosin Y-metal coordination were also obtained, with a possible interaction between the metal ion and the phenoxide ion, and thus the xanthene moiety (chromophore), observed for all the complexes. This interaction is extremely relevant since it implies a potential influence of the metal ion on the properties of the fundamental and excited states of the complexes, ultimately determining their photo-reactivity. Furthermore, in both cases the formation of by-products was also observed. Such by-products, mostly metal carbonates and eosin Y, are detected and identified here for the first time.

Based on these outcomes, in the second part of Chapter 5 preliminary results on the natural ageing of the synthesized Geranium lake pigments were obtained. The monitoring of the natural ageing of pigments synthesized with different protocols clearly highlighted the role played by light on the degradation, and the link existing between the composition of Geranium lake pigments and their degradation kinetics. The strong influence of the synthesis on the composition of the pigments can therefore reflect into different reactivities for the final products. In particular, the presence of by-products of the synthesis, especially for Pb-based lakes, should be taken into account as a potential risk for the pigments. This evidence should raise awareness in the field on the capital importance of employing the same synthesis method(s) in order to ensure the inter comparability of degradation studies. Hopefully, a greater attention to this parameter will finally lead to an agreement in the literature on the degradation mechanism of these pigments in paintings.

In addition, some first relevant insights into the solubility of Geranium lake pigments were also obtained. The results showed how Pb- and Al-based complexes of eosin Y can dissociate when in contact with aqueous electrolyte solutions. The formation of dianionic eosin Y, confirmed by UV-Vis and ATR-FTIR spectroscopies by comparison with reference compounds, is particularly relevant. The well-known high reactivity of deprotonated eosin Y in solution, and its possible formation due to the contact between moisture and Geranium lake particles in paintings, in fact, could in principle be linked to the poor photostability of these pigments. In order to obtain conclusive results on the factors influencing the solubility of Geranium lake pigments and on the role played by

this property on their stability in paintings, however, further studies will have to be performed.

The role of the painting medium, excluded for simplicity from these initial investigations on the reactivity of the pigments, will certainly have to be thoroughly studied (also in relation to the presence of reactive by-products such as lead carbonate in Geranium lakes). Moreover, the possible solubilization and migration of dianionic eosin Y in paintings could be the starting point to understand the information, reported in the literature, on the role played by semiconducting pigments in enhancing the fading of Geranium lakes. Photoelectrochemical studies can be performed in order to decipher the nature of this potential interaction.

**O-PTIR spectroscopy for the analysis of paintings**

One of the most challenging aspects of the analysis of Geranium lake pigments is their identification in paint samples. Their detection is, in fact, often complicated by the poor conservation state of these pigments in paintings and by the fact that they were often employed in very small amounts in the first place, due to their extremely intense color. For these reasons, micrometric red particles are often all that remains in Geranium lake-containing paintings. This poses extreme analytical challenges, in particular when it comes to the molecular characterization of such particles in microscopic paint samples.

Chapter 6 of this PhD work focused on testing the potential of the novel optical photo-thermal IR (O-PTIR) spectroscopy to overcome these challenges and achieve the non-contact sub-micron molecular imaging of a paint microsample in thin section. The striking results obtained on a small fragment from the painting *L'Arlésienne (portrait of Madame Ginoux)*, by Vincent Van Gogh, clearly highlight the great potential of this technique for the study of micrometric particles in paint samples. In the first place, O-PTIR allowed to non-destructively identify the red particles present in the paint film as Geranium lake pigments. Due to the limited size of the particles and the presence of additional compounds in the film, other state-of-the-art analytical techniques (SR-μ-FTIR and μ-Raman spectroscopy) failed to unambiguously identify these species. The high spatial resolution obtainable with O-PTIR (≈450 nm) allowed to identify and map micro- and nano-heterogeneities in the stratigraphy of the painting, despite the small size of the sample. This presents clear advantages for the study and preservation of cultural heritage, maximizing the obtainable information while minimizing the size of the sample needed.

Moreover, although no sample preparation is inherently necessary for O-PTIR, the technique appeared highly efficient for the analysis of thin sections of embedded painting fragments. The suitability of this sample preparation for O-PTIR analysis highlights the compatibility of this technique with other commonly employed high-resolution characterization methods, hence opening to the possibility of a full integration of O-PTIR in multitechnique studies of cultural heritage objects.

**Sensors in conservation environments**

For the purpose of preventive conservation, having a deep knowledge of the object and of the environment-specific reactivity of the single materials composing it is not sufficient. Identifying potential threats in the conservation environment by continuously monitoring its quality is also of capital importance. Traditionally, heritage institutions record and evaluate their indoor environmental quality (IEQ) by continuously monitoring temperature, relative humidity, and -more rarely- light. However, technological solutions exist that allow the monitoring of other factors influencing the overall environmental 'air aggressiveness'. One of these factors is airborne PM, however, commercial sensors for PM monitoring are either expensive, if well-tested and calibrated, or not-sufficiently tested. In order to make possible the implementation of PM analysis in routine IEQ monitoring, therefore, field testing is needed.

Chapter 7 clearly showed how, including PM in the IEQ calculations for conservation environments, allows to identify potential risks for museum collections that remain invisible when only traditional parameters are considered. In particular, a straightforward methodology to include PM in the evaluation and visualization of the IEQ is discussed. The different amount of information obtainable with discrete (daily averages) and continuous monitoring is evaluated, highlighting the potential loss of information associated with discrete sampling. In conclusion, the monitoring of the IEQ in two different environments in the museum, one well-insulated HVAC-equipped storage and one poorly insulated exposition room, ultimately allowed to recognize in which periods the collection was at risk, identifying the factors posing a threat and proposing possible mitigation actions.

In the second part of the chapter, the performances of a selection of low-costs sensors for PM monitoring were tested on the field (monitoring campaign in the St. Martin's church in Aalst, Belgium). Advantages and drawbacks were highlighted with the final aim of verifying their applicability in conservation environments, which would make the

implementation of continuous PM monitoring in the practice of museums and heritage institutions affordable and, therefore, feasible. In addition, in the final part of the chapter, some preliminary results on the performances of low-cost sensors for gaseous pollutants were also obtained.

Generally speaking, the low-cost sensors tested showed promising results, with advantages and disadvantages that are thoroughly discussed in this section of the thesis. Nonetheless, further testing in a wider range of environments will be necessary before drawing further conclusions, e.g. in museums equipped with HVAC and filtration systems. Such a "clean" indoor environment could in fact push the low-cost sensors, designed with households and industrial applications in mind, towards their limit of detection.

**Generic insights**

In addition to the individual outcomes of the single stages of this PhD research, some more general considerations can be derived from the results of this work. One of the most general outcomes of this PhD work is highlighting the great amount of information that can be obtained indirectly, i.e. by studying stable objects, on the properties governing the reactivity and long-term behavior of different classes of materials. This emerges clearly from the results of Chapter 2 and Chapter 4 in this work. The thorough investigation of the material properties and conservation state of the extraordinarily well-preserved brass sequins in the enclosed gardens, in fact, allowed to draw general conclusions on the factors regulating the long-term behavior of α-brass in an indoor environment. In a similar fashion, the study of the optoelectronic properties and photo-induced behavior of the stable lead pyroantimonate artists' pigments, made it possible to further the understanding of the features governing the photo-reactivity of semiconductors.

These two results have also another aspect in common, namely the clear relevance of the obtained information for fields beyond conservation science and cultural heritage. This is a common aspect when it comes to research in the field of conservation, giving the strong overlap between conservation and material science, and it is not necessarily limited to the study of stable materials. This is clearly highlighted, for example, by the results of Chapter 5 on the study of the unstable Geranium lake pigments. The general information obtained on the properties of metal complexes of eosin Y, including a thorough band assignment of their FTIR and Raman spectra and a deeper understanding

of their structure, in fact, holds great relevance for a wide range of fields, from DSSCs to photocatalysis.

Another relevant theme that repeatedly appears in the results of this PhD work is the fundamental importance of the synthesis method on the properties of materials. This intuitive connection between synthesis conditions, composition (and physical properties) and reactivity is central in the chapters focusing on the properties of artists' pigments. In Chapter 4, in particular, the fundamental role of different lattice substitutions, induced by the use of different reagents in the synthesis, on the stabilization of $Pb_2Sb_2O_7$ in a pyrochlore structure is demonstrated. In a similar fashion, throughout Chapter 5, the great influence of the synthesis protocol on the composition of Geranium lake pigments is first demonstrated, and then linked to different ageing kinetics.

An additional fundamental outcome of this research, which holds a great potential for the advancement of the field of conservation science, is the applicability of optical photo-thermal IR (O-PTIR) spectroscopy to the study of different types of cultural heritage materials. The technique allows the non-destructive and non-contact chemical characterization of organic and inorganic IR-active materials with sub-micron resolution. Both point analysis and chemical distribution maps were obtained, allowing to unravel micro- and nano-heterogeneities in the samples. Given the extreme versatility and high resolution, together with the non-destructive (and non-invasive for small samples) nature of the technique, it is likely that O-PTIR will become a fundamental tool in the future of cultural heritage analyses.

# Bibliography

(1) Thomson, G. *The Museum Environment*; Butterworth-Heinemann: London, 1986. https://doi.org/10.4324/9780080512310.

(2) ICOM-CC. Terminology to Characterize the Conservation of Tangible Cultural Heritage. In *ICOM-CC 15th Triennial Conference, New Delhi, 22-26 September 2008*; 2008.

(3) Del Monte, M. *The Cultural Heritage: Causes of Damage*; ECSC-EEC-EAEC, Brussels-Luxembourg, 1991. https://doi.org/10.1016/b978-0-7506-0237-2.50015-0.

(4) Mercier, J. P.; Zambelli, G.; Kurz, W. Corrosion, Degradation and Ageing. In *Introduction to Materials Science*; 2002; pp 379–399. https://doi.org/10.1016/b978-2-84299-286-6.50021-4.

(5) May, E.; Jones, M. *Conservation Science. Heritage Materials*; The Royal Society of Chemistry: Cambridge, 2007. https://doi.org/10.1016/j.culher.2007.07.005.

(6) Institute, S. H. Roman Glass Round Bottom Vase.

(7) Dillmann, P.; Watkinson, D.; Angelini, E.; Adriaens, A. *Corrosion and Conservation of Cultural Heritage Metallic Artefacts*; 2013; Vol. 53.

(8) Nord, A. G.; Tronner, K.; Mattsson, E.; Borg, G. C.; Ullén, I. Environmental Threats to Buried Archaeological Remains. *Ambio* **2005**, *34* (3), 256–262. https://doi.org/10.1579/0044-7447-34.3.256.

(9) Eggert, G. Corroding Glass, Corroding Metals: Survey of Joint Metal/Glass Corrosion Products on Historic Objects. *Corros. Eng. Sci. Technol.* **2010**, *45* (5), 414–419. https://doi.org/10.1179/147842210X12754747500603.

(10) Ahmad, Z. Atmospheric Corrosion. In *Principles of Corrosion Engineering and Corrosion Control*; Ahmad, Z., Ed.; Elsevier: Amsterdam, 2006; pp 550–575. https://doi.org/10.1016/B978-0-7506-5924-6.50011-8.

(11) Li, S.; Hihara, L. H. In Situ Raman Spectroscopic Study of NaCl Particle-Induced Marine Atmospheric Corrosion of Carbon Steel. *J. Electrochem. Soc.* **2012**, *159* (4), C147–C154. https://doi.org/10.1149/2.013204jes.

(12) Bunker, B. C. Molecular Mechanisms for Corrosion of Silica and Silicate Glasses. *J. Non. Cryst. Solids* **1994**, *179* (C), 300–308. https://doi.org/10.1016/0022-3093(94)90708-0.

(13) Schreiner, M. Glass of the Past: The Degradation and Deterioration of Medieval Glass Artifacts. *Mikrochim. Acta* **1991**, *104* (1–6), 255–264. https://doi.org/10.1007/BF01245513.

(14) Rodrigues, A.; Fearn, S.; Vilarigues, M. Historic K-Rich Silicate Glass Surface Alteration: Behaviour of High-Silica Content Matrices. *Corros. Sci.* **2018**, *145* (July), 249–261. https://doi.org/10.1016/j.corsci.2018.10.010.

(15) Thickett, D.; Pretzel, B. FTIR Surface Analysis for Conservation. *Herit. Sci.* **2020**, *8* (1), 1–10. https://doi.org/10.1186/s40494-020-0349-8.

(16) Fieberg, J. E.; Knutås, P.; Hostettler, K.; Smith, G. D. ``Paintings Fade Like Flowers'': Pigment Analysis and Digital Reconstruction of a Faded Pink Lake Pigment in Vincent van Gogh's Undergrowth with Two Figures. *Appl. Spectrosc.* **2017**, *71* (5), 794–808.

(17) Centeno, S. A.; Hale, C.; Carò, F.; Cesaratto, A.; Shibayama, N.; Delaney, J.; Dooley, K.; van der Snickt, G.; Janssens, K.; Stein, S. A. Van Gogh's Irises and Roses: The Contribution of Chemical Analyses and Imaging to the Assessment of Color Changes in the Red Lake Pigments. *Herit. Sci.* **2017**, *5* (1), 1–11. https://doi.org/10.1186/s40494-017-0131-8.

(18) Van Der Snickt, G.; Dik, J.; Cotte, M.; Janssens, K.; Jaroszewicz, J.; De Nolf, W.; Groenewegen, J.; Van Der Loeff, L. Characterization of a Degraded Cadmium Yellow (CdS) Pigment in an Oil Painting by Means of Synchrotron Radiation Based X-Ray Techniques. *Anal. Chem.* **2009**, *81* (7), 2600–2610. https://doi.org/10.1021/ac802518z.

(19) Vanmeert, F.; Vandersnickt, G.; Janssens, K. Plumbonacrite Identified by X-Ray Powder Diffraction

Tomography as a Missing Link during Degradation of Red Lead in a van Gogh Painting. *Angew. Chemie - Int. Ed.* **2015**, *54* (12), 3607–3610. https://doi.org/10.1002/anie.201411691.

(20)   Monico, L.; Janssens, K.; Hendriks, E.; Vanmeert, F.; Van Der Snickt, G.; Cotte, M.; Falkenberg, G.; Brunetti, B. G.; Miliani, C. Evidence for Degradation of the Chrome Yellows in Van Gogh's Sunflowers: A Study Using Noninvasive in Situ Methods and Synchrotron-Radiation-Based X-Ray Techniques. *Angew. Chemie - Int. Ed.* **2015**, *54* (47), 13923–13927. https://doi.org/10.1002/anie.201505840.

(21)   Vagnini, M.; Vivani, R.; Viscuso, E.; Favazza, M.; Brunetti, B. G.; Sgamellotti, A.; Miliani, C. Investigation on the Process of Lead White Blackening by Raman Spectroscopy, XRD and Other Methods: Study of Cimabue's Paintings in Assisi. *Vib. Spectrosc.* **2018**, *98* (May), 41–49. https://doi.org/10.1016/j.vibspec.2018.07.006.

(22)   Gent, A. *Colour Change in Paintings*; Archetype Books, 2016.

(23)   Geldof, M.; Proaño Gaibor, A. N.; Ligterink, F.; Hendriks, E.; Kirchner, E. Reconstructing Van Gogh's Palette to Determine the Optical Characteristics of His Paints. *Herit. Sci.* **2018**, *6* (1), 1–20. https://doi.org/10.1186/s40494-018-0181-6.

(24)   Kirchner, E.; van der Lans, I.; Ligterink, F.; Geldof, M.; Megens, L.; Meedendorp, T.; Pilz, K.; Hendriks, E. Digitally Reconstructing Van Gogh's *Field with Irises near Arles* Part 3: Determining the Original Colors. *Color Res. Appl.* **2017**, No. November. https://doi.org/10.1002/col.22197.

(25)   Pauling, L. *General Chemistry*, Third edit.; Dover Publications, 1988.

(26)   Roberge, P. R. *Corrosion Engineering. Principles and Practice*; The McGraw-Hill Companies: New York, 2008. https://doi.org/10.1016/S0007-0785(74)80043-8.

(27)   Conradt, R. Chemical Durability of Oxide Glasses in Aqueous Solutions: A Review. *J. Am. Ceram. Soc.* **2008**, *91* (3), 728–735. https://doi.org/10.1111/j.1551-2916.2007.02101.x.

(28)   Scott, D. A. *Copper and Bronze in Art: Corrosion, Colorants, Conservation*; Getty Conservation Institute: Los Angeles, 2002.

(29)   Selvaraj, S.; Ponmariappan, S.; Natesan, M.; Palaniswamy, N. Dezincification of Brass and Its Control-an Overview. *Corros. Rev.* **2003**, *21* (1), 41–74. https://doi.org/10.1515/CORRREV.2003.21.1.41.

(30)   Winston Revie, R.; Uhlig, H. H. *Corrosion and Corrosion Control*, Fourth Edi.; John Wiley and Sons: Hoboken New Jersey, 2008.

(31)   Davies, D. *A Note on the Dezincification of Brass and the Inhibiting Effect of Elemental Additions*; Copper Development Association Inc.: New York, 1993.

(32)   Ralston, K. D.; Birbilis, N. Effect of Grain Size on Corrosion: A Review. *Corrosion* **2010**, *66* (7), 0750051–07500513. https://doi.org/10.5006/1.3462912.

(33)   Li, W.; Li, D. Y. Influence of Surface Morphology on Corrosion and Electronic Behavior. *Acta Mater.* **2006**, *54* (2), 445–452. https://doi.org/10.1016/j.actamat.2005.09.017.

(34)   Toloei, A.; Stoilov, V.; Northwood, D. The Relationship between Surface Roughness and Corrosion. In *Proceedings of the ASME 2013 International Mechanical Engineering Congress and Exposition IMECE2013*; San Diego, 2013.

(35)   Meng, F.; Han, E. H.; Wang, J.; Zhang, Z.; Ke, W. Localized Corrosion Behavior of Scratches on Nickel-Base Alloy 690TT. *Electrochim. Acta* **2011**, *56* (4), 1781–1785. https://doi.org/10.1016/j.electacta.2010.08.028.

(36)   Rahemi, V.; Sarmadian, N.; Anaf, W.; Janssens, K.; Lamoen, D.; Partoens, B.; De Wael, K. Unique Optoelectronic Structure and Photoreduction Properties of Sulfur-Doped Lead Chromates Explaining Their Instability in Paintings. *Anal. Chem.* **2017**, *89* (6), 3326–3334. https://doi.org/10.1021/acs.analchem.6b03803.

(37)   Rondão, R.; Seixas De Melo, J. S.; Pina, J.; Melo, M. J.; Vitorino, T.; Parola, A. J. Brazilwood Reds: The (Photo)Chemistry of Brazilin and Brazilein. *J. Phys. Chem. A* **2013**, *117* (41), 10650–10660. https://doi.org/10.1021/jp404789f.

(38)   Rondão, R. Unveiling the Excited States of Indigo, Maya Blue, Brazilwood and Dragon's Blood. **2012**.

(39)   Monico, L.; Chieli, A.; De Meyer, S.; Cotte, M.; de Nolf, W.; Falkenberg, G.; Janssens, K.; Romani, A.; Miliani, C. Role of the Relative Humidity and the Cd/Zn Stoichiometry in the Photooxidation Process

of Cadmium Yellows (CdS/Cd1–xZnxS) in Oil Paintings. *Chem. - A Eur. J.* **2018**, *24* (45), 11584–11593. https://doi.org/10.1002/chem.201801503.

(40)   Miliani, C.; Monico, L.; Melo, M. J.; Fantacci, S.; Angelin, E. M.; Romani, A.; Janssens, K. Photochemistry of Artists' Dyes and Pigments: Towards Better Understanding and Prevention of Colour Change in Works of Art. *Angew. Chemie - Int. Ed.* **2018**, *57* (25), 7324–7334. https://doi.org/10.1002/anie.201802801.

(41)   Ghirardello, M.; Otero, V.; Comelli, D.; Toniolo, L.; Dellasega, D.; Nessi, L.; Cantoni, M.; Valentini, G.; Nevin, A.; Melo, M. J. An Investigation into the Synthesis of Cadmium Sulfide Pigments for a Better Understanding of Their Reactivity in Artworks. *Dye. Pigment.* **2020**, No. August, 108998. https://doi.org/10.1016/j.dyepig.2020.108998.

(42)   GILES, C. H.; WALSH, D. J.; SINCLAIR, R. S. The Relation between Light Fastness of Colorants and Their Particle Size. *J. Soc. Dye. Colour.* **1977**, *93* (9), 348–352. https://doi.org/10.1111/j.1478-4408.1977.tb03369.x.

(43)   Radepont, M.; Coquinot, Y.; Janssens, K.; Ezrati, J. J.; De Nolf, W.; Cotte, M. Thermodynamic and Experimental Study of the Degradation of the Red Pigment Mercury Sulfide. *J. Anal. At. Spectrom.* **2015**, *30* (3), 599–612. https://doi.org/10.1039/c4ja00372a.

(44)   Vermeulen, M.; Janssens, K.; Sanyova, J.; Rahemi, V.; McGlinchey, C.; De Wael, K. Assessing the Stability of Arsenic Sulfide Pigments and Influence of the Binding Media on Their Degradation by Means of Spectroscopic and Electrochemical Techniques. *Microchem. J.* **2018**, *138*, 82–91. https://doi.org/10.1016/j.microc.2018.01.004.

(45)   Monico, L.; Janssens, K.; Miliani, C.; Van Der Snickt, G.; Brunetti, B. G.; Cestelli Guidi, M.; Radepont, M.; Cotte, M. Degradation Process of Lead Chromate in Paintings by Vincent van Gogh Studied by Means of Spectromicroscopic Methods. 4. Artificial Aging of Model Samples of Co-Precipitates of Lead Chromate and Lead Sulfate. *Anal. Chem.* **2013**, *85* (2), 860–867. https://doi.org/10.1021/ac3021592.

(46)   van Driel, B. A.; Kooyman, P. J.; van den Berg, K. J.; Schmidt-Ott, A.; Dik, J. A Quick Assessment of the Photocatalytic Activity of TiO2 Pigments - From Lab to Conservation Studio! *Microchem. J.* **2016**, *126*, 162–171. https://doi.org/10.1016/j.microc.2015.11.048.

(47)   M., L. Titanium White. In *Artists' pigments: a handbook of their history and characteristics, vol. 3.*; National gallery of Art: Washington, 1997; pp 295–355.

(48)   Fischer, A.; Eggert, G.; Stelzner, J.; Bette, S.; Dinnebier, R. E. When Glass and Metal Corrode Together , VII : Zinc Formates and Further Unknown Zinc Compounds. In *METAL 2019. Proceedings of the Interim Meeting of the ICOM-CC Metals Working Group*; Chemello, C., Brambilla, L., Joseph, E., Eds.; ICOM-CC, HE-Arc CR: Neuchatel, Switzerland, 2019; pp 158–167.

(49)   Bette, S.; Eggert, G.; Fischer, A.; Dinnebier, R. E. Glass-Induced Lead Corrosion of Heritage Objects: Structural Characterization of K(OH)·2PbCO3. *Inorg. Chem.* **2017**, *56* (10), 5762–5770. https://doi.org/10.1021/acs.inorgchem.7b00391.

(50)   Fischer, A.; Eggert, G.; Stelzner, J. When Glass and Metal Corrode Together, VI: Chalconatronite. *Stud. Conserv.* **2020**, *65* (3), 152–159. https://doi.org/10.1080/00393630.2019.1677081.

(51)   Keheyan, Y.; Eliazyan, G.; Engel, P.; Rittmeier, B. Py/GC/MS Characterisation of Naturally and Artificially Aged Inks and Papers. *J. Anal. Appl. Pyrolysis* **2009**, *86* (1), 192–199. https://doi.org/10.1016/j.jaap.2009.06.004.

(52)   Wilson, H. Analysis of the Current Research into the Chemistry of Iron Gall Ink and Its Implications for Paper Conservation., St Anne's College, 2007.

(53)   Cotte, M.; Checroun, E.; De Nolf, W.; Taniguchi, Y.; De Viguerie, L.; Burghammer, M.; Walter, P.; Rivard, C.; Salomé, M.; Janssens, K.; Susini, J. Lead Soaps in Paintings: Friends or Foes? *Stud. Conserv.* **2017**, *62* (1), 2–23. https://doi.org/10.1080/00393630.2016.1232529.

(54)   *Metal Soaps in Art. Conservation and Research*; Casadio, F., Keune, K., Hendriks, E., Centeno, S. A., Eds.; Springer International Publishing, 2019.

(55)   Anaf, W.; Schalm, O.; Janssens, K.; De Wael, K. Understanding the (in)Stability of Semiconductor Pigments by a Thermodynamic Approach. *Dye. Pigment.* **2015**, *113*, 409–415. https://doi.org/10.1016/j.dyepig.2014.09.015.

(56)     Monico, L.; Cartechini, L.; Rosi, F.; Chieli, A.; Grazia, C.; de Meyer, S.; Nuyts, G.; Vanmeert, F.; Janssens, K.; Cotte, M.; de Nolf, W.; Falkenberg, G.; Sandu, I. C. A.; Tveit, E. S.; Mass, J.; de Freitas, R. P.; Romani, A.; Miliani, C. Probing the Chemistry of CdS Paints in the Scream by in Situ Noninvasive Spectroscopies and Synchrotron Radiation X-Ray Techniques. *Sci. Adv.* **2020**, *6* (20), 1–12. https://doi.org/10.1126/sciadv.aay3514.

(57)     Young, C. R. T. Measurement of the Biaxial Tensile Properties of Paintings on Canvas By, University of London, 1996.

(58)     Hendrickx, R.; Ferreira, E. S. B.; Boon, J. J.; Desmarais, G.; Derome, D.; Angelova, L.; Mannes, D.; Kaestner, A.; Huinink, H. (H P. ).; Kuijpers, K. (C J. ).; Voogt, B.; Richardson, E. Distribution of Moisture in Reconstructed Oil Paintings on Canvas during Absorption and Drying: A Neutron Radiography and NMR Study. *Stud. Conserv.* **2017**, *62* (7), 393–409. https://doi.org/10.1080/00393630.2016.1181899.

(59)     Pavlopoulou, L.-C.; Watkinson, D. The Degradation of Oil Painted Copper Surfaces. *Stud. Conserv.* **2006**, *51* (sup1), 55–65. https://doi.org/10.1179/sic.2006.51.supplement-1.55.

(60)     Veiga, A. R. Oil Painting on Tinplate by Francisco José Resende. Techniques, Materials and Degradation of Three Nineteenth Century Paintings. *CeROArt* **2010**, *EGG 1*.

(61)     Deformazioni del Supporto. https://artenet.it/deformazioni-del-supporto-2/ (accessed Feb 22, 2021).

(62)     Gibson, L. T.; Watt, C. M. Acetic and Formic Acids Emitted from Wood Samples and Their Effect on Selected Materials in Museum Environments. *Corros. Sci.* **2010**, *52* (1), 172–178. https://doi.org/10.1016/j.corsci.2009.08.054.

(63)     Grzywacz, C. M. *Monitoring for Gaseous Pollutants in Museum Environments*; 2006.

(64)     Anaf, W. The Influence of Particulate Matter on Cultural Heritage, University of Antwerp, 2014.

(65)     Camuffo, D.; Sturaro, G.; Valentino, A. Showcases: A Really Effective Mean for Protecting Artworks? *Thermochim. Acta* **2000**, *365* (1–2), 65–77. https://doi.org/10.1016/S0040-6031(00)00614-6.

(66)     Camuffo, D. Microclimate, Air and Temperature. In *Microclimate for cultural heritage. Conservation, Restoration, and Maintenance of Indoor and Outdoor Monuments*; Elsevier B.V.: San Diego, 2014; pp 3–47.

(67)     Camuffo, D. Indoor Dynamic Climatology: Investigations on the Interactions between Walls and Indoor Environment. *Atmos. Environ.* **1983**, *17* (9), 1803–1809. https://doi.org/10.1016/0004-6981(83)90188-9.

(68)     Camuffo, D.; Sturaro, G.; Valentino, A. Thermodynamic Exchanges between the External Boundary Layer and the Indoor Microclimate at the Basilica of Santa Maria Maggiore, Rome, Italy: The Problem of Conservation of Ancient Works of Art. *Boundary-Layer Meteorol.* **1999**, *92* (2), 243–262. https://doi.org/10.1023/A:1002026711404.

(69)     Camuffo, D. Humidity and Conservation. In *Microclimate for cultural heritage. Conservation, Restoration, and Maintenance of Indoor and Outdoor Monuments*; San Diego, 2014; pp 77–118.

(70)     Hosseinpour, S.; Forslund, M.; Johnson, C. M.; Pan, J.; Leygraf, C. Atmospheric Corrosion of Cu, Zn, and Cu-Zn Alloys Protected by Self-Assembled Monolayers of Alkanethiols. *Surf. Sci.* **2016**, *648*, 170–176. https://doi.org/10.1016/j.susc.2015.10.045.

(71)     Crispim, C. A.; Gaylarde, C. C. Cyanobacteria and Biodeterioration of Cultural Heritage: A Review. *Microb. Ecol.* **2005**, *49* (1), 1–9. https://doi.org/10.1007/s00248-003-1052-5.

(72)     Anaf, W.; Janssens, K.; De Wael, K. Formation of Metallic Mercury during Photodegradation/Photodarkening of α-HgS: Electrochemical Evidence. *Angew. Chemie - Int. Ed.* **2013**, *52* (48), 12568–12571. https://doi.org/10.1002/anie.201303977.

(73)     Arends, T.; Pel, L.; Schellen, H. L.; Smeulders, D. M. J. Relating Relative Humidity Fluctuations to Damage in Oak Panel Paintings by a Simple Experiment. *Stud. Conserv.* **2019**, *64* (2), 101–114. https://doi.org/10.1080/00393630.2018.1481351.

(74)     American Society of Heating, Refrigerating and Air-Conditioning Engineers, I. (ASHRAE). Museums, Galleries, Archives, and Libraries. In *ASHRAE Handbook - Heating, Ventilating, and Air-Conditioning Applications*; Atlanta, GA, 2011.

(75)     Cuttle, C. Damage to Museum Objects Due to Light Exposure. *Light. Res. Technol.* **1996**, *28* (1), 1–

9. https://doi.org/10.1177/14771535960280010301.

(76) Ayalew, E.; Janssens, K.; De Wael, K. Unraveling the Reactivity of Minium toward Bicarbonate and the Role of Lead Oxides Therein. *Anal. Chem.* **2016**, *88* (3), 1564–1569. https://doi.org/10.1021/acs.analchem.5b02503.

(77) Nazaroff, W. W.; Ligocki, M. P.; Salmon, L. G.; Cass, C. R.; Fall, T.; Jones, M. C.; Lui, H. I. H.; Ma, T. *Airborne Particles in Museums*; Getty Conservation Institute: Los Angeles, USA., 1993; Vol. 6.

(78) Kontozova-Deutsch, V.; Moreton Godoi, R. H.; Worobiec, A.; Spolnik, Z.; Krata, A.; Deutsch, F.; Van Grieken, R. Investigation of Gaseous and Particulate Air Pollutants at the Basilica Saint-Urbain in Troyes, Related to the Preservation of the Medieval Stained Glass Windows. *Microchim. Acta* **2008**, *162* (3–4), 425–432. https://doi.org/10.1007/s00604-007-0930-9.

(79) Tétreault, J. *Airborne Pollutants in Museums Galleries, and Archives: Risk Assessment, Control Strategies, and Preservation Management.*; Minister of Public Works and Government Services: Ottawa, Canada, 2003.

(80) Tidblad, J. Chapter 6: Air Pollution Damage to Metals. In *Urban Pollution and Changes to Materials and Building Surfaces*; Brimblecombe, P., Ed.; City University of Hong Kong: Hong Kong, 2016; pp 143–164.

(81) Whitmore, P. M.; Cass, G. R. The Ozone Fading of Traditional Japanese Colorants. *Stud. Conserv.* **1988**, *33* (1), 29–40. https://doi.org/10.1179/sic.1988.33.1.29.

(82) Spezzano, P. Mapping the Susceptibility of UNESCO World Cultural Heritage Sites in Europe to Ambient (Outdoor) Air Pollution. *Sci. Total Environ.* **2021**, *754*, 142345. https://doi.org/10.1016/j.scitotenv.2020.142345.

(83) Lloyd, H.; Brimblecombe, P.; Lithgow, K. Economics of Dust. *Stud. Conserv.* **2007**, *52* (2), 135–146. https://doi.org/10.1179/sic.2007.52.2.135.

(84) WEI, W.; JOOSTEN, I.; KEIM, K.; DOUNA, H.; MEKKING, W., \; REUSS, M.; WAGEMAKERS, J. Experience with Dust Measurements in Three Dutch Museums. *Zeitschrift für Kunsttechnologie und Konserv.* **2007**, *21* (2), 261–269.

(85) Brimblecombe, P.; Thickett, D.; Yoon, Y. H. The Cementation of Coarse Dust to Indoor Surfaces. *J. Cult. Herit.* **2009**, *10* (3), 410–414. https://doi.org/10.1016/j.culher.2008.12.003.

(86) Prajapati, C. L. Accumulation of Solid Particles on Documents, a Threat for Preservation of Documentary Heritage: The Example of the National Archives of India. *Restaurator* **2003**, *24* (1), 46–54. https://doi.org/10.1515/REST.2003.46.

(87) Garg, K. L.; Jain, K. K.; Mishra, A. K. Role of Fungi in the Deterioration of Wall Paintings. *Sci. Total Environ.* **1995**, *167* (1–3), 255–271. https://doi.org/10.1016/0048-9697(95)04587-Q.

(88) Centeno, S. A.; Schulte, F.; Kennedy, N. W.; Schrott, A. G. The Formation of Chlorine-Induced Alterations in Daguerreotype Image Particles: A High Resolution SEM-EDS Study. *Appl. Phys. A Mater. Sci. Process.* **2011**, *105* (1), 55–63. https://doi.org/10.1007/s00339-011-6570-2.

(89) Thickett, D.; David, F.; Luxford, N. Air Exchange Rate - the Dominant Parameter for Preventive Conservation? *Conserv.* **2005**, *29* (1), 19–34. https://doi.org/10.1080/01410096.2005.9995210.

(90) Silva, H. E.; Henriques, F. M. A.; Henriques, T. A. S.; Coelho, G. A Sequential Process to Assess and Optimize the Indoor Climate in Museums. *Build. Environ.* **2016**, *104*, 21–34. https://doi.org/10.1016/j.buildenv.2016.04.023.

(91) Ligocki, M. P.; Salmon, L. G.; Fall, T.; Jones, M. C.; Nazaroff, W. W.; Cass, G. R. Characteristics of Airborne Particles inside Southern California Museums. *Atmos. Environ. Part A, Gen. Top.* **1993**, *27* (5), 697–711. https://doi.org/10.1016/0960-1686(93)90188-5.

(92) Grau-Bové, J.; Strlič, M. Fine Particulate Matter in Indoor Cultural Heritage: A Literature Review. *Herit. Sci.* **2013**, *1* (1), 1–17. https://doi.org/10.1186/2050-7445-1-8.

(93) Brimblecombe, P. The Composition of Museum Atmospheres. *Atmos. Environ.* **1991**, *24B* (1), 1–8.

(94) van Schijndel, A. W. M.; Schellen, H. L.; Wijffelaars, J. L.; van Zundert, K. Application of an Integrated Indoor Climate, HVAC and Showcase Model for the Indoor Climate Performance of a Museum. *Energy Build.* **2008**, *40* (4), 647–653. https://doi.org/10.1016/j.enbuild.2007.04.021.

(95) Smith, G. D.; Clark, R. J. H. The Role of H2S in Pigment Blackening. *J. Cult. Herit.* **2002**, *3* (2), 101–105. https://doi.org/10.1016/S1296-2074(02)01173-1.

(96)     Tang, X.; Misztal, P. K.; Nazaroff, W. W.; Goldstein, A. H. Volatile Organic Compound Emissions from Humans Indoors. *Environ. Sci. Technol.* **2016**, *50* (23), 12686–12694. https://doi.org/10.1021/acs.est.6b04415.

(97)     Yoon, Y. H.; Brimblecombe, P. Clothing as a Source of Fibres within Museums. *J. Cult. Herit.* **2000**, *1* (4), 445–454.

(98)     Yoon, Y. H.; Brimblecombe, P. The Distribution of Soiling by Coarse Particulate Matter in the Museum Environment. *Indoor Air* **2001**, *11* (4), 232–240. https://doi.org/10.1034/j.1600-0668.2001.110404.x.

(99)     Anaf, W.; Horemans, B.; Madeira, T. I.; Carvalho, M. L.; De Wael, K.; Van Grieken, R. Effects of a Constructional Intervention on Airborne and Deposited Particulate Matter in the Portuguese National Tile Museum, Lisbon. *Environ. Sci. Pollut. Res.* **2013**, *20* (3), 1849–1857. https://doi.org/10.1007/s11356-012-1086-7.

(100)    Stuart, B. *Analytical Techniques in Materials Conservation*; Wiley, 2007.

(101)    Skoog, D. A.; James, H. F.; Crouch, S. R. *Principles of Instrumental Analysis*, Sixth Edit.; Thomson Brooks/Cole: Belmont, CA, 2007. https://doi.org/10.1016/s0003-2670(00)84936-3.

(102)    Janssens, K.; Van der Snickt, G.; Vanmeert, F.; Legrand, S.; Nuyts, G.; Alfeld, M.; Monico, L.; Anaf, W.; De Nolf, W.; Vermeulen, M.; Verbeeck, J.; De Wael, K. Non-Invasive and Non-Destructive Examination of Artistic Pigments, Paints, and Paintings by Means of X-Ray Methods. *Top. Curr. Chem.* **2016**, *374* (6), 1–52. https://doi.org/10.1007/s41061-016-0079-2.

(103)    Janssens, K. X-Ray Based Methods of Analysis. In *Modern Methods for Analysing Archaeological and Historical Glass*; Janssens, K., Ed.; Wiley & Sons, 2013; pp 79–128.

(104)    Reffner, J. A. Advances in Infrared Microspectroscopy and Mapping Molecular Chemical Compositionat Submicrometer Spatial Resolution. *Spectroscopy* **2018**, *33*, 12–17.

(105)    Ma, X.; Beltran, V.; Ramer, G.; Pavlidis, G.; Parkinson, D. Y.; Thoury, M.; Meldrum, T.; Centrone, A.; Berrie, B. H. Revealing the Distribution of Metal Carboxylates in Oil Paint from the Micro- to Nanoscale. *Angew. Chemie Int. Ed.* **2019**. https://doi.org/10.1002/anie.201903553.

(106)    Morsch, S.; Van Driel, B. A.; Van Den Berg, K. J.; Dik, J. Investigating the Photocatalytic Degradation of Oil Paint Using ATR-IR and AFM-IR. *ACS Appl. Mater. Interfaces* **2017**, *9* (11), 10169–10179. https://doi.org/10.1021/acsami.7b00638.

(107)    Photothermal Spectroscopy Corp. O-PTIR non-contact submicron visible probe infrared spectroscopy https://www.photothermal.com/o-ptir/ (accessed Feb 22, 2021).

(108)    Pletcher, D.; Greff, R.; Peat, R.; Peter, L. M.; Robinson, J. *Instrumental Methods in Electrochemistry*, 1st editio.; Elsevier, 2001.

(109)    Rahemi, V.; Sarmadian, N.; Anaf, W.; Janssens, K.; Lamoen, D.; Partoens, B.; De Wael, K. Unique Optoelectronic Structure and Photoreduction Properties of Sulfur-Doped Lead Chromates Explaining Their Instability in Paintings. *Anal. Chem.* **2017**, *89* (6), 3326–3334. https://doi.org/10.1021/acs.analchem.6b03803.

(110)    Bonaduce, I.; Ribechini, E.; Modugno, F.; Colombini, M. P. Analytical Approaches Based on Gas Chromatography Mass Spectrometry (GC/MS) to Study  Organic Materials in Artworks and Archaeological Objects. *Top. Curr. Chem.* **2016**, *374* (1), 6. https://doi.org/10.1007/s41061-015-0007-x.

(111)    Degano, I.; La Nasa, J. Trends in High Performance Liquid Chromatography for Cultural Heritage. *Top. Curr. Chem.* **2016**, *374* (2), 1–28. https://doi.org/10.1007/s41061-016-0020-8.

(112)    Camuffo, D. *Microclimate for Cultural Heritage*, Third edit.; Elsevier Science B.V.: San Diego, 2019.

(113)    Michalski, S. *Agent of Deterioration: Light, Ultraviolet and Infrared*; 2018.

(114)    Borrego, C.; Costa, A. M.; Ginja, J.; Amorim, M.; Coutinho, M.; Karatzas, K.; Sioumis, T.; Katsifarakis, N.; Konstantinidis, K.; Vito, S. De; Esposito, E.; Smith, P.; G, P.; Andr, N.; Reimringer, W.; Otjes, R. P.; Sicard, O. Von; Pohle, R.; Elen, B. Assessment of Air Quality Microsensors versus Reference Methods : The EuNetAir Joint Exercise. **2016**, *147* (2), 246–263. https://doi.org/10.1016/j.atmosenv.2016.09.050.

(115)    Morawska, L.; Thai, P. K.; Liu, X.; Asumadu-Sakyi, A.; Ayoko, G.; Bartonova, A.; Bedini, A.; Chai, F.; Christensen, B.; Dunbabin, M.; Gao, J.; Hagler, G. S. W.; Jayaratne, R.; Kumar, P.; Lau, A. K. H.; Louie,

P. K. K.; Mazaheri, M.; Ning, Z.; Motta, N.; Mullins, B.; Rahman, M. M.; Ristovski, Z.; Shafiei, M.; Tjondronegoro, D.; Westerdahl, D.; Williams, R. Applications of Low-Cost Sensing Technologies for Air Quality Monitoring and Exposure Assessment: How Far Have They Gone? *Environ. Int.* **2018**, *116* (February), 286–299. https://doi.org/10.1016/j.envint.2018.04.018.

(116)  Specifications for MS&T Area Sampler Harvard-type impactor on Air Diagnostics and Engineering Inc. website https://www.airdiagnostics.com/indoor_samp_equip.html (accessed Feb 17, 2021).

(117)  Fondazione Salvatore Maugeri. No Title http://www.radiello.com/english/index_en.html.

(118)  Schmidt-Ott, A.; Ristovski, Z. D. Measurement of Airborne Particles. In *Indoor Environment: Airborne Particles and Settled Dust*; Morawska, L., Salthammer, T., Eds.; Wiley, 2003; pp 56–81. https://doi.org/10.1002/9783527610013.ch2b.

(119)  Manikonda, A.; Zíková, N.; Hopke, P. K.; Ferro, A. R. Laboratory Assessment of Low-Cost PM Monitors. *J. Aerosol Sci.* **2016**, *102*, 29–40. https://doi.org/10.1016/j.jaerosci.2016.08.010.

(120)  Liu, D.; Zhang, Q.; Jiang, J.; Chen, D. R. Performance Calibration of Low-Cost and Portable Particular Matter (PM) Sensors. *J. Aerosol Sci.* **2017**, *112*, 1–10. https://doi.org/10.1016/j.jaerosci.2017.05.011.

(121)  Rai, A. C.; Kumar, P.; Pilla, F.; Skouloudis, A. N.; Di Sabatino, S.; Ratti, C.; Yasar, A.; Rickerby, D. End-User Perspective of Low-Cost Sensors for Outdoor Air Pollution Monitoring. *Sci. Total Environ.* **2017**, *607–608*, 691–705. https://doi.org/10.1016/j.scitotenv.2017.06.266.

(122)  Besloten Hofjes https://www.hofvanbusleyden.be/besloten-hofjes (accessed Aug 12, 2020).

(123)  Watteeuw, L.; Iterbeke, H. *Enclosed Gardens of Mechelen. Late Medieval Paradise Gardens Revealed*; Amsterdam University Press: Amsterdam, 2018.

(124)  Stephan, S.; Hildebrandt, G.; Moro, R.; Pietsch, A.; Wenzel, F. Die Restaurierung Cler Reliquiengarten Aus Kloster Bentlage. In *Westfalen. 77. Band 1999. Hefte für Geschichte Kund und Volkskunde*; Schedensack, C., Ed.; Aschendorff Verlag GmbH: Munster, 2002; pp 137–173.

(125)  The British Museum. boss; jewellery-fitting; jewellery https://www.britishmuseum.org/collection/object/G_1888-0601-3 (accessed Jul 7, 2020).

(126)  The State Hermitage Museum. Plaque, Pierced so it could be Sewn on to Fabric, in the Form of a Rosette https://hermitagemuseum.org/wps/portal/hermitage/digital-collection/25.+archaeological+artifacts/3481310 (accessed Jul 7, 2020).

(127)  Gold fabric appliqués and ornaments from near Kendirlik https://sardisexpedition.org/en/artifacts/latw-133 (accessed Jul 7, 2020).

(128)  Reeves, C. N. *After Tutankhamun. Research and Excavation in the Royal Necropolis at Thebes*; Rouledge: London, 1992.

(129)  Kot Diji phase gold sequins (India) https://www.harappa.com/indus5/32.html (accessed Jul 7, 2020).

(130)  Sailko. File:Ambrogio bevilacqua, madonna col bambino, 1495-1499, tempera su tela e ricamo in seta 02.JPG https://commons.wikimedia.org/wiki/File:Ambrogio_bevilacqua,_madonna_col_bambino,_1495-1499,_tempera_su_tela_e_ricamo_in_seta_02.JPG (accessed Jul 7, 2020).

(131)  Segrest, J. Medieval "Bezants" https://www.flickr.com/photos/verybigjen/albums/72157594497838345 (accessed Jul 7, 2020).

(132)  Staniland, K. *Medieval Craftsmen: Embroiderers*; University of Toronto Press: Toronto, 1991.

(133)  Gostelow, M. *Blackwork*; Dover Publications Inc.: Mineola, New York, 1998.

(134)  Clark, J. *The Medieval Horse and Its Equipment, c. 1150-1450.*; The Boydell Press: Woodbridge, UK, 1995.

(135)  Peeters Publishers. *Tongeren. Basiliek van O.-L.-Vrouw Geboorte. I. Textiel van de Vroege Middeleeuwen Tot Het Consilie van Trente*; Peeters Publishers: Leuven, 1988.

(136)  Lowe, B. Early Records of the Morris in England. *J. English Folk Danc. Song Soc.* **1957**, *8* (2), 61–82.

(137)  Thomas, N. L'industrie Du Cuivre Au Bas Moyen-Âge. Formes Du Marché et de La Production. *Hist. images Médiévales* **2010**, *34* (May), 32–37.

(138)  Sutton, A. F. Marcellus Maures Alias Selis, of Utrecht and London. A Goldsmith Of The Yorkist Kings. *The Ricardian* **2007**, *17*, 72–82.

(139) McCall, T. Brilliant Bodies: Material Culture and the Adornment of Men in North Italy's Quattrocento Courts. *I Tatti Stud. Ital. Renaiss.* **2013**, *16* (1/2), 445–490. https://doi.org/10.1086/673421.

(140) Buss, C. *Silk, Gold and Crimson: Opulence in the Workshops of the Courts of the Visconti and the Sforza*; Silvana Editoriale: Milan, 2009.

(141) Bourgarit, D.; Thomas, N. Late Medieval Copper Alloying Practices: A View from a Parisian Workshop of the 14th Century AD. *J. Archaeol. Sci.* **2012**, *39* (10), 3052–3070. https://doi.org/10.1016/j.jas.2012.04.009.

(142) Zanoboni, M. P. *Artigiani, Imprenditori, Mercanti.Organizzazione Del Lavoro e Conflitti Sociali Nella Milano Sforzesca (1450-1476)*; La Nuova Italia: Firenze, 1996.

(143) Castelle, M.; Dillmann, P.; Vega, E.; Blanc-Riehl, C.; Vilain, A.; Chastang, P.; Anheim, E. Seal the Deal: An Extensive Study of European Historical Copper-Based Seal Matrices Using a Multimodal Protocol. *J. Archaeol. Sci.* **2020**, *113* (December 2019), 105061. https://doi.org/10.1016/j.jas.2019.105061.

(144) Qiu, P.; Leygraf, C. Initial Oxidation of Brass Induced by Humidified Air. *Appl. Surf. Sci.* **2011**, *258* (3), 1235–1241. https://doi.org/10.1016/j.apsusc.2011.09.080.

(145) Goidanich, S.; Brunk, J.; Herting, G.; Arenas, M. A.; Odnevall Wallinder, I. Atmospheric Corrosion of Brass in Outdoor Applications. Patina Evolution, Metal Release and Aesthetic Appearance at Urban Exposure Conditions. *Sci. Total Environ.* **2011**, *412–413*, 46–57. https://doi.org/10.1016/j.scitotenv.2011.09.083.

(146) Gener, M.; Montero-Ruiz, I.; Murillo-Barroso, M.; Manzano, E.; Vallejo, A. Lead Provenance Study in Medieval Metallic Materials from Madinat Al-Zahra (Medina Azahara, Córdoba). *J. Archaeol. Sci.* **2014**, *44* (1), 154–163. https://doi.org/10.1016/j.jas.2014.01.029.

(147) Mears, R. B.; Brown, R. H. Causes of Corrosion Currents. *Ind. Eng. Chem.* **1941**, *33* (8), 1001–1010. https://doi.org/10.1021/ie50380a010.

(148) Welter, J. M. Contact Tinning: A Millennia-Old Plating Technology. *Archaeometry* **2019**, *61* (4), 906–920. https://doi.org/10.1111/arcm.12454.

(149) Oddy, A. *Gilding of Metals in the Old World*; Butterworth-Heinemann Ltd, 1993. https://doi.org/10.1016/b978-0-7506-1611-9.50019-4.

(150) Miśta-Jakubowska, E. A.; Fijał-Kirejczyk, I.; Diduszko, R.; Gójska, A. M.; Kalbarczyk, P.; Milczarek, J. J.; Trela, K.; Żabiński, G. A Silvered Shield Grip from the Roman Period: A Technological Study of Its Silver Coating. *Archaeol. Anthropol. Sci.* **2019**, *11* (7), 3343–3355. https://doi.org/10.1007/s12520-018-0761-0.

(151) Heginbotham, A.; Bassett, J.; Bourgarit, D.; Eveleigh, C.; Glinsman, L.; Hook, D.; Smith, D.; Speakman, R. J.; Shugar, A.; Van Langh, R. The Copper CHARM Set: A New Set of Certified Reference Materials for the Standardization of Quantitative X-Ray Fluorescence Analysis of Heritage Copper Alloys. *Archaeometry* **2015**, *57* (5), 856–868. https://doi.org/10.1111/arcm.12117.

(152) Thomas, N.; Bougarit, D. Les Techniques de Production Des Batteurs et Fondeurs Mosans Au Moyen Age (XII-XVI Siecles). In *L'or des dinandiers*; Thomas, N., Leroy, I., Plumier, J., Eds.; 2014; pp 43–65.

(153) Gaudenzi Asinelli, M.; Martinón-Torres, M. Copper-Alloy Use in a Tyrrhenian Medieval Town: The Case of Leopoli-Cencelle (Italy). *J. Archaeol. Sci. Reports* **2016**, *7*, 597–608. https://doi.org/10.1016/j.jasrep.2015.09.023.

(154) Tylecote, R. F. *A History of Metallurgy*, Second Edi.; Maney Publishing: London, 2002.

(155) Massa, G.; Aldenderfer, M.; Martinón-Torres, M. Of Gold Masks, Bronze Mirrors and Brass Bracelets: Analyses of Metallic Artefacts from Samdzong, Upper Mustang, Nepal 450–650 CE. *Archaeol. Res. Asia* **2019**, *18* (August 2018), 68–81. https://doi.org/10.1016/j.ara.2019.02.004.

(156) Martinon-Torres, M.; Rehren, T. Agricola and Zwickau: Theory and Practice of Renaissance Brass Production in SE Germany. *Hist. Metall.* **2002**, *36* (Fig 1), 95–111.

(157) Otero, V.; Sanches, D.; Montagner, C.; Vilarigues, M.; Carlyle, L.; Lopes, J. A.; Melo, M. J. Characterisation of Metal Carboxylates by Raman and Infrared Spectroscopy in Works of Art. *J. Raman Spectrosc.* **2014**, *45*, 1197–1206.

(158) Beltran, V.; Salvadó, N.; Butí, S.; Cinque, G. Micro Infrared Spectroscopy Discrimination Capability

310

of Compounds in Complex Matrices of Thin Layers in Real Sample Coatings from Artworks. *Microchem. J.* **2015**, *118*, 115–123.

(159)   Bellamy, L. J. F. C. *The Infra-Red Spectra of Complex Molecules*; Springer Science & Business Media, 2013.

(160)   Movasaghi, Z.; Rehman, S.; Rehman, D. I. Fourier Transform Infrared (FTIR) Spectroscopy of Biological Tissues. *Appl. Spectrosc. Rev.* **2008**, *43* (2), 134–179.

(161)   Frost, R. L.; Yang, J.; Ding, Z. Raman and FTIR Spectroscopy of Natural Oxalates: Implications for the Evidence of Life on Mars. *Chinese Sci. Bull.* **2003**, *48* (17), 1844–1852.

(162)   Monico, L.; Rosi, F.; Miliani, C.; Daveri, A.; Brunetti, B. G. Non-Invasive Identification of Metal-Oxalate Complexes Spectroscopy, on Polychrome Artwork Surfaces by Reflection Mid-Infrared Spectroscopy. *Spectrochim. Acta Part A Mol. Biomol.* **2013**, *116*, 270–280.

(163)   Spivack, E. Mechanical Glamour. *Art in America*. 2016.

(164)   Horton, R. M. New Metallographic Evidence for Dezincification of Brass by Redisposition of Copper. *Corrosion*. 1970, pp 260–264. https://doi.org/10.5006/0010-9312-26.6.260.

(165)   Kenworthy, L.; O'Driscoll, W. G. Dezincification of Brasses. *Anti-Corrosion Methods Mater.* **1955**, *2* (8), 317–340. https://doi.org/10.1108/eb019087.

(166)   Di Fazio, M.; Felici, A. C.; Catalli, F.; De Vito, C. Microstructure and Chemical Composition of Roman Orichalcum Coins Emitted after the Monetary Reform of Augustus (23 B.C.). *Sci. Rep.* **2019**, *9* (1), 1–11. https://doi.org/10.1038/s41598-019-48941-4.

(167)   Langenegger, E. E.; Robinson, F. P. A. A Study of the Mechanism of Dezincification of Brasses. *Corrosion* **1969**, *25* (2), 59–66.

(168)   Caley, E. A. *Orichalcum and Related Ancient Alloys: Origin, Composition and Manufacture with Special Reference to the Coinage of the Roman Empire*; The American Numismatic Society: New York, 1964.

(169)   Untracht, O. *Jewelery Concepts and Technology*; Doubleday: New York, 1982.

(170)   Scott, D. A. A Review of Copper Chlorides and Related Salts in Bronze Corrosion and as Painting Pigments. *Stud. Conserv.* **2000**, *45* (1), 39–53. https://doi.org/10.1179/sic.2000.45.1.39.

(171)   Zahner, L. W. *Copper, Brass, and Bronze Surfaces: A Guide to Alloys, Finishes, Fabrication and Maintenance in Architecture and Art*; John Wiley & Sons: Hoboken, New Jersey, 2020.

(172)   Hughes, C.; Wolf, S. TSG Chapter VI. Treatment of Textiles - Section A. Humidification https://www.conservation-wiki.com/wiki/TSG_Chapter_VI._Treatment_of_Textiles_-_Section_A._Humidification#Moisture_sensitivity_of_textile_and_associated_components. (accessed Aug 16, 2020).

(173)   Linthicum, M. C. Oes. *Rev. English Stud.* **1931**, *os-VII* (26), 198–200. https://doi.org/10.1017/S0017816000010208.

(174)   Blanco, J.; Doering, M. D. *Clothing and Fashion: American Fashion from Head to Toe. Volume One: Pre-Colonial Times through the American Revolution*; ABC-CLIO, LCC: Santa Barbara, California, 2016.

(175)   Svensson, R. *Renovatio Monetae. Bracteates and Coinage Policies in Medieval Europe*; SPINK & SON LTD: London, 2013.

(176)   Scott, D. A. *Metallography and Microstructure of Ancient and Historic Metals*; The Getty Conservation Institute: Singapore, 1991.

(177)   Svensson, R. Classifying Medieval Bracteates. *SSRN Electron. J.* **2019**, No. October. https://doi.org/10.2139/ssrn.3463634.

(178)   Hawthorne, J. G.; Smith, C. S. *Theophilus: On Divers Arts.*; Dover Publications: New York, 1979.

(179)   Dejonghe, L. Zinc-Lead Deposits of Belgium. *Ore Geol. Rev.* **1998**, *12* (5), 329–354. https://doi.org/10.1016/S0169-1368(98)00007-9.

(180)   Oman, C. C. The Founders of Malines and England, 1460=1560. *Oud Holl.* **1933**, *50*, 77–82. https://doi.org/10.1163/187501733X00131.

(181)   Cosaert, K. De Gietindustrie in Mechelen. ETWIE-Expertisecentrum voor Technisch, Wetenschappelijk en Industrieel Erfgoed: Ghent 2011.

(182)   van Doorslaer, G. *L'ancienne Industrie Du Cuivre à Malines.*; L. et A. Godenne, 1910.

(183) Pedretti, C. *Leonardo Da Vinci, Codex Atlanticus: A Catalogue of Its Newly Restored Sheets*; Giunti: Milan, 1979.

(184) Scher, S. K. An Introduction to the Reinassance Portrait Medal. In *Perspectives on the Renaissance Medal: Portrait Medals of the Renaissance*; Garland Publishing Inc.: New York, 2000; pp 1–9.

(185) LUCAS., J. L. *Dies and Die Making*, First edit.; Journal of Commerce Co.: Providence, 1897.

(186) Tavenor-Perry, J. *Dinanderie: A History and Description of Mediaeval Art Work in Copper, Brass and Bronze*; George Allen and Sons: London, 1910.

(187) Babouri, L.; Belmokre, K.; Abdelouas, A.; Bardeau, J. F.; El Mendili, Y. The Inhibitive Effect of Cerium Carbonate on the Corrosion of Brass in 3% NaCl Solution. *Int. J. Electrochem. Sci* **2015**, *10* (9), 7818–7839.

(188) Colomban, P.; Tournié, A.; Maucuer, M.; Meynard, P. On-site Raman and XRF Analysis of Japanese/Chinese Bronze/Brass Patina–the Search for Specific Raman Signatures. *J. Raman Spectrosc.* **2012**, *43* (6), 799–808.

(189) Bouchard, M.; Smith., D. C. Catalogue of 45 Reference Raman Spectra of Minerals Concerning Research in Art History or Archaeology, Especially on Corroded Metals and Coloured Glass. *Spectrochim. Acta Part A Mol. Biomol. Spectrosc.* **2003**, *59* (10), 2247–2266.

(190) Beccaria, A. M.; Poggi, G. Analysis of Aluminum-Brass Corrosion Products in Sea Water and in Chloride Solutions. *Anal. Lett.* **1985**, *18* (18), 2259–2275. https://doi.org/10.1080/00032718508068617.

(191) Martini, C.; Chiavari, C.; Ospitali, F.; Grazzi, F.; Scherillo, A.; Soffritti, C.; Garagnani, G. L. Investigations on a Brass Armour: Authentic or Forgery? *Mater. Chem. Phys.* **2013**, *142* (1), 229–237. https://doi.org/10.1016/j.matchemphys.2013.07.010.

(192) Fischer, A.; Eggert, G.; Dinnebier, R.; Runčevski, T. When Glass and Metal Corrode Together, V: Sodium Copper Formate. *Stud. Conserv.* **2018**, *63* (6), 342–355. https://doi.org/10.1080/00393630.2017.1359472.

(193) Bette, S.; Fischer, A.; Stelzner, J.; Eggert, G.; Dinnebier, R. E. Brass and Glass: Crystal Structure Solution and Phase Characterisation of the Corrosion Product Zn 4 Cu 3 (Zn 1−x Cu x ) 6 (HCOO) 8 (OH) 18 ·6(H 2 O). *Eur. J. Inorg. Chem.* **2019**, *2019* (7), 920–927. https://doi.org/10.1002/ejic.201801420.

(194) Eggert, G.; Haseloff, S.; Euler, H.; Barbier, B. When Glass and Metal Corrode Together, III: The Formation of Dicoppertrihydroxyformate. In *ICOM-CC 16th Triennial Conference Preprints*; Bridgland, J., Ed.; Almada: Critério Produção Gráfica, Lda: Lisbon, 2011.

(195) Euler, H.; Barbier, B.; Kirfel, A.; Haseloff, S.; Eggert, G. Crystal Structure of Trihydroxydicopper Formate, Cu2(OH) 3(HCOO). *Zeitschrift fur Krist. - New Cryst. Struct.* **2009**, *224* (4), 609–610. https://doi.org/10.1524/ncrs.2009.0268.

(196) Eggert, G.; Bührer, A.; Barbier, B.; Euler, H. When Glass and Metal Corrode Together. II, A Black Forest Schäppel and Further Occurrences of Socoformacite. *Glas. Ceram. Conserv. 2010 interim Meet. ICOM-CC Work. Group, Oct. 3-6 2010 Corning, New York, U.S.A.* **2010**, No. January 2018, 174–180.

(197) Fischer, A.; Eggert, G.; Kirchner, D. When Glass and Metal Corrode Together, IV: Sodium Lead Carbonate Hydroxide. *Interim Meet. ICOM-CC Met. Gr. 2013 Edinburgh, Scotl.* **2013**, No. January 2018, 13–19.

(198) Dinnebier, R. E.; Fischer, A.; Eggert, G.; Runčevski, T.; Wahlberg, N. X-Ray Powder Diffraction in Conservation Science: Towards Routine Crystal Structure Determination of Corrosion Products on Heritage Art Objects. *J. Vis. Exp.* **2016**, *2016* (112), 1–17. https://doi.org/10.3791/54109.

(199) Eggert, G.; Fischer, A.; Dinnebier, R. E. One Heritage Corrosion Product Less: Basic Sodium Copper Carbonate. *Herit. Sci.* **2016**, *4* (1). https://doi.org/10.1186/s40494-016-0092-3.

(200) Schmutzler, B.; Eggert, G.; Kuhn-Wawrzinek, C. F. Copper(II) Hydroxide on Artefacts: Corrosion, Conservation, Colourants. *Stud. Conserv.* **2017**, *62* (2), 61–67. https://doi.org/10.1080/00393630.2016.1215591.

(201) Doremus, R. H. Diffusion of Water and Oxygen in Quartz: Reaction-Diffusion Model. *Earth Planet. Sci. Lett.* **1998**, *163* (1–4), 43–51. https://doi.org/10.1016/S0012-821X(98)00173-3.

312

(202) Sterpenich, J.; Libourel, G. Water Diffusion in Silicate Glasses under Natural Weathering Conditions: Evidence from Buried Medieval Stained Glasses. *J. Non. Cryst. Solids* **2006**, *352* (50–51), 5446–5451. https://doi.org/10.1016/j.jnoncrysol.2006.08.041.

(203) Scholze, H. Chemical Durability of Glasses. *J. Non. Cryst. Solids* **1982**, *52*, 91–103. https://doi.org/10.1007/978-3-319-93728-1_12.

(204) Melcher, M.; Schreiner, M. Statistical Evaluation of Potash-Lime-Silica Glass Weathering. *Anal. Bioanal. Chem.* **2004**, *379*, 628–639. https://doi.org/10.1007/s00216-004-2595-0.

(205) Cagno, S.; Nuyts, G.; Bugani, S.; De Vis, K.; Schalm, O.; Caen, J.; Helfen, L.; Cotte, M.; Reischig, P.; Janssens, K. Evaluation of Manganese-Bodies Removal in Historical Stained Glass Windows via SR-μ-XANES/XRF and SR-μ-CT. *J. Anal. At. Spectrom.* **2011**, *26* (12), 2442–2451. https://doi.org/10.1039/c1ja10204d.

(206) Eggert, G.; Wollmann, A.; Schwahn, B. When Glass and Metal Corrode Together. In *ICOM COMMITTEE FOR CONSERVATION*; New Delhi, India, 2008; pp 209–214.

(207) Schalm, O.; Janssens, K.; Wouters, H.; Caluwé, D. Composition of 12-18th Century Window Glass in Belgium: Non-Figurative Windows in Secular Buildings and Stained-Glass Windows in Religious Buildings. *Spectrochim. Acta - Part B At. Spectrosc.* **2007**, *62* (6-7 SPEC. ISS.), 663–668. https://doi.org/10.1016/j.sab.2007.03.006.

(208) Solé, V. A.; Papillon, E.; Cotte, M.; Walter, P.; Susini, J. A Multiplatform Code for the Analysis of Energy-Dispersive X-Ray Fluorescence Spectra. *Spectrochim. Acta - Part B At. Spectrosc.* **2007**, *62* (1), 63–68. https://doi.org/10.1016/j.sab.2006.12.002.

(209) Toplak, M.; Birarda, G.; Read, S.; Sandt, C.; Rosendahl, S. M.; Vaccari, L.; Demšar, J.; Borondics, F. Infrared Orange: Connecting Hyperspectral Data with Machine Learning. *Synchrotron Radiat. News* **2017**, *30* (4), 40–45.

(210) Demšar, J.; Curk, T.; Erjavec, A.; Gorup, Č.; Hočevar, T.; Milutinovič, M.; Možina, M.; Polajnar, M.; Toplak, M.; Starič, A.; Štajdohar, M.; Umek, L.; Žagar, L.; Žbontar, J.; Žitnik, M.; Zupan, B. Orange: Data Mining Toolbox in Python. *J. Mach. Learn. Res.* **2013**, *14*, 2349–2353.

(211) De Nolf, W.; Vanmeert, F.; Janssens, K. XRDUA: Crystalline Phase Distribution Maps by Two-Dimensional Scanning and Tomographic (Micro) X-Ray Powder Diffraction. *J. Appl. Crystallogr.* **2014**, *47* (3), 1107–1117. https://doi.org/10.1107/S1600576714008218.

(212) Zhou, P.; Hutchison, M. J.; Erning, J. W.; Scully, J. R.; Ogle, K. An in Situ Kinetic Study of Brass Dezincification and Corrosion. *Electrochim. Acta* **2017**, *229* (December), 141–154. https://doi.org/10.1016/j.electacta.2017.01.078.

(213) Rohanová, D.; Hradecká, H.; Klikarová, L.; Hauková, P.; Švarcová, S. Leach Testing of Model Glasses Containing Sodium or Potassium Ions as a Flux. *Glas. Technol. Eur. J. Glas. Sci. Technol. Part A* **2012**, *53* (3), 109–117. https://doi.org/10.1007/BF00668500.

(214) Robinet, L.; Eremin, K.; Cobo Del Arco, B.; Gibson, L. T. A Raman Spectroscopic Study of Pollution-Induced Glass Deterioration. *J. Raman Spectrosc.* **2004**, *35* (8–9), 662–670. https://doi.org/10.1002/jrs.1133.

(215) Anaf, W.; Bencs, L.; Van Grieken, R.; Janssens, K.; De Wael, K. Indoor Particulate Matter in Four Belgian Heritage Sites: Case Studies on the Deposition of Dark-Colored and Hygroscopic Particles. *Sci. Total Environ.* **2015**, *506–507*, 361–368. https://doi.org/10.1016/j.scitotenv.2014.11.018.

(216) Ito, K.; Bernstein, H. J. The Vibrational Spectra of the Formate, Acetate, and Oxalate Ions. *Can. J. Chem.* **1956**, *34* (2), 170–178. https://doi.org/10.1139/v56-021.

(217) Nakamoto, K. Infrared and Raman Spectra of Inorganic and Coordination Compounds. Handbook of Vibrational Spectroscopy. *Handb. Vib. Spectrosc.* **2006**, 1872–1892. https://doi.org/10.1002/9780470027325.s4104.

(218) Frost, R. L.; Martens, W. N.; Wain, D. L.; Hales, M. C. Infrared and Infrared Emission Spectroscopy of the Zinc Carbonate Mineral Smithsonite. *Spectrochim. Acta - Part A Mol. Biomol. Spectrosc.* **2008**, *70* (5), 1120–1126. https://doi.org/10.1016/j.saa.2007.10.027.

(219) Weir, C. E.; Lippincott, E. R. Infrared Studies of Aragonite, Calcite, and Vaterite Type Structures in the Borates, Carbonates, and Nitrates. *J. Res. Natl. Bur. Stand. Sect. A Phys. Chem.* **1961**, *65A* (3), 173. https://doi.org/10.6028/jres.065a.021.

(220) Kadikova, I. F.; Morozova, E. A.; Yuryeva, T. V.; Grigorieva, I. A.; Yuryev, V. A. Study of Deteriorating Semiopaque Turquoise Lead-Potassium Glass Beads at Different Stages of Corrosion Using Micro-FTIR Spectroscopy. *arXiv* **2017**, No. May.

(221) Carter, R. O.; Poindexter, B. D.; Weber, W. H. Vibrational Spectra of Copper Formate Tetrahydrate, Copper Formate Dihydrate and Three Anhydrous Forms of Copper Formate. *Anal. Chim. Acta* **1991**, *253* (2–3), 125–134. https://doi.org/10.1016/0003-2670(91)87167-6.

(222) Krishnan, R. S.; Ramanujam, P. S. Raman and Infrared Spectra of Copper Formate Tetrahydrate. *Spectrochim. Acta* **1972**, *28A*, 2227–2231. https://doi.org/10.1007/978-94-011-4742-2_23.

(223) Secco, E. A. Spectroscopic Properties of SO4 (and OH) in Different Molecular and Crystalline Environments. I. Infrared Spectra of Cu4(OH)6SO4, Cu4(OH)4OSO4, and CU3(OH)4SO4. *Can. J. Chem.* **1988**, *66*, 329–336.

(224) Derrick, M. R.; Stulik, D.; Landry, J. M. *Infrared Spectroscopy in Conservation Science*; The Getty Conservation Institute: Los Angeles, 1999. https://doi.org/10.1002/9781118162897.ch5.

(225) Vilarigues, M.; da Silva, R. C. The Effect of Mn, Fe and Cu Ions on Potash-Glass Corrosion. *J. Non. Cryst. Solids* **2009**, *355* (31–33), 1630–1637. https://doi.org/10.1016/j.jnoncrysol.2009.05.051.

(226) Antonoglou, O.; Moustaka, J.; Adamakis, I. D. S.; Sperdouli, I.; Pantazaki, A. A.; Moustakas, M.; Dendrinou-Samara, C. Nanobrass CuZn Nanoparticles as Foliar Spray Nonphytotoxic Fungicides. *ACS Appl. Mater. Interfaces* **2018**, *10* (5), 4450–4461. https://doi.org/10.1021/acsami.7b17017.

(227) Cagno, S.; Van der Snickt, G.; Legrand, S.; Caen, J.; Patin, M.; Meulebroeck, W.; Dirkx, Y.; Hillen, M.; Steenackers, G.; Rousaki, A.; Vandenabeele, P.; Janssens, K. Comparison of Four Mobile, Non-Invasive Diagnostic Techniques for Differentiating Glass Types in Historical Leaded Windows: MA-XRF, UV–Vis–NIR, Raman Spectroscopy and IRT. *X-Ray Spectrom.* **2020**, 1–17. https://doi.org/10.1002/xrs.3185.

(228) Henderson, J. *Ancient Glass: An Interdisciplinary Exploration*; Cambridge University Press: New York, 2013.

(229) Dik, J.; Hermens, E.; Peschar, R.; Schenk, H. Early Production Recipes for Lead Antimonate Yellow in Italian Art. *Archaeometry* **2005**, *47* (3), 593–607. https://doi.org/10.1111/j.1475-4754.2005.00221.x.

(230) Wainwright, I. N. M. R.; Taylor, J. M.; Harley, R. D. Cadmium Yellows, Oranges and Reds. In *Artists' pigments: a handbook of their history and characteristics*; Feller, R. L., Ed.; National Gallery of Art: Washington DC, 1986; pp 65–108.

(231) Dik, J.; Peschar, R.; Schenk, H. The Introduction of Lead Antimonate Yellow in the 18th Century. *Zeitschrift für Kunsttechnologie und Konserv.* **2006**, *20*, 138–146.

(232) Agresti, G.; Baraldi, P.; Pelosi, C.; Santamaria, U. Yellow Pigments Based on Lead, Tin, and Antimony: Ancient Recipes, Synthesis, Characterization, and Hue Choice in Artworks. *Color Res. Appl.* **2016**, *41* (3), 226–231. https://doi.org/10.1002/col.22026.

(233) Eastaugh, N.; Walsh, V.; Chaplin, T.; Ruth, S. *Pigment Compendium: A Dictionary and Optical Microscopy of Historical Pigments*; Butterworth-Heinemann: London, 2008.

(234) Chiarantini, L.; Gallo, F.; Rimondi, V.; Benvenuti, M.; Costagliola, P.; Dini, A. Early Renaissance Production Recipes for Naples Yellow Pigment: A Mineralogical and Lead Isotope Study of Italian Majolica from Montelupo (Florence). *Archaeometry* **2015**, *57* (5), 879–896. https://doi.org/10.1111/arcm.12146.

(235) Kirmizi, B.; Göktürk, E. H.; Colomban, P. Colouring Agents in the Pottery Glazes of Western Anatolia: New Evidence for the Use of Naples Yellow Pigment Variations During The Late Byzantine Period. *Archaeometry* **2015**, *57* (3), 476–496. https://doi.org/10.1111/arcm.12101.

(236) Seccaroni, C. *Giallorino. Storia Dei Pigmenti Gialli Di Natura Sintetica*; De Luca Editore, Ed.; Rome, 2006.

(237) Pelosi, C.; Agresti, G.; Santamaria, U.; Mattei, E. Artificial Yellow Pigments: Production and Characterization through Spectroscopic Method of Analysis. *ePreserv. Sci.* **2010**, *7*, 108–115.

(238) Santamaria, U.; Agresti, G.; Pelosi, C. Memory and Matter of Cultural Heritage: Lead, Tin and Antimony Based Yellow Pigments. In *Fatto d'Archimia*; Kroustallis, S., del Egido, M., Eds.; Ministerio de Educatión, Cultura y Deporte: Madrid, 2012; pp 145–156.

314

(239)  Zecchin, L. *Il Ricettario Darduin. Un Codice Vetrario Del Seicento Trascritto e Commentato.*; Arsenale: Venezia, 1984.

(240)  Zecchin, L. *Vetro e Vetrai Di Murano. Studi Di Storia Del Vetro. Vol.1*; Arsenale: Venezia, 1987.

(241)  Zecchin, L. *Vetro e Vetrai Di Murano. Studi Di Storia Del Vetro. Vol. 2.*; Arsenale: Venezia, 1989.

(242)  Zecchin, L. *Vetro e Vetrai Di Murano. Studi Di Storia Del Vetro. Vol. 3.*; Arsenale: Venezia, 1990.

(243)  Rico, L. Pigmenti Del XVI Secolo Tra Venezia e La Spagna. Tiziano, l'Escorial e Il Commercio Con Venezia. *Kermes* **2000**, *37*, 58–71.

(244)  Moretti, C.; Salerno, C. S.; Tommasi Ferroni, S. *Ricette Vetrarie Muranesi. Gaspare Brunuoro e Il Manoscritto Di Danzica*; Nardini Editore, Ed.; Firenze, 2004.

(245)  Janssens, K. H. A. *Modern Methods for Analysing Archaeological and Historical Glass. Vol.1*; John Wiley & Sons: Chichester, 2013.

(246)  Ferrer, P.; Ruiz-Moreno, S.; López-Gil, A.; Chillón, M. C.; Sandalinas, C. New Results in the Characterization by Raman Spectroscopy of Yellow Pigments Used in Ceramic Artworks of the 16th and 17th Centuries. *J. Raman Spectrosc.* **2012**, *43* (11), 1805–1810.

(247)  Kock, L. D.; De Waal, D. Raman Analysis of Ancient Pigments on a Tile from the Citadel of Algiers. *Spectrochim. Acta A* **2008**, *71*, 1348–1354.

(248)  Bensi, P.; Montiani Bensi, M. R. Osservazioni Tecniche e Iconografiche Sui Colori Gialli Nella Pittura Del XVI e XVII Sec. In *Scritti ed immagini in onore di Corrado Maltese*; Marconi, S., Dalai, M., Eds.; Quasar: Rome, 1999; pp 167–175.

(249)  Montanari, R.; Alberghina, M. F.; Casanova Municchia, A.; Massa, E.; Pelagotti, A.; Pelosi, C.; Schiavone, S.; Sodo, A. A Polychrome Mukozuke (1624–1644) Porcelain Offers a New Hypothesis on the Introduction of European Enameling Technology in Japan. *J. Cult. Herit.* **2018**, *32*, 232–237.

(250)  Montanari, R.; Murakami, N.; Alberghina, M. F.; Pelosi, C.; Schiavone, S. The Origin of Overglaze-Blue Enameling in Japan: New Discoveries and a Reassessment. *J. Cult. Herit.* **2019**, *37*, 94–102.

(251)  Rosi, F.; Manuali, V.; Grygar, T.; Bezdicka, P.; Brunetti, B. G.; Sgamellotti, A.; Burgio, L.; Seccaroni, C.; Miliani, C. Raman Scattering Features of Lead Pyroantimonate Compounds: Implication for the Non-Invasive Identification of Yellow Pigments on Ancient Ceramics. Part II. in Situ Characterisation of Renaissance Plates by Portable Micro-Raman and XRF Studies. *J. Raman Spectrosc.* **2011**, *42* (3), 407–414. https://doi.org/10.1002/jrs.2699.

(252)  Buzzegoli, E.; Cardaropoli, R.; Kunzelman, D.; Moioli, P.; Montalbano, L.; Piccolo, M.; Seccaroni, C. Valerio Mariani Da Pesaro, Il Trattato "Della Miniatura": Primi Raffronti Con Le Analisi e Le Opere. *OPD Restauro. Riv. dell'Opificio delle Pietre Dure e Lab. di Restauro di Firenze* **2000**, *12*, 248–256.

(253)  Berrie, B. H. Mining for Color: New Blues , Yellows , and Translucent Paint. *Early Sci. Med.* **2015**, *20*, 308–334. https://doi.org/10.1163/15733823-02046p02.

(254)  Roy, A.; Berrie, B. H. A New Lead-Based Yellow in the Seventeenth Century. *Stud. Conserv.* **1998**, *43* (sup1), 160–165. https://doi.org/10.1179/sic.1998.43.Supplement-1.160.

(255)  Sandalinas, C.; Ruiz-moreno, S. Lead-Tin-Antimony Yellow: Historical Manufacture, Molecular Characterization and Identification in Seventeenth-Century Italian Paintings. *Stud. Conserv.* **2004**, *49* (1), 41–52.

(256)  Subramanian, M. A.; Aravamudan, G.; Subba Rao, G. V. Oxide Pyrochlores - A Review. *Prog. Solid State Chem.* **1983**, *15* (2), 55–143. https://doi.org/10.1016/0079-6786(83)90001-8.

(257)  Atencio, D.; Gieré, R.; Andrade, M. B.; Christy, A. G.; Kartashov, P. M. The Pyrochlore Supergroup of Minerals: Nomenclature. *Can. Mineral.* **2010**, *48* (3), 673–678. https://doi.org/10.3749/canmin.48.3.673.

(258)  Anaf, W.; Schalm, O.; Janssens, K.; De Wael, K. Understanding the (in)Stability of Semiconductor Pigments by a Thermodynamic Approach. *Dye. Pigment.* **2015**, *113*, 409–415. https://doi.org/10.1016/j.dyepig.2014.09.015.

(259)  Anaf, W.; Trashin, S.; Schalm, O.; Van Dorp, D.; Janssens, K.; De Wael, K. Electrochemical Photodegradation Study of Semiconductor Pigments: Influence of Environmental Parameters. *Anal. Chem.* **2014**, *86* (19), 9742–9748. https://doi.org/10.1021/ac502303z.

(260)  Burchard, V. G.; Rudorff, W. Zur Frage Nach Der Existenz Eines Kubischen Pyrochlors Pb2Sb2O7. *Z. anorg. allg. Chem* **1978**, *447*, 149–152.

(261) Brisse, F.; Stewart, D. J.; Seidl, V.; Knop, O. Pyrochlores . VIII . Studies of Some 2-5 Pyrochlores and Related Compounds and Minerals. *Can. J. Chem.* **1972**, *5*, 3648–3666.

(262) Cloutis, E.; Norman, L.; Cuddy, M.; Mann, P. Spectral Reflectance (350-2500 Nm) Properties of Historic Artists' Pigments. II. Red-Orange-Yellow Chromates, Jarosites, Organics, Lead(-Tin) Oxides, Sulphides, Nitrites and Antimonates. *J. Near Infrared Spectrosc.* **2016**, *24* (2), 119–140. https://doi.org/10.1255/jnirs.1207.

(263) Allen, J. P.; Scanlon, D. O.; Watson, G. W. Comparison of the Defective Pyrochlore and Ilmenite Polymorphs of AgSbO 3 Using GGA and Hybrid DFT. *Phys. Rev. B - Condens. Matter Mater. Phys.* **2011**, *83* (3), 1–8. https://doi.org/10.1103/PhysRevB.83.035207.

(264) Mizoguchi, H.; Woodward, P. M. Electronic Structure Studies of Main Group Oxides Possessing Edge-Sharing Octahedra. Implications for the Design of Transparent Conducting Oxides. *Chem. Mater.* **2004**, *16* (2), 5233–5248. https://doi.org/10.1021/cm049249w.

(265) Mizoguchi, H.; Eng, H. W.; Woodward, P. M. Probing the Electronic Structures of Ternary Perovskite and Pyrochlore Oxides Containing Sn4+ or Sb5+. *Inorg. Chem.* **2004**, *43* (5), 1667–1680. https://doi.org/10.1021/ic034551c.

(266) Shi, J.; Ma, L.; Wu, P.; Zhou, Z.; Guo, P.; Shen, S.; Jing, D.; Guo, L. A Novel Sn 2 Sb 2 O 7 Nanophotocatalyst for Visible-Light-Driven H 2 Evolution. **2012**, *5* (8), 576–583. https://doi.org/10.1007/s12274-012-0243-0.

(267) Agresti, G. *I Gialli Di Piombo, Stagno, Antimonio: Colore e Materia Dell'opera d'arte*; PhD thesis, University of Tuscia: Viterbo, 2017.

(268) Capobianco, G.; Pelosi, C.; Agresti, G.; Bonifazi, G.; Santamaria, U.; Serranti, S. X-Ray Fluorescence Investigation on Yellow Pigments Based on Lead, Tin and Antimony through the Comparison between Laboratory and Portable Instruments. *J. Cult. Herit.* **2017**. https://doi.org/10.1016/j.culher.2017.09.002.

(269) Picolpasso, C. *The Three Books of the Potter's Art*, facsimil.; Victoria & Albert Museum: London, 1976.

(270) Hradil, D.; Grygar, T.; Hradilová, J.; Bezdička, P.; Grunwaldová, V.; Fogaš, I.; Miliani, C. Microanalytical Identification of Pb-Sb-Sn Yellow Pigment in Historical European Paintings and Its Differentiation from Lead Tin and Naples Yellows. *J. Cult. Herit.* **2007**, *8* (4), 377–386. https://doi.org/10.1016/j.culher.2007.07.001.

(271) Cascales, C.; Alonso, J. A.; Rasines, I. The New Pyrochlores Pb2 ( MSb ) O6 . 5 ( M = Ti , Zr , Sn , Hf ). *J. Mater. Sci. Lett.* **1986**, *5*, 675–677. https://doi.org/10.1007/BF01731548.

(272) Jutten, C.; Herault, J. Blind Separation of Sources, Part I: An Adaptive Algorithm Based on Neuromimetic Architecture. *Signal Processing* **1991**, *24* (1), 1–10. https://doi.org/10.1016/0165-1684(91)90079-X.

(273) Sangiorgi, N.; Aversa, L.; Tatti, R.; Verucchi, R.; Sanson, A. Spectrophotometric Method for Optical Band Gap and Electronic Transitions Determination of Semiconductor Materials. *Opt. Mater. (Amst).* **2017**, *64*, 18–25. https://doi.org/10.1016/j.optmat.2016.11.014.

(274) Zhang, Y.; Yin, J.; Parida, M. R.; Ahmed, G. H.; Pan, J.; Bakr, O. M.; Brédas, J. L.; Mohammed, O. F. Direct-Indirect Nature of the Bandgap in Lead-Free Perovskite Nanocrystals. *J. Phys. Chem. Lett.* **2017**, *8* (14), 3173–3177. https://doi.org/10.1021/acs.jpclett.7b01381.

(275) Kresse, G.; Furthmüller, J. Efficient Iterative Schemes for Ab Initio Total-Energy Calculations Using a Plane-Wave Basis Set. *Phys. Rev. B - Condens. Matter Mater. Phys.* **1996**, *54* (16), 11169–11186. https://doi.org/10.1103/PhysRevB.54.11169.

(276) Kresse, G.; Joubert, D. Kresse, Joubert - Unknown - From Ultrasoft Pseudopotentials to the Projector Augmented-Wave Method. **1999**, *59* (3), 11–19.

(277) Perdew, J. P.; Burke, K.; Ernzerhof, M. Generalized Gradient Approximation Made Simple. *Phys. Rev. Lett.* **1996**, *77* (18), 3865–3868. https://doi.org/10.1103/PhysRevLett.77.3865.

(278) Heyd, J.; Scuseria, G. E.; Ernzerhof, M. Hybrid Functionals Based on a Screened Coulomb Potential. *J. Chem. Phys.* **2003**, *118* (18), 8207–8215. https://doi.org/10.1063/1.1564060.

(279) Van De Walle, C. G.; Laks, D. B.; Neumark, G. F.; Pantelides, S. T. First-Principles Calculations of Solubilities and Doping Limits: Li, Na, and N in ZnSe. *Phys. Rev. B* **1993**, *47* (15), 9425–9434.

https://doi.org/10.1103/PhysRevB.47.9425.

(280)   Rosi, F.; Manuali, V.; Miliani, C.; Brunetti, B. G.; Sgamellotti, A.; Grygar, T.; Hradil, D. Raman Scattering Features of Lead Pyroantimonate Compounds. Part I: XRD and Raman Characterization of Pb2Sb2O7 Doped with Tin and Zinc. *J. Raman Spectrosc.* **2009**, *40* (1), 107–111. https://doi.org/10.1002/jrs.2092.

(281)   Shannon, R. D. Revised Effective Ionic Radii and Systematic Studies of Interatomic Distances in Halides and Chalcogenides. *Acta Cryst.* **1976**, *A32*, 751–767.

(282)   Hålenius, U.; Bosi, F. Oxyplumboroméite, Pb2Sb2O7, a New Mineral Species of the Pyrochlore Supergroup from Harstigen Mine, Värmland, Sweden. *Mineral. Mag.* **2013**, *77*, 2931–2939.

(283)   Cartechini, L.; Rosi, F.; Miliani, C.; D'Acapito, F.; Brunetti, B. G.; Sgamellotti, A. Modified Naples Yellow in Renaissance Majolica: Study of Pb–Sb–Zn and Pb–Sb–Fe Ternary Pyroantimonates by X-Ray Absorption Spectroscopy. *Journal of Analytical Atomic Spectrometry*. 2011, p 2500. https://doi.org/10.1039/c1ja10190k.

(284)   Davidson, R. S.; Willsher, C. J. Mercury(II) Sulphide: A Photo-Stable Semiconductor. *Nature* **1979**, *278*, 238.

(285)   Zhang, Z.; Yuan, Y.; Fang, Y.; Liang, L.; Ding, H.; Shi, G.; Jin, L. Photoelectrochemical Oxidation Behavior of Methanol on Highly Ordered TiO2nanotube Array Electrodes. *J. Electroanal. Chem.* **2007**, *610* (2), 179–185. https://doi.org/10.1016/j.jelechem.2007.07.028.

(286)   Hosono, H.; Ueda, K. Transparent Conductive Oxides. In *Springer Handbook of Electronic and Photonic Materials*; Kasap, S., Capper, P., Eds.; Springer International, 2017; pp 1391–1404. https://doi.org/10.1007/978-3-319-48933-9.

(287)   Setyawan, W.; Gaume, R. M.; Lam, S.; Feigelson, R. S.; Curtarolo, S. High-Throughput Combinatorial Database of Electronic Band Structures for Inorganic Scintillator Materials. *ACS Comb. Sci.* **2011**, *13*, 382–390.

(288)   Seto, J. Y. . W. The Electrical Properties of Polycrystalline Silicon Films. *J. Appl. Phys.* **1975**, *46* (12), 5247–5254. https://doi.org/10.1063/1.321593.

(289)   Broniatowski, A. Electronic States at Grain Boundaries in Semiconductors. In *Polycrystalline Semiconductors*; Harbeke, G., Ed.; Springer: Heidelberg, 1985; pp 95–117.

(290)   Kudo, A.; Miseki, Y. Heterogeneous Photocatalyst Materials for Water Splitting. *Chem. Soc. Rev.* **2009**, *38* (1), 253–278. https://doi.org/10.1039/b800489g.

(291)   Pavlov, D. Semiconductor Mechanism of the Processes during Electrochemical Oxidation of PbO to PbO2. *J. Electroanal. Chem.* **1981**, *118* (C), 167–185. https://doi.org/10.1016/S0022-0728(81)80539-6.

(292)   Haugland, R. P. *Handbook of Fluorescent Probes and Research Products*; Molecular Probes: Paris, 2002.

(293)   Alvarez-Martin, A.; Trashin, S.; Cuykx, M.; Covaci, A.; De Wael, K.; Janssens, K. Photodegradation Mechanisms and Kinetics of Eosin-Y in Oxic and Anoxic Conditions. *Dye. Pigment.* **2017**, *145*, 376–384. https://doi.org/10.1016/j.dyepig.2017.06.031.

(294)   Rahman, H. Utilization of Eosin Dye as an Ion Pairing Agent for Determination of Pharmaceuticals: A Brief Review. *Int. J. Pharm. Pharm. Sci.* **2017**, *9* (12), 1.

(295)   Derayea, S. M.; Nagy, D. M. Application of a Xanthene Dye, Eosin Y, as Spectroscopic Probe in Chemical and Pharmaceutical Analysis; a Review. *Rev. Anal. Chem.* **2018**, *37* (3), 1–14.

(296)   Yoshida, T.; Iwaya, M.; Ando, H.; Oekermann, T.; Nonomura, K.; Schlettwein, D.; Wöhrle, D.; Minoura, H. Improved Photoelectrochemical Performance of Electrodeposited ZnO/EosinY Hybrid Thin Films by Dye Re-Adsorption. *Chem. Commun.* **2004**, *4* (4), 400–401.

(297)   Yoshida, T.; Terada, K.; Schlettwein, D.; Oekermann, T.; Sugiura, T.; Minoura, H. Electrochemical Self-Assembly of Nanoporous ZnO/Eosin Y Thin Films and Their Sensitized Photoelectrochemical Performance. *Adv. Mater.* **2000**, *12* (16), 1214–1217.

(298)   Hazebroucq, S.; Labat, F.; Lincot, D.; Adamo, C. Theoretical Insights on the Electronic Properties of Eosin Y, an Organic Dye for Photovoltaic Applications. *J. Phys. Chem. A* **2008**, *112* (31), 7264–7270. https://doi.org/10.1021/jp8011624.

(299)   Eastaugh, N.; Walsh, V.; Chaplin, T.; Siddal, R. *Pigment Compendium. A Dictionary and Optical*

*Microscopy of Historical Pigments*; 2013; Vol. 53. https://doi.org/10.1017/CBO9781107415324.004.

(300) Gabrieli, F.; Doherty, B.; Miliani, C.; Degano, I.; Modugno, F.; Uldank, D.; Kunzelman, D.; Buzzegoli, E.; Patti, M.; Rosi, F. Micro-Raman and SER Spectroscopy to Unfold Lefranc's Early Organic Pigment Formulations. *J. Raman Spectrosc.* **2016**, *47* (12), 1505–1513. https://doi.org/10.1002/jrs.5052.

(301) Vellekoop, M.; Jansen, L.; Geldof, M.; Hendriks, E.; de Tagle, A. *Van Gogh's Studio Practice*; Mercatorfonds, 2013.

(302) Distel, A.; Stein, S. A. *Cézanne to Van Gogh : The Collection of Doctor Gachet*; Metropolitan Museum of Art, 1999.

(303) Peres, C.; Hoyle, M.; Tilborgh, L. van. *A Closer Look : Technical and Art-Historical Studies on Works by Van Gogh and Gauguin*; Waanders Publishers: Zwolle, 1991.

(304) Saunders, D.; Kirby, J. A Comparison of Light-Induced Damage under Common Museum Illuminants. In *ICOM Committee for Conservation, ICOM-CC, 15th Triennial Conference New Delhi, 22-26 September 2008: preprints*; Allied Publishers PVT: New Delhi, 2008; pp 766–774.

(305) Burnstock, A.; Lanfear, I.; van den Berg, K. J.; Carlyle, L.; Clarke, M.; Hendriks, E.; Kirby, J. Comparison of the Fading and Surface Deterioration of Red Lake Pigments in Six Paintings by Vincent van Gogh with Artificially Aged Paint Reconstructions. *14th Trienn. Meet. Hague, 12-16 Sept. 2005 Prepr. (ICOM Comm. Conserv.* **2005**, No. March, 459–466.

(306) Alvarez-martin, A.; Janssens, K. Protecting and Stimulating e Ff Ect on the Degradation of Eosin Lakes . Part 1 : Lead White and Cobalt Blue. *Microchem. J.* **2020**, *141* (May 2018), 51–63. https://doi.org/10.1016/j.microc.2018.05.005.

(307) Chieli, A.; Miliani, C.; Degano, I.; Sabatini, F.; Tognotti, P.; Romani, A. New Insights into the Fading Mechanism of Geranium Lake in Painting Matrix". *Dye. Pigment.* **2020**, *181*, 108600. https://doi.org/10.1016/j.dyepig.2020.108600.

(308) Sabatini, F.; Eis, E.; Degano, I.; Thoury, M.; Bonaduce, I.; Lluveras-tenorio, A. The Issue of Eosin Fading: A Combined Spectroscopic and Mass Spectrometric Approach Applied to Historical Lakes. *Dye. Pigment.* **2020**, *180*, 108436–108448.

(309) Claro, A.; Melo, M. J.; Schäfer, S.; de Melo, J. S. S.; Pina, F.; van den Berg, K. J.; Burnstock, A. The Use of Microspectrofluorimetry for the Characterization of Lake Pigments. *Talanta* **2008**, *74* (4), 922–929. https://doi.org/10.1016/j.talanta.2007.07.036.

(310) Claro, A.; Melo, M. J.; Seixas de Melo, J. S.; van den Berg, K. J.; Burnstock, A.; Montague, M.; Newman, R. Identification of Red Colorants in van Gogh Paintings and Ancient Andean Textiles by Microspectrofluorimetry. *J. Cult. Herit.* **2010**, *11* (1), 27–34. https://doi.org/10.1016/j.culher.2009.03.006.

(311) Kirby, J. The Reconstruction of Late 19th-Century French Red Lake Pigments. In *Art of the Past: Sources and Reconstructions. Proceedings of the first symposium of the Art Technological Source Research study group*; Clarke, M., Townsend, J. H., Stijnman, A., Eds.; Archetype Publications: London, 2005.

(312) Vanzin, D.; Freitas, C. F.; Pellosi, D. S.; Batistela, V. R.; Machado, A. E. H.; Pontes, R. M.; Caetano, W.; Hioka, N. Experimental and Computational Studies of Protolytic and Tautomeric Equilibria of Erythrosin B and Eosin y in Water/DMSO. *RSC Adv.* **2016**, *6* (111), 110312–110328. https://doi.org/10.1039/c6ra12198e.

(313) Schweitzer, C.; Schmidt, R. Physical Mechanisms of Generation and Deactivation of Singlet Oxygen. *Chem. Rev.* **2003**, *103* (5), 1685–1758. https://doi.org/10.1021/cr010371d.

(314) Anselmi, C.; Capitani, D.; Tintaru, A.; Doherty, B.; Sgamellotti, A.; Miliani, C. Beyond the Color: A Structural Insight to Eosin-Based Lakes. *Dye. Pigment.* **2017**, *140*, 297–311. https://doi.org/10.1016/j.dyepig.2017.01.046.

(315) van den Berg, K. J.; Burnstock, A.; Carlyle, L.; Clarke, M.; Hendriks, E.; Hoppenbrouwers, R.; Kirby, J.; Lanfear, I. Fading of Red Lake Paints after Vincent van Gogh - an Interdisciplinary Study Involving Three De Mayerne Projects. *Report. Highlights Mayerne Program.* **2006**, 89–96.

(316) Amat-Guerri, F.; López-González, M. M. C.; Martínez-Utrilla, R.; Sastre, R. Synthesis and Spectroscopic Properties of New Rose Bengal and Eosin Y Derivatives. *Dye. Pigment.* **1990**, *12* (4),

249–272. https://doi.org/10.1016/0143-7208(90)85017-I.

(317)  Lamberts, J. J. M.; Neckers, D. C. Rose Bengal and Non-Polar Derivatives: The Birth of Dye Sensitizers for Photooxidation. *Zeitschrift für Naturforsch. B* **2014**, *39* (4), 474–484.

(318)  Markuszewski, R.; Diehl, H. The Infrared Spectra and Structures of the Three Solid Forms of Fluorescein and Related Compounds. *Talanta* **1980**, *27* (11), 937–946. https://doi.org/10.1016/0039-9140(80)80125-1.

(319)  Bellamy, L. *The Infra-Red Spectra of Complex Molecules.*; 1975.

(320)  Lin-Vien, D.; Colthup, N. B.; Fateley, W. G.; Grasselli, J. G. (Professor). *The Handbook of Infrared and Raman Characteristic Frequencies of Organic Molecules*; Academic Press, 1991.

(321)  Majoube, M.; Henry, M. Fourier Transform Raman and Infrared and Surface-Enhanced Raman Spectra for Rhodamine 6G. *Spectrochim. Acta Part A Mol. Spectrosc.* **1991**, *47* (9–10), 1459–1466. https://doi.org/10.1016/0584-8539(91)80237-D.

(322)  Greeneltch, N. G.; Davis, A. S.; Valley, N. A.; Casadio, F.; Schatz, G. C.; Van Duyne, R. P.; Shah, N. C. Near-Infrared Surface-Enhanced Raman Spectroscopy (NIR-SERS) for the Identification of Eosin Y: Theoretical Calculations and Evaluation of Two Different Nanoplasmonic Substrates. **2012**. https://doi.org/10.1021/jp3081035.

(323)  Watanabe, H.; Hayazawa, N.; Inouye, Y.; Kawata, S. DFT Vibrational Calculations of Rhodamine 6G Adsorbed on Silver: Analysis of Tip-Enhanced Raman Spectroscopy. **2005**. https://doi.org/10.1021/jp045771u.

(324)  Wang, L.; Roitberg, A.; Meuse, C.; Gaigalas, A. K. Raman and FTIR Spectroscopies of Fluorescein in Solutions. *Spectrochim. Acta - Part A Mol. Biomol. Spectrosc.* **2001**, *57* (9), 1781–1791. https://doi.org/10.1016/S1386-1425(01)00408-5.

(325)  Davies, M.; Jones, R. L. Infra-Red Absorptions and Molecular Structures of Phenol, Phenolphthalein, Fluorescein, and Some Alkali Derivatives. *J. Chem. Soc.* **1954**, No. 0, 120–125. https://doi.org/10.1039/JR9540000120.

(326)  Aronson, M.; Beckmann, P.; Ross, B.; Tan, S. L. Intramolecular Reorientations and the Effects of Thermal History and Hydrogen Bonding in Four Closely Related Organic Molecular Solids. *Chem. Phys.* **1981**, *63* (3), 349–358. https://doi.org/10.1016/0301-0104(81)87010-3.

(327)  Pouchert, C. *Aldrich Library of FT-IR Spectra*; The Aldrich Library of FT-IR Spectra; Wiley: Milwaukee, 1989.

(328)  Wysocki, L. M.; Lavis, L. D. Advances in the Chemistry of Small Molecule Fluorescent Probes. *Current Opinion in Chemical Biology*. Elsevier Ltd December 2011, pp 752–759. https://doi.org/10.1016/j.cbpa.2011.10.013.

(329)  Alvarez-Martin, A.; Janssens, K. Protecting and Stimulating Effect on the Degradation of Eosin Lakes. Part 1: Lead White and Cobalt Blue. *Microchem. J.* **2018**, *141* (September 2017), 51–63. https://doi.org/10.1016/j.microc.2018.05.005.

(330)  Zhang, F.; Shi, F.; Ma, W.; Gao, F.; Jiao, Y.; Li, H.; Wang, J.; Shan, X.; Lu, X.; Meng, S. Controlling Adsorption Structure of Eosin y Dye on Nanocrystalline TiO 2 Films for Improved Photovoltaic Performances. *J. Phys. Chem. C* **2013**, *117* (28), 14659–14666. https://doi.org/10.1021/jp404439p.

(331)  Mehandzhiyski, A. Y.; Riccardi, E.; Van Erp, T. S.; Koch, H.; Åstrand, P. O.; Trinh, T. T.; Grimes, B. A. Density Functional Theory Study on the Interactions of Metal Ions with Long Chain Deprotonated Carboxylic Acids. *J. Phys. Chem. A* **2015**, *119* (40), 10195–10203. https://doi.org/10.1021/acs.jpca.5b04136.

(332)  Bellamy, L. J.; Branch, R. F. The Infra-Red Spectra of Chelate Compounds. Part II. Metal Chelate Compounds of p -Diketones and of Salicylaldehyde. *J. Chem. Soc.* **1954**, 4491–4494.

(333)  Nishikiori, H.; Uesugi, Y.; Takami, S.; Setiawan, R. A.; Fujii, T.; Qian, W.; El-Sayed, M. A. Influence of Steam Treatment on Dye-Titania Complex Formation and Photoelectric Conversion Property of Dye-Doped Titania Gel. *J. Phys. Chem. C* **2011**, *115* (6), 2880–2887. https://doi.org/10.1021/jp109958z.

(334)  Alvarez-Martin, A.; Cleland, T. P.; Kavich, G. M.; Janssens, K.; Newsome, G. A. Rapid Evaluation of the Debromination Mechanism of Eosin in Oil Paint by Direct Analysis in Real Time and Direct Infusion-Electrospray Ionization Mass Spectrometry. *Anal. Chem.* **2019**, *91* (16), 10856–10863.

https://doi.org/10.1021/acs.analchem.9b02568.

(335) Alwin, S.; Sahaya Shajan, X.; Menon, R.; Nabhiraj, P. Y.; Warrier, K. G. K.; Mohan Rao, G. Surfacemodification of Titania Aerogel Films by Oxygen Plasma Treatment for Enhanced Dye Adsorption. *Thin Solid Films* **2015**, *595*, 164–170. https://doi.org/10.1016/j.tsf.2015.10.071.

(336) Narayanan, V. A.; Stokes, D. L.; Vo-Dinh, T. Vibrational Spectral Analysis of Eosin Y and Erythrosin B-Intensity Studies for Quantitative Detection of the Dyes. *J. Raman Spectrosc.* **1994**, *25* (6), 415–422. https://doi.org/10.1002/jrs.1250250607.

(337) Azmi, S. N. H.; Al-Fazari, A.; Al-Badaei, M.; Al-Mahrazi, R. Utility of Eosin Y as a Complexing Reagent for the Determination of Citalopram Hydrobromide in Commercial Dosage Forms by Fluorescence Spectrophotometry. *Luminescence* **2015**, *30* (8), 1352–1359. https://doi.org/10.1002/bio.2905.

(338) Nakamoto, K. *Infrared and Raman Spectra of Inorganic and Coordination Compounds*, 3rd ed.; Wiley: New York, 1978.

(339) Keim, M. F.; Gassmann, B.; Markl, G. Formation of Basic Lead Phases during Fire-Setting and Other Natural and Man-Made Processes. *Am. Mineral.* **2017**, *102* (7), 1482–1500. https://doi.org/10.2138/am-2017-5931.

(340) Bilinski, H.; Schindler, P. Solubility and Equilibrium Constants of Lead in Carbonate Solutions (25°C, I = 0.3 Mol Dm-3). *Geochim. Cosmochim. Acta* **1982**, *46* (6), 921–928. https://doi.org/10.1016/0016-7037(82)90048-5.

(341) Kvech, S.; Edwards, M. Solubility Controls on Aluminum in Drinking Water at Relatively Low and High PH. *Water Res.* **2002**, *36* (17), 4356–4368. https://doi.org/10.1016/S0043-1354(02)00137-9.

(342) Farrell, N.; Qu, Y.; Feng, L.; Van Houten, B. Comparison of Chemical Reactivity, Cytotoxicity, Interstrand Cross-Linking and DNA Sequence Specificity of Bis(Platinum) Complexes Containing Monodentate or Bidentate Coordination Spheres with Their Monomeric Analogues. *Biochemistry* **1990**, *29* (41), 9522–9531. https://doi.org/10.1021/bi00493a005.

(343) Ducháčková, L.; Schröder, D.; Roithová, J. Effect of the Carboxylate Shift on the Reactivity of Zinc Complexes in the Gas Phase. *Inorg. Chem.* **2011**, *50* (7), 3153–3158. https://doi.org/10.1021/ic2002767.

(344) Siidra, O.; Nekrasova, D.; Depmeier, W.; Chukanov, N.; Zaitsev, A.; Turner, R. Hydrocerussite-Related Minerals and Materials: Structural Principles, Chemical Variations and Infrared Spectroscopy. *Acta Crystallogr. Sect. B Struct. Sci. Cryst. Eng. Mater.* **2018**, *74* (2), 182–195. https://doi.org/10.1107/S2052520618000768.

(345) Contreras, C. A.; Sugita, S.; Ramos, E. Preparation of Sodium Aluminate From Basic Aluminium Sulfate. *Adv. Technol. Mater. Mater. Process. J.* **2006**, *2* (8), 122–129. https://doi.org/10.2240/azojomo0220.

(346) Schaller, R. F.; Jove-Colon, C. F.; Taylor, J. M.; Schindelholz, E. J. The Controlling Role of Sodium and Carbonate on the Atmospheric Corrosion Rate of Aluminum. *npj Mater. Degrad.* **2017**, *1* (1), 1–8. https://doi.org/10.1038/s41529-017-0020-3.

(347) Zamorategui Molina, A.; del Ángel Soto, J.; Martínez Rosales, M.; Romero Toledo, R. Ammonium Alunite and Basic Aluminum Sulfate: Effect of Precipitant Agent. *Int. J. Mater. Sci. Appl.* **2015**, *4* (2), 100. https://doi.org/10.11648/j.ijmsa.20150402.14.

(348) Spring, M.; Ricci, C.; Peggie, D. A.; Kazarian, S. G. ATR-FTIR Imaging for the Analysis of Organic Materials in Paint Cross Sections: Case Studies on Paint Samples from the National Gallery, London. *Anal. Bioanal. Chem.* **2008**, *392* (1–2), 37–45. https://doi.org/10.1007/s00216-008-2092-y.

(349) Salvadó, N.; Butí, S.; Nicholson, J.; Emerich, H.; Labrador, A.; Pradell, T. Identification of Reaction Compounds in Micrometric Layers from Gothic Paintings Using Combined SR-XRD and SR-FTIR. *Talanta* **2009**, *79* (2), 419–428. https://doi.org/10.1016/j.talanta.2009.04.005.

(350) Beltran, V.; Salvadó, N.; Butí, S.; Pradell, T. Ageing of Resin from Pinus Species Assessed by Infrared Spectroscopy. *Anal. Bioanal. Chem.* **2016**, *408* (15), 4073–4082. https://doi.org/10.1007/s00216-016-9496-x.

(351) Dietemann, P.; Higgitt, C.; Kälin, M.; Edelmann, M. J.; Knochenmuss, R.; Zenobi, R. Aging and Yellowing of Triterpenoid Resin Varnishes - Influence of Aging Conditions and Resin Composition. *J. Cult. Herit.* **2009**, *10* (1), 30–40. https://doi.org/10.1016/j.culher.2008.04.007.

320

(352) Van den Berg, J. D. J.; Van den Berg, K. J.; Boon, J. J. Chemical Changes in Curing and Ageing Oil Paints. In *Proceedings of 12th Triennial ICOM-CC Meeting Lyon*; Bridgeland, J., Ed.; James and James: London, 1999; pp 248–253.

(353) Tempest, H.; Burnstock, A.; Saltmarsh, P.; van den Berg, K. J. Sensitivity of Oil Paint Surfaces to Aqueous and Other Solvents. *Smithson. Contrib. to Museum Conserv.* **2012**, No. November 2010, 107–114.

(354) Keune, K.; Mass, J.; Mehta, A.; Church, J.; Meirer, F. Analytical Imaging Studies of the Migration of Degraded Orpiment, Realgar, and Emerald Green Pigments in Historic Paintings and Related Conservation Issues. *Herit. Sci.* **2016**, *4* (1), 1–14. https://doi.org/10.1186/s40494-016-0078-1.

(355) Casadio, F.; Keune, K.; Noble, P.; van Loon, A.; Hendriks, E.; Centeno, S. A.; Osmond, G. *Metal Soaps in Art*; Springer International Publishing, 2019.

(356) Alvarez-Martin, A.; Trashin, S.; Cuykx, M.; Covaci, A.; De Wael, K.; Janssens, K. Photodegradation Mechanisms and Kinetics of Eosin-Y in Oxic and Anoxic Conditions. *Dye. Pigment.* **2017**, *145*, 376–384. https://doi.org/10.1016/j.dyepig.2017.06.031.

(357) Majek, M.; Filace, F.; Von Wangelin, A. J. On the Mechanism of Photocatalytic Reactions with Eosin Y. *Beilstein J. Org. Chem.* **2014**, *10*, 981–989. https://doi.org/10.3762/bjoc.10.97.

(358) Srivastava, V.; Singh, P. P. Eosin y Catalysed Photoredox Synthesis: A Review. *RSC Adv.* **2017**, *7* (50), 31377–31392. https://doi.org/10.1039/c7ra05444k.

(359) Cesaratto, A.; Leona, M.; Lombardi, J. R.; Comelli, D.; Nevin, A.; Londero, P. Detection of Organic Colorants in Historical Painting Layers Using UV Laser Ablation Surface-Enhanced Raman Microspectroscopy. *Angew. Chemie* **2014**, *126* (52), 14601–14605. https://doi.org/10.1002/ange.201408016.

(360) Serrano, A.; van den Doel, A.; van Bommel, M.; Hallett, J.; Joosten, I.; Van den Berg, K. J. Investigation of Crimson-Dyed Fibres for a New Approach on the Characterization of Cochineal and Kermes Dyes in Historical Textiles. *Anal. Chim. Acta* **2015**, *897*, 116–127. https://doi.org/10.1016/j.aca.2015.09.046.

(361) Salvadó, N.; Butí, S.; Aranda, M. A. G.; Pradell, T. New Insights on Blue Pigments Used in 15th Century Paintings by Synchrotron Radiation-Based Micro-FTIR and XRD. *Anal. Methods* **2014**, *6* (11), 3610. https://doi.org/10.1039/c4ay00424h.

(362) de la Codre, H.; Radepont, M.; Echard, J.; Belhadj, O.; Vaiedelich, S.; Rouchon, V. The Use of <scp>XRF</scp> Imaging for the Chemical Discrimination of Iron-gall Ink Inscriptions: A Case Study in Stradivari's Workshop. *X-Ray Spectrom.* **2020**, xrs.3160. https://doi.org/10.1002/xrs.3160.

(363) Gonzalez, V.; Van Loon, A.; Wt Price, S.; Noble, P.; Keune, K. Synchrotron Micro-XRD and Micro-XRD-CT Reveal Newly Formed Lead-Sulfur Compounds in Old Master Paintings. *J. Anal. At. Spectrom.* **2020**, *35* (10), 2267–2273. https://doi.org/10.1039/d0ja00169d.

(364) Tan, H.; Tian, H.; Verbeeck, J.; Monico, L.; Janssens, K.; Van Tendeloo, G. Nanoscale Investigation of the Degradation Mechanism of a Historical Chrome Yellow Paint by Quantitative Electron Energy Loss Spectroscopy Mapping of Chromium Species. *Angew. Chemie - Int. Ed.* **2013**, *52* (43), 11360–11363. https://doi.org/10.1002/anie.201305753.

(365) Welsh, F. S. Particle Characteristics of Prussian Blue in an Historical Oil Paint. *J. Am. Inst. Conserv.* **1988**, *27* (2), 55. https://doi.org/10.2307/3179402.

(366) Salvadó, N.; Butí, S.; Aranda, M. A. G.; Pradell, T. New Insights on Blue Pigments Used in 15th Century Paintings by Synchrotron Radiation-Based Micro-FTIR and XRD. *Anal. Methods* **2014**, *6* (11), 3610–3621. https://doi.org/10.1039/c4ay00424h.

(367) Alfeld, M.; de Viguerie, L. Recent Developments in Spectroscopic Imaging Techniques for Historical Paintings - A Review. *Spectrochimica Acta - Part B Atomic Spectroscopy*. Elsevier B.V. October 2017, pp 81–105. https://doi.org/10.1016/j.sab.2017.08.003.

(368) Cotte, M.; Genty-Vincent, A.; Janssens, K.; Susini, J. Applications of Synchrotron X-Ray Nano-Probes in the Field of Cultural Heritage. *Comptes Rendus Physique*. Elsevier Masson SAS November 2018, pp 575–588. https://doi.org/10.1016/j.crhy.2018.07.002.

(369) Salzer, R.; Siesler, H. W. *Infrared and Raman Spectroscopic Imaging*; Salzer, R., Siesler, H. W., Eds.; Wiley-VCH : Weinheim, 2014. https://doi.org/10.1002/9783527678136.

(370) Smith, G. D.; Burgio, L.; Firth, S.; Clark, R. J. H. Laser-Induced Degradation of Lead Pigments with Reference to Botticelli's Trionfo d'Amore. *Anal. Chim. Acta* **2001**, *440* (2), 185–188. https://doi.org/10.1016/S0003-2670(01)01053-4.

(371) De Santis, A.; Mattei, E.; Pelosi, C. Micro-Raman and Stratigraphic Studies of the Paintings on the 'Cembalo' Model Musical Instrument (A.D. 1650) and Laser-Induced Degradation of the Detected Pigments. *J. Raman Spectrosc.* **2007**, *38* (10), 1368–1378. https://doi.org/10.1002/jrs.1777.

(372) De Faria, D. L. A.; Venâncio Silva, S.; De Oliveira, M. T. Raman Microspectroscopy of Some Iron Oxides and Oxyhydroxides. *J. Raman Spectrosc.* **1997**, *28* (11), 873–878. https://doi.org/10.1002/(sici)1097-4555(199711)28:11<873::aid-jrs177>3.0.co;2-b.

(373) Baden, N.; Kobayashi, H.; Urayama, N. Submicron-Resolution Polymer Orientation Mapping by Optical Photothermal Infrared Spectroscopy. *Int. J. Polym. Anal. Charact.* **2020**, *25* (1), 1–7. https://doi.org/10.1080/1023666X.2020.1735851.

(374) Klementieva, O.; Sandt, C.; Martinsson, I.; Kansiz, M.; Gouras, G. K.; Borondics, F. Super-Resolution Infrared Imaging of Polymorphic Amyloid Aggregates Directly in Neurons. *Adv. Sci.* **2020**, *7* (6), 1903004. https://doi.org/10.1002/advs.201903004.

(375) Pozzi, F.; Basso, E.; Centeno, S. A.; Smieska, L. M.; Shibayama, N.; Berns, R.; Fontanella, M.; Stringari, L. Altered Identity: Fleeting Colors and Obscured Surfaces in Van Gogh's Landscapes in Paris, Arles, and Saint-Rémy. *Herit. Sci.* **2021**, *9* (1), 15. https://doi.org/10.1186/s40494-021-00489-1.

(376) Salvadó, N.; Butí, S.; Tobin, M. J.; Pantos, E.; Prag, A. J. N. W.; Pradell, T. Advantages of the Use of SR-FT-IR Microspectroscopy: Applications to Cultural Heritage. *Anal. Chem.* **2005**, *77* (11), 3444–3451. https://doi.org/10.1021/ac050126k.

(377) Cotte, M.; Dumas, P.; Taniguchi, Y.; Checroun, E.; Walter, P.; Susini, J. Recent Applications and Current Trends in Cultural Heritage Science Using Synchrotron-Based Fourier Transform Infrared Micro-Spectroscopy. *Comptes Rendus Physique*. No longer published by Elsevier September 2009, pp 590–600. https://doi.org/10.1016/j.crhy.2009.03.016.

(378) Böke, H.; Akkurt, S.; Özdemir, S.; Göktürk, E. H.; Caner Saltik, E. N. Quantification of CaCO3-CaSO3·0.5H 2O-CaSO4·2H2O Mixtures by FTIR Analysis and Its ANN Model. *Mater. Lett.* **2004**, *58* (5), 723–726. https://doi.org/10.1016/j.matlet.2003.07.008.

(379) Kirchner, E.; van der Lans, I.; Ligterink, F.; Geldof, M.; Ness Proano Gaibor, A.; Hendriks, E.; Janssens, K.; Delaney, J. Digitally Reconstructing van Gogh's Field with Irises near Arles Part 2: Pigment Concentration Maps. *Color Res. Appl.* **2017**, No. June. https://doi.org/10.1002/col.22164.

(380) Fieberg, J. E.; Knutås, P.; Hostettler, K.; Smith, G. D. "Paintings Fade Like Flowers": Pigment Analysis and Digital Reconstruction of a Faded Pink Lake Pigment in Vincent van Gogh's *Undergrowth with Two Figures*. *Appl. Spectrosc.* **2017**, *71* (5), 794–808. https://doi.org/10.1177/0003702816685097.

(381) Krimm, B. S.; Bandekart, J. Vibrational Spectroscopy and Conformation of Peptides, Polypeptides, and Proteins. *Adv. Protein Chem.* **1986**, *38*, 181–364.

(382) Faix, O.; Bremer, J.; Schmidt, O.; Tatjana, S. J. Monitoring of Chemical Changes in White-Rot Degraded Beech Wood by Pyrolysis—Gas Chromatography and Fourier-Transform Infrared Spectroscopy. *J. Anal. Appl. Pyrolysis* **1991**, *21* (1–2), 147–162. https://doi.org/10.1016/0165-2370(91)80022-Z.

(383) Hackney, S. *On Canvas: Preserving the Structure of Paintings*; Getty Publications: Los Angeles, 2020.

(384) Beltran, V.; Salvadó, N.; Butí, S.; Cinque, G.; Wehbe, K.; Pradell, T. Optimal Sample Preparation for the Analysis of Micrometric Heterogeneous Samples. *Anal. Chem.* **2015**, *87* (13), 6500–6504. https://doi.org/10.1021/acs.analchem.5b01997.

(385) Salvadó, N.; Butí, S.; Beltran, V.; Pradell, T.; Clemente, C.; Juanhuix, J.; Cinque, G. Microanalytical Study of Luster Glazed Gilding and Silvering from Baroque Altarpieces. *Pure Appl. Chem.* **2017**, *90* (3). https://doi.org/10.1515/pac-2017-0602.

(386) Burgio, L.; Clark, R. J. H.; Firth, S. Raman Spectroscopy as a Means for the Identification of Plattnerite (PbO2), of Lead Pigments and of Their Degradation Products. *Analyst* **2001**, *126* (2), 222–227. https://doi.org/10.1039/b008302j.

(387) Pozzi, F.; Lombardi, J. R.; Leona, M. Winsor & Newton Original Handbooks: A Surface-Enhanced Raman Scattering (SERS) and Raman Spectral Database of Dyes from Modern Watercolor Pigments.

322

*Herit. Sci.* **2013**, *1* (1), 23. https://doi.org/10.1186/2050-7445-1-23.

(388) Haberová, K.; Jančovičová, V.; Veselá, D.; Machatová, Z.; Oravec, M. Impact of Organic Binders on the Carminic-Colorants Stability Studied by: ATR-FTIR, VIS and Colorimetry. *Dye. Pigment.* **2021**, *186*, 108971. https://doi.org/10.1016/j.dyepig.2020.108971.

(389) Kirby, J.; Spring, M.; Higgitt, C. The Technology of Eighteenth- and Nineteenth-Century Red Lake Pigments. *Natl. Gall. Tech. Bull.* **2007**, *28*, 69–95.

(390) Dooley, K. A.; Chieli, A.; Romani, A.; Legrand, S.; Miliani, C.; Janssens, K.; Delaney, J. K. Molecular Fluorescence Imaging Spectroscopy for Mapping Low Concentrations of Red Lake Pigments: Van Gogh's Painting The Olive Orchard. *Angew. Chemie* **2020**, *132* (15), 6102–6109. https://doi.org/10.1002/ange.201915490.

(391) UNI; Italian Ministry of Cultural Activity and Heritage; CNR. Beni Di Interesse Storico Artístico. Condizioni Ambientali Di Conservazione. Misurazione Ed Analisi. In *Italian Standard UNI 10829*; 1999.

(392) Ashley-Smith, J.; Burmester, A.; Eibl, M. Climate for Collections. Standards and Uncertainties. In *Postprints of the Munich Climate Conference*; Doerner Institut: Munich, 2012.

(393) Silva, H. E.; Henriques, F. M. A. Preventive Conservation of Historic Buildings in Temperate Climates. The Importance of a Risk-Based Analysis on the Decision-Making Process. *Energy Build.* **2015**, *107*, 26–36. https://doi.org/10.1016/j.enbuild.2015.07.067.

(394) Atkinson, J. K. Environmental Conditions for the Safeguarding of Collections : A Background to the Current Debate on the Control of Relative Humidity and Temperature. *Stud. Conserv.* **2014**, *59* (4), 205–212. https://doi.org/10.1179/2047058414Y.0000000141.

(395) Martens, M. Climate Risk Assessment in Museums., Technische Universiteit Eindhoven, The Netherlands., 2012.

(396) Michalski, S. Damage to Museum Objects by Visible Radiation (Light) and Ultraviolet Radiation (Uv). In *Lighting in museums, galleries and historic houses. Proceedings of the conference.*; Bristol, 1987.

(397) Ferdyn-Grygierek, J. Monitoring of Indoor Air Parameters in Large Museum Exhibition Halls with and without Air-Conditioning Systems. *Build. Environ.* **2016**, *107*, 113–126. https://doi.org/10.1016/j.buildenv.2016.07.024.

(398) Feilden, B. *Conservation of Historic Buildings*; Architectural Press: Oxford, UK., 1982.

(399) Grau-Bové, J.; Budič, B.; Cigić, I. K.; Thickett, D.; Signorello, S.; Strlič, M. The Effect of Particulate Matter on Paper Degradation. *Herit. Sci.* **2016**, *4* (1), 4–11. https://doi.org/10.1186/s40494-016-0071-8.

(400) Krupińska, B.; Van Grieken, R.; De Wael, K. Air Quality Monitoring in a Museum for Preventive Conservation: Results of a Three-Year Study in the Plantin-Moretus Museum in Antwerp, Belgium. *Microchem. J.* **2013**, *110*, 350–360. https://doi.org/10.1016/j.microc.2013.05.006.

(401) Cavicchioli, A.; Orsini, R.; Souza, C. De; Reis, G. R.; Fornaro, A. Indoor Ozone and Nitrogen Dioxide Concentration in Two Museums of the São Paulo Megacity - Brazil. *Preserv. Sci.* **2013**, 114–122.

(402) Brimblecombe, P.; Blades, N.; Camuffo, D.; Sturaro, G.; Valentino, A.; Gysels, K.; Van Grieken, R.; Busse, H.-J.; Kim, O.; Ulrych, U.; Wieser, M. The Indoor Environment of a Modern Museum Building, the Sainsbury Centre for Visual Arts, Norwich, UK. *Indoor Air* **1999**, *9* (3), 146–164. https://doi.org/10.1111/j.1600-0668.1999.t01-1-00002.x.

(403) Worobiec, A.; Samek, L.; Krata, A.; Van Meel, K.; Krupinska, B.; Anna Stefaniak, E.; Karaszkiewicz, P.; Van Grieken, R. Transport and Deposition of Airborne Pollutants in Exhibition Areas Located in Historical Buildings-Study in Wawel Castle Museum in Cracow, Poland. *J. Cult. Herit.* **2010**, *11* (3), 354–359. https://doi.org/10.1016/j.culher.2009.11.009.

(404) Horemans, B.; Cardell, C.; Bencs, L.; Kontozova-Deutsch, V.; De Wael, K.; Van Grieken, R. Evaluation of Airborne Particles at the Alhambra Monument in Granada, Spain. *Microchem. J.* **2011**, *99* (2), 429–438. https://doi.org/10.1016/j.microc.2011.06.018.

(405) Saraga, D.; Pateraki, S.; Papadopoulos, A.; Vasilakos, C.; Maggos, T. Studying the Indoor Air Quality in Three Non-Residential Environments of Different Use: A Museum, a Printery Industry and an Office. *Build. Environ.* **2011**, *46* (11), 2333–2341. https://doi.org/10.1016/j.buildenv.2011.05.013.

(406) Krupińska, B.; Worobiec, A.; Gatto Rotondo, G.; Novaković, V.; Kontozova, V.; Ro, C.-U.; Van

Grieken, R.; De Wael, K. Assessment of the Air Quality (NO2, SO2, O3 and Particulate Matter) in the Plantin-Moretus Museum/Print Room in Antwerp, Belgium, in Different Seasons of the Year. *Microchem. J.* **2012**, *102* (2), 49–53. https://doi.org/10.1016/j.microc.2011.11.008.

(407)  Godoi, R. H. M.; Carneiro, B. H. B.; Paralovo, S. L.; Campos, V. P.; Tavares, T. M.; Evangelista, H.; Van Grieken, R.; Godoi, A. F. L. Indoor Air Quality of a Museum in a Subtropical Climate: The Oscar Niemeyer Museum in Curitiba, Brazil. *Sci. Total Environ.* **2013**, *452–453*, 314–320. https://doi.org/10.1016/j.scitotenv.2013.02.070.

(408)  Camuffo, D.; Brimblecombe, P.; Van Grieken, R.; Busse, H. J.; Sturaro, G.; Valentino, A.; Bernardi, A.; Blades, N.; Shooter, D.; De Bock, L.; Gysels, K.; Wieser, M.; Kim, O. Indoor Air Quality at the Correr Museum, Venice, Italy. *Sci. Total Environ.* **1999**, *236* (1–3), 135–152. https://doi.org/10.1016/S0048-9697(99)00262-4.

(409)  Gysels, K.; Delalieux, F.; Deutsch, F.; Van Grieken, R.; Camuffo, D.; Bernardi, A.; Sturaro, G.; Busse, H. J.; Wieser, M. Indoor Environment and Conservation in the Royal Museum of Fine Arts, Antwerp, Belgium. *J. Cult. Herit.* **2004**, *5* (2), 221–230. https://doi.org/10.1016/j.culher.2004.02.002.

(410)  Cartechini, L.; Castellini, S.; Moroni, B.; Palmieri, M.; Scardazza, F.; Sebastiani, B.; Selvaggi, R.; Vagnini, M.; Delogu, G. L.; Brunetti, B. G.; Cappelletti, D. Acute Episodes of Black Carbon and Aerosol Contamination in a Museum Environment: Results of Integrated Real-Time and off-Line Measurements. *Atmos. Environ.* **2015**, *116*, 130–137. https://doi.org/10.1016/j.atmosenv.2015.06.033.

(411)  Hu, T.; Jia, W.; Cao, J.; Huang, R.; Li, H.; Liu, S.; Ma, T.; Zhu, Y. Indoor Air Quality at Five Site Museums of Yangtze River Civilization. *Atmos. Environ.* **2015**, *123*, 449–454. https://doi.org/10.1016/j.atmosenv.2015.10.022.

(412)  Aleixandre, L.; Gerboles, M. Review of Small Commercial Sensors for Indicative Monitoring of Ambient Gas. *Chem. Eng. Trans.* **2012**, *30*, 169–174.

(413)  Ozone Meter Model Z-1200 technical datasheet on Environmental Sensor Co. Website http://www.environmentalsensors.com/PDF/ESC New Brochure/ozone z-1200.pdf (accessed Feb 17, 2021).

(414)  Model 205 Dual Beam Ozone Monitor™ technical datasheet on 2B Technologies website http://twobtech.com/docs/brochures/model_205.pdf (accessed Feb 17, 2021).

(415)  Personal Ozone Monitor™ technical datasheet on 2B Technologies website http://twobtech.com/docs/brochures/model_POM.pdf (accessed Feb 17, 2021).

(416)  Nitrogen Dioxide Meter Model Z-1400 technical sheet on Environmental Sensor Co. Website http://www.environmentalsensors.com/PDF/ESC New Brochure/nitrogen dioxide z-1400.pdf.

(417)  Sulfur Dioxide Meter Model Z-1300 technical datasheet on Environmental Sensor Co. Website http://www.environmentalsensors.com/PDF/ESC New Brochure/sulfur dioxie z-1300.pdf (accessed Feb 17, 2021).

(418)  Hydrogen Sulfide Meter Model Z-900 technical datasheet on Environmental Sensor Co. Website http://www.environmentalsensors.com/PDF/ESC New Brochure/hydrogen sulfide z-900.pdf (accessed Feb 17, 2021).

(419)  Formaldehyde Meter Model Z-300 technical datasheet on Environmental Sensor Co. Website http://www.environmentalsensors.com/PDF/ESC New Brochure/formaldehyde z-300.pdf (accessed Feb 17, 2021).

(420)  Acetic Acid Gas Sensor Cell specifications on PureAire monitoring systems, Inc. website https://www.pureairemonitoring.com/product/acetic-acid-gas-sensor-cell/ (accessed Feb 17, 2021).

(421)  Portable and Fixed Monitor Gas Sensor Specifications on Aeroqual™ website http://www.aeroqual.com/wp-content/uploads/Aeroqual-Portable-Fixed-Gas-Sensor-Specifications-V6.pdf (accessed Feb 17, 2021).

(422)  Ciuzas, D.; Prasauskas, T.; Krugly, E.; Sidaraviciute, R.; Jurelionis, A.; Seduikyte, L.; Kauneliene, V.; Wierzbicka, A.; Martuzevicius, D. Characterization of Indoor Aerosol Temporal Variations for the Real-Time Management of Indoor Air Quality. *Atmos. Environ.* **2015**, *118*, 107–117. https://doi.org/10.1016/j.atmosenv.2015.07.044.

324

(423) Steinle, S.; Reis, S.; Sabel, C. E.; Semple, S.; Twigg, M. M.; Braban, C. F.; Leeson, S. R.; Heal, M. R.; Harrison, D.; Lin, C.; Wu, H. Personal Exposure Monitoring of PM2.5in Indoor and Outdoor Microenvironments. *Sci. Total Environ.* **2015**, *508*, 383–394. https://doi.org/10.1016/j.scitotenv.2014.12.003.

(424) War Heritage Institute website www.warheritage.be (accessed Feb 17, 2021).

(425) Riley, W. J.; McKone, T. E.; Lai, A. C. K.; Nazaroff, W. W. Indoor Particulate Matter of Outdoor Origin: Importance of Size-Dependent Removal Mechanisms. *Environ. Sci. Technol.* **2002**, *36* (2), 200–207.

(426) Leyva, D.; Demeyer, S.; Schalm, O.; Anaf, W.; Meert, C. New Approach to Indoors Air Quality Assessment for Cultural Heritage Conservation. **2013**.

(427) 't Hart, L.; Storme, P.; Anaf, W.; Nuyts, G.; Vanmeert, F.; Dorrine, W.; Janssens, K.; De Wael, K.; Schalm, O. Monitoring the Impact of the Indoor Air Quality on Silver Cultural Heritage Objects Using Passive and Continuous Corrosion Rate Assessments. *Appl. Phys. A* **2016**, *122* (923). https://doi.org/10.1007/s00339-016-0456-2.

(428) Thermo Fisher Scientific. No Title http://www.datataker.com/DT85.php (accessed Sep 10, 2018).

(429) Vaisala. No Title http://www.vaisala.com/en/products/carbondioxide/Pages/GMW90.aspx (accessed Sep 10, 2018).

(430) SKL310 visible light sensor technical datasheet on Skye Instruments website http://www.skyeinstruments.info/index_htm_files/LUX SENSOR v3.pdf (accessed Feb 17, 2021).

(431) SKU421 UV light sensor technical datasheet on Skye Instruments website http://www.skyeinstruments.info/index_htm_files/UVA SENSOR v3.pdf (accessed Feb 17, 2021).

(432) Burmester, A.; M., E. *Stable Is Safe. The Munich Position on Climate and Cultural Heritage.*; Doerner Institut: Munich, 2014.

(433) Lighthouse. No Title http://www.golighthouse.com/media/files/Handheld_datasheet_for_2016_3016_3016IAQ_5016 _3.pdf (accessed Sep 10, 2018).

(434) Portable Aethalometer® Model AE42 technical datasheet on Magee Scientific Corporation website http://www.mageesci.com/images/stories/docs/AE42_specSheet_oct2010_rev02_web.pdf (accessed Feb 17, 2021).

(435) IRCELINE. Carbon dioxide levels (ppm) from 11/04/2016 to 9/05/2017, monitoring stations 41WOL1 and 41002 http://viewer.irceline.be/?ts=6636__irceline,6612__irceline&span=2016-04-11T00:00:00+02:00/2016-05-09T00:00:00+02:00 (accessed Feb 20, 2018).

(436) You, Y.; Bai, Z.; Jia, C.; Wan, Z.; Ran, W.; Zhang, J. Measuring Air Exchanges Rates Using Continuous CO 2 Sensors. *Simulation* **2007**.

(437) Colbeck, I. Particle Emission from Outdoor and Indoor Sources. In *Airborne Particulate Matter*; Kouimtzis, T., Samara, C., Eds.; Springer: Berlin, 1995; pp 1–34.

(438) USEPA; US-EPA. Report to Congress on Black Carbon. **2012**, No. March, 388. https://doi.org/10.1016/j.icrp.2009.12.007.

(439) IRCELINE. Black carbon concentration (µg/m3) from 11/04/2016 to 8/05/2017, monitoring stations 41001 http://viewer.irceline.be/?ts=6569__irceline&span=2016-04-11T01:29:42+02:00/2016-05-08T02:24:42+02:00. (accessed Feb 20, 2018).

(440) Yoon, Y. H.; Brimblecombe, P. Contribution of Dust at Floor Level to Particle Deposit within the Sainsbury Centre for Visual Arts. *Stud. Conserv.* **2000**, *45* (2), 127–136. https://doi.org/10.1179/sic.2000.45.2.127.

(441) Pinnick, R. G.; Fernandez, G.; Martinez-Andazola, E.; Hinds, B. D.; Hansen, A. D. A.; Fuller, K. Aerosol in the Arid Southwestern United States: Measurements of Mass Loading, Volatility, Size Distribution, Absorption Characteristics, Black Carbon Content, and Vertical Structure to 7 Km Above Sea Level. *J. Geophys. Res.* **1993**, *98* (92), 2651–2666.

(442) Snyder, E. G.; Watkins, T. H.; Solomon, P. A.; Thoma, E. D.; Williams, R. W.; Hagler, G. S. W.; Shelow, D.; Hindin, D. A.; Kilaru, V. J.; Preuss, P. W. The Changing Paradigm of Air Pollution Monitoring. *Environ. Sci. Technol.* **2013**, *47* (20), 11369–11377. https://doi.org/10.1021/es4022602.

(443) Pang, X.; Shaw, M. D.; Gillot, S.; Lewis, A. C. Sensors and Actuators B : Chemical The Impacts of Water Vapour and Co-Pollutants on the Performance of Electrochemical Gas Sensors Used for Air

Quality Monitoring. *Sensors Actuators B. Chem.* **2018**, *266*, 674–684. https://doi.org/10.1016/j.snb.2018.03.144.

(444)   Prabakar, J.; Mohan, V.; Ravisankar, K. Evaluation of Low Cost Particulate Matter Sensor for Indoor Air Quality Measurement. *Int. J. Innov. Res. Sci. Eng. Technol. (An ISO Certif. Organ.* **2015**, *3297* (2), 366–369. https://doi.org/10.15680/IJIRSET.2015.0402076.

(445)   Northcross, A. L.; Edwards, R. J.; Johnson, M. A.; Wang, Z. M.; Zhu, K.; Allen, T.; Smith, K. R. A Low-Cost Particle Counter as a Realtime Fine-Particle Mass Monitor. *Environ. Sci. Process. Impacts* **2013**, *15* (2), 433–439. https://doi.org/10.1039/c2em30568b.

(446)   Dacunto, P. J.; Klepeis, N. E.; Cheng, K. C.; Acevedo-Bolton, V.; Jiang, R. T.; Repace, J. L.; Ott, W. R.; Hildemann, L. M. Determining PM2.5 Calibration Curves for a Low-Cost Particle Monitor: Common Indoor Residential Aerosols. *Environ. Sci. Process. Impacts* **2015**, *17* (11), 1959–1966. https://doi.org/10.1039/c5em00365b.

(447)   Semple, S.; Ibrahim, A. E.; Apsley, A.; Steiner, M.; Turner, S. Using a New, Low-Cost Air Quality Sensor to Quantify Second-Hand Smoke (SHS) Levels in Homes. *Tob. Control* **2015**, *24* (2), 153–158. https://doi.org/10.1136/tobaccocontrol-2013-051188.

(448)   Sousan, S.; Koehler, K.; Thomas, G.; Park, J. H.; Hillman, M.; Halterman, A.; Peters, T. M. Inter-Comparison of Low-Cost Sensors for Measuring the Mass Concentration of Occupational Aerosols. *Aerosol Sci. Technol.* **2016**, *50* (5), 462–473. https://doi.org/10.1080/02786826.2016.1162901.

(449)   Han, I.; Symanski, E.; Stock, T. H. Feasibility of Using Low-Cost Portable Particle Monitors for Measurement of Fine and Coarse Particulate Matter in Urban Ambient Air. *J. Air Waste Manag. Assoc.* **2017**, *67* (3), 330–340. https://doi.org/10.1080/10962247.2016.1241195.

(450)   Amouei Torkmahalleh, M.; Kabay, K.; Bazhanova, M.; Mohiuddin, O.; Obaidullah, M.; Gorjinezhad, S. Investigating the Impact of Different Sport Trainings on Particulate Matter Resuspension in a Sport Center Using Well-Characterized Reference Instruments and a Low-Cost Monitor. *Sci. Total Environ.* **2018**, *612*, 957–965. https://doi.org/10.1016/j.scitotenv.2017.08.107.

(451)   Dobson, R.; Semple, S. "How Do You Know Those Particles Are from Cigarettes?": An Algorithm to Help Differentiate Second-Hand Tobacco Smoke from Background Sources of Household Fine Particulate Matter. *Environ. Res.* **2018**, *166* (May), 344–347. https://doi.org/10.1016/j.envres.2018.06.019.

(452)   Borghi, F.; Spinazzè, A.; Rovelli, S.; Campagnolo, D.; Del Buono, L.; Cattaneo, A.; Cavallo, D. M. Miniaturized Monitors for Assessment of Exposure to Air Pollutants: A Review. *Int. J. Environ. Res. Public Health* **2017**, *14* (8). https://doi.org/10.3390/ijerph14080909.

(453)   Borghi, F.; Spinazzè, A.; Campagnolo, D.; Rovelli, S.; Cattaneo, A.; Cavallo, D. M. Precision and Accuracy of a Direct-Reading Miniaturized Monitor in PM2.5 Exposure Assessment. *Sensors* **2018**, *18* (9), 3089. https://doi.org/10.3390/s18093089.

(454)   Jayaratne, R.; Liu, X.; Thai, P.; Dunbabin, M.; Morawska, L. The Influence of Humidity on the Performance of Low-Cost Air Particle Mass Sensors and the Effect of Atmospheric Fog. *Atmos. Meas. Tech. Discuss.* **2018**, No. April, 1–15. https://doi.org/10.5194/amt-2018-100.

(455)   Feinberg, S.; Williams, R.; Hagler, G. S. W.; Rickard, J.; Brown, R.; Garver, D.; Harshfield, G.; Stauffer, P.; Mattson, E.; Judge, R.; Garvey, S. Long-Term Evaluation of Air Sensor Technology under Ambient Conditions in Denver, Colorado. *Atmos. Meas. Tech. Discuss.* **2018**, No. February, 1–18. https://doi.org/10.5194/amt-2018-12.

(456)   Johnson, K. K.; Bergin, M. H.; Russell, A. G.; Hagler, G. S. W. Field Test of Several Low-Cost Particulate Matter Sensors in High and Low Concentration Urban Environments. *Aerosol Air Qual. Res.* **2018**, *18* (3), 565–578. https://doi.org/10.4209/aaqr.2017.10.0418.

(457)   Holstius, D. M.; Pillarisetti, A.; Smith, K. R.; Seto, E. Field Calibrations of a Low-Cost Aerosol Sensor at a Regulatory Monitoring Site in California. *Atmos. Meas. Tech.* **2014**, *7* (4), 1121–1131. https://doi.org/10.5194/amt-7-1121-2014.

(458)   Kelly, K. E.; Whitaker, J.; Petty, A.; Widmer, C.; Dybwad, A.; Sleeth, D.; Martin, R.; Butterfield, A. Ambient and Laboratory Evaluation of a Low-Cost Particulate Matter Sensor. *Environ. Pollut.* **2017**, *221*, 491–500. https://doi.org/10.1016/j.envpol.2016.12.039.

(459)   Gao, M.; Cao, J.; Seto, E. A Distributed Network of Low-Cost Continuous Reading Sensors to

Measure Spatiotemporal Variations of PM2.5 in Xi'an, China. *Environ. Pollut.* **2015**, *199*, 56–65. https://doi.org/10.1016/j.envpol.2015.01.013.

(460)   Austin, E.; Novosselov, I.; Seto, E.; Yost, M. G. Laboratory Evaluation of the Shinyei PPD42NS Low-Cost Particulate Matter Sensor. *PLoS One* **2015**, *10* (9), 1–17. https://doi.org/10.1371/journal.pone.0137789.

(461)   Campagnolo, D.; Saraga, D. E.; Cattaneo, A.; Spinazzè, A.; Mandin, C.; Mabilia, R.; Perreca, E.; Sakellaris, I.; Canha, N.; Mihucz, V. G.; Szigeti, T.; Ventura, G.; Madureira, J.; de Oliveira Fernandes, E.; de Kluizenaar, Y.; Cornelissen, E.; Hänninen, O.; Carrer, P.; Wolkoff, P.; Cavallo, D. M.; Bartzis, J. G. VOCs and Aldehydes Source Identification in European Office Buildings - The OFFICAIR Study. *Build. Environ.* **2017**, *115*, 18–24. https://doi.org/10.1016/j.buildenv.2017.01.009.

(462)   Kerchich, Y.; Kerbachi, R. Measurement of BTEX (Benzene, Toluene, Ethybenzene, and Xylene) Levels at Urban and Semirural Areas of Algiers City Using Passive Air Samplers. *J. Air Waste Manag. Assoc.* **2012**, *62* (12), 1370–1379. https://doi.org/10.1080/10962247.2012.712606.

(463)   Lattuati-Derieux, A.; Egasse, C.; Thao-Heu, S.; Balcar, N.; Barabant, G.; Lavédrine, B. What Do Plastics Emit? HS-SPME-GC/MS Analyses of New Standard Plastics and Plastic Objects in Museum Collections. *J. Cult. Herit.* **2013**, *14* (3), 238–247. https://doi.org/10.1016/j.culher.2012.06.005.

(464)   Brady, D.; Pratt, G. C. Volatile Organic Compound Emissions from Dry Mill Fuel Ethanol Production. *J. Air Waste Manage. Assoc.* **2007**, *57* (9), 1091–1102. https://doi.org/10.3155/1047-3289.57.9.1091.

(465)   Mleczkowska, A.; Strojecki, M.; Bratasz, Ł.; Kozłowski, R. Particle Penetration and Deposition inside Historical Churches. *Build. Environ.* **2016**, *95*, 291–298. https://doi.org/10.1016/j.buildenv.2015.09.017.

(466)   Arling, J.; O'Connor, K.; Mercieca, M. *Air Quality Sensor Network for Philadelphia. Data Validation*; 2010.

(467)   Asadi, E.; Costa, J. J.; Gameiro da Silva, M. Indoor Air Quality Audit Implementation in a Hotel Building in Portugal. *Build. Environ.* **2011**, *46* (8), 1617–1623. https://doi.org/10.1016/j.buildenv.2011.01.027.

(468)   Spinazzè, A.; Fanti, G.; Borghi, F.; Del Buono, L.; Campagnolo, D.; Rovelli, S.; Cattaneo, A.; Cavallo, D. M. Field Comparison of Instruments for Exposure Assessment of Airborne Ultrafine Particles and Particulate Matter. *Atmos. Environ.* **2017**, *154*, 274–284. https://doi.org/10.1016/j.atmosenv.2017.01.054.

(469)   Cha, Y.; Tu, M.; Elmgren, M.; Silvergren, S.; Olofsson, U. Factors Affecting the Exposure of Passengers, Service Staff and Train Drivers inside Trains to Airborne Particles. *Environ. Res.* **2018**, *166* (May), 16–24. https://doi.org/10.1016/j.envres.2018.05.026.

(470)   Assimakopoulos, M. N.; Dounis, A.; Spanou, A.; Santamouris, M. Indoor Air Quality in a Metropolitan Area Metro Using Fuzzy Logic Assessment System. *Sci. Total Environ.* **2013**, *449*, 461–469. https://doi.org/10.1016/j.scitotenv.2012.12.043.

(471)   Ramos, C. A.; Wolterbeek, H. T.; Almeida, S. M. Exposure to Indoor Air Pollutants during Physical Activity in Fitness Centers. *Build. Environ.* **2014**, *82*, 349–360. https://doi.org/10.1016/j.buildenv.2014.08.026.

(472)   Prasauskas, T.; Martuzevicius, D.; Krugly, E.; Ciuzas, D.; Stasiulaitiene, I.; Sidaraviciute, R.; Kauneliene, V.; Seduikyte, L.; Jurelionis, A.; Haverinen-Shaughnessy, U. Spatial and Temporal Variations of Particulate Matter Concentrations in Multifamily Apartment Buildings. *Build. Environ.* **2014**, *76*, 10–17. https://doi.org/10.1016/j.buildenv.2014.02.010.

(473)   Dorizas, P. V.; Assimakopoulos, M. N.; Helmis, C.; Santamouris, M. An Integrated Evaluation Study of the Ventilation Rate, the Exposure and the Indoor Air Quality in Naturally Ventilated Classrooms in the Mediterranean Region during Spring. *Sci. Total Environ.* **2015**, *502*, 557–570. https://doi.org/10.1016/j.scitotenv.2014.09.060.

(474)   Yu, K. P.; Yang, K. R.; Chen, Y. C.; Gong, J. Y.; Chen, Y. P.; Shih, H. C.; Candice Lung, S. C. Indoor Air Pollution from Gas Cooking in Five Taiwanese Families. *Build. Environ.* **2015**, *93* (P2), 258–266. https://doi.org/10.1016/j.buildenv.2015.06.024.

(475)   Pereira, L. D.; Gaspar, A. R.; Costa, J. J. Assessment of the Indoor Environmental Conditions of a

Baroque Library in Portugal. *Energy Procedia* **2017**, *133*, 257–267. https://doi.org/10.1016/j.egypro.2017.09.385.

(476) Vilcekova, S.; Meciarova, L.; Burdova, E. K.; Katunska, J.; Kosicanova, D.; Doroudiani, S. Indoor Environmental Quality of Classrooms and Occupants' Comfort in a Special Education School in Slovak Republic. *Build. Environ.* **2017**, *120*, 29–40. https://doi.org/10.1016/j.buildenv.2017.05.001.

(477) Traversari, A. A. L.; Bottenheft, C.; van Heumen, S. P. M.; Goedhart, C. A.; Vos, M. C. Effect of Switching off Unidirectional Downflow Systems of Operating Theaters during Prolonged Inactivity on the Period before the Operating Theater Can Safely Be Used. *Am. J. Infect. Control* **2017**, *45* (2), 139–144. https://doi.org/10.1016/j.ajic.2016.07.019.

(478) Alphasense. No Title http://www.alphasense.com/index.php/safety/application-notes/ (accessed Sep 10, 2018).

(479) Jerrett, M.; Donaire-gonzalez, D.; Popoola, O.; Jones, R.; Cohen, R. C.; Almanza, E.; Nazelle, A. De; Mead, I.; Carrasco-turigas, G.; Cole-hunter, T.; Triguero-mas, M.; Seto, E.; Nieuwenhuijsen, M. Validating Novel Air Pollution Sensors to Improve Exposure Estimates for Epidemiological Analyses and Citizen Science. *Environ. Res.* **2017**, *158* (August 2016), 286–294. https://doi.org/10.1016/j.envres.2017.04.023.

(480) Castell, N.; Dauge, F. R.; Schneider, P.; Vogt, M.; Lerner, U.; Fishbain, B.; Broday, D.; Bartonova, A. Can Commercial Low-Cost Sensor Platforms Contribute to Air Quality Monitoring and Exposure Estimates ? *Environ. Int.* **2017**, *99*, 293–302. https://doi.org/10.1016/j.envint.2016.12.007.

(481) Pang, X.; Shaw, M. D.; Lewis, A. C.; Carpenter, L. J.; Batchellier, T. Sensors and Actuators B : Chemical Electrochemical Ozone Sensors : A Miniaturised Alternative for Ozone Measurements in Laboratory Experiments and Air-Quality Monitoring. *Sensors Actuators B. Chem.* **2017**, *240*, 829–837. https://doi.org/10.1016/j.snb.2016.09.020.

(482) Cordero, J. M.; Borge, R.; Narros, A. Sensors and Actuators B : Chemical Using Statistical Methods to Carry out in Field Calibrations of Low Cost Air Quality Sensors. *Sensors Actuators B. Chem.* **2018**, *267* (2), 245–254. https://doi.org/10.1016/j.snb.2018.04.021.

(483) Alvia, L. D.; Palermo, E.; Prete, Z. Del. Validation and Application of a Novel Solution for Environmental Monitoring : A Three Months Study at " Minerva Medica " Archaeological Site in Rome. *Measurement* **2018**, *129* (April), 31–36. https://doi.org/10.1016/j.measurement.2018.07.004.

(484) Cross, E. S.; Williams, L. R.; Lewis, D. K.; Magoon, G. R.; Onasch, T. B.; Kaminsky, M. L.; Worsnop, D. R.; Jayne, J. T. Use of Electrochemical Sensors for Measurement of Air Pollution: Correcting Interference Response and Validating Measurements. *Atmos. Meas. Tech.* **2017**, *10* (9), 3575–3588. https://doi.org/10.5194/amt-10-3575-2017.

(485) Rutolo, M. F.; Clarkson, J. P.; Harper, G.; Covington, J. A. Postharvest Biology and Technology The Use of Gas Phase Detection and Monitoring of Potato Soft Rot Infection in Store. *Postharvest Biol. Technol.* **2018**, *145* (May), 15–19. https://doi.org/10.1016/j.postharvbio.2018.05.016.

(486) Jian, R.-S.; Huang, Y.-S.; Lai, S.-L.; Sung, L.-Y.; Lu, C.-J. Compact Instrumentation of a μ-GC for Real Time Analysis of Sub-Ppb VOC Mixtures.Pdf. *Microchem. J.* **2013**, *108*, 161–167.

(487) Spinelle, L.; Gerboles, M.; KoK, G.; Persijn, S.; Sauerwald, T. Review of Portable and Low-Cost Sensors for the Volatile Organic Compounds. *Sensors* **2017**, *17*, 1520. https://doi.org/10.3390/s17071520.

(488) Popoola, O. A. M.; Carruthers, D.; Lad, C.; Bright, V. B.; Mead, M. I.; Stettler, M. E. J.; Sa, J. R.; Jones, R. L. Use of Networks of Low Cost Air Quality Sensors to Quantify Air Quality in Urban Settings. **2018**, *194* (September), 58–70. https://doi.org/10.1016/j.atmosenv.2018.09.030.

(489) Kot-Wasik, A.; Zabiegała, B.; Urbanowicz, M.; Dominiak, E.; Wasik, A.; Namieśnik, J. Advances in Passive Sampling in Environmental Studies. *Anal. Chim. Acta* **2007**, *602* (2), 141–163. https://doi.org/10.1016/j.aca.2007.09.013.

(490) Woolfenden, E. Sorbent-Based Sampling Methods for Volatile and Semi-Volatile Organic Compounds in Air. Part 1: Sorbent-Based Air Monitoring Options. *J. Chromatogr. A* **2010**, *1217* (16), 2674–2684. https://doi.org/10.1016/j.chroma.2009.12.042.

(491) Marć, M.; Tobiszewski, M.; Zabiegała, B.; Guardia, M. de la; Namieśnik, J. Current Air Quality

328

Analytics and Monitoring: A Review. *Anal. Chim. Acta* **2015**, *853* (1), 116–126. https://doi.org/10.1016/j.aca.2014.10.018.

(492)   Zauli Sajani, S.; Marchesi, S.; Trentini, A.; Bacco, D.; Zigola, C.; Rovelli, S.; Ricciardelli, I.; Maccone, C.; Lauriola, P.; Cavallo, D. M.; Poluzzi, V.; Cattaneo, A.; Harrison, R. M. Vertical Variation of PM2.5mass and Chemical Composition, Particle Size Distribution, NO2, and BTEX at a High Rise Building. *Environ. Pollut.* **2018**, *235*, 339–349. https://doi.org/10.1016/j.envpol.2017.12.090.

(493)   Villanueva, F.; Tapia, A.; Lara, S.; Amo-Salas, M. Indoor and Outdoor Air Concentrations of Volatile Organic Compounds and NO2in Schools of Urban, Industrial and Rural Areas in Central-Southern Spain. *Sci. Total Environ.* **2018**, *622–623*, 222–235. https://doi.org/10.1016/j.scitotenv.2017.11.274.

(494)   Ielpo, P.; Mangia, C.; Marra, G. P.; Comite, V.; Rizza, U.; Uricchio, V. F.; Fermo, P. Outdoor Spatial Distribution and Indoor Levels of NO2and SO2in a High Environmental Risk Site of the South Italy. *Sci. Total Environ.* **2019**, *648* (2), 787–797. https://doi.org/10.1016/j.scitotenv.2018.08.159.

(495)   Loupa, G.; Karageorgos, E.; Rapsomanikis, S. Potential Effects of Particulate Matter from Combustion during Services on Human Health and on Works of Art in Medieval Churches in Cyprus. *Environ. Pollut.* **2010**, *158* (9), 2946–2953. https://doi.org/10.1016/j.envpol.2010.06.005.

(496)   Shinyei Kaisha. No Title http://c1233384.r84.cf3.rackcdn.com/UK_SHN_PPD20V_Dust_Sensor_How_it_works_AN.pdf (accessed Sep 10, 2018).

(497)   Williams, R.; Kaufman, A.; Hanley, T.; Rice, J.; Garvey, S. Evaluation of Field-Deployed Low Cost PM Sensors. **2014**, No. December. https://doi.org/EPA/600/R-14/464 (NTIS PB 2015-102104).

(498)   Lee, J. Y.; Shin, H. J.; Bae, S. Y.; Kim, Y. P.; Kang, C.-H. Seasonal Variation of Particle Size Distributions of PAHs at Seoul, Korea. *Air Qual. Atmos. Heal.* **2008**, *1* (1), 57–68. https://doi.org/10.1007/s11869-008-0002-2.

(499)   Tittarelli, A.; Borgini, A.; Bertoldi, M.; De Saeger, E.; Ruprecht, A.; Stefanoni, R.; Tagliabue, G.; Contiero, P.; Crosignani, P. Estimation of Particle Mass Concentration in Ambient Air Using a Particle Counter. *Atmos. Environ.* **2008**, *42* (36), 8543–8548. https://doi.org/10.1016/j.atmosenv.2008.07.056.

(500)   Militello-hourigan, R. E.; Miller, S. The Impacts of Cooking and an Assessment of Indoor Air Quality in Colorado Passive and Tightly Constructed Homes. *To Be Publ.* **2018**. https://doi.org/10.1016/j.buildenv.2018.08.044.

(501)   Kontozova-Deutsch, V.; Deutsch, F.; Bencs, L.; Krata, A.; Van Grieken, R.; De Wael, K. Optimization of the Ion Chromatographic Quantification of Airborne Fluoride, Acetate and Formate in the Metropolitan Museum of Art, New York. *Talanta* **2011**, *86* (1), 372–376. https://doi.org/10.1016/j.talanta.2011.09.030.

# Communications

## Peer review articles

<u>Accepted</u>

Victoria Beltran\*, **Andrea Marchetti\***, Steven De Meyer, Gert Nuyts, Karolien De Wael
*Geranium lake pigments: the role of the synthesis on the structure and composition*
Dyes and Pigments, 189, Pages XX-XX, **2021**.
Impact factor: 4.613


**Andrea Marchetti**, Rolando Saniz, Dileep Krishnan, Laura Rabbachin, Gert Nuyts, Steven De Meyer, Johan Verbeeck, Koen Janssens, Claudia Pelosi, Dirk Lamoen, Bart Partoens, and Karolien De Wael
*Unraveling the Role of Lattice Substitutions on the Stabilization of the Intrinsically Unstable $Pb_2Sb_2O_7$ Pyrochlore: Explaining the Lightfastness of Lead Pyroantimonate Artists' Pigments,*
Chemistry of Materials, 32, 7, Pages 2863–2873, **2020**.
Impact factor: 9.567


Dario Battistel, Marco Roman, **Andrea Marchetti**, Natalie Kehrwald, Marta Radaelli, Eleonora Balliana, Giuseppa Toscano, Carlo Barbante,
*Anthropogenic Impact in the Maya Lowlands of Petén, Guatemala, during the last 5500 years,*
Journal of Quaternary Science, Volume 33, Pages 166-176, **2018.**
Impact factor: 2.469


**Andrea Marchetti\***, Sanaz Pilehvar\*, Lucy't Hart\*, Diana Leyva Pernia, Olivier Voet, Willemien Anaf, Gert Nuyts, Elke Otten, Serge Demeyer, Olivier Schalm and Karolien De Wael,
*Indoor environmental quality index for conservation environments: The importance of including particulate matter,*
Building and Environment, Volume 126, Pages 132-146, **2017.**
Impact factor: 4.053

In preparation

**Andrea Marchetti\***, Victoria Beltran\*, Patrick Storme, Gert Nuyts, Louis Van Der Meeren, Andre Skirtach, Elke Otten, Marjolijn Debulpaep, Lieve Watteeuw, Karolien De Wael
*All that glitters is not gold: unraveling the material secrets behind the pristine appearance of 16th-century brass sequins.*


**Andrea Marchetti**\*, Victoria Beltran\*, Gert Nuyts, Jakub Jaroszewicz, Ferenc Borondics, Christophe Sandt, Marina Van Bos, Steven De Meyer, Elke Otten, Marjolijn Debulpaep, Karolien De Wael
*Glass-induced metal corrosion of otherwise extraordinarily stable brass decorative elements.*


Victoria Beltran\*, **Andrea Marchetti**\*, Gert Nuyts, Margje Leeuwestein, Christophe Sandt, Ferenc Borondics, Karolien De Wael
Nanoscale analysis of historical paintings by means of optical-photothermal infrared (O-PTIR) spectroscopy: The identification of the organic particles in *L'Arlésienne (portrait of Madame Ginoux)* by Van Gogh


**Andrea Marchetti**, Willemien Anaf, Olivier Schalm, Ana Cabal, Jan Callier, Olivier Voet, Piet Van Espen, Karolien De Wael
*Field testing of low-cost sensors for the monitoring of PM and gaseous pollutants for heritage applications.*

# Conference and workshop contributions

<u>**Andrea Marchetti**</u>, Rolando Saniz, Laura Rabbachin, Gert Nuyts, Steven De Meyer, Ligia Maria Moretto, Koen Janssens, Dirk Lamoen, Bart Partoens, Claudia Pelosi, Karolien De Wael
*Optoelectronic structure and photochemical properties of lead pyroantimonate pigments: understanding their lightfastness.*
Oral presentation at Technart 2019 - Bruges, Belgium 7-10.05.2019
332

**Andrea Marchetti**, Patrick Storme, Gert Nuyts, Victoria Beltran, Lieve Watteeuw, Marjolijn Debulpaep, Karolien De Wael
*All that glitters is not gold: characterization of metallic decorative elements from five Enclosed Gardens.*
Poster presentation at Technart 2019 - Bruges, Belgium 7-10.05.2019

**Andrea Marchetti**, Willemien Anaf, Olivier Schalm, Ana Cabal, Jan Callier, Olivier Voet, Piet Van Espen, Karolien De Wael
*Field testing of low-cost sensors for the monitoring of PM and gaseous pollutants for heritage applications.*
Oral presentation at IAQ2018 - Krakow, Poland 10-12.10.2018

Accepted contributions cancelled due to the on-going health crisis

**A. Marchetti,** R. Saniz, D. Krishnan, L. Rabbachin, G. Nuyts, S. De Meyer, J. Verbeeck, K. Janssens, C. Pelosi, D. Lamoen, B. Partoens, K. De Wael
*Unraveling the effect of lattice substitutions on the structural stability and optoelectronic properties of lead pyroantimonate artists' pigments*
Oral presentation at InArt2020 - Paris, France (programmed for 30.09-03.10.2020)

**A. Marchetti,** V. Beltran, J. Jaroszewicz, P. Storme, G. Nuyts, M. Debulpaep, K. De Wael
*The influence of glass on the degradation of brass: evidence from five Enclosed Gardens*
Poster presentation at InArt2020 - Paris, France (programmed for 30.09-03.10.2020)

V. Beltran, **A.Marchetti,** K. De Wael
*Geranium lake pigments: structure and changes during ageing*
Oral presentation at IRUG14 - Amersfoort, The Netherlands (programmed for 27.05-29.05.2020)